eman ta zabal zazu

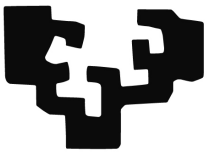

Universidad del País Vasco
Euskal Herriko Unibertsitatea

DEPARTAMENTO DE CIENCIAS DE LA COMPUTACIÓN E INTELIGENCIA ARTIFICIAL

FUNDACIÓN PARA LA INVESTIGACIÓN Y LA DOCÉNCIA MARIA ANGUSTIAS GIMÉNEZ (FIDMAG)

CENTRO DE INVESTIGACIÓN BIOMÉDICA EN RED DE SALUD MENTAL (CIBERSAM)

COMPENDIO DE MÉTODOS PARA CARACTERIZAR LA GEOMETRÍA DE LOS TEJIDOS CEREBRALES A PARTIR DE IMÁGENES DE RESONANCIA MAGNÉTICA POR DIFUSIÓN DEL AGUA

Trabajo de Tesis para optar al grado de
Doctor en Ingeniería Informática

Erick Jorge Canales Rodríguez

San Sebastián, España
2015

COMPENDIO DE MÉTODOS PARA CARACTERIZAR LA GEOMETRÍA DE LOS TEJIDOS CEREBRALES A PARTIR DE IMÁGENES DE RESONANCIA MAGNÉTICA POR DIFUSIÓN DEL AGUA

Trabajo de Tesis para optar al grado de
Doctor en Ingeniería Informática

Por

Autor: M.Sc. Erick Jorge Canales Rodríguez

Tutores: Ph.D. Jesús María Yurramendi Mendizabal

Ph.D. Raymond Salvador Civil

San Sebastián, España
2015

"*Y todo, como el diamante,*

Antes que luz es carbón"

José Martí (Versos Sencillos, 1891)

RESUMEN

La técnica de imagen de resonancia magnética por difusión es una modalidad de imagen de resonancia magnética empleada para estudiar el proceso de difusión molecular del agua en tejidos biológicos y medios porosos. Cuando el movimiento natural de las moléculas se ve restringido y modificado por la presencia de barreras, los experimentos de resonancia magnética por difusión brindan información sobre la geometría confinante. En los últimos años esta técnica ha sido la principal herramienta para estudiar la microestructura y organización espacial de los tejidos del cerebro de forma no invasiva. Existen numerosas aplicaciones radiológicas en tejidos de otros órganos, incluyendo los que conforman la columna vertebral, el corazón, la lengua y músculos estriados unidos al esqueleto.

Entre los métodos de análisis que se han propuesto para modelar e interpretar los datos observados, el modelo del tensor de difusión fue el primero en considerar la anisotropía del proceso de difusión del agua en el cerebro, donde la difusión ocurre de forma desigual en diferentes direcciones debido a la disposición espacial de los tejidos. Sin embargo, en este modelo se asume que el proceso de difusión tiene una geometría elipsoidal, suposición inválida para muchas regiones del cerebro que compromete la interpretación de los resultados. Tal limitación ha impulsado el reciente desarrollo de nuevos modelos teóricos, esquemas de medición y algoritmos de reconstrucción. Mientras algunas de estas técnicas se han basado en considerar un número mínimo de suposiciones teóricas, como las técnicas de imagen q-ball, la imagen espectral de difusión y en cierto grado la transformada de orientación de la difusión, otras técnicas se han basado en modelos paramétricos, como el modelo de mezcla de múltiples tensores de difusión y el método de deconvolución esférica. A pesar de la notable mejora que introducen estos métodos en relación al tensor de difusión, algunos de ellos tienen limitaciones prácticas y su formulación teórica aún se encuentra en creciente desarrollo; en otros, los métodos numéricos empleados en la estimación no son necesariamente óptimos debido a que han obviado aspectos que podrían ser relevantes.

Con el objetivo de extender y perfeccionar varias de las herramientas modernas dedicadas a la modelización de imágenes de resonancia magnética por difusión, en el marco de esta tesis se presenta un compendio de métodos para obtener estimadores más realistas de la estructura arquitectónica del cerebro humano. Las nuevas metodologías propuestas van acompañadas de desarrollos teóricos que permiten entender con mayor amplitud los conceptos sobre las que se basan y su interrelación. Las técnicas desarrolladas en este compendio encuentran aplicación en las neurociencias, la medicina y la psiquiatría. Estas han sido publicadas en revistas científicas de alto impacto y son actualmente empleadas en el estudio de las alteraciones cerebrales en pacientes con enfermedades mentales, así como en el mapeo del ‘conectoma humano’ – el mapa de las conexiones estructurales en todo cerebro.

ÍNDICE

PARTE I: INTRODUCCIÓN

CAPÍTULO 1: INTRODUCCIÓN

1.1 Motivación

El cerebro humano contiene miles de millones de neuronas que se comunican entre sí por medio de sus axones, formando complejas redes neurales. Uno de los preceptos fundamentales de la neurociencia moderna, planteado explícitamente en el trabajo de sus fundadores, establece que las propiedades computacionales del cerebro son una consecuencia directa de sus circuitos (1). La complejidad estructural de estos circuitos condiciona en gran medida el funcionamiento de las redes neuronales, mediante las cuales el cerebro realiza complejas tareas neurofisiológicas como el lenguaje, la atención y la percepción. El mapeo estructural de tales redes durante estados patológicos y de salud es esencial para entender el funcionamiento de tan complicado órgano (2). Sin embargo, el estudio de la conectividad estructural del cerebro se ha visto limitado históricamente por la falta de métodos no invasivos que permitan el adecuado estudio de la anatomía axonal.

Durante las últimas décadas, el advenimiento de modernas técnicas de neuroimagen como la resonancia magnética (del inglés: *Magnetic Resonance Imaging,* MRI) (3) ha posibilitado un aumento sin precedentes en el número de investigaciones destinadas al estudio del cerebro. Esta técnica permite visualizar las estructuras cerebrales por medio de la aplicación de fuertes campos magnéticos que actúan selectivamente sobre los átomos de hidrógeno de nuestro organismo. A diferencia de muchas otras técnicas empleadas en radiología, la resonancia magnética no produce radiaciones ionizantes dañinas, lo que permite obtener visualizaciones anátomo-funcionales tridimensionales del cerebro *in vivo* sin afectar al sujeto que se somete a ella. Esta característica, unida a que es la técnica de neuroimagen que posee mayor resolución espacial, explica su liderazgo como herramienta para el mapeo del cerebro humano, uno de los principales retos científicos del presente siglo (1).

En los últimos años ha emergido una nueva modalidad de imagen de resonancia magnética, conocida como resonancia magnética por difusión (del inglés: *Diffusion Magnetic Resonance Imaging,* dMRI) (4). Esta técnica es empleada en el estudio de la geometría tridimensional del proceso de difusión del agua en tejidos biológicos. Debido a que el proceso de difusión del agua está estrechamente relacionado con la geometría del medio que lo confina, esta herramienta permite a su vez el estudio de la organización axonal en los tejidos del sistema

nervioso, donde el movimiento de las moléculas de agua se encuentra especialmente obstaculizado (5).

La técnica de imagen dMRI sustenta sus bases en principios físicos establecidos en las teorías cinético-molecular, cuántica y electromagnética de la materia. Dichas teorías establecen que el momento magnético de un espín (protón de hidrógeno) bajo la acción de un campo magnético estático externo (producido por el escáner mediante un electroimán) realiza un movimiento de precesión en torno a la dirección de dicho campo (6). Como consecuencia, un conjunto de espines orienta su magnetización neta de forma paralela a la dirección del campo magnético externo aplicado. Mediante la aplicación adicional de pulsos electromagnéticos de radiofrecuencia es posible rotar el vector de magnetización neta hacia el plano transversal correspondiente a la dirección del campo magnético estático. El proceso de difusión debido al movimiento molecular de las moléculas provoca una disminución en la magnetización transversal neta del sistema. La idea básica de la dMRI reside en cuantificar la difusión molecular a lo largo de diferentes direcciones espaciales por medio de este decaimiento de la magnetización transversal y en usar estas medidas para caracterizar y determinar, mediante modelación inversa, la estructura de los tejidos (6). Este procedimiento ha permitido visualizar estructuras celulares que no se pueden detectar con técnicas convencionales de resonancia magnética (7). Desde el punto de vista clínico tiene importantes aplicaciones en la detección de anomalías en la masa encefálica, causadas por tumores, isquemia e infartos cerebrales, enfermedades neurodegenerativas como el Alzheimer, Esclerosis, Ataxia, enfermedad de Huntington, enfermedad de Parkinson, atrofia muscular espinal, o enfermedades mentales como la esquizofrenia y otros trastornos psicóticos (2).

El diseño experimental de adquisición de neuroimágenes de resonancia magnética por difusión se basa en medir la señal generada en cada uno de los cientos de miles de pequeños rectángulos/píxeles tridimensionales (llamados *voxels*) en que es estructurado el cerebro para su medición. En cada uno de estos voxels se realizan múltiples mediciones en diferentes direcciones espaciales para caracterizar la anisotropía del proceso de difusión. Dicha anisotropía se debe a la presencia de barreras celulares que obstaculizan el movimiento del agua en determinadas direcciones, en función de su orientación espacial y su forma geométrica. Mediante esta metodología se pueden obtener estimaciones a nivel local de la organización direccional de los haces de fibras nerviosas en la sustancia blanca del cerebro. Como resultado, se pueden construir campos vectoriales que representan la orientación de las fibras nerviosas en cada punto del cerebro. Posteriormente, esta información puede ser

aprovechada para determinar, mediante el uso de algoritmos de trazado de fibras (8) (del inglés: *fiber tracking* o *tractography*), si dos regiones del cerebro se encuentran conectadas por fibras nerviosas y para establecer la disposición espacial de dichos tractos (9).

El desarrollo de la dMRI ha incrementado el interés en la estimación y visualización de los patrones de conectividad anatómica presentes en el cerebro humano. Tanto es así que el trazado de fibras nerviosas a partir de datos dMRI constituye la principal herramienta para llevar a cabo el proyecto del 'conectoma humano' – un proyecto científico internacional que tiene como objetivo básico el conocimiento de las vías axonales que conectan las neuronas del cerebro humano (5). Esta técnica también ha encontrado aplicación en el campo de la neurocirugía, para informar al cirujano sobre las relaciones anatómicas tridimensionales de cada paciente (10).

La calidad de la estimación de los patrones de conectividad cerebral depende en gran medida de la exactitud de los métodos empleados en la determinación de la orientación axonal en cada voxel. Por esta razón la comunidad científica está dedicando un considerable esfuerzo al desarrollo de nuevos modelos teóricos y algoritmos de estimación 'intravoxel' que tienen como propósito obtener estimadores realistas de la geometría microscópica de los tejidos. En los últimos años se han venido realizando concursos internacionales (véase, por ejemplo (11) y (12)) para identificar las mejores técnicas de reconstrucción.

1.2 Resonancia magnética por difusión: Breve recuento histórico

Poco después del descubrimiento del fenómeno de la resonancia magnética nuclear (del inglés: *Nuclear Magnetic Resonance*) por Bloch (13,14) y Purcell (15), laureados con el premio nobel de física en 1952 por dicho hallazgo, Hahn publicó un trabajo (16) en el cual notó que el movimiento térmico aleatorio de los espines podía reducir la amplitud de la señal observada en presencia de un campo magnético no homogéneo. Seguidamente Carr y Purcell (17) desarrollaron un conjunto de ecuaciones que relacionaban la atenuación de la amplitud de la señal con saltos discretos de los espines y Torrey (18) llevó a cabo una descripción continua basándose en la ecuación de movimiento de la magnetización neta del sistema, a la que añadió un término que consideraba el proceso de difusión, conocida por ecuación de Bloch-Torrey.

En 1965 Stejskal y Tanner (19) desarrollaron la metodología y teoría de un experimento de resonancia magnética basado en una secuencia de pulsos de gradientes que permitió la

medición cuantitativa de los coeficientes de difusión molecular. Las primeras imágenes de resonancia magnética del cuerpo humano se obtuvieron en la década de los setenta, gracias a los trabajos de Paul C. Lauterbur (20) y Peter Mansfield (21), condecorados con el premio nobel de fisiología y medicina en 2003 por su invención, la cual fue posteriormente mejorada con la propuesta de Richard Ernst (22) de codificación por frecuencia y fase, y el uso de la transformada de Fourier, hallazgo por el cual este último investigador recibió el premio nobel de química en 1991.

Varios estudios acerca de la difusión en espacios restringidos fueron reportados por Woessner (23), Stejskal y Tanner (19,24,25) y Cotts (26). A partir de la década de los setenta se comenzó a estudiar la difusión molecular aplicada a la biología (4)(27). Con el objetivo de caracterizar por vez primera la anisotropía que presentan los tejidos cerebrales, en 1994 Basser (28) introdujo el formalismo del tensor de difusión del agua (del inglés: *Diffusion Tensor Imaging* (DTI)) y propuso un método para estimarlo. Posteriormente se han desarrollado otros modelos más realistas y calculado otras magnitudes para describir y cuantificar la difusión del agua.

Finalmente, en esta última década se han empleado técnicas de difusión en diversas aplicaciones, desde el estudio de complejos fluidos en movimiento, medios porosos y compuestos químicos, hasta la caracterización de la anatomía cerebral y la cuantificación de su afectación en diversas patologías. A modo de ejemplo, la base de datos de literatura biomédica 'PubMed' muestra más de 8700 artículos publicados en los últimos 10 años bajo el término '*Diffusion Tensor Imaging*'.

1.3 Métodos de reconstrucción intravoxel: Breve revisión y situación actual

La técnica del tensor de difusión posibilitó por vez primera obtener información relevante sobre la estructura y orientación de los tejidos biológicos *in vivo* y de forma no invasiva (29). Sin embargo, esta técnica se sustenta en suposiciones teóricas que condicionan su validez e interpretación. La principal limitación de la metodología es que sólo puede identificar la orientación de un haz de fibras nerviosas paralelas en cada voxel. Por tanto, la técnica falla en regiones del cerebro donde existe más de un haz de fibras por voxel, por ejemplo, en regiones donde diferentes fibras se cruzan, divergen o convergen. Existe evidencia de que la sustancia blanca del cerebro está compuesta en gran parte por este tipo de regiones de estructura compleja (30).

Para superar esta dificultad se han desarrollado otros métodos de reconstrucción, usualmente basados en esquemas de medición de la señal que emplean un mayor número de direcciones que las requeridas para estimar el tensor. Estos esquemas de alta resolución angular (del inglés: *High Angular Resolution Diffusion Imaging* (HARDI)) (31,32)(33), posibilitan una mejor caracterización angular de la anisotropía.

Una clase muy popular de métodos de reconstrucción basados en esquemas HARDI son los métodos 'multi-compartimentos', en los que se asume que el volumen contenido en el voxel está formado por un número pequeño de compartimentos inconexos y que cada compartimento contiene un único haz de fibras nerviosas paralelas. En estos métodos se asume que la señal medida es la mezcla, o suma ponderada, de las señales provenientes de cada compartimento de fibras y que las señales son proporcionales a los volúmenes que estos ocupan. Un ejemplo de este tipo de modelo es el multi-tensor (33), el cual asume que el proceso de difusión en cada compartimento se describe por un tensor de difusión. El objetivo de tal modelización es obtener información, mediante estimación inversa, sobre los parámetros relevantes de cada compartimento, como la orientación de las fibras contenidas, su grado de empaquetamiento, volumen, etc. En la práctica la estimación de este tipo de modelo posee algunos problemas. Por una parte, el modelo resultante de la señal pasa de ser mono-exponencial, en el caso del tensor de difusión, a multi-exponencial para el modelo multi-tensor, requiriendo este último de la aplicación de algoritmos numéricos inestables, altamente dependientes del nivel de ruido en los datos y de los parámetros del algoritmo. Por otra parte, en el modelo multi-tensor también se hace necesario especificar de antemano el número 'k' de compartimentos que existe en cada voxel del cerebro, información de la que no se dispone y que ha obligado a aplicar métodos estadísticos de comparación de modelos para seleccionar el más apropiado. Por ejemplo, Tuch y col. (33) utilizaron un máximo de k=2 compartimentos; Hosey y col. (34) extendieron el marco de modelación Bayesiana propuesto por Behrens y col. (35) para calcular las probabilidades relativas de los modelos de k=1 y k=2 compartimentos de fibras; Behrens y col. (36) desarrollaron un método basado en el formalismo de la 'Determinación automática de relevancia Bayesiana' (del inglés: *Bayesian Automatic Relevance Determination* (ARD)) para inferir el número de fibras en el voxel, el cual permitió detectar en algunos casos hasta k=3 compartimentos diferentes de fibras.

Otro tipo de aproximación muy relacionado con los modelos multi-compartimentos es la técnica de deconvolución esférica (del inglés: *Spherical Deconvolution* (SD)) (37–40), la cual se basa en una formulación integral-continua de modelo de mezcla. Esta técnica permite

estimar directamente la función de distribución orientacional de las fibras de sustancia blanca (del inglés: *fiber Orientational Distribution Function* (fODF)), sin necesidad de tener que asumir *a priori* el número de compartimentos de fibras en el voxel. En el método SD primero se estima el valor promedio de la señal de difusión en regiones donde se sabe que sólo existen fibras nerviosas paralelas (término conocido por función de respuesta de un haz de fibras), y posteriormente, para cada voxel se estima la función fODF mediante un procedimiento de inversión (deconvolución) entre la señal medida y la función de respuesta estimada. Entre los métodos de estimación más populares se encuentran la deconvolución esférica restringida (del inglés: *Constrained Spherical Deconvolution* (CSD)) (38) y la deconvolución esférica amortiguada de Richardson-Lucy (del inglés: *damped Richardson-Lucy Spherical Deconvolution* (dRL-SD)) (41). Sin embargo, a pesar de su buen funcionamiento en comparación con otras técnicas tradicionales de estimación, estos métodos aún poseen limitaciones relevantes. Ambos asumen, en cierto grado, que el ruido producido por el escáner es aditivo y proveniente de una distribución gaussiana con valor medio igual a cero, por lo que son potencialmente vulnerables a situaciones donde estos requisitos no se cumplen. De hecho, se sabe que el ruido producido en los escáneres de resonancia magnética no sigue una distribución gaussiana y que la distribución real depende de muchos factores tales como el número de bobinas usadas en la medición y el método usado para combinar las señales resultantes. En concreto, los datos experimentales muestran que el ruido obedece distribuciones de 'Rice' (42) y 'Chi no central' (43), evidenciando lo inapropiado de asumir una distribución gaussiana especialmente en imágenes de difusión, usualmente contaminadas con altos niveles de ruido.

Existen otras metodologías, también de uso muy extendido, que se basan en obtener información sobre la microgeometría del medio sin tener que asumir un modelo paramétrico de señal para cada posible compartimento. Por esta razón, a estas técnicas se les denomina frecuentemente como 'independientes de modelo'. Dentro de las más avanzadas se encuentran la imagen q-ball (del inglés: *q-Ball Imaging* QBI) (44,45) y la imagen espectral de difusión (del inglés: *Diffusion Spectrum Imaging* (DSI)) (46) que han generado un considerable interés debido a importantes ventajas, como son la mencionada independencia de modelo, solidez teórica y la habilidad intrínseca de resolver la heterogeneidad intravoxel. El método DSI permite estimar la función de densidad de probabilidad de los desplazamientos moleculares, conocida también como propagador de difusión, sin la necesidad de asumir ningún modelo paramétrico para la señal ni el propagador (46). En la práctica, el propagador de difusión

dentro de cada voxel es reconstruido usando la Transformada discreta de Fourier de la señal de difusión medida en una 'rejilla' tridimensional, la cual se crea experimentalmente empleando diferentes direcciones e intensidades de gradientes de difusión. Posteriormente, este propagador es proyectado a un retículo esférico para calcular la función de distribución orientacional de la difusión (del inglés: *diffusion Orientation Distribution Function* (ODF)). El valor de la ODF en una dirección dada se obtiene a través de la sumatoria de los valores del propagador de difusión en dicha dirección para todos los valores de longitud de desplazamiento. Debido a que el proceso de difusión ocurre con mayor intensidad en las direcciones paralelas a las fibras nerviosas, los valores de probabilidad de desplazamiento son más altos en estas direcciones. Por tanto, es de esperar que los valores de la función ODF sean máximos justamente a lo largo de las orientaciones principales de las fibras. Por esta razón, la geometría de la ODF, obtenida al calcular esta función en muchas direcciones espaciales diferentes, se utiliza para cuantificar la geometría y direccionalidad de los tejidos. Aunque el método DSI en gran medida es el que ofrece mayor información y además emplea el número menor de suposiciones teóricas, su implementación en la clínica se ha visto limitada por la gran cantidad de datos experimentales que requiere. Por ejemplo, en un escáner clínico esta técnica necesita alrededor de 40 minutos para la adquisición de datos, tiempo que no es tolerado por muchos pacientes. No obstante, resulta interesante mencionar que gracias a recientes avances tecnológicos que permiten acelerar el proceso de medición, esta técnica actualmente constituye una de las principales herramientas con las que se pretende construir el 'conectoma' macroscópico del cerebro humano (47).

En contraposición, el método QBI reconstruye la ODF directamente a partir de los datos sin la necesidad de computar previamente el propagador de difusión. La ODF es estimada indirectamente midiendo la señal de difusión en una superficie esférica (lo cual es posible experimentalmente al emplear una intensidad de gradiente de difusión constante para todas las diferentes direcciones) y aplicando la transformada de Radon sobre la esfera a la señal medida (44,45). Este procedimiento hace el QBI más apropiado que el DSI para aplicaciones clínicas debido a que requiere un menor tiempo de adquisición de datos en el escáner – usualmente menos de la mitad. Sin embargo, la ODF computada por el QBI es sólo una aproximación de la ODF exacta, teniendo ésta aproximación menor capacidad que el DSI para detectar diferentes grupos de fibras en un voxel, especialmente cuando estas se encuentran dispuestas de tal forma que el ángulo entre las fibras es pequeño (44,45)(48).

La transformada de orientación de difusión (48) (del inglés: *Diffusion Orientation Transform Imaging* (DOT)) es otro modelo propuesto para caracterizar la microgeometría de los tejidos fibrosos. En el modelo DOT la Transformada de Fourier que aparece en el método DSI es evaluada analíticamente en coordenadas esféricas bajo la suposición de que la señal de difusión se atenúa mono-exponencialmente a lo largo de cada dirección espacial y como función de los valores de intensidad de los gradientes de difusión empleados y el coeficiente de difusión 'aparente' en dicha dirección (del inglés: *Apparent Diffusion Coefficient* (ADC)). Bajo esta aproximación, el modelo DOT transforma la función ADC en la función de probabilidad de los desplazamientos moleculares evaluada a una longitud de desplazamiento constante y que debe ser especificada de antemano – usualmente se elige en el rango de 10 a 20 micrómetros, una distancia mayor que el radio de los axones. Resulta interesante notar que a diferencia de las técnicas DSI y QBI, que caracterizan la heterogeneidad en la orientación de las fibras mediante la función ODF, en el modelo DOT se accede a esta heterogeneidad mediante una función diferente, la probabilidad de desplazamiento evaluada a la longitud especificada. La principal limitación de esta metodología es que el modelo mono-exponencial asumido es inexacto bajo algunas condiciones experimentales, tales como las que se encuentran en esquemas de medición que usan largos tiempos de difusión y fuertes gradientes de campos magnéticos. Además, resulta complejo elegir de antemano el valor de longitud de desplazamiento que posibilitará caracterizar los tejidos de forma óptima.

En resumen, a pesar de que en los últimos años ha habido un avance importante en el desarrollo de nuevos métodos para caracterizar la organización de los tejidos cerebrales, aún existen problemas en las metodologías existentes. En el marco de esta tesis cada una de las técnicas mencionadas será abordada en profundidad para identificar y solucionar sus principales limitaciones.

1.4 Planteamiento del problema

Las técnicas de estimación intravoxel basadas en datos de resonancia magnética por difusión aún no permiten obtener de forma precisa la información morfológica de los tejidos del cerebro. Varias de las principales técnicas tienen margen de mejora en cuanto a su formulación teórica, diseño de medición experimental y algoritmos de reconstrucción. Para obtener una mejor caracterización de la microestructura de los tejidos es necesario mejorar los modelos y técnicas de estimación actuales. Por otro lado, estos deben de adecuarse a las restricciones que imponen la práctica clínica y la investigación.

1.5 Hipótesis

El desarrollo de modelos físico-matemáticos y algoritmos de estimación adecuados permitirá una caracterización más realista de la estructura y orientación del tejido cerebral, y una mejor aplicación en la práctica clínica y en la investigación.

1.6 Objetivo general

Desarrollar y proponer un compendio de métodos que permita mejorar y extender las principales herramientas modernas dedicadas al tratamiento de imágenes de difusión para obtener estimadores más confiables de la estructura arquitectónica del cerebro humano.

1.6.1 *Objetivos específicos principales*

- Desarrollo de un método que determine la función de orientación del proceso de difusión del agua (ODF) como extensión a la técnica de imagen q-ball. Obtención de una expresión teórica exacta para estimar la ODF a partir de imágenes de difusión de alta resolución angular en el espacio-q.
- Desarrollo de un formalismo matemático que extienda el método de la transformada de orientación de la difusión. Investigar aspectos teóricos y experimentales relevantes a la calidad de la reconstrucción. Desarrollo de nuevas ecuaciones analíticas para estimar diferentes variantes de la ODF que sean inmunes a los artefactos producidos por la implementación actual de la técnica.
- Desarrollo de un marco general para rectificar y descontaminar la función de distribución de probabilidad de los desplazamientos moleculares estimada por la

técnica de imagen espectral de difusión. Obtención de mapas cuantitativos del proceso de difusión con mayor contraste de los tejidos.

- Desarrollo de un nuevo enfoque Bayesiano-Estadístico y su aplicación en un algoritmo de estimación para la identificación de los principales haces de fibras nerviosas en cada voxel, así como de los parámetros físicos que lo caracterizan. Obtención de mapas probabilísticos de los cruces de fibras en el cerebro.
- Desarrollo de un algoritmo robusto para la estimación de la orientación de las fibras nerviosas mediante deconvolución esférica que tenga en cuenta la verdadera distribución del ruido generado en los escáneres de resonancia magnética y su sesgo. Incorporación de un término de corrección espacial que tenga en cuenta la continuidad espacial de las imágenes del cerebro para minimizar el efecto del alto nivel de ruido experimental.
- Validación de cada uno de los métodos anteriores en datos simulados y en datos reales obtenidos a partir de un 'phantom' (compuesto por paquetes de capilares inmersos en agua) que simula las fibras nerviosas del cerebro. Comparación de la calidad de reconstrucción de los nuevos métodos propuestos con sus predecesores. Aplicación de los métodos en datos reales de cerebros humanos.
- Creación de una página web ubicada en la web de la Sociedad Española de Neuroimagen donde esté disponible gratuitamente la implementación de los métodos abordados en la tesis.

1.7 Estructura de la tesis

La tesis consta de cuatro partes fundamentales:

I) Introducción: Compuesta por el Capítulo 1, en el que se introduce el tema bajo estudio, se exponen las motivaciones e hipótesis y se detallan los objetivos del trabajo.

II) Bases teóricas: Capítulos 2, 3 y 4. En ellos se describen brevemente los fundamentos teóricos que se abordan en la tesis y que son útiles para entender los capítulos que le suceden. En particular estos capítulos abordan los principios del proceso de la difusión molecular, la formación de imágenes de resonancia magnética por difusión y las características de la difusión en los tejidos cerebrales.

III) Compendio de publicaciones: Capítulo 5, compuesto por cinco secciones. Presenta en detalle el compendio de contribuciones que constituyen el aporte fundamental de esta tesis. Las cinco secciones corresponden a artículos que ya han sido publicados en revistas internacionales de alto impacto.

IV) Discusión: Capítulo 6 y apartados de apéndices y referencias. Contiene la discusión y conclusiones generales de la tesis donde se resumen los aportes de este trabajo, así como las recomendaciones para los trabajos futuros que sigan desarrollando esta temática. Además, se incluyen apéndices donde se amplían con mayor detalle algunas de las demostraciones matemáticas de interés. Se listan todas las contribuciones del autor, así como los premios y reconocimientos a los trabajos incluidos en la presente memoria. En el último apéndice se describe una página web creada para facilitar los códigos que implementan las técnicas propuestas en esta tesis. Finalmente se incluye un apartado general de referencias bibliográficas.

PARTE II: BASES TEÓRICAS

CAPÍTULO 2: PRINCIPIOS DE LA DIFUSIÓN MOLECULAR

2.1 Ecuaciones de Fick

El concepto de difusión molecular hace referencia al transporte neto de moléculas entre regiones del espacio con diferentes concentraciones como resultado del movimiento aleatorio molecular. Este fenómeno pertenece a la familia de los procesos irreversibles de transporte tales como la conducción de calor o de electricidad. La descripción fenomenológica clásica de la difusión se sustenta en dos conceptos físicos principales. El primero establece que el transporte neto de material (en un fluido homogéneo como el agua) a través de un elemento de superficie es proporcional al gradiente de la densidad del material, en la dirección perpendicular al elemento de área. Este concepto es conocido como la primera ley de Fick, y en el caso unidimensional se escribe mediante la expresión (49):

$$J = -D\frac{\partial C}{\partial x}, \qquad \textbf{(2.1)}$$

donde J es la densidad de flujo molecular, D es el coeficiente de difusión (cuyo valor depende de la sustancia que difunde) y C es la concentración de moléculas.

El segundo principio establece que durante el movimiento la materia que difunde ni se crea ni se destruye (no hay fuentes ni sumideros). Este concepto se conoce como condición de continuidad, y se expresa matemáticamente como:

$$\frac{\partial C}{\partial t} = -\frac{\partial J}{\partial x}. \qquad \textbf{(2.2)}$$

Sustituyendo la ecuación (2.2) en (2.1) obtenemos la ecuación diferencial básica del proceso de difusión, conocida por segunda ley de Fick (49):

$$\frac{\partial C}{\partial t} = \frac{\partial}{\partial x}\left(D\frac{\partial C}{\partial x} \right). \qquad \textbf{(2.3)}$$

Si el coeficiente de difusión no depende de la posición espacial la ecuación anterior toma la forma:

$$\frac{\partial C}{\partial t} = D\frac{\partial^2 C}{\partial x^2}. \qquad \textbf{(2.4)}$$

Estas ecuaciones pueden ser generalizadas de forma directa a un medio homogéneo tridimensional, donde la sustancia que difunde tiene la misma libertad de movimiento en todas las direcciones. A este tipo de proceso de difusión se le llama *isótropo*. En tres dimensiones, la ecuación (2.1) se escribe como:

$$\vec{\mathbf{J}} = \begin{pmatrix} J_x & J_y & J_z \end{pmatrix} = -D\begin{pmatrix} \frac{\partial C}{\partial x} & \frac{\partial C}{\partial y} & \frac{\partial C}{\partial z} \end{pmatrix} = -D\nabla C. \qquad \textbf{(2.5)}$$

Similarmente, la ecuación (2.2) se transforma en:

$$\frac{\partial C}{\partial t} = -\left(\frac{\partial J}{\partial x} + \frac{\partial J}{\partial y} + \frac{\partial J}{\partial z}\right) = -\nabla \cdot \vec{\mathbf{J}}. \qquad \textbf{(2.6)}$$

Combinando las ecuaciones (2.5) y (2.6) obtenemos la segunda ley de Fick en un medio homogéneo tridimensional:

$$\frac{\partial C}{\partial t} = \nabla \cdot \left(D\nabla C\right) = D\left(\frac{\partial^2 C}{\partial x^2} + \frac{\partial^2 C}{\partial y^2} + \frac{\partial^2 C}{\partial z^2}\right). \qquad \textbf{(2.7)}$$

2.2 Movimiento Browniano

A escala microscópica las moléculas están en constante movimiento. Este movimiento errático de las moléculas se conoce cómo movimiento Browniano después que Robert Brown observó el fenómeno en granos de polen suspendidos en agua (50). Posteriormente el proceso fue formulado por Albert Einstein (51), cuya teoría proporciona una explicación cinético-molecular del fenómeno macroscópico de difusión, regido por las leyes de Fick. Las predicciones de Einstein fueron verificadas por Jean Baptiste Perrin, quién por vez primera logró estimar el tamaño del átomo y la cantidad de átomos en un volumen (52); resultados que le hicieron merecedor del premio Nobel de física.

En su investigación teórica sobre el movimiento Browniano y su relación con el coeficiente de difusión Einstein hizo dos suposiciones (53)(51):

1) Cada partícula ejecuta un movimiento que es independiente del movimiento de las otras partículas.

2) El movimiento de una partícula en un intervalo de tiempo puede ser considerado como un proceso independiente de los movimientos ejecutados en los intervalos de tiempos anteriores. Esta suposición se considera válida aún en el límite de pequeños intervalos de tiempo τ (comparado con el intervalo de tiempo total observado).

Notablemente, la formulación de Einstein permite obtener la segunda ley de Fick (ecuación (2.4)) y permite relacionar el coeficiente de difusión molecular D, una magnitud macroscópica, con la función de distribución de probabilidad de los desplazamientos moleculares $P(L,\tau)$, una entidad microscópica:

$$\begin{aligned} &\frac{\partial C}{\partial t} = D\frac{\partial^2 C(x,t)}{\partial x^2}, \\ &D = \frac{1}{2\tau}\int_{-\infty}^{+\infty} L^2 P(L,\tau)\, dL. \end{aligned} \qquad \textbf{(2.8)}$$

La derivación detallada de este resultado se presenta en el APÉNDICE A de la tesis, en el cual también se incluye un desarrollo matemático encaminado a encontrar una expresión analítica para la función $P(L,\tau)$. En particular, se demuestra que en un medio homogéneo en el que no existen direcciones preferenciales al movimiento la ley de los desplazamientos moleculares sigue una distribución de probabilidad de Gauss. Si todas las partículas en el instante inicial $t=0$ se encuentran en el origen de coordenadas $x'=0$, la dependencia espacio-temporal de la concentración molecular también viene dada por la misma ley de distribución de los desplazamientos. Para el caso unidimensional se obtiene,

$$P(L,\tau) = \frac{1}{\sqrt{4\pi D\tau}}\exp\left(-\frac{L^2}{4D\tau}\right). \qquad \textbf{(2.9)}$$

Esta ecuación establece una distribución de Gauss con valor medio igual a cero y una dispersión que depende del tiempo y el coeficiente de difusión, $\sigma = \sqrt{2D\tau}$. Con ayuda de esta ecuación es posible cuantificar los desplazamientos cuadráticos medios que experimentan las partículas. Por ejemplo, en el caso unidimensional – eje X:

$$\overline{x^2} = \int_{-\infty}^{\infty} x^2 P(x,\tau)\,dx = 2D\tau\,. \qquad \textbf{(2.10)}$$

La extensión al caso tridimensional es directa, denotando a r como el desplazamiento total de la partícula, entonces $r^2 = x^2 + y^2 + z^2$, luego $\overline{r^2} = \overline{x^2} + \overline{y^2} + \overline{z^2}$. Tomando en cuenta la homogeneidad del líquido obtenemos: $\overline{r^2} = 3\overline{x^2} = 6D\tau$.

2.3 Difusión anisótropa

2.3.1 *Ley de Fick generalizada*

En las secciones previas se ha analizado el proceso de difusión en medios homogéneos isótropos, donde el coeficiente de difusión es suficiente para cuantificar el desplazamiento cuadrático medio de las partículas en cualquier dirección espacial. En medios anisótropos, donde existen direcciones preferenciales al transporte de materia, las ecuaciones derivadas en las secciones anteriores deben ser generalizadas.

En tres dimensiones, la ley de Fick anteriormente expresada por la ecuación (2.4) se puede generalizar (54) a:

$$\frac{\partial C}{\partial t} = \sum_{n=1}^{\infty}\sum_{k=0}^{n}\sum_{q=0}^{k}\binom{n}{k}\binom{k}{q}\nabla_{n-k,k-q,q}C(\vec{\mathbf{r}},t)\,D_{n-k,k-q,q}\,, \qquad \textbf{(2.11)}$$

donde

$$D_{n-k,k-q,q} = \frac{(-1)^n}{n!\tau}\int \Delta x^{n-k}\Delta y^{k-q}\Delta z^{q} P(\Delta\vec{\mathbf{r}},\tau)\,d\Delta\vec{\mathbf{r}}\,, \qquad \textbf{(2.12)}$$

$\Delta\vec{\mathbf{r}} = (\Delta x\ \Delta y\ \Delta z)$ es el vector de desplazamiento relativo y

$$\nabla_{n-k,k-q,q}C(\vec{\mathbf{r}},t) = \left\{\left(\frac{\partial}{\partial x'}\right)^{n-k}\left(\frac{\partial}{\partial y'}\right)^{k-q}\left(\frac{\partial}{\partial z'}\right)^{q} C(\vec{\mathbf{r}}',t)\right\}_{\substack{x'=x\\ y'=y\\ z'=z}}. \qquad \textbf{(2.13)}$$

La ecuación (2.11) ofrece una generalización a la segunda ley de Fick para el proceso de la difusión (54–56). El término $D_{n-k,k-q,q}$ es un elemento escalar o componente de un tensor de difusión de orden n. Dichos tensores contienen información sobre la anisotropía del proceso de difusión. Si la función de distribución de probabilidad de los desplazamientos tiene simetría 'antipodal' (para una misma orientación es igual en direcciones opuestas $P(\Delta\vec{\mathbf{r}},\tau) = P(-\Delta\vec{\mathbf{r}},\tau)$) los tensores de difusión de orden impar son idénticamente iguales a cero (54).

2.3.2 *Tensor de difusión*

La aproximación más simple que podemos hacer para describir un proceso de difusión anisótropo con simetría antipodal, es asumir que un tensor de difusión de segundo orden ($n=2$) es suficiente para describir el proceso. En tal caso, la ley de Fick generalizada (ecuación (2.11)) toma la forma:

$$\frac{\partial C}{\partial t} = \sum_{k=0}^{2}\sum_{q=0}^{k}\binom{2}{k}\binom{k}{q}\nabla_{2-k,k-q,q} C(\vec{\mathbf{r}},t)\, D_{2-k,k-q,q}\,, \qquad \textbf{(2.14)}$$

nótese que el tensor sólo tiene seis componentes independientes: $\{D_{2,0,0}, D_{1,1,0}, D_{1,0,1}, D_{0,2,0}, D_{0,1,1}, D_{0,0,2}\}$. Esta expresión se puede reescribir como

$$\begin{aligned}\frac{\partial C}{\partial t} = {} & D_{xx}\frac{\partial^2 C}{\partial x^2} + 2D_{xy}\frac{\partial^2 C}{\partial x\partial y} + 2D_{xz}\frac{\partial^2 C}{\partial x\partial z} + \\ & D_{yy}\frac{\partial^2 C}{\partial y^2} + 2D_{yz}\frac{\partial^2 C}{\partial y\partial z} + D_{zz}\frac{\partial^2 C}{\partial z^2},\end{aligned} \qquad \textbf{(2.15)}$$

donde se ha hecho el cambio de nomenclatura: $\{D_{xx} = D_{2,0,0},\ D_{xy} = D_{1,1,0},\ D_{xz} = D_{1,0,1},\ D_{yy} = D_{0,2,0},\ D_{yz} = D_{0,1,1}$ y $D_{zz} = D_{0,0,2}\}$. Finalmente la expresión en (2.15) se puede escribir en la forma compacta:

$$\frac{\partial C}{\partial t} = \nabla\cdot(\mathbf{D}\nabla C)\,, \qquad \textbf{(2.16)}$$

donde

$$\mathbf{D} = \begin{pmatrix} D_{xx} & D_{xy} & D_{xz} \\ D_{xy} & D_{yy} & D_{yz} \\ D_{xz} & D_{yz} & D_{zz} \end{pmatrix}. \qquad \textbf{(2.17)}$$

La matriz $\mathbf{D}$ representa el tensor de difusión de segundo orden, el cual por construcción es simétrico (57). Siguiendo un desarrollo matemático similar al presentado en la sección anterior (véase ecuaciones (2.8)-(2.9)) se puede demostrar que la probabilidad de los desplazamientos moleculares correspondientes a la ecuación diferencial (2.16) es una distribución de Gauss multivariada (58):

$$P(\vec{\mathbf{r}}, \tau) = \frac{1}{\sqrt{4\pi |\mathbf{D}| \tau}} \exp\left(-\frac{\vec{\mathbf{r}} \mathbf{D}^{-1} \vec{\mathbf{r}}^{T}}{4\tau} \right), \qquad \textbf{(2.18)}$$

donde el símbolo $\mathbf{D}^{-1}$ representa la inversa de la matriz $\mathbf{D}$. En esta expresión, por simplicidad, se ha hecho el cambio de nomenclatura $\vec{\mathbf{r}} = \Delta\vec{\mathbf{r}}$ para representar al vector de desplazamiento relativo introducido en la sección anterior. Nótese que si todos los elementos de la diagonal en $\mathbf{D}$ son idénticos a la constante D, y todos los elementos fuera de la diagonal son iguales a cero, la ecuación (2.16) se transforma en la segunda ley de Fick obtenida para un proceso de difusión *isótropo* en tres dimensiones (véase la ecuación (2.7)). En la próxima sección se discutirán varias propiedades importantes relacionadas al tensor de difusión de segundo orden.

2.3.3 *Propiedades del Tensor de difusión*

Los elementos diagonales del tensor de difusión D_{xx}, D_{yy} y D_{zz} son los "coeficientes de difusión efectivos" medidos o estimados a lo largo de los tres ejes ortogonales X, Y, Z del sistema de referencia de laboratorio. Las componentes no diagonales son las covarianzas entre los desplazamientos ocurridos entre estos ejes ortogonales.

El tensor de difusión adquiere su estructura más simple en el sistema de referencia en el cual todos sus elementos no diagonales son idénticamente iguales a cero. En este sistema el flujo difusivo a lo largo de sus tres ejes ortogonales X′, Y′, Z′ está desacoplado. A tal sistema de referencia se le llama sistema de referencia principal o sistema propio del tensor. Este sistema de referencia puede ser obtenido mediante el cálculo estándar de los vectores y valores

propios del tensor (59), también conocidos como autovectores y autovalores, que satisfacen la siguiente ecuación:

$$\mathbf{D}\hat{\mathbf{v}}_i = \lambda_i \hat{\mathbf{v}}_i, \quad \text{para } i = \{1,2,3\}, \tag{2.19}$$

donde $\hat{\mathbf{v}}_i$ y λ_i son los autovectores y autovalores respectivamente. Las tres ecuaciones en **(2.19)** se pueden reescribir en la forma matricial:

$$\mathbf{DR} = \mathbf{RA}, \quad \mathbf{R} = \left(\hat{\mathbf{v}}_1 \mid \hat{\mathbf{v}}_2 \mid \hat{\mathbf{v}}_3\right), \quad \mathbf{A} = \begin{pmatrix} \lambda_1 & 0 & 0 \\ 0 & \lambda_2 & 0 \\ 0 & 0 & \lambda_3 \end{pmatrix}, \tag{2.20}$$

siendo $\mathbf{A}$ una matriz diagonal con los autovalores y $\mathbf{R}$ es la matriz de autovectores, ordenados en columnas. Debido a que **D** es simétrica y definida positiva, los tres autovalores son positivos y los tres autovectores son 'ortonormales' (vectores unitarios ortogonales, cuyo producto escalar es cero). Los autovalores suelen ordenarse de forma que $\lambda_1 \geq \lambda_2 \geq \lambda_3$. De acuerdo a este análisis el tensor de difusión puede ser descompuesto en autovectores y autovalores mediante:

$$\mathbf{D} = \mathbf{RAR}^T, \tag{2.21}$$

nótese que $\mathbf{R}$ puede ser interpretada como la matriz de rotación que transforma al tensor de difusión desde el sistema de referencia principal al sistema de coordenadas de laboratorio.

Resulta instructivo analizar la forma geométrica de los contornos de igual probabilidad de desplazamiento de la función de distribución definida por la ecuación (2.18) evaluada en un tiempo determinado. Estos contornos pueden ser obtenidos igualando el exponente del término exponencial a una constante. En particular, si se considera que el término es igual a 1/2, se obtiene

$$\frac{\vec{\mathbf{r}}\mathbf{D}^{-1}\vec{\mathbf{r}}^T}{2\tau} = 1. \tag{2.22}$$

Insertando la descomposición definida por (2.21) en la ecuación (2.22),

$$\begin{aligned}\frac{\vec{\mathbf{r}}\mathbf{D}^{-1}\vec{\mathbf{r}}^{T}}{2\tau} &= \frac{\vec{\mathbf{r}}\left(\mathbf{R}\mathbf{A}\mathbf{R}^{T}\right)^{-1}\vec{\mathbf{r}}^{T}}{2\tau} \\ &= \frac{\vec{\mathbf{r}}'\mathbf{A}^{-1}\vec{\mathbf{r}}'^{T}}{2\tau} \\ &= \left(\frac{x'}{\sqrt{2\tau\lambda_1}}\right)^2 + \left(\frac{y'}{\sqrt{2\tau\lambda_2}}\right)^2 + \left(\frac{z'}{\sqrt{2\tau\lambda_3}}\right)^2 = 1,\end{aligned} \qquad \textbf{(2.23)}$$

donde $\vec{\mathbf{r}}' = \vec{\mathbf{r}}\mathbf{R}$ es el vector $\vec{\mathbf{r}}$ (medido en el sistema de coordenadas de laboratorio) transformado o rotado al sistema de referencia principal del tensor. La ecuación (2.23) es la ecuación de un elipsoide cuyo eje principal se encuentra orientado según la dirección del eje X' con longitud igual a $\sqrt{2\tau\lambda_1}$. La orientación de este eje está dada por el autovector principal del tensor de difusión $\hat{\mathbf{v}}_1$ (autovector correspondiente al mayor autovalor). Esto se puede verificar considerando que cuando $\vec{\mathbf{r}} = \hat{\mathbf{v}}_1$, se cumple que $\vec{\mathbf{r}}' = [1 \quad 0 \quad 0]$ (nótese que $[1 \quad 0 \quad 0] = \hat{\mathbf{v}}_1\mathbf{R}$). De forma análoga, los restantes ejes del elipsoide se encuentran orientados a lo largo de los ejes Y' (dado por el autovector $\hat{\mathbf{v}}_2$) y Z' (dado por el autovector $\hat{\mathbf{v}}_3$). Las longitudes de estos ejes son $\sqrt{2\tau\lambda_2}$ y $\sqrt{2\tau\lambda_3}$ respectivamente (60).

Del análisis anterior se puede concluir que el tensor de difusión calculado para un medio anisótropo, con una marcada preferencia al proceso de difusión en una dirección determinada, contiene información útil sobre la geometría del medio. En particular, el autovector asociado al mayor autovalor define el eje de difusión preferencial (máxima) del medio, mientras que los otros dos autovectores definen los ejes ortogonales restantes. Además, la anisotropía del proceso de difusión puede ser caracterizada en función del valor de los autovalores (coeficientes de difusión efectivos principales), ya que estos especifican la excentricidad del elipsoide de difusión.

En la práctica se emplean varias medidas para cuantificar las propiedades intrínsecas del medio. Las medidas más usadas poseen invariancia rotacional, o sea, son cantidades que no dependen de la orientación relativa del medio con respecto al sistema de referencia de laboratorio. Tres valores escalares típicos que cumplen con esta propiedad son los invariantes I_1, I_2 y I_3 del tensor, los cuales sólo dependen de los autovalores (60):

$$
\begin{aligned}
I_1 &= \lambda_1 + \lambda_2 + \lambda_3 = Tr(\mathbf{D}) = Tr(\mathbf{A}), \\
I_2 &= \lambda_1\lambda_2 + \lambda_1\lambda_3 + \lambda_2\lambda_3, \\
I_2 &= \lambda_1\lambda_2\lambda_3 = |\mathbf{D}| = |\mathbf{A}|,
\end{aligned}
\qquad \textbf{(2.24)}
$$

donde la función $Tr(\mathbf{X})$ representa la traza de la matriz $\mathbf{X}$.

Los índices más naturales para cuantificar el grado de anisotropía del proceso de difusión son las razones entre sus autovalores. Estos índices adimensionales cuantifican la razón entre los coeficientes de difusión efectivos medidos en las direcciones principales del medio. Por ejemplo, la magnitud λ_2/λ_3 caracteriza la anisotropía rotacional del elipsoide de difusión entorno a su eje principal, mientras que λ_1/λ_2 y λ_1/λ_3, indican la magnitud relativa entre los coeficientes de difusión efectivos en las direcciones preferenciales y transversales del medio. Estos índices son indicadores directos de la excentricidad del elipsoide. También se han propuesto otros índices escalares construidos a partir de los autovalores del tensor (59)(60), entre ellos, el que ha presentado mayor aceptación debido a su alto contraste para diferenciar tejidos de sustancia blanca y gris y su relativamente mayor inmunidad al ruido, es la fracción de anisotropía (del inglés: *Fractional Anisotropy* (FA)).

$$
FA = \sqrt{\frac{(\lambda_1-\lambda_2)^2 + (\lambda_1-\lambda_3)^2 + (\lambda_2-\lambda_3)^2}{2(\lambda_1^2+\lambda_2^2+\lambda_3^2)}}\,. \qquad \textbf{(2.25)}
$$

En regiones del cerebro donde se cumple que $\lambda_1 \gg \lambda_2 \simeq \lambda_3$ (fibras muy alineadas entre sí) la fracción de anisotropía tiene un valor cercano a uno, mientras que en regiones donde se cumple que $\lambda_1 \simeq \lambda_2 \simeq \lambda_3$ (fibras no alineadas, sustancia gris, líquido cefalorraquídeo) la fracción de anisotropía tiene un valor cercano a cero. El valor de este índice es una medida de la coherencia en la orientación del proceso de difusión local y por tanto de la coherencia en la orientación y densidad de los tejidos que lo confinan. En el Capítulo 4 (sección 4.2.1) se presentará la teoría relacionada con la estimación del tensor de difusión y se mostrarán las imágenes resultantes calculadas en un cerebro real.

CAPÍTULO 3: IMAGEN DE RESONANCIA MAGNÉTICA POR DIFUSIÓN

En este capítulo se revisan los principios básicos que sustentan la técnica de imagen de resonancia magnética por difusión. Sin embargo, no se discutirán en detalle los conceptos ni desarrollos matemáticos relacionados al fenómeno de la resonancia magnética nuclear, debido a que estos conceptos son tratados ampliamente en diversos libros de texto (por ejemplo, véase (61) y (62)), y no son imprescindibles para entender el contenido presentado en esta tesis.

3.1 Principios básicos

La técnica de imagen por resonancia magnética es un método de tomografía basado en los principios de la resonancia magnética nuclear (61). La resonancia magnética nuclear involucra los núcleos del objeto a ser muestreado, los campos magnéticos generados por un imán, y el fenómeno de la resonancia producto de las interacciones del núcleo con los campos magnéticos. El cuerpo humano está compuesto aproximadamente de un 60% de átomos de Hidrógeno, los cuales se encuentran principalmente en el agua y las grasas de nuestro organismo. Es por ello que los núcleos de los átomos de Hidrógeno son empleados para obtener imágenes de resonancia magnética del cuerpo humano (61). Existen diferencias en el contenido de agua entre diversos tejidos y órganos, y en muchas enfermedades los procesos patológicos producen cambios en el contenido de agua, estas características se ven reflejadas en las imágenes de resonancia magnética (2).

Esta técnica produce imágenes relacionadas a características físicas y químicas internas del objeto o tejido bajo estudio y en casos particulares nos puede informar sobre el comportamiento temporal de sus componentes. El valor o intensidad de la imagen en un voxel depende de dos grupos de parámetros: (a) los parámetros intrínsecos de la muestra que incluyen la densidad de espín, los tiempos de relajación, los movimientos moleculares tales como difusión y flujo etc. y (b) los parámetros extrínsecos o parámetros del experimento, por ejemplo, la intensidad del campo magnético externo aplicado, la intensidad y duración de los gradientes de campos magnéticos, las características de los pulsos electromagnéticos de radiofrecuencia y el ruido experimental (61). Mediante la elección adecuada de la secuencia de medición experimental y los valores de los parámetros extrínsecos se pueden obtener

imágenes individuales para cada uno de los parámetros intrínsecos mencionados anteriormente. Las imágenes que se analizan en esta tesis son las que dependen del proceso de difusión.

3.2 Señal de resonancia magnética dependiente de la difusión molecular

3.2.1 *Secuencia de Stejskal-Tanner*

La técnica de imagen de resonancia magnética se basa en el hecho de que la frecuencia de precesión, o frecuencia de Larmor, de un espín bajo la acción de un campo magnético no homogéneo depende de su posición absoluta en el espacio. Para el caso de un campo magnético homogéneo de intensidad B_0 la frecuencia de Larmor viene dada por la siguiente relación (62):

$$\omega_0 = \gamma B_0 , \qquad \textbf{(3.1)}$$

donde γ es la razón giromagnética del espín, ($\gamma = 42.58$ MHz/T para el núcleo ^{1}H). Para un campo no homogéneo paralelo al eje Z del sistema de coordenadas de laboratorio de la forma $\mathbf{B}(\vec{\mathbf{r}}) = \left(0 \quad 0 \quad B_0 + \vec{\mathbf{r}}\vec{\mathbf{G}}\right)^T$, donde $\vec{\mathbf{G}}$ es el gradiente del campo magnético aplicado, la frecuencia de Larmor de los espines individuales se encuentra relacionada con la posición de los espines $\vec{\mathbf{r}}$ a lo largo de la coordenada Z.

$$\omega(\vec{\mathbf{r}}) = \omega_0 + \gamma\vec{\mathbf{r}}\vec{\mathbf{G}} . \qquad \textbf{(3.2)}$$

Para sistemas de espines móviles el vector de posición de los espines cambia en el tiempo. Por consiguiente, los espines móviles exhiben una velocidad angular dependiente del tiempo. El factor de fase Φ acumulado durante un periodo de tiempo t dependerá de la trayectoria en el espacio-tiempo de la partícula (6):

$$\Phi(t) = \gamma B_0 t + \gamma\int_0^t \vec{\mathbf{r}}(t')\vec{\mathbf{G}}(t')dt' , \qquad \textbf{(3.3)}$$

donde el primer término del lado derecho corresponde al cambio de fase debido al campo magnético estático y el segundo término representa el cambio de fase debido al efecto del gradiente.

El efecto del proceso de difusión en la señal de resonancia magnética suele estudiarse a partir de la secuencia de Stejskal-Tanner de pulsos de gradiente de campo magnético ilustrada en la Figura 1. El propósito de estos pulsos de gradiente es "diferenciar" magnéticamente los espines portados por las moléculas de acuerdo a su posición espacial en la muestra bajo estudio.

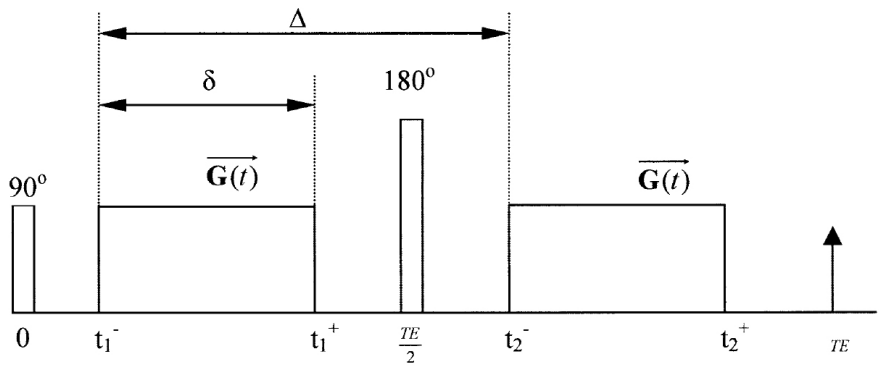

Figura 1. Secuencia de Stejskal-Tanner de pulsos de gradiente, con magnitud de gradiente G, duración δ y separación entre pulsos Δ. La imagen de resonancia magnética es obtenida al medir la señal en el instante de tiempo TE, conocido por tiempo eco.

Para entender el efecto de esta secuencia experimental es necesario primero analizar el efecto de la secuencia sobre un sistema de espines estáticos. El pulso de radiofrecuencia de 90° (rectángulo estrecho en el tiempo 0 de la figura) provoca que la magnetización neta del sistema de espines rote desde su posición de equilibrio (eje de coordenadas Z) hacia el plano transversal (plano formado por los ejes X-Y del sistema de coordenadas). Posteriormente el primer pulso de gradiente (rectángulo comprendido entre los tiempos t_1^- y t_1^+ en la figura) causa que los espines en diferentes posiciones espaciales a lo largo de la coordenada Z roten con diferentes velocidades angulares. Por consiguiente se crea un desfase (dispersión en la distribución de la fase) en el movimiento de rotación de los espines, y ocurre un decaimiento en el valor de la magnetización neta en el plano transversal. El pulso de radiofrecuencia de 180° aplicado en el instante de tiempo $TE/2$ hace que la magnetización neta del sistema rote 180° respecto a su posición anterior. Este pulso de radiofrecuencia provoca un cambio de signo en la fase acumulada. Como consecuencia el movimiento posterior de los espines ocurre en la dirección de la convergencia de la fase, y en una dirección opuesta a la de partida. La aplicación del segundo pulso de gradientes (rectángulo comprendido entre los tiempos t_2^- y t_2^+ en la figura) causa que la velocidad angular a la que rota cada espín (en el sentido de la convergencia de la fase) sea exactamente la misma que la inducida durante la aplicación del primer pulso de gradiente. Como

consecuencia, en el instante de tiempo TE se obtiene una magnetización neta igual a la que existía en el instante inicial del experimento después de la aplicación del pulso de radiofrecuencia de 90°.
Para el caso de espines móviles, por ejemplo espines que experimentan un proceso de difusión, la situación es un tanto diferente. Debido a que durante la aplicación del segundo pulso de gradiente la distribución espacial de los espines es diferente a la distribución espacial inicial, las velocidades angulares de precesión de los espines (en el sentido de la convergencia de la fase) serán diferentes a las generadas por el primer pulso de gradiente. Como consecuencia en el instante de tiempo TE existirá un desfase remanente y la magnetización neta transversal no se recuperará completamente. De esta forma se obtiene una secuencia de medición experimental en la que el desfase y el decaimiento resultante de la magnetización depende de las distancias recorridas por los espines durante su movimiento de difusión en el intervalo de tiempo Δ.

Para el análisis siguiente resulta útil denotar la intensidad y duración del gradiente por las variables $G = \left|\vec{\mathbf{G}}\right|$ y δ respectivamente. El intervalo de tiempo entre el inicio de los pulsos es denotado por Δ. El primer pulso de gradiente induce un cambio en la fase del movimiento de precesión del momento magnético de los espines, la cual depende de su posición espacial. Si el gradiente de campo magnético es aplicado a lo largo de la dirección Z del sistema de coordenadas, el cambio de fase en el instante de tiempo $TE/2$ se puede estimar mediante la siguiente relación:

$$\Phi\left(\frac{TE}{2}\right) = \gamma B_0 \frac{TE}{2} + \gamma \int_{t_1^-}^{t_1^+} z_1 G dt = \gamma B_0 \frac{TE}{2} + \gamma z_1 G \delta, \qquad \textbf{(3.4)}$$

donde z_1 es la posición del espín, asumida constante durante la corta duración del pulso de gradiente (δ). Después de la aplicación del pulso de radiofrecuencia de 180°, el cambio de fase se transforma en $-\Phi(TE/2)$. Similarmente, después de la aplicación del segundo pulso de gradiente, con la misma duración e intensidad que el primero, el cambio de fase en el instante de tiempo TE se puede calcular como:

$$\begin{aligned}\Phi(TE) &= -\Phi\left(\frac{TE}{2}\right) + \gamma B_0 \left(TE - \frac{TE}{2}\right) + \gamma \int_{t_2^-}^{t_2^+} z_2 G dt \\ &= -\gamma B_0 \frac{TE}{2} - \gamma z_1 G \delta + \gamma B_0 \frac{TE}{2} + \gamma z_2 G \delta \qquad \textbf{(3.5)} \\ &= \gamma G \delta (z_2 - z_1),\end{aligned}$$

donde z_2 es la posición del espín durante la aplicación del segundo pulso de gradiente. De este resultado se puede apreciar que para espines estáticos ($z_1 = z_2$), la secuencia de pulsos de gradientes antes descrita no produce un cambio en la fase del movimiento de precesión del sistema. Por otra parte, para espines móviles que cambian su posición espacial en el tiempo existe un desfase neto que dependerá de la distancia recorrida por los espines durante el intervalo de tiempo Δ que separa los pulsos. Esta diferencia de fase afecta la magnetización transversal neta del sistema de espines y se usa para obtener señales que dependen de la difusión molecular.

3.2.2 *La relación de Fourier*

La señal medida en la técnica de resonancia magnética mediante la secuencia de Stejskal-Tanner, la cual da lugar a la imagen observada, es proporcional a la magnetización transversal neta del sistema de espines bajo estudio, que es la suma vectorial de los momentos magnéticos de los núcleos en el volumen de interés. Debido a que estos núcleos pueden tener diferentes historias de movimiento (diferentes valores de desfase), la magnetización neta resultante se calcula como:

$$M(TE) = M_0 \sum_{j=1}^{N_s} \exp\left[i\Phi_j(TE) \right] / N_s , \qquad \textbf{(3.6)}$$

donde N_s es el número de espines que contribuyen a la magnetización neta en el volumen, M_0 es la magnetización transversal neta inicial del sistema de espines y $\Phi_j(TE)$ es el cambio de fase que sufre el espín *j* durante el tiempo TE .

Hasta el momento se han obviado los procesos de relajación que ocurren en el sistema de espines producto de las interacciones electromagnéticas entre los espines (61). Estas interacciones causan un decaimiento adicional de la magnetización transversal neta. Para desacoplar el efecto de los procesos de relajación con el de difusión, la expresión (3.6) suele reescribirse de la siguiente forma:

$$M(TE) = M(TE)_{G=0} \sum_{j=1}^{N_s} \exp\left[i\Phi_j(TE) \right] / N_s , \qquad \textbf{(3.7)}$$

donde $M(TE)_{G=0}$ es la magnetización transversal neta medida en el instante de tiempo TE usando una secuencia de medición similar a la descrita en la Figura 1 pero sin la aplicación de los pulsos de gradientes ($G=0$). Esta magnetización contiene el efecto de los procesos de relajación del sistema de espines que ocurren durante la secuencia experimental.

La expresión (3.7) se puede escribir en forma integral como:

$$M = M_{G=0} \int_{-\infty}^{\infty} \exp(2\pi i q L)\, P(L,\Delta)\, dL, \qquad \textbf{(3.8)}$$

donde $L = z_2 - z_1$, $q = \gamma G\delta / 2\pi$, y $P(L,\Delta)$ es la probabilidad de que ocurra un desplazamiento de longitud L durante un intervalo de tiempo igual a Δ. A esta probabilidad se le conoce como el propagador de difusión promedio del 'ensemble' o conjunto de espines. La relación de Fourier (3.8) es una de las ecuaciones pilares que forman la base de todos los experimentos de imagen en difusión. En esta formulación no se ha asumido ninguna forma específica para la ley de los desplazamientos moleculares, a diferencia del modelo del tensor de difusión donde se asume una distribución de Gauss. En particular, esta relación de Fourier permite estimar el propagador de difusión promedio del ensemble de espines mediante la transformada inversa de la señal medida, la cual es proporcional a la magnetización.

Las propiedades geométricas microscópicas de los materiales están relacionadas con, y pueden ser derivadas a través de, el propagador de difusión promedio. Esta relación es fundamental pues permite inferir las propiedades de la microestructura subyacente sin la necesidad de invocar a una representación analítica de la geometría. Las condiciones asumidas en los modelos analíticos son raramente alcanzadas en aplicaciones biológicas (45,46). Varias de las contribuciones metodológicas desarrolladas en esta tesis tienen como punto de partida esta relación fundamental.

3.2.3 *Ecuación de Bloch-Torrey generalizada*

En la sección anterior se presentó un enfoque 'microscópico' basado en la ecuación 'integral' de Fourier para obtener una relación entre la señal medida y las propiedades del proceso de difusión. En esta sección se presenta un enfoque 'macroscópico' fundamental basado en la ecuación 'diferencial' que describe el movimiento del vector de magnetización neta del tejido.

La ecuación que describe el movimiento del vector de magnetización nuclear macroscópica $\vec{\mathbf{M}}$ de un conjunto de espines inmersos en un campo magnético $\vec{\mathbf{B}}$ se conoce por ley de Bloch, que en el sistema de coordenadas de laboratorio puede ser escrita como (6):

$$\frac{d\vec{\mathbf{M}}}{dt} = \gamma\vec{\mathbf{M}}\times\vec{\mathbf{B}} - \begin{pmatrix} 1/T_2 & 0 & 0 \\ 0 & 1/T_2 & 0 \\ 0 & 0 & 1/T_1 \end{pmatrix}\vec{\mathbf{M}} + \vec{\mathbf{M}}_0\begin{pmatrix} 0 \\ 0 \\ 1/T_1 \end{pmatrix}, \qquad \textbf{(3.9)}$$

donde $\vec{\mathbf{B}}(\vec{\mathbf{r}},t) = \begin{pmatrix} 0 & 0 & B_0 + \vec{\mathbf{r}}\vec{\mathbf{G}}(t) \end{pmatrix}^T$, siendo $\vec{\mathbf{G}} = \begin{pmatrix} G_x & G_y & G_z \end{pmatrix}^T$ el gradiente lineal de campo magnético, $\vec{\mathbf{M}}_0$ denota el vector de magnetización de equilibrio en la dirección del campo magnético estático aplicado $\vec{\mathbf{B}}_0$ (eje Z del sistema de coordenadas de laboratorio), $\vec{\mathbf{r}}$ es el vector de posición, T_2 y T_1 representan los tiempos de relajación transversal (espín-espín) y longitudinal (espín-retículo) respectivamente.

Pasando al sistema de coordenadas rotatorio, que rota a la frecuencia de resonancia $\omega_0 = \gamma B_0$ y teniendo en cuenta la siguiente relación:

$$\frac{d\vec{\mathbf{M}}}{dt} = \frac{\partial\vec{\mathbf{M}}^{rot}}{\partial t} + \begin{pmatrix} 0 \\ 0 \\ \omega_0 \end{pmatrix}\times\vec{\mathbf{M}}^{rot}, \qquad \textbf{(3.10)}$$

se obtiene

$$\frac{\partial\vec{\mathbf{M}}^{rot}}{\partial t} = \gamma\vec{\mathbf{M}}^{rot}\vec{\mathbf{r}}\vec{\mathbf{G}}(t) - \begin{pmatrix} 1/T_2 & 0 & 0 \\ 0 & 1/T_2 & 0 \\ 0 & 0 & 1/T_1 \end{pmatrix}\vec{\mathbf{M}}^{rot} + \vec{\mathbf{M}}_0\begin{pmatrix} 0 \\ 0 \\ 1/T_1 \end{pmatrix}. \qquad \textbf{(3.11)}$$

A esta ecuación se le puede adicionar la contribución que hace el efecto de la difusión sobre la magnetización, esta generalización se conoce como la ecuación de Bloch-Torrey (6), que puede ser escrita de forma más general considerando la ley de fick generalizada (véase la ecuación (2.11)):

$$\frac{\partial \vec{\mathbf{M}}^{rot}}{\partial t} = \gamma \vec{\mathbf{M}}^{rot} \vec{\mathbf{r}} \vec{\mathbf{G}}(t) - \begin{pmatrix} 1/T_2 & 0 & 0 \\ 0 & 1/T_2 & 0 \\ 0 & 0 & 1/T_1 \end{pmatrix} \vec{\mathbf{M}}^{rot} + \vec{\mathbf{M}}_0 \begin{pmatrix} 0 \\ 0 \\ 1/T_1 \end{pmatrix} + \sum_{n=1}^{\infty} \sum_{k=0}^{n} \sum_{q=0}^{k} \binom{n}{k} \binom{k}{q} D_{n-k,k-q,q} \nabla_{n-k,k-q,q} \vec{\mathbf{M}}^{rot}(\vec{\mathbf{r}}, t). \quad \textbf{(3.12)}$$

En la ecuación anterior se considera que el vector de densidad de magnetización nuclear es proporcional a la concentración de espines.

Designando a $M = \mathbf{M}_x^{rot} + i\mathbf{M}_y^{rot}$ como la representación compleja de la magnetización transversal, la ecuación anterior se transforma en (54):

$$\frac{\partial M}{\partial t} = \left(-i\gamma \vec{\mathbf{r}} \vec{\mathbf{G}}(t) - 1/T_2\right) M + \sum_{n=1}^{\infty} \sum_{k=0}^{n} \sum_{q=0}^{k} \binom{n}{k} \binom{k}{q} D_{n-k,k-q,q} \nabla_{n-k,k-q,q} M(\vec{\mathbf{r}}, t) . \quad \textbf{(3.13)}$$

Para la secuencia de medición experimental de Stejskal-Tanner (véase la Figura 1) la ecuación (3.13) tiene la siguiente solución analítica (54):

$$M(TE) = M(TE)_{G=0} \exp\left(\sum_{n=2}^{\infty} \sum_{k=0}^{n} \sum_{q=0}^{k} i^n \binom{n}{k} \binom{k}{q} D_{n-k,k-q,q} b_{n-k,k-q,q} \right), \quad \textbf{(3.14)}$$

donde:

$$b_{n-k,k-q,q} = \gamma^n |G|^n q_x^{n-k} q_y^{k-q} q_z^q \delta^n \left(\Delta - \frac{n-1}{n+1} \delta \right),$$

siendo $\hat{\mathbf{q}} = \begin{pmatrix} q_x & q_y & q_z \end{pmatrix}^T$ el vector unitario en la dirección del pulso de gradiente de campo magnético $\vec{\mathbf{G}}$ ($\vec{\mathbf{G}} = G\hat{\mathbf{q}}$). La ecuación (3.14) revela una importante propiedad de los tensores $D_{n-k,k-q,q}$; los tensores de orden par afectan la magnitud de la señal, mientras que los de orden impar la fase (54).

La aproximación más simple que podemos hacer para caracterizar un proceso de difusión anisótropo es asumir que un tensor de difusión de segundo orden ($n = 2$) es suficiente para modelar la evolución de la magnetización (véase la sección **2.4.2**), bajo tal aproximación la expresión (3.14) se transforma en:

$$M(TE) \cong M(TE)_{G=0} \exp\left(-\sum_{k=0}^{2} \sum_{q=0}^{k} \binom{2}{k} \binom{k}{q} D_{2-k,k-q,q} b_{2-k,k-q,q} \right). \qquad \textbf{(3.15)}$$

Resulta interesante notar que

$$\sum_{k=0}^{2} \sum_{q=0}^{k} \binom{2}{k} \binom{k}{q} D_{2-k,k-q,q} b_{2-k,k-q,q} = D_{xx} b_{xx} + 2D_{xy} b_{xy} + 2D_{xz} b_{xz} + D_{yy} b_{yy} + 2D_{yz} b_{yz} + D_{zz} b_{zz}, \qquad \textbf{(3.16)}$$

donde se ha hecho el cambio de nomenclatura: $\{ D_{xx} = D_{2,0,0}$, $D_{xy} = D_{1,1,0}$, $D_{xz} = D_{1,0,1}$, $D_{yy} = D_{0,2,0}$, $D_{yz} = D_{0,1,1}$ y $D_{zz} = D_{0,0,2} \}$ y $\{ b_{xx} = b_{2,0,0}$, $b_{xy} = b_{1,1,0}$, $b_{xz} = b_{1,0,1}$, $b_{yy} = b_{0,2,0}$, $b_{yz} = b_{0,1,1}$ y $b_{zz} = b_{0,0,2} \}$. La expresión derecha de la igualdad establecida en la ecuación (3.16) se puede reescribir de forma matricial como $Tr(\mathbf{BD})$, donde $Tr(\mathbf{X})$ representa la traza de la matriz $\mathbf{X}$, $\mathbf{D}$ es el tensor de difusión y la matriz simétrica $\mathbf{B}$ se define como

$$\mathbf{B} = b \begin{pmatrix} q_x^2 & q_x q_y & q_x q_z \\ q_y q_x & q_y^2 & q_y q_z \\ q_z q_x & q_z q_y & q_z^2 \end{pmatrix}, \qquad \textbf{(3.17)}$$

siendo $b = (\gamma G \delta)^2 (\Delta - \delta/3)$, este factor (conocido por *b*-valor) cuantifica el efecto de los gradientes aplicados sobre la secuencia experimental. Nótese que $\mathbf{B} = b\hat{\mathbf{q}} \otimes \hat{\mathbf{q}} = b\hat{\mathbf{q}}\hat{\mathbf{q}}^T$, donde el símbolo $\otimes$ denota el producto tensorial. Por tanto, $Tr(\mathbf{BD}) = Tr\left(b\hat{\mathbf{q}}\hat{\mathbf{q}}^T\mathbf{D}\right) = Tr\left(b\hat{\mathbf{q}}^T\mathbf{D}\hat{\mathbf{q}}\right) = b\hat{\mathbf{q}}^T\mathbf{D}\hat{\mathbf{q}}$. Integrando este resultado en la expresión (3.15) se obtiene

$$M \cong M_{G=0} \exp\left(-b\hat{\mathbf{q}}^T\mathbf{D}\hat{\mathbf{q}}\right). \qquad \textbf{(3.18)}$$

Esta ecuación es fundamental por basarse en ella el cálculo del tensor de difusión. Resulta interesante notar que para un proceso de difusión isótropo ($\hat{\mathbf{q}}^T\mathbf{D}\hat{\mathbf{q}} = D$), la solución exacta de la atenuación de la magnetización es

$$\frac{M}{M_{G=0}} = \exp\left[-(\gamma G \delta)^2 (\Delta - \delta/3) D \right]. \qquad \textbf{(3.19)}$$

Al aplicar el logaritmo a ambos lados de la expresión anterior se obtiene una relación directa entre la atenuación de la señal medida y el coeficiente de difusión D de la sustancia bajo estudio. El formalismo descrito anteriormente es la base para la medición de los coeficientes de difusión molecular usando técnicas de imagen de resonancia magnética.

CAPÍTULO 4: DIFUSIÓN EN TEJIDOS CEREBRALES

4.1 Estructura de la sustancia blanca: difusión en tejidos cerebrales

La sustancia blanca del sistema nervioso central (SNC) está formada por cientos de millones de axones que se agrupan para dar lugar a los tractos de fibras nerviosas que se extienden a lo largo del SNC, conectado estructuralmente sus regiones. En adultos, la sustancia blanca forma el 40% de los tejidos del SNC. En cada tracto de sustancia blanca la mayoría de sus axones se encuentran dispuestos de forma paralela entre sí. Esta estructura axonal altamente orientada es la principal causa de que el proceso de difusión en la sustancia blanca tenga marcadas preferencias direccionales. La Figura 2 muestra una corte coronal de un cerebro humano, donde puede observarse el complejo y compacto entramado de fibras nerviosas.

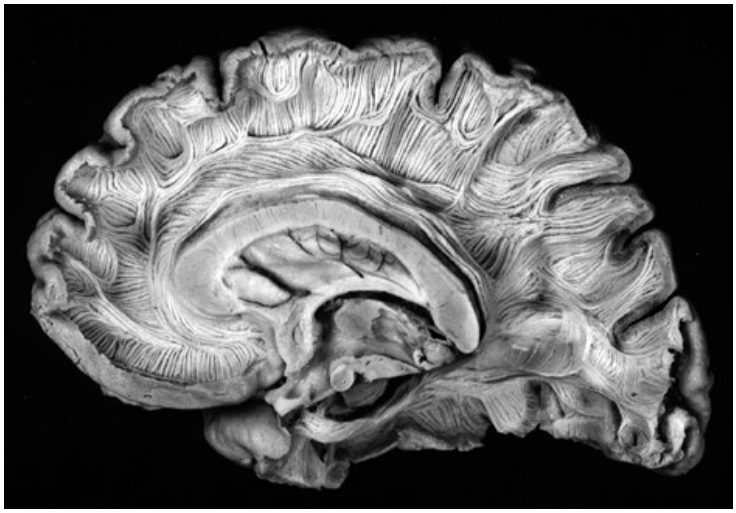

Figura 2. Corte coronal de un cerebral humano. En la figura puede apreciarse el complejo entramado de fibras nerviosas que se extienden a través de las diferentes regiones de la corteza cerebral.

La mayoría de los axones están rodeados por una capa de mielina rica en lípidos, que le confieren un aspecto visual blanco a la vista del ojo humano. Además de axones, la sustancia blanca contiene células gliales, que pueden ser catalogadas por su función y morfología en dos clases principales: macrogliales y microgliales. Los astrocitos y los oligodentrocitos

constituyen las dos poblaciones principales de células macrogliales. Los oligodentrocitos son los responsables de producir la capa de mielina, mientras que los astrocitos regulan la concentración extracelular de iones y dan soporte estructural para las neuronas y los oligodentrocitos. Por otra parte, las células microgliales reparan y limitan el daño tisular y participan en la retirada de restos celulares (63). La Figura 3 muestra los principales tipos de células descritos anteriormente.

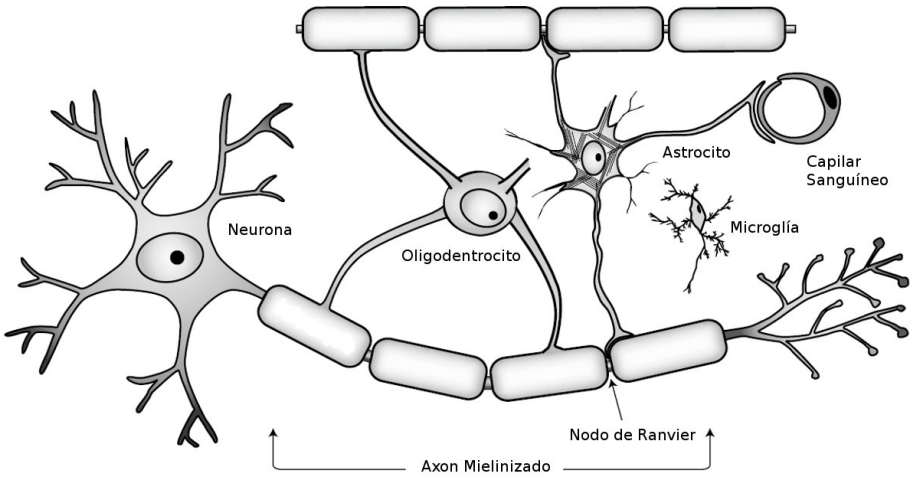

Figura 3. Representación esquemática de las principales células del sistema nervioso central, tomada de la referencia (63). La neurona, en la sustancia gris, presenta una prolongación llamada axón que se encuentra cubierta por capas de mielina generadas por los oligodentrocitos. Estas capas dieléctricas confieren una mayor velocidad de transmisión a los impulsos eléctricos originados en el núcleo de la neurona y que se propagan hacia los terminales del axón. De acuerdo a varias estimaciones la corteza cerebral humana contiene al menos 10^{10} neuronas enlazadas por 10^{14} conexiones sinápticas.

En el sistema nervioso central los núcleos de las neuronas se encuentran en la sustancia gris, mientras que sus axones forman los tractos de la sustancia blanca. En los mamíferos, las neuronas sólo constituyen el 10% del número total de células del SNC. Las neuronas poseen propiedades de excitabilidad y conductividad, lo que significa que son capaces de responder a estímulos y de conducir impulsos eléctricos. Los axones transmiten estos impulsos hacia sus terminales sinápticas donde la información es transferida hacia otras neuronas. En el sistema nervioso humano los axones pueden recorrer largas distancias, sobrepasando longitudes de un metro; su radio promedio se encuentra en el orden de los micrómetros (63).

En su interior, los axones contienen un fluido viscoso llamado citoplasma o axoplasma dentro del cual se encuentran neurotúbulos, neurofilamentos, mitocondrias, gránulos y vesículas. Los neurofilamentos y los microtúbulos se encuentran dispuestos de forma paralela al axón y tienen una apariencia cilíndrica tubular, como se ilustra en la Figura 4. Los constituyentes del axón muestran diferentes concentraciones a lo largo de su longitud.

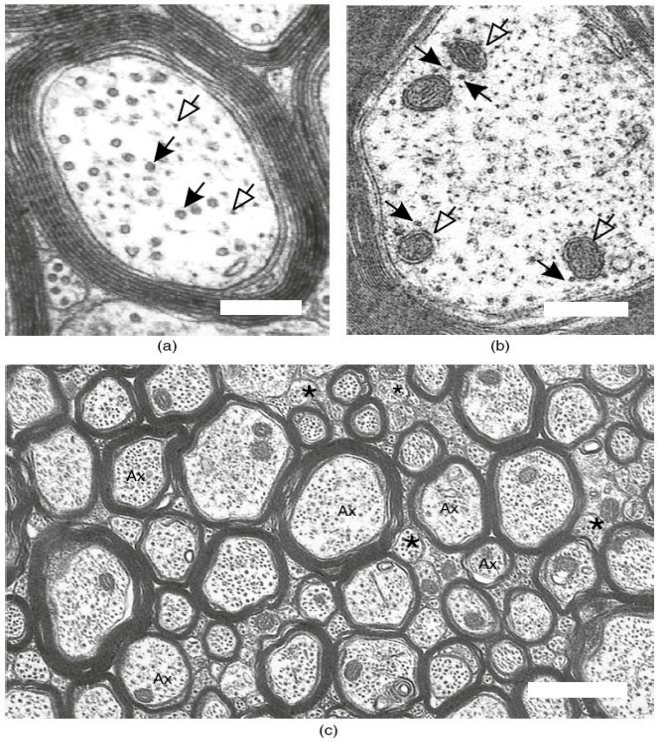

Figura 4. Imagen obtenida mediante microscopía electrónica de axones del sistema nervioso, tomada de la referencia (63). Panel (a): sección transversal de un axón mielinizado. Los neurofilamentos (flechas en blanco) dan estructura a los axones, mientras que los microtúbulos (flechas rellenas) proveen las vías para el transporte de materiales a lo largo de estos. Panel (b): sección transversal de un segundo axón mielinizado. Las mitocondrias (flechas en blanco) son las estructuras axonales que se encuentran con mayor frecuencia, las dimensión de su sección transversal varía entre 0.1 a 0.3 μm y su longitud puede alcanzar hasta 10 μm. Los microtúbulos se encuentran señalizados por las flechas rellenas. Panel (c): sección transversal de un conjunto de axones del cuerpo calloso. En el sistema nervioso central la mayoría de los axones que sobrepasan un diámetro de 0.2 μm se encuentran mielinizados (bandas oscuras alrededor de los axones). Algunos pequeños axones (señalizados con asteriscos) no poseen capa de mielina. Ax: Axón; Escala de barras (a): 0.25, (b): 0.5 y (c): 1.0 μm respectivamente.

El agua es un componente importante de la sustancia blanca. Esta se encuentra en el espacio extracelular, el cual es reducido en la sustancia blanca debido al alto empaquetamiento de los axones, y en el intracelular: en el citoplasma de las células y en el axoplasma. La capa de mielina contiene agua intracelular principalmente en sus regiones menos compactas. También se encuentra agua en los pequeños compartimientos localizados entre las capas de mielina y el axón (63).

En la sustancia blanca del cerebro esta distribución de axones altamente empaquetados constituyen barreras y obstáculos que restringen el movimiento molecular del agua, penalizando el proceso de difusión de forma desigual en diferentes direcciones. Como resultado, la difusión del agua en la sustancia blanca ocurre preferencialmente a lo largo de las fibras nerviosas. Este fenómeno es descrito en la literatura cómo difusión restringida anisótropa (del inglés: *anisotropic restricted diffusion*). Esta peculiaridad es justamente la que permite, a través del estudio del proceso de difusión, determinar las direcciones espaciales en que se encuentran orientadas las fibras nerviosas en cada elemento de volumen del cerebro. En este tipo de análisis la señal de resonancia magnética por difusión es adquirida en cada uno de los cientos de miles de pequeños píxeles tridimensionales en que es estructurado el cerebro para su medición. Para cada uno de estos voxels se realizan mediciones a lo largo de diferentes direcciones espaciales, lo que permite una caracterización tridimensional de la anisotropía del proceso de difusión.

La sustancia gris del cerebro y el líquido cefalorraquídeo son medios donde el agua presente en ellos difunde aproximadamente con la misma probabilidad en todas las direcciones espaciales, por lo que son llamados medios isótropos. En el líquido cefalorraquídeo el agua es abundante y tiene una gran movilidad. Por tanto, el proceso de difusión ocurre de forma similar a como ocurriría en un medio infinito y homogéneo. A este tipo de proceso se le conoce como difusión libre (del inglés: *free diffusion*). Por otra parte, en la sustancia gris el agua es menos abundante y su movimiento se encuentra obstaculizado por la presencia de un gran número de células con diversas formas y orientaciones. Este tipo de proceso de difusión es conocido bajo el nombre de difusión restringida isótropa (del inglés: *isotropic restricted diffusion*). La Figura 5 ilustra las trayectorias hipotéticas del movimiento aleatorio de una molécula de agua en dos entornos diferentes. El panel (a) corresponde a un proceso de difusión libre. En dicho proceso (en el tiempo que dura el experimento) la molécula no interactúa con obstáculos y por tanto no hay direcciones preferenciales. En este caso la

envolvente del proceso de difusión, o superficie de igual probabilidad de desplazamiento, tiene una forma esférica. El panel (b) ilustra un proceso de difusión restringido anisótropo. En este caso el proceso de difusión tiene una dirección preferencial que corresponde con la dirección en que se encuentran orientadas las fibras nerviosas. En el plano perpendicular a la orientación de las fibras los desplazamientos moleculares de larga longitud son menos probables, debido a que justamente en este plano el proceso de difusión encuentra un número mayor de obstáculos. En este caso la envolvente del proceso de difusión puede ser visualizada (o modelada) como un elipsoide, donde su excentricidad dependerá en gran medida del grado de empaquetamiento y grosor del grupo de axones. Este esquema pone en evidencia que a través del estudio del proceso de difusión en los tejidos cerebrales se pueden determinar características morfológicas inherentes a estos tejidos. La técnica de imagen de resonancia magnética por difusión es la técnica empleada por excelencia para este propósito, debido a que la señal medida en cada voxel del cerebro depende de las características del proceso de difusión en dicho voxel.

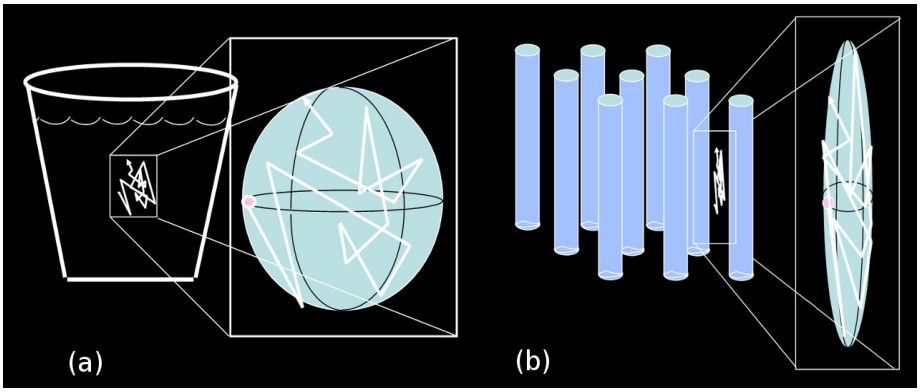

Figura 5. Movimiento Browniano hipotético de una molécula de agua (a) en un medio isótropo (por ejemplo, el líquido cefalorraquídeo en el cerebro) y (b) en un medio anisótropo (por ejemplo, la sustancia blanca del cerebro).

4.2 Principales métodos para caracterizar la geometría de los tejidos biológicos

En esta sección se introducen algunos de los principales métodos dedicados al estudio del proceso de difusión en tejidos cerebrales mediante el uso de la técnica de resonancia magnética por difusión del agua.

4.2.1 *Reconstrucción del tensor de difusión*

El modelo del tensor de difusión de segundo orden fue descrito en las secciones 2.3.2 y 2.3.3 y en la sección 3.2.3 se planteó la ecuación (3.18), que relaciona directamente la señal medida en un voxel con el tensor de difusión asociado a dicho voxel. En esta sección se presenta el desarrollo matemático básico relacionado al proceso de estimación del tensor a partir de los datos medidos en un escáner de resonancia magnética.

El modelo del tensor de difusión asume que la señal de difusión S medida en un voxel del cerebro, la cual es proporcional al módulo de la magnetización transversal compleja definida en (3.18), se describe por la expresión:

$$S(b,\hat{\mathbf{q}}) = S_0 \exp\left(-b\hat{\mathbf{q}}^T \mathbf{D}\hat{\mathbf{q}}\right), \qquad \textbf{(4.1)}$$

siendo S_0 la señal obtenida en ausencia de gradientes de campo magnético (para $b = 0$). Nótese que el valor de la señal depende explícitamente de la dirección $\hat{\mathbf{q}}$ en que se aplica el gradiente de campo magnético y del tensor de difusión $\mathbf{D}$.

El tensor de difusión tiene 6 componentes independientes [$D_{xx}, D_{xy}, D_{xz}, D_{yy}, D_{yz}, D_{zz}$], por tanto se necesitan al menos 7 mediciones para estimarlo: 6 mediciones a lo largo de diferentes direcciones espaciales para obtener los 6 elementos únicos del tensor y otra medición adicional para estimar la magnitud de la señal S_0. El método estándar de estimar el tensor consiste en aplicar el logaritmo a los elementos del vector $\mathbf{S}$ (Nx1), formado por la señal de difusión medida a lo largo de las diferentes direcciones espaciales, $\mathbf{Y} = \log(\mathbf{S})$, y luego resolver el sistema de ecuaciones resultante mediante regresión lineal:

$$\mathbf{Y} = \mathbf{X}\beta + \boldsymbol{\varepsilon}, \qquad \textbf{(4.2)}$$

donde $\boldsymbol{\varepsilon}$ representa el ruido, β^T = [$\log(S_0)$ $D_{xx}, D_{xy}, D_{xz}, D_{yy}, D_{yz}, D_{zz}$], y

$$\mathbf{X} = \begin{bmatrix} 1 & -bq_{x1}^2 & -bq_{y1}^2 & -bq_{z1}^2 & -2bq_{x1}q_{y1} & -2bq_{x1}q_{z1} & -2bq_{y1}q_{z1} \\ \vdots & \vdots & \vdots & \vdots & \vdots & \vdots & \vdots \\ 1 & -bq_{xi}^2 & -bq_{yi}^2 & -bq_{zi}^2 & -2bq_{xi}q_{yi} & -2bq_{xi}q_{zi} & -2bq_{yi}q_{zi} \\ \vdots & \vdots & \vdots & \vdots & \vdots & \vdots & \vdots \\ 1 & -bq_{xN}^2 & -bq_{yN}^2 & -bq_{zN}^2 & -2bq_{xN}q_{yN} & -2bq_{xN}q_{zN} & -2bq_{yN}q_{zN} \end{bmatrix}. \qquad \textbf{(4.3)}$$

En la ecuación (4.3) los términos $(q_{xi}\ q_{yi}\ q_{zi})$ denotan las componentes Cartesianas del vector unitario $\hat{\mathbf{q}}_i$ orientado a lo largo de la dirección i del gradiente de campo magnético. El estimador de máxima verosimilitud de este modelo es

$$\hat{\beta} = \left(\mathbf{X}^T\Sigma^{-1}\mathbf{X}\right)^{-1}\mathbf{X}^T\Sigma^{-1}\mathbf{Y}\,, \qquad \textbf{(4.4)}$$

donde Σ es la matriz de varianza del ruido asociada con la variable $\mathbf{Y} = \log(\mathbf{S})$.

Los diseños experimentales que se emplean actualmente en aplicaciones clínicas y de investigación para calcular el tensor de difusión en cerebros humanos realizan un número entre 12 a 30 mediciones a lo largo de diferentes direcciones espaciales y de 2 a 5 mediciones adicionales para obtener la magnitud de la señal S_0. El aumento del número de mediciones con respecto a los valores mínimos impuestos por la teoría compensa el alto nivel de ruido que afecta el proceso de medición de la señal de resonancia magnética por difusión. El tiempo promedio de adquisición de un cerebro completo para este tipo de diseño es de 5 a 10 minutos para un valor del parámetro experimental b = 1000 s/mm^2, que es el valor estándar empleado comúnmente. La Figura 6 muestra imágenes del tensor de difusión reconstruidas en un cerebro real humano.

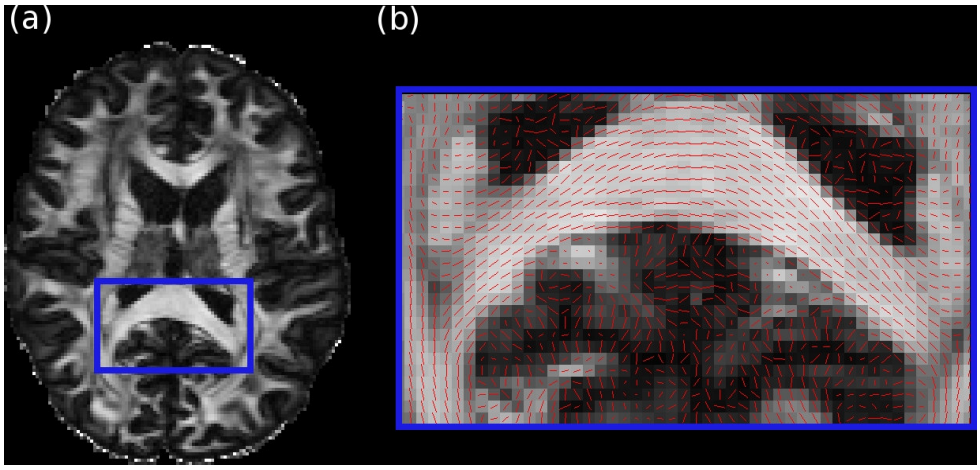

Figura 6. Mapas derivados del cálculo del tensor de difusión a partir de imágenes de resonancia magnética por difusión de un sujeto sano. El panel (a) muestra la fracción de anisotropía (ecuación (2.25)) estimada en un plano axial del cerebro; la fracción de anisotropía es un indicador de la densidad y coherencia de orientación de los haces de fibras nerviosas en cada voxel. Se puede apreciar que la fracción de anisotropía es alta en la sustancia blanca, mientras que en la sustancia gris es menor y casi nula en el líquido cefalorraquídeo. El panel (b) muestra una región aumentada donde se han superpuesto segmentos que denotan el vector principal del tensor; estos segmentos son un indicador de la orientación local de los haces de fibras nerviosas. La región aumentada corresponde a una porción del cuerpo calloso, compuesto por fibras muy alineadas y compactas que conectan ambos hemisferios del cerebro.

4.2.2 *Limitación del tensor de difusión*

En el cerebro humano las complejas estructuras de los tejidos tienden a alterar el proceso de difusión que se observa en sustancias simples como el agua en un medio infinito. La difusión queda bien cuantificada con el coeficiente de difusión molecular en un voxel donde el tejido es isótropo o contenido en cavidades llenas de agua. Para un voxel donde el tejido presenta una alta organización estructural, siendo esta de la forma más simple, como es el caso de un voxel situado en la sustancia blanca por dónde solamente pasa un grupo de fibras nerviosas, la difusión se caracteriza satisfactoriamente utilizando el tensor de difusión. Sin embargo, en la sustancia blanca es común encontrar regiones donde la estructura es más compleja, apareciendo cruces de dos o más grupos de fibras, doblamientos y enrollamientos (33). En estos casos el formalismo del tensor de difusión no permite modelar satisfactoriamente la complejidad del proceso de difusión, véase la Figura 7.

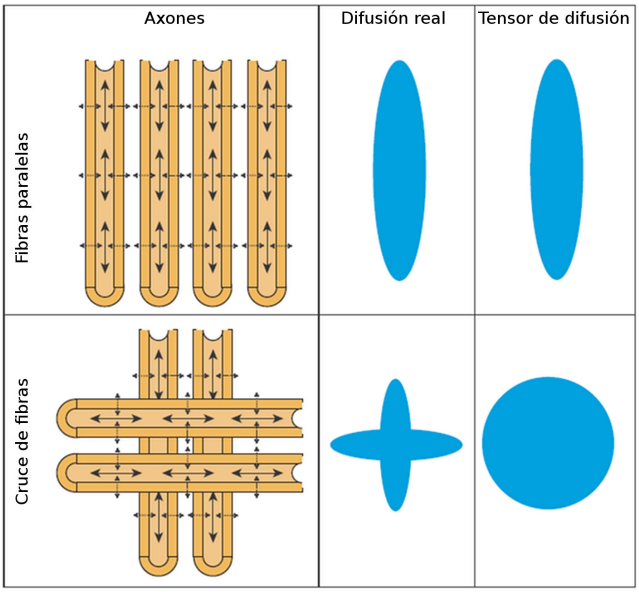

Figura 7. Relación entre la organización axonal de los tejidos y la geometría del proceso de difusión del agua. El proceso de difusión del agua suele ser mayor a lo largo de las direcciones paralelas a los haces de fibras nerviosas debido a que en esas direcciones las moléculas encuentran menos obstáculos al movimiento. En un voxel donde sólo existe un grupo de fibras paralelas, el modelo del tensor de difusión nos da una aproximación realista. Sin embargo, cuando varios grupos de fibras pasan por un voxel, la geometría elipsoidal del tensor es demasiado simple para identificar la verdadera organización multidireccional de los tejidos. (Figura modificada a partir de la referencia (64))

4.2.3 *Imágenes de alta resolución angular y el coeficiente de difusión aparente*

Una aplicación novedosa para lidiar con las limitaciones del tensor de difusión consiste en extender el modelo de señal del tensor (ecuación (4.1)) a la siguiente forma (65):

$$E(b,\hat{\mathbf{q}}) = \exp\left(-bADC(\hat{\mathbf{q}})\right)$$
$$E(b,\hat{\mathbf{q}}) = S(b,\hat{\mathbf{q}}) / S_0 \qquad \textbf{(4.5)}$$

donde $E(b,\hat{\mathbf{q}})$ es el valor de la señal de difusión normalizada (relativa a la señal medida en ausencia de gradientes de campo magnético, S_0), y el término $ADC(\hat{\mathbf{q}}) = D(\hat{\mathbf{q}})$ se define como el valor del coeficiente de difusión 'observado' a lo largo de la dirección $\hat{\mathbf{q}}$. A este término se le denomina coeficiente de difusión aparente, o *ADC* (del inglés: *Apparent*

Diffusion Coefficient) (65). Nótese que para el caso particular en que el *ADC* tiene forma elipsoidal, $ADC(\hat{\mathbf{q}}) = \hat{\mathbf{q}}^T \mathbf{D} \hat{\mathbf{q}}$, el modelo anterior se reduce al tensor de difusión. Sin embargo la ventaja de este modelo es que no asume ninguna forma paramétrica específica para la geometría del *ADC*, lo que le confiere mayor libertad para captar la organización multidireccional de los tejidos.

El paradigma experimental para obtener la función *ADC* consiste en medir la señal de difusión para un valor constante del parámetro *b* a lo largo de múltiples direcciones utilizando una alta resolución angular (secuencia HARDI, véase la Figura 8) y calcular el valor del coeficiente de difusión aparente para cada dirección invirtiendo el modelo (4.5), lo que resulta en:

$$ADC(\hat{\mathbf{q}}) = -\frac{1}{b} \log\left(E(b, \hat{\mathbf{q}})\right) . \qquad \textbf{(4.6)}$$

Las secuencias HARDI suelen emplear entre 60 y 250 direcciones diferentes y valores del parámetro experimental *b* mayores que el que se emplea en el tensor de difusión (entre 1200 y 6000 s/mm^2) para obtener un mayor contraste angular del proceso de difusión. El tiempo promedio de adquisición de un cerebro completo es de 15 a 45 minutos.

Una forma extendida en la literatura para representar y estimar el *ADC* es su expansión en términos de armónicos esféricos Y_{lm} (32), los cuales forman una base ortonormal completa sobre la esfera:

$$ADC(\hat{\mathbf{q}}) = \sum_{l=0}^{\infty} \sum_{m=-l}^{l} a_{lm} Y_{lm}(\hat{\mathbf{q}}) . \qquad \textbf{(4.7)}$$

Los coeficientes a_{lm} de la expansión pueden calcularse mediante un ajuste estándar de mínimos cuadrados. En la práctica se suele usar una versión truncada de la expresión (4.7), que emplea valores máximos del parámetro l de 4 a 8. Las funciones base de armónicos esféricos son suaves sobre la esfera, por lo que esta representación suele ser efectiva para eliminar parte del ruido presente en el dato.

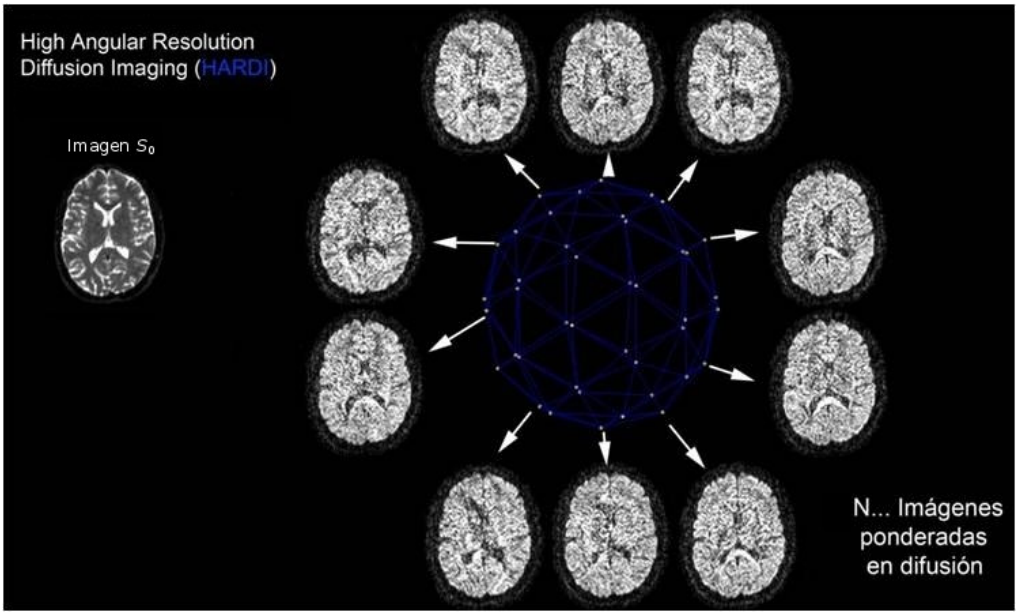

Figura 8. Esquema de adquisición de imágenes de alta resolución angular (del inglés: *High Angular Resolution Diffusion Imaging* (HARDI)). Este tipo de secuencia se basa en medir los valores de señal de resonancia magnética por difusión para diferentes orientaciones espaciales. En contraste con el tensor de difusión, donde se suelen emplear entre 12 y 30 orientaciones, las secuencias HARDI suelen emplear entre 60 y 250.

Este modelo permite obtener mucha más información direccional sobre el proceso de difusión que el modelo del tensor de difusión, limitado a geometrías del tipo elipsoidal. Una de las ventajas principales de esta representación, que será explotada a lo largo de esta tesis, es que permite extrapolar e interpolar la señal de forma analítica para diferentes valores del parámetro experimental *b* y para diferentes orientaciones espaciales.

Sin embargo este modelo también tiene limitaciones. En regiones donde ocurren cruces de dos o más grupos de fibras la forma del *ADC* no es directamente proporcional a la geometría del proceso de difusión real. En la Figura 9 se pone un ejemplo donde los máximos de la función *ADC* no coinciden con las orientaciones espaciales de los grupos de fibras. Por esta razón la función *ADC* no puede ser usada de forma directa para extraer las direcciones principales en que ocurre el proceso de difusión. Las siguientes secciones están dedicadas a comentar los principales métodos que se han propuesto para resolver este problema.

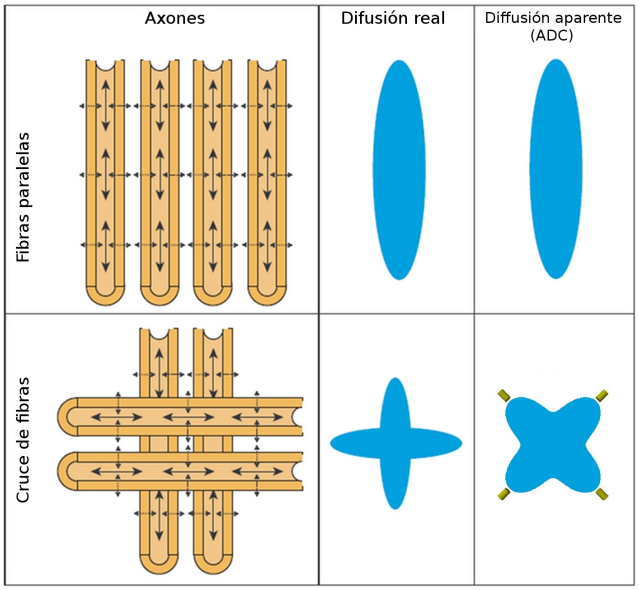

Figura 9. Relación entre la organización axonal de los tejidos y la geometría del proceso de difusión del agua. En un voxel donde sólo existe un grupo de fibras paralelas el *ADC* nos da una aproximación realista. Sin embargo cuando varios grupos de fibras pasan por un voxel la forma del *ADC* no es directamente proporcional a la envolvente del proceso de difusión real. Por esta razón los valores máximos del *ADC* no se pueden usar para identificar las principales orientaciones del medio. (Figura modificada a partir de la referencia (64))

4.2.4 *Métodos de imagen del espacio-q*

El descriptor más completo que se puede obtener para caracterizar el proceso de difusión es la función de distribución de probabilidad de los desplazamientos moleculares (también conocida por propagador de difusión), la cual nos informa sobre la probabilidad que tienen las moléculas en el voxel de moverse una distancia dada en cualquier dirección del espacio en un tiempo dado. La señal de resonancia magnética por difusión está estrechamente relacionada al propagador mediante la relación de Fourier (46)(66):

$$E(\vec{\mathbf{q}}) = \int P(\vec{\mathbf{r}}) \exp(2\pi i \vec{\mathbf{r}}\vec{\mathbf{q}})\, d\vec{\mathbf{r}} \,. \qquad \textbf{(4.8)}$$

Esto significa que la señal medida es el espectro del propagador de difusión. Advierta que esta ecuación es una extensión tridimensional de la relación unidimensional obtenida previamente

en la ecuación (3.8), donde también se han reemplazado los términos de magnetización transversal por la señal de difusión normalizada E definida en (4.5). En esta expresión el vector del espacio de Fourier, también conocido por vector del *espacio-q*, se denota por $\vec{\mathbf{q}} = \gamma\tau\vec{\mathbf{G}}/2\pi$ donde τ es la duración de la aplicación del vector de gradiente de campo magnético $\vec{\mathbf{G}}$, y el vector de los desplazamientos moleculares se denota por $\vec{\mathbf{r}}$.

En la práctica el propagador puede ser obtenido mediante la relación inversa

$$P(\vec{\mathbf{r}}) = \int E(\vec{\mathbf{q}}) \exp(-2\pi i \vec{\mathbf{r}}\vec{\mathbf{q}})\, d\vec{\mathbf{q}}. \qquad \textbf{(4.9)}$$

A continuación se describen las tres técnicas principales dedicadas a la caracterización del proceso de difusión basado en este formalismo, al que se le conoce de forma general como métodos de imagen del espacio-q.

4.2.4.1 Imagen espectral de difusión

La estrategia más directa para calcular la función $P(\vec{\mathbf{r}})$ consiste en medir la señal de difusión para los valores discretos del vector $\vec{\mathbf{q}}$ que corresponden con los puntos de una rejilla cuadriculada tridimensional (formada por puntos equidistantes dentro de un volumen en un sistema de referencia de coordenadas Cartesiano) y calcular la transformada rápida de Fourier del dato adquirido. Esta metodología devuelve el propagador evaluado sobre los puntos de la rejilla definida en el experimento. Para extraer la información direccional contenida en el propagador, en (46) se propuso calcular la siguiente proyección radial

$$ODF(\hat{\mathbf{r}}) = \frac{1}{Z}\int_0^\infty P(\rho, \hat{\mathbf{r}})\, \rho^2 d\rho\,, \qquad \textbf{(4.10)}$$

donde $\vec{\mathbf{r}} = \rho\hat{\mathbf{r}}$, siendo ρ y $\hat{\mathbf{r}}$ la longitud y el vector unitario de $\vec{\mathbf{r}}$ respectivamente. El término *ODF* define la función de distribución de orientación de la difusión. Esta proyección sacrifica toda la información radial del propagador pero retiene, en promedio, el contraste angular relevante. Para evaluar la expresión (4.10) primero es necesario interpolar el propagador en una rejilla tridimensional auxiliar construida en coordenadas esféricas y luego computar la integral usando métodos numéricos de integración, véase la Figura 10.

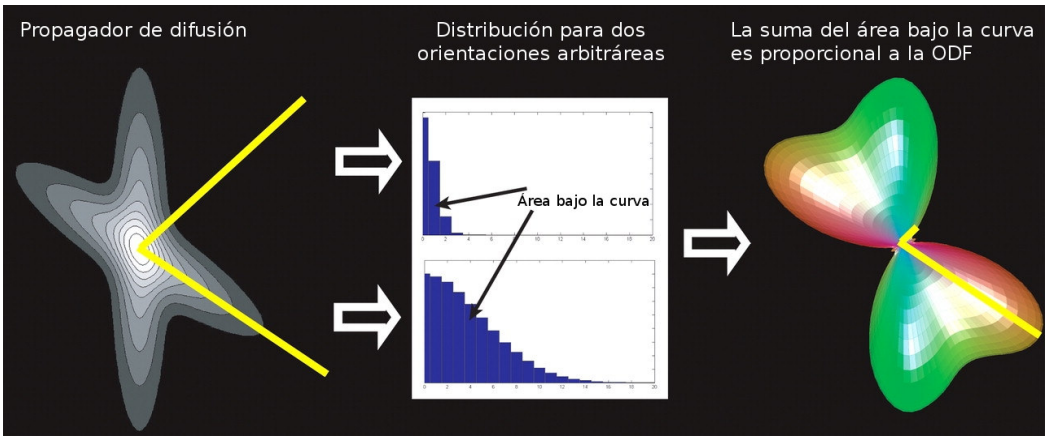

Figura 10. Diagrama que muestra cómo se calcula y representa una función de distribución de orientación (*ODF*) (Figura modificada a partir de la referencia (67)). A la izquierda se muestra un plano de una función de distribución de desplazamientos moleculares tridimensional. El cálculo de la *ODF* se ejemplifica para dos orientaciones específicas denotadas por dos líneas amarillas. En el centro se muestran histogramas que representan la distribución de los desplazamientos para las dos orientaciones. El valor de la *ODF* en cada orientación depende del área bajo la curva y se calcula como la sumatoria de las alturas de las barras del histograma multiplicadas por la longitud de desplazamiento que codifican (véase la ecuación (4.10)). A la derecha, la ODF calculada para todas las orientaciones posibles se muestra mediante un esferoide deformado y en colores. Los valores correspondientes a las dos orientaciones anteriores se señalan con líneas amarillas. La *ODF* se suele visualizar usando una escala espacial de colores 'RGB' (Red, Green, Blue) de acuerdo a la proximidad de cada orientación a los ejes de coordenadas 'XYZ' respectivamente.

Al formalismo de medición y estimación presentado en esta sección se le conoce como técnica de imagen espectral de difusión. La principal limitación de esta técnica radica en el alto número de mediciones que es necesario adquirir para reconstruir la transformada de Fourier en cada voxel del cerebro. La adquisición de datos requiere en torno a 515 mediciones por voxel y excede los 40 minutos de duración para cada paciente. Un tiempo de adquisición tan largo limita su empleo en estudios clínicos, donde también se suelen adquirir conjuntamente imágenes de resonancia magnética de otras modalidades que aportan información complementaria y que requieren un tiempo extra de medición.

Esta técnica será retomada en el Capítulo 5, donde se exponen los detalles técnico-metodológicos en mayor profundidad, se discuten algunas de sus deficiencias y limitaciones,

y se validan las nuevas extensiones y algoritmos de estimación que nuestro grupo de investigación ha propuesto (68) para mejorar su calidad de reconstrucción.

4.2.4.2 Imagen q-ball

La técnica de imagen q-ball (44) se desarrolló con el objetivo de disponer de un método alternativo a la técnica espectral de difusión que pudiera trabajar con un número menor de mediciones experimentales. En contraste a la técnica espectral de difusión que adquiere datos en todo el volumen del *espacio-q*, esta técnica emplea imágenes de difusión de alta resolución angular adquiridas sobre una esfera del *espacio-q* (esquema HARDI, Figura 8). Para caracterizar la distribución de orientación de los tejidos en la técnica imagen q-ball se redefine la función de distribución de orientación de la siguiente manera:

$$ODF\left(\hat{\mathbf{r}}\right)=\frac{1}{Z}\int_0^\infty P\left(\rho,\hat{\mathbf{r}}\right)d\rho\,\mathbf{.} \qquad \textbf{(4.11)}$$

Nótese que esta definición difiere con respecto a la definición original (ecuación (4.10)) en que se elimina el término ρ^2.

El autor de este método demostró que existe una transformación matemática definida sobre la esfera, que al aplicarla a la señal medida, produce una función que se aproxima a la *ODF* (44). En particular, esta transformación es la transformada de Funk-Radon, también conocida por transformada de Radon sobre la esfera. La expresión matemática que establece esta relación es (44):

$$G[S(q')]=2\pi q'\int P(r,\theta)J_0(2\pi q' r)rdrd\theta\approx ODF\,\mathbf{,} \qquad \textbf{(4.12)}$$

Donde $G[S(q')]$ representa la transformada de Funk-Radon de la señal medida, la cual crea una nueva función sobre la esfera tal que a cada punto le asigna un valor que es igual a la integral de la señal medida sobre el ecuador asociado al punto. En la expresión anterior q' denota el radio de la esfera en el *espacio-q* y $P(r,\theta)=\int P(r,\theta,z)dz$ es la proyección radial del propagador de difusión, que en este caso y sin pérdida de generalidad se calcula a lo largo del eje Z en coordenadas cilíndricas (r,θ,z).

Este resultado se interpreta de la siguiente manera: sumar la señal de difusión sobre un círculo alrededor del origen de coordenadas devuelve el mismo valor que se obtendría al proyectar el

propagador de difusión en el plano que contiene al círculo, multiplicar esta proyección por la función de Bessel de orden cero J_0 y sumar/integrar sobre toda la proyección modificada. Esta aproximación es más exacta a medida que la función J_0 se encuentra más concentrada en torno al origen de coordenadas. En el caso limite que J_0 se asemeje a una función delta centrada en el origen entonces la expresión resultante en (4.12) coincide exactamente con la *ODF* teórica (4.11). Por esta razón en la práctica se suelen usar altos valores experimentales del parámetro q' que reducen el ancho de la función J_0. Sin embargo esta estrategia se ve comprometida por el hecho de que el ruido relativo en el dato aumenta al aumentar el parámetro q'.

Aunque este método produce soluciones de buena calidad y puede resolver múltiples orientaciones de fibras sin realizar hipótesis sobre las características del proceso de difusión local, la expresión en la cual se basa la reconstrucción es aproximada. La contaminación no deseada que introduce la función de Bessel de orden cero reduce el poder separador de la técnica en relación a la técnica espectral de difusión.

Como alternativa a esta importante herramienta, en el Capítulo 5 de esta tesis se introduce una descripción matemática (69) propuesta por nuestro grupo de investigación que permite encontrar una relación analítica y exacta entre la *ODF* teórica (según la expresión (4.11)) y la señal medida, en la que no aparece ningún término contaminante que arruine la validez de la formulación.

4.2.4.3 Transformada de orientación de la difusión

La transformada de orientación de la difusión es otra metodología de reconstrucción propuesta como alternativa a la técnica de imagen espectral de difusión (48). Este método permite evaluar la integral de Fourier (4.9) en coordenadas esféricas de forma analítica, empleando el modelo generativo mono-exponencial del coeficiente de difusión aparente descrito por la ecuación (4.5). Bajo esta aproximación el método es capaz de transformar la función *ADC* (medido mediante imágenes de alta resolución angular) a la función de probabilidad de los desplazamientos moleculares.

La principal diferencia entre la técnica de imagen espectral de difusión y la transformada de orientación de la difusión radica en que mientras en la imagen espectral de difusión se calcula el propagador de difusión en todo el volumen (sobre una rejilla tridimensional) y luego se proyecta sobre la esfera, en la transformada de orientación de la difusión sólo se calcula un

contorno único del propagador de difusión, evaluado para una longitud de desplazamiento especificado de antemano, de la forma $P(\rho = \text{valor específico}, \hat{\mathbf{r}})$. Para conocer el propagador de difusión en todo el volumen es necesario repetir el cálculo para diferentes valores del parámetro ρ de longitud de los desplazamientos moleculares. Sin embargo esto aumenta considerablemente el tiempo de cálculo del algoritmo.

Los detalles matemáticos de la reconstrucción de esta técnica se encuentran contenidos en el Capítulo 5 de esta tesis, donde también se presenta la extensión propuesta por nuestro grupo de investigación (70). En particular, se analizan en detalle las fuentes de error y limitaciones prácticas de la técnica y se obtienen nuevas expresiones analíticas para calcular las funciones de distribución de orientación *ODF* – previamente definidas en las técnicas de imagen espectral de difusión e imagen q-ball – que no estaban reportadas para este método.

4.2.5 *Modelo del multi-tensor de difusión*

A diferencia de los métodos de imagen del *espacio-q* descritos en las secciones anteriores, el modelo del multi-tensor de difusión asume una relación paramétrica entre la señal medida y las propiedades del medio. Este modelo extiende el modelo del tensor de difusión al asumir que dentro del voxel existen múltiples tensores asociados a diferentes compartimentos. Cada compartimento se hace corresponder con una población o grupo de fibras paralelas, por tanto la difusión dentro de cada compartimento se describe satisfactoriamente mediante un único tensor. La expresión de la señal normalizada correspondiente a este modelo tiene la forma:

$$E(b,\hat{\mathbf{q}}) = S(b,\hat{\mathbf{q}}) / S_0 = \sum_{i=1}^{k} \mathrm{f}_i \exp\left(-b\hat{\mathbf{q}}^T \mathbf{D}^{(i)} \hat{\mathbf{q}}\right), \qquad \textbf{(4.13)}$$

donde *k* es el número de compartimentos de fibras en el voxel bajo estudio, f_i es la fracción de volumen del agua en el compartimento *i* ($\sum_{i=1}^{k} \mathrm{f}_i = 1$), y $\mathbf{D}^{(i)}$ es el tensor de difusión de segundo orden asociado a este compartimento.

Mediante el ajuste de este modelo a mediciones de alta resolución angular es posible obtener las fracciones de volumen y los tensores de difusión asociados a cada grupo de fibras y por tanto es posible conocer sus orientaciones espaciales y factores de anisotropía. Sin embargo, en la práctica este tipo de formulación tiene dos inconvenientes principales. El primer inconveniente es el carácter no lineal de la función objetivo a ser minimizada, que conduce al

empleo de algoritmos de ajuste que son inestables. El segundo inconveniente es el desconocimiento previo sobre el número de compartimentos de fibras que deben ser asumidos en cada voxel. En la literatura se han propuesto diversas estrategias para seleccionar el número óptimo de compartimentos, sin embargo, la principal limitación de estos métodos es que pueden reconstruir apropiadamente hasta un número máximo de $k = 2$ fibras (por ejemplo, véase (33)(71) (72) (34)). Un aporte considerable fue la introducción del método de determinación automática de relevancia Bayesiana (36), el cual permite la reconstrucción de hasta $k = 3$ grupos de fibras ortogonales. Posteriormente nuestro grupo de investigación ha propuesto una nueva solución (73) basada en el método de saltos reversibles de Monte Carlo usando cadenas de Markov (del inglés: *Reversible Jump Markov Chain Monte Carlo method*) – la cual se incluye entre las contribuciones presentadas en el Capítulo 5 – que permite la estimación de hasta $k = 5$ haces de fibras por voxel.

4.2.6 *Deconvolución esférica*

La deconvolución esférica agrupa un conjunto de técnicas de estimación de múltiples compartimentos que pueden ser implementadas usando tanto modelos de señal paramétricos cómo no paramétricos (36,37,40,74–80). Los métodos de deconvolución esférica se han hecho populares debido a su habilidad para identificar múltiples fibras con pequeños ángulos de separación en datos HARDI adquiridos en un tiempo tolerado en muchas aplicaciones clínicas. El alto poder resolutivo de estas técnicas se basa en que, a diferencia de las técnicas independientes de modelo que estiman la *ODF* del proceso de difusión, el resultado de la deconvolución esférica es justamente la función de distribución de orientación de las fibras.

Entre los diferentes algoritmos propuestos, el método de deconvolución esférica restringida CSD (40,81) ha despertado un gran interés debido a su buen funcionamiento y bajo coste computacional. En este método primero se estima la señal promedio medida a lo largo de cada una de las direcciones del espacio en regiones de la sustancia blanca que contienen un único grupo de fibras paralelas; a esta señal promedio se le llama función de respuesta de un haz de fibras. Posteriormente se estima la función de distribución de las fibras mediante la deconvolución (modelación inversa) entre la señal medida en cada voxel y la función de respuesta calculada.

La formulación de este modelo se basa en asumir que la señal medida en un voxel que contiene múltiples poblaciones de fibras es la suma de la función de respuesta rotada a lo

largo de cada orientación de fibra y ponderada por sus fracciones de volumen. Esto se puede escribir como:

$$S(\hat{\mathbf{q}}) = \sum_{i=1} \mathrm{f}_i \hat{\mathbf{A}}_i \mathbf{R}_\mathbf{z} \ , \qquad \textbf{(A.14)}$$

donde f_i es la fracción de volumen de la fibra *i* y $\hat{\mathbf{A}}_i$ es un operador que rota a la función de respuesta de un haz de fibras $\mathbf{R}_\mathbf{z}$, definida como la función de respuesta de una fibra orientada a lo largo del eje Z de coordenadas, hacia la orientación de la fibra *i*. Esta expresión se puede representar mediante el operador de convolución $\otimes$ sobre la esfera entre la función de respuesta y la función de distribución de orientación de las fibras *F* que contiene toda la información de las fracciones de volumen de las fibras en diferentes orientaciones:

$$S(\theta,\phi) = F(\theta,\phi) \otimes \mathbf{R}_\mathbf{z} \ , \qquad \textbf{(A.15)}$$

donde el vector unitario $\hat{\mathbf{q}}$ se ha escrito en coordenadas esféricas (θ,ϕ). En la Figura 11 se muestra un ejemplo de deconvolución hipotética en el caso de dos grupos de fibras.

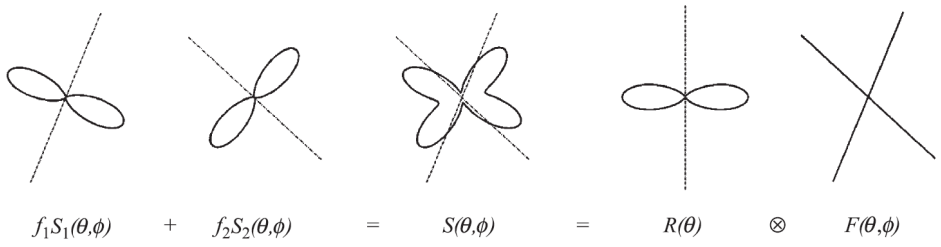

Figura 11. En esta ilustración se ejemplifica en dos dimensiones el proceso de deconvolución esférica en un voxel que contiene dos grupos de fibras (Figura tomada de la referencia (40)). La señal medida $S(\theta,\phi)$, representada en la parte central de la figura, es la suma de las señales correspondientes a las dos poblaciones de fibras representadas en la parte izquierda del gráfico. La orientación de cada grupo de fibras paralelas se representa por una recta discontinua. Nótese que la señal de cada grupo de fibras alcanza sus valores máximos en el plano perpendicular a la orientación de la fibra. En la parte derecha se muestra la convolución de la función de respuesta de un haz de fibras orientada a lo largo del eje Z de coordenadas, $\mathbf{R}_\mathbf{z} = R(\theta)$, con la función de orientación de las

fibras. En la práctica la función de distribución de las fibras se estima mediante un proceso de estimación inversa llamado deconvolución.

En el método CSD el proceso de deconvolución se realiza trabajando en coordenadas esféricas y expandiendo en armónicos esféricos las funciones involucradas.

Recientemente se ha propuesto un nuevo método alternativo, dRL-SD , el cual se basa en el algoritmo de deconvolución de Richardson-Lucy (41). Una evaluación extensiva entre los métodos CSD y dRL-SD (82) reveló una capacidad superior para CSD en la identificación de cruces de fibra con baja anisotropía, un menor porcentaje para dRL-SD de producir orientaciones de fibras espurias y una mayor robustez para dRL-SD en la selección de la función de respuesta de un haz de fibras. Esta última característica tiene gran relevancia ya que la asunción de una función de respuesta única para todos los tractos del cerebro es claramente una simplificación de ambos métodos. De acuerdo a estos resultados el método dRL-SD es el que minimiza las consecuencias de esta simplificación.

La implementación del método dRL-SD se diferencia en varios aspectos a su análogo CSD. En el dRL-SD la función de respuesta se crea empleando el modelo del tensor de difusión, de forma similar al modelo de múltiples compartimentos revisado en la sección anterior (ecuación (4.13)). Además, la expresión de la señal incluye dos términos extras que permiten considerar un compartimento de tejido de la sustancia gris y otro de líquido cefalorraquídeo. Esta extensión hace posible que el método produzca mejores resultados en voxels que contienen porciones de diferentes tejidos. Otra característica de esta metodología es que no emplea la expansión en harmónicos esféricos; en su lugar, al igual que en otros métodos anteriores (76), la función de orientación de las fibras es estimada a lo largo de muchas orientaciones discretas distribuidas uniformemente sobre la superficie de la esfera. Para esto se asume de antemano que en el voxel existe una orientación de fibra a lo largo de cada una de estas orientaciones especificadas, siendo el objetivo estimar su fracción de volumen. A cada orientación se le asigna una función de respuesta y se crea un diccionario que contiene todas las funciones rotadas. La fracción de volumen de cada una de las fibras se puede estimar entonces mediante regresión lineal entre el dato medido y el diccionario. Este proceso se esquematiza en la Figura 12.

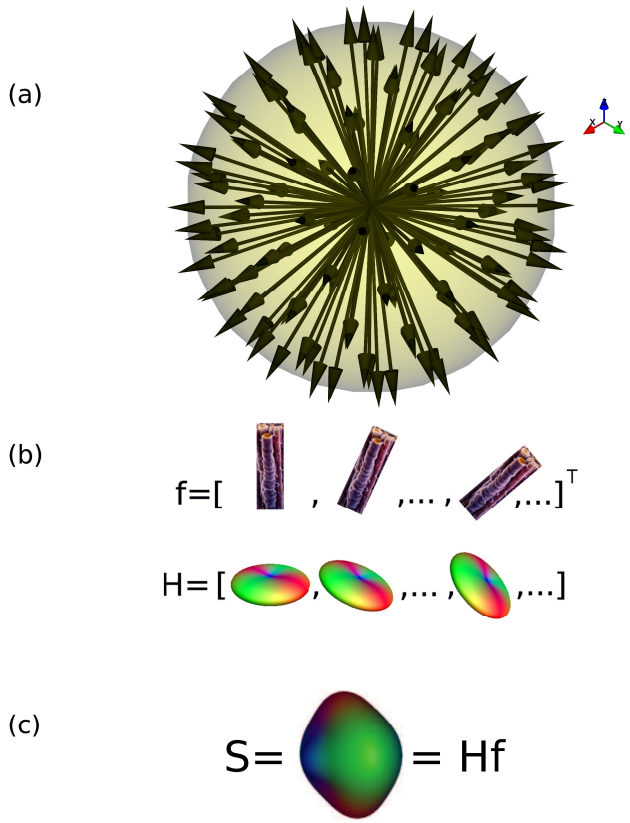

Figura 12. Esquema de deconvolución esférica. El panel (a) muestra un conjunto de vectores equidistantes (igualmente espaciados) sobre la superficie de una esfera. Se asume de antemano que existe un grupo de fibras nerviosas a lo largo de cada una de estas direcciones y el objetivo es estimar la fracción de volumen de cada una de estas fibras a partir del dato medido. Para cada una de estas orientaciones se crea el valor de señal de resonancia magnética por difusión que correspondería a un grupo de fibras con esta orientación bajo los mismos parámetros de adquisición del experimento (empleando como modelo generativo el tensor de difusión). Con estas señales se crea un diccionario de señales de difusión rotadas **H**, mostrado en el panel (b). La fracción de volumen de cada grupo de fibras se estima mediante regresión lineal entre el dato medido **S** y el diccionario empleando la relación que se ilustra en el panel (c). En la estimación se espera obtener una fracción de volumen mayor que cero sólo en las orientaciones que coinciden con las fibras reales.

En el Capítulo 5 de esta tesis se discuten las principales limitaciones de las técnicas comentadas anteriormente y se presenta un nuevo método de estimación (83) que mejora en varios aspectos a los métodos existentes.

PARTE III: COMPENDIO DE PUBLICACIONES

CAPÍTULO 5: COMPENDIO DE CONTRIBUCIONES

En este Capítulo se presenta el compendio de contribuciones que constituyen el aporte fundamental de esta tesis. El Capítulo está formado por cinco secciones que incluyen cinco artículos científicos diferentes.

5.1 Mathematical description of q-space in spherical coordinates: exact q-ball imaging

Autores: Erick J Canales-Rodríguez, Lester Melie-García, Yasser Iturria-Medina

Título: *Mathematical Description of q-Space in Spherical Coordinates: Exact q-Ball Imaging*

Revista: *Magnetic Resonance in Medicine*

Año y volumen: 2009, Vol 61, 3, 1350-1367

Factor de impacto (en el año de publicación): 3.23

Magnetic Resonance in Medicine 61:1350–1367 (2009)

Mathematical Description of q-Space in Spherical Coordinates: Exact q-Ball Imaging

Erick Jorge Canales-Rodríguez,[1–3] Lester Melie-García,[1*] and Yasser Iturria-Medina[1]

Novel methodologies have been recently developed to characterize the microgeometry of neural tissues and porous structures via diffusion MRI data. In line with these previous works, this article provides a detailed mathematical description of q-space in spherical coordinates that helps to highlight the differences and similarities between various related q-space methodologies proposed to date such as q-ball imaging (QBI), diffusion spectrum imaging (DSI), and diffusion orientation transform imaging (DOT). This formulation provides a direct relationship between the orientation distribution function (ODF) and the diffusion data without using any approximation. Under this relationship, the exact ODF can be computed by means of the Radon transform of the radial projection (in q-space) of the diffusion MRI signal. This new methodology, termed exact q-ball imaging (EQBI), was put into practice using an analytical ODF estimation in terms of spherical harmonics that allows obtaining model-free and model-based reconstructions. This work provides a new framework for combining information coming from diffusion data recorded on multiple spherical shells in q-space (hybrid diffusion imaging encoding scheme), which is capable of mapping ODF to a high accuracy. This represents a step toward a more efficient development of diffusion MRI experiments for obtaining better ODF estimates. Magn Reson Med 61:1350–1367, 2009. © 2008 Wiley-Liss, Inc.

Key words: diffusion magnetic resonance imaging (dMRI); q-space; diffusion spectrum imaging (DSI); q-ball imaging (QBI); orientation distribution function (ODF); hybrid diffusion imaging (HYDI)

Diffusion MRI (dMRI) data are routinely used for studying molecular diffusion in fluids (1). When the diffusion is constrained by the presence of obstacles, dMRI experiments yield information about the confining geometry (2). Recently, there has been a large amount of interest in using dMRI techniques to obtain information about the microgeometry of porous structures and biological cells, which is supported by the noninvasive nature of these measurements. Also, dMRI techniques are able to probe the pore geometry over a range of length scales not accessible to standard techniques like x-ray and small-angle neutron scattering.

[1]Neuroimaging Department, Cuban Neuroscience Center, Havana, Cuba.

[2]Benito Menni Complex Assistencial en Salut Mental, Barcelona, Spain.

[3]Centro de Investigación Biomédica en Red de Salud Mental (CIBERSAM), Spain.

Grant sponsor: Cuban Neuroscience Center; Grant sponsor: Instituto de Salud Carlos III, Centro de Investigación Biomédica en Red de Salud Mental (CIBERSAM).

The first two authors contributed equally.

*Correspondence to: Lester Melie-García, Cuban Neuroscience Center. Ave. 25, Esq. 158, #15202, PO Box 6412/6414, Cubanacan, Playa, Havana, Cuba. E-mail: lester@cneuro.edu.cu

Received 19 September 2007; revised 9 October 2008; accepted 14 November 2008.

DOI 10.1002/mrm.21917
Published online 24 March 2009 in Wiley InterScience (www.interscience.wiley.com).

Diffusion tensor imaging (DTI) is the first dMRI technique that has been proposed to quantify in vivo the anisotropy of the water self-diffusion process in fibrous tissues (3). This approach allows estimating a second-order self-diffusion tensor **D** from a series of dMRI data without requiring exogenous contrast agents. DTI provides relevant information that is not available from other imaging modalities; however, this technique can only resolve a single fiber direction within each voxel.

In the last few years a number of novel methodologies have been developed to characterize more accurately the microgeometry of neural tissues (for a partial list of such publications, see Refs. 4–15). Among these advanced methods and algorithms, q-ball imaging (QBI) (6) and diffusion spectrum imaging (DSI) (11) have generated considerable interest due to a number of benefits such as model independence, theoretical soundness, and the ability to resolve intravoxel orientational heterogeneity.

In DSI the molecular displacement probability density function (also known as diffusion propagator) is measured by means of the Fourier relation between the dMRI signal and the diffusion propagator, without needing generative models of diffusion (11). The diffusion propagator within each voxel is reconstructed by taking the fast Fourier transform (FFT) of the dMRI signal on a 3D Cartesian grid. Subsequently, this propagator is projected to a spherical lattice in real space. Typically, to quantify the geometry of the fluid-filled pore space, a measure termed diffusion orientation distribution function (ODF) is computed. The ODF is obtained by means of the radial projection of the diffusion propagator. However, because of the large amount of experimental data required for its practical implementation, DSI is time-intensive (16).

In contrast to DSI, QBI measures the ODF directly from the data without computing the diffusion propagator. The ODF is estimated by sampling the dMRI signal on a spherical shell and taking the Radon transform on the sphere (4). This procedure makes QBI more suitable than DSI for clinical applications. However, the ODF computed by QBI is only an approximation of the exact ODF. Implicitly, the QBI ODF is estimated as the convolution of the diffusion propagator with a zeroth-order Bessel function, which gives rise to an undesirable contamination of the probability profiles along a particular direction with probabilities from other directions (4,12). This procedure induces spectral broadening of the diffusion peaks (17).

The diffusion orientation transform (DOT) (12) is another mathematical model proposed to characterize the microgeometry of fibrous tissues. In DOT the q-space Fourier integral is analytically evaluated in spherical coordinates under the assumption that dMRI signal attenuates monoexponentially. Under this approximation, DOT is able to transform water diffusivity profiles into displace-

ment probability profiles. The intravoxel orientational heterogeneity of fibers is measured by evaluating these probability profiles (or diffusion propagator) at a fixed displacement length. The main limitation of this methodology stems from the monoexponential model that is inaccurate under some experimental conditions, i.e., long diffusion times and strong magnetic field gradients.

In line with these previous works, this article provides a detailed mathematical description of q-space in spherical coordinates that helps to highlight the differences and similarities between various related q-space methodologies proposed to date such as DSI, QBI, and DOT. This formulation allows us to obtain a direct relationship between the ODF and dMRI data without using any approximation. Under this relationship, the exact ODF can be computed by means of the Radon transform of the radial projection of the dMRI signal in q-space. Since the proposed approach can be viewed as an extension to QBI, it was termed exact q-ball imaging (EQBI).

The rest of this article is organized as follows. A Theory section is devoted to obtain the exact ODF expression. In addition, in this part a practical ODF inversion via spherical harmonics is presented as well as a new model-based reconstruction. The Materials and Methods section describes computer simulations and image acquisition strategies designed to evaluate the performance of EQBI in relation to DSI and QBI. In the Results and Discussion sections the relevant findings are succinctly described. Finally, main results and contributions of this work are addressed in the Conclusions section. The Appendices present useful and rigorous mathematical derivations for the understanding of the particular aspects of the proposed methodology.

THEORY

q-Space Imaging

The fundamental relationship between the dMRI signal $A(\vec{\mathbf{q}})$ and the diffusion propagator $P(\vec{\mathbf{r}})$ is given by the following Fourier transform (1):

$$P(\vec{\mathbf{r}}) = \int A(\vec{\mathbf{q}})\exp(-2\pi i\vec{\mathbf{r}}\vec{\mathbf{q}})\, d\vec{\mathbf{q}}, \qquad [1]$$

where the Fourier space vector (q-space) is denoted, in Cartesian coordinates, by $\vec{\mathbf{q}} = (q_x, q_y, q_z)$, and the real-space vector is denoted by $\vec{\mathbf{r}} = (r_x, r_y, r_z)$. The q-space vector is defined as $\vec{\mathbf{q}} = \gamma\tau\vec{\mathbf{G}}/2\pi$, where γ is the gyromagnetic ratio for the nucleus of interest (i.e., hydrogen proton in the water molecule), $\vec{\mathbf{G}}$ is the diffusion-sensitizing gradient vector (i.e., magnetic field gradient vector) and τ is the diffusion-sensitizing gradient duration.

In general, the dMRI signal recorded by any MRI system is complex-valued. Practically, to exclude phase contamination arising from magnetic field inhomogeneities and biological motion (e.g., physiologic and involuntary patient motion), the diffusion propagator is reconstructed by taking the Fourier transform of the modulus of the complex signal (11,16):

$$P(\vec{\mathbf{r}}) = \int E(\vec{\mathbf{q}})\exp(-2\pi i\vec{\mathbf{r}}\vec{\mathbf{q}})\, d\vec{\mathbf{q}}, \qquad [2]$$

where $E(\vec{\mathbf{q}}) = |A(\vec{\mathbf{q}})|$. As a result, diffusion propagators recovered through Eq. [2] are constrained to be symmetric, i.e., $P(\vec{\mathbf{r}}) = P(-\vec{\mathbf{r}})$, because the information related to asymmetric components of a microstructure is contained in the phase of the signal (18). Since this loss of information is a common limitation of all the aforementioned dMRI techniques, throughout this article we will use a simpler nomenclature—we will refer to the modulus of the complex signal simply as diffusion signal or diffusion image. Approaches that estimate diffusion propagators or quantities derived from it by means of Eq. [2] and the discrete (or fast) Fourier transform are known as q-space imaging or diffusion spectrum imaging (see Refs. 1,11).

It is important to mention that the relationship given by Eq. [1] is based on the assumption that the temporal shape of the diffusion-sensitizing gradient vector is infinitely narrow, so that the molecules do not diffuse significantly during its application. This criterion is usually known as the *narrow pulse approximation*. However, acquisition methods cannot currently meet this condition, especially on clinical systems. Any deviations to this criterion will have an impact on the diffusion propagator that is estimated, regardless of particular sampling strategy or reconstruction algorithm, since for finite diffusion gradient pulses the diffusion propagator becomes the center-of-mass propagator (see Ref. 19 for a detailed description). Nevertheless, previous experimental results in porous materials suggest that the breakdown of the narrow pulse approximation does not have a significant impact on the orientational structure of the diffusion propagator (20,21).

Exact q-Ball Imaging

Orientation Distribution Function (ODF)

This section focuses on a mathematical description of q-space in spherical coordinates that allows obtaining quantities derived from the diffusion propagator, such as the orientation distribution function, in a compact and simple form. To this end, let us first rewrite Eq. [2] as:

$$P(\rho, \hat{\mathbf{r}}) = \int E(\vec{\mathbf{q}})\left[\int \exp(-2\pi i\rho\lambda)\delta(\hat{\mathbf{r}}\vec{\mathbf{q}} - \lambda)\, d\lambda\right] d\vec{\mathbf{q}}, \qquad [3]$$

where δ is the Dirac delta function, λ is an auxiliary parameter, and $\vec{\mathbf{r}} = \rho\hat{\mathbf{r}}$, being ρ and $\hat{\mathbf{r}}$ the length and unit vector of $\vec{\mathbf{r}}$. This result is a direct consequence of the Fourier slice theorem (22).

The above representation for the diffusion propagator is more complex than the original form given by Eq. [2]. However, as we shall see later, it is convenient for computing the exact ODF in a straightforward way. Following this representation, the diffusion propagator can be written:

$$P(\rho, \hat{\mathbf{r}}) = \int \widehat{E}(\lambda, \hat{\mathbf{r}})\exp(-2\pi i\rho\lambda)\, d\lambda, \qquad [4]$$

where $\widehat{E}(\lambda, \hat{\mathbf{r}})$ is the 3D Radon transform of $E(\vec{\mathbf{q}})$ evaluated at λ and $\hat{\mathbf{r}}$, which is defined by:

$$\widehat{E}(\lambda, \hat{\mathbf{r}}) = \int E(\vec{\mathbf{q}})\delta(\hat{\mathbf{r}}\vec{\mathbf{q}} - \lambda)\, d\vec{\mathbf{q}}. \quad [5]$$

Geometrically, $\widehat{E}(\lambda, \hat{\mathbf{r}})$ is the surface integral of the function $E(\vec{\mathbf{q}})$ on a plane perpendicular to $\hat{\mathbf{r}}$ with distance λ from the origin.

Typically, the ODF is calculated from the following line integral (4):

$$ODF(\hat{\mathbf{r}}) = \frac{1}{Z}\int P(\rho, \hat{\mathbf{r}})\, d\rho, \quad [6]$$

where Z is a normalization constant. The ODF sacrifices the radial information in the diffusion propagator but retains, on average, relevant angular contrast (4). At this stage we can use the diffusion propagator in Eq. [4] to evaluate (by means of the Dirac delta function) the integral in Eq. [6]. Consequently, the ODF can be computed as follows:

$$\begin{aligned} ODF(\hat{\mathbf{r}}) &= \frac{1}{Z}\int \widehat{E}(\lambda, \hat{\mathbf{r}})\left[\int \exp(-2\pi i\rho\lambda)\, d\rho\right] d\lambda \\ &= \frac{1}{Z}\int \widehat{E}(\lambda, \hat{\mathbf{r}})\delta(\lambda)\, d\lambda \\ &= \frac{1}{Z}\widehat{E}(0, \hat{\mathbf{r}}). \end{aligned} \quad [7]$$

Therefore:

$$ODF(\hat{\mathbf{r}}) = \frac{1}{Z}\int E(\vec{\mathbf{q}})\delta(\hat{\mathbf{r}}\vec{\mathbf{q}})\, d\vec{\mathbf{q}}, \quad [8]$$

where we make use of Eq. [5] with $\lambda = 0$.

To evaluate the above integral we need to simplify its structure. We can do this in spherical coordinates by breaking down the 3D integral into radial and angular components (see Appendix A for a detailed description). Therefore, Eq. [8] can be rewritten as:

$$ODF(\hat{\mathbf{r}}) = \frac{1}{Z}\int_{\mathrm{r}\perp\hat{\mathbf{q}}} S(\hat{\mathbf{q}})\, d\hat{\mathbf{q}}, \quad [9]$$

with

$$S(\hat{\mathbf{q}}) = \int_0^\infty E(q, \hat{\mathbf{q}})q\, dq. \quad [10]$$

Equations [9] and [10] are the angular and radial integrals respectively, where q and $\hat{\mathbf{q}}$ are the length and unit vector of $\vec{\mathbf{q}}$ (i.e., $\vec{\mathbf{q}} = q\hat{\mathbf{q}}$, $d\vec{\mathbf{q}} = q^2\, dq\, d\hat{\mathbf{q}}$); and $d\hat{\mathbf{q}}$ denotes the 2D differential area element on the surface of the unit sphere in the Fourier space (i.e., $d\hat{\mathbf{q}} = \sin\alpha d\alpha d\beta$ with elevation angle $\alpha \in [0,\pi]$, and azimuthal angle $\beta \in [0,2\pi]$).

The methodology of ODF reconstruction based on Eqs. [9] and [10] will be termed *exact q-ball imaging (EQBI)* and constitutes the main theoretical contribution of this article. Under this formulation the ODF is computed by the Radon transform (Eq. [9]) of the radial projection of the signal in q-space (Eq. [10]). That is, the ODF evaluated at a particular direction $\hat{\mathbf{r}}$ is given by the integral in q-space of the function $E(q,\hat{\mathbf{q}})q$ over the plane orthogonal to $\hat{\mathbf{r}}$. As a result, all the relevant information concerned with the probability for a water molecule to diffuse any distance in the direction $\hat{\mathbf{r}}$ (in the experimental diffusion time) is contained in the plane perpendicular to that direction in q-space.

Practical Considerations: Relationship between EQBI and QBI

No theoretical approximation has been used in the previous section for the ODF estimation. However, with reference to practical implementations of EQBI several points deserve to be discussed. For instance, in a model-free reconstruction the upper limit of integration in Eq. [10] cannot be taken to infinity. Hence, in practice it must be computed as:

$$S(\hat{\mathbf{q}}) \cong \int_0^{q_{\max}} E(q, \hat{\mathbf{q}})q\, dq, \quad [11]$$

where $q_{\max}$ is the maximum experimental value of q. This approximation is possible due to the strong diffusion signal attenuation in q-space. Making use of the main value theorem for integration (23) the above expression can be evaluated as:

$$S(\hat{\mathbf{q}}) \propto E(q'', \hat{\mathbf{q}})q'', \quad [12]$$

where q'' is some value of q in the interval from 0 to $q_{\max}$ (i.e., $q'' \in [0,q_{\max}]$). In general, in voxels within the brain white matter the diffusion signal attenuation profile $E(q,\hat{\mathbf{q}})$ is different for each particular direction $\hat{\mathbf{q}}$. For that reason, in such voxels the appropriated value q'' depends on $\hat{\mathbf{q}}$, i.e., $q'' = q''(\hat{\mathbf{q}})$. As a consequence, if the signal is sampled using an orientationally depended sampling scheme, i.e., on the closed surface $q'' = q''(\hat{\mathbf{q}})$, then we could obtain accurate results for the radial projection in Eq. [11] by means of Eq. [12]. However, in practice it is not possible to know a priori this surface, which is different for every voxel. Therefore, the integral in Eq. [11] must be numerically evaluated. That is, by sampling the signal on a spherical lattice in q-space ($0 \le q \le q_{\max}$, $0 \le \alpha \le \pi$, and $0 < \beta \le 2\pi$) and computing the integral along each direction via standard quadrature methods.

Alternatively, in QBI the ODF is computed as (4):

$$ODF_{QBI}(\hat{\mathbf{r}}) \approx \frac{q'}{Z'}\int_{\mathrm{r}\perp\hat{q}} E(q', \hat{\mathbf{q}})\, d\hat{\mathbf{q}}, \quad [13]$$

where Z' is a normalization constant. Hence, QBI implicitly calculates the radial projection of the signal (see Eqs. [9] and [10]) as the signal evaluated directly on a spherical shell with a particular radius q', so that

$$S(\hat{\mathbf{q}}) \propto E(q', \hat{\mathbf{q}})q'. \quad [14]$$

Consequently, the precision of the QBI ODF to represent the exact ODF depends on the accuracy of the approximation given in Eq. [14].

In principle, the orientationally depended surface $q'' = q''(\hat{\mathbf{q}})$ can be written as $q'' = q_{ISO} + \Delta q(\hat{\mathbf{q}})$ where q_{ISO} is the isotropic component of q'', and $\Delta q(\hat{\mathbf{q}})$ is the anisotropic remainder. It is important to notice that the approximation given in Eq. [14] is strictly correct only for an isotropic diffusion process in which the signal is measured on the spherical shell $q' = q_{ISO}$. This is due to the fact that for isotropic diffusion the signal attenuation profile $E(q,\hat{\mathbf{q}})$ is equal for each particular direction $\hat{\mathbf{q}}$, and therefore the value q'' (in Eq. [12]) does not depend on $\hat{\mathbf{q}}$ (i.e., $\Delta q(\hat{\mathbf{q}}) = 0$). The accuracy of the above approximation will be tested in the Results section under several fiber configurations and experimental sampling schemes. From the analysis developed in this section we conclude that: 1) the performance of QBI depends on intravoxel tissue properties; therefore, its accuracy of reconstruction will be different for every voxel in the brain; 2) QBI can be considered as a special case or approximation to the more general EQBI methodology.

Practical Considerations: Inversion via Spherical Harmonics

Since $S(\hat{\mathbf{q}})$ and the exact $ODF(\hat{\mathbf{r}})$ are functions of orientation, they can be expanded in terms of spherical harmonics, which represents the generalization of the Fourier series to the domain of the sphere. Therefore:

$$ODF(\hat{\mathbf{r}}) = \sum_{l=0}^{\infty} \sum_{m=-l}^{l} o_{lm} Y_{lm}(\hat{\mathbf{r}}), \quad [15]$$

and

$$S(\hat{\mathbf{q}}) = \sum_{l=0}^{\infty} \sum_{m=-l}^{l} s_{lm} Y_{lm}(\hat{\mathbf{q}}). \quad [16]$$

The coefficients of the spherical harmonic expansions are related by (see Appendix B for a detailed description):

$$o_{lm} = \frac{1}{2\pi^{1/2}} \frac{s_{lm}}{s_{00}} P_l(0), \quad [17]$$

where P_l is the Legendre polynomials of order l. Hence, the exact ODF can be recovered as:

$$ODF(\hat{\mathbf{r}}) = \frac{1}{2\pi^{1/2} s_{00}} \sum_{l=0}^{\infty} \sum_{m=-l}^{l} s_{lm} P_l(0) Y_{lm}(\hat{\mathbf{r}}). \quad [18]$$

Note that only even values of l figure into this sum because $P_l(0) = 0$ for odd l.

Practical Considerations: Model-Free and Model-Based Reconstructions

The new formalism allows us to obtain different types of reconstructions that can be classified as model-free and model-based solutions. The above taxonomy emerges from the way in which the radial projection of the signal (see Eq. [10]) can be computed. For instance, in model-free reconstructions, as previously stated, the radial projection is computed numerically through the acquisitions of a large number of measurements along each direction in q-space. Alternatively, in model-based reconstructions the radial projection is evaluated (analytically) assuming a specific model for the attenuation of the signal in q-space, which can be computed with fewer measurements. To put into practice the new framework, in the next subsection a model-based analytical reconstruction will be derived, which is just the ODF corresponding to the diffusion propagator forecasted by DOT.

Monoexponential EQBI (MeEQBI)

For the development of this subsection, it is important to recall that DOT methodology is a dMRI technique that computes (analytically) the Fourier integral in Eq. [2] under the assumption that the normalized diffusion signal attenuates monoexponentially as follows (12):

$$E(q, \hat{\mathbf{q}}) = \exp[-4\pi^2 t q^2 ADC(\hat{\mathbf{q}})], \quad [19]$$

where ADC is the apparent diffusion coefficient (or diffusivity profile) and t is the effective diffusion time. The main difference between EQBI and DOT is that while EQBI reconstructs a projection of the propagator, DOT reconstructs a single contour of the propagator.

Under this assumption, the radial projection of the signal given by Eq. [10] is computed as:

$$S(\hat{\mathbf{q}}) = \int_0^{\infty} \exp[-4\pi^2 t q^2 ADC(\hat{\mathbf{q}})] q \, dq. \quad [20]$$

This integral can be evaluated with the standard integral (e.g., integral 15.77, p. 98 in Ref. 24):

$$\int_0^{\infty} \exp(-aq^2) q^m \, dq = \frac{1}{2} \Gamma\left(\frac{m+1}{2}\right) a^{-(m+1)/2}. \quad [21]$$

In our case $a = 4\pi^2 t ADC(\Omega_q)$ and $m = 1$, therefore:

$$S(\hat{\mathbf{q}}) \propto \frac{1}{ADC(\hat{\mathbf{q}})}, \quad [22]$$

where we dropped the irrelevant numerical constants that can be collapsed into the ODF normalization constant.

At this step, the ODF given by Eq. [18] can be computed using the harmonic coefficients $\{s_{lm}\}$ obtained from the series:

$$\frac{1}{ADC(\hat{\mathbf{q}})} = \sum_{l=0}^{\infty} \sum_{m=-l}^{l} s_{lm} Y_{lm}(\hat{\mathbf{q}}). \quad [23]$$

This approach provides a closed-form relationship between the *ADC* and the ODF; it enables one to transform the diffusivity profiles into ODF profiles by means of the Radon transform of the inverse of the diffusivity profiles. We will refer to this reconstruction as monoexponential EQBI (MeEQBI).

It is important to note that in DOT (12) a theoretical expression for the diffusion ODF (defined by means of Eq. [6]) was not reported. Hence, the above derivation can be viewed as an extension to the DOT methodology. Some points with reference to MeEQBI will be addressed in the Discussion section.

MATERIALS AND METHODS

Simulated Data Description: Local Diffusion Model

To evaluate the performance of the new technique some synthetic data were generated using the multitensor model (5), which allows us to consider the presence of several fiber populations inside the voxel. Under this model, the expression for the signal can be written as:

$$E(q, \hat{\mathbf{q}}) = E_0 \sum_{i=1}^{M} \mathrm{f}_i \exp(-b\hat{\mathbf{q}}^{\mathrm{T}}\mathbf{D}^{(i)}\hat{\mathbf{q}}), \quad [24]$$

where M is the number of fiber-compartments, the diffusion-weighting factor b (also known as b-value) is defined as $b = 4\pi^2 tq^2$; the volume fraction of the i^{th} compartment is denoted by f_i, so that $\sum_{i=1}^{M} \mathrm{f}_i = 1$; $\mathbf{D}^{(i)}$ represents the second-order self-diffusion tensor of the i^{th} compartment, and E_0 is the signal amplitude in the absence of magnetic field gradients (i.e., $b = 0$). It is assumed that the compartments have equal relaxation rates and water density. In addition, the molecular exchange between compartments is neglected. This model is an extension to the diffusion tensor model (25) that is obtained for the particular case $M = 1$.

The i^{th} self-diffusion tensor can be parameterized as $\mathbf{D}^{(i)} = \mathbf{R}^{\mathrm{T}}(\theta, \phi)\mathbf{A}\mathbf{R}(\theta, \phi)$, where $\mathbf{R}(\theta, \phi)$ is the rotation matrix or operator that rotates a unit vector initially oriented along the x-axis toward the main axis (θ, ϕ) of the i^{th} fiber. The diagonal matrix $\mathbf{A}$ contains information about the anisotropy of the diffusion process within each fiber-compartment and can be written as:

$$\mathbf{A} = \begin{bmatrix} \lambda_1 & 0 & 0 \\ 0 & \lambda_2 & 0 \\ 0 & 0 & \lambda_3 \end{bmatrix}, \quad [25]$$

where λ_1 is the diffusivity along the main fiber-axis ($\lambda_1 \geq \lambda_2 \geq \lambda_3$), λ_2 and λ_3 are the diffusivities in the plane perpendicular to this axis.

The theoretical expression for the exact ODF corresponding to the diffusion tensor model was derived in Ref. (4). This result can be easily extended to the multitensor model (by linearity and the superposition principle) as:

$$ODF_T(\hat{\mathbf{r}}) = \frac{1}{Z''}(\pi t)^{1/2} \sum_{i=1}^{M} \mathrm{f}_i \cdot (\hat{\mathbf{r}}^T \mathbf{D}^{(i)^{-1}} \hat{\mathbf{r}})^{-1/2}, \quad [26]$$

where Z'' is a normalization constant, and $\mathbf{D}^{(i)^{-1}}$ is the inverse of $\mathbf{D}^{(i)}$. This ODF will be used as a reference to test the accuracy of ODF reconstructions.

Simulated Data Description: General Algorithm

In order to test the performance of the different q-space methodologies (i.e., QBI, DSI, and EQBI) in complex fiber geometries, we generate a set of 200 random fiber configurations with two or three fibers, which is typically the number of fiber populations detected in voxels with fiber crossings, and their corresponding diffusion signals for some signal-to-noise ratio (SNR) values and q-space sampling schemes by means of the following algorithm:

1) Generation of a number of fiber-compartments in the interval $M \in [2,3]$ by means of a discrete uniform distribution.
2) For each fiber i:
   a) Generation of a spatial orientation (θ, ϕ) by means of a uniform distribution on the surface of the unit sphere.
   b) Generation of a volume fraction by means of a uniform distribution in the interval $\mathrm{f}_i \in [0,1]$.
3) Scaling the generated volume fractions according to $\mathrm{f}_i = \mathrm{f}_i / \sum_{k=1}^{M} \mathbf{f}_k$.
4) Generation of the diffusivities by means of uniform distributions in the following range: $\lambda_1 \in [1, 2] \times 10^{-3}$ mm^2/s, $\lambda_2 = \lambda_3 \in [0.1, 0.6] \times 10^{-3}$ mm^2/s. These diffusivities are typically observed (or estimated) in human brain regions (26,27).
5) Computation of the true ODF given by Eq. [26].
6) Computation of the local diffusion signal (via Eq. [24]) corresponding to each method by using a particular set of experimental parameters (i.e., sampling scheme and maximum b-value), and taking into account the fiber parameters generated in the above steps. The signals are corrupted by Rician random noise, which is generated with a particular SNR.
7) Computation of the ODF pertinent to each q-space methodology.
8) Evaluation of the Kullback–Leibler (KL) divergence between true and estimated ODFs (see Eq. [28]).
9) Repeat from step 6) to step 8) 20 times.
10) Repeat from step 1) to step 9) 200 times.
11) Repeat from step 1) to step 10) using different experimental parameters such as maximum b-value, SNR, and q-space encoding scheme.

The following subsections provide details about the generation of the specific steps 6), 7), 8), and 11). The above algorithm was designed to compare the KL divergences between ODFs computed by each method and for predict-

Table 1
EQBI and QBI q-Space Encoding Schemes

Method	Shell	No. of directions	Status	*b*-value (s/mm^2)
$EQBI_r$		6		0
	1st	85	Fixed	500
	2nd	85	Fixed	1000
	3rd	85	Fixed	2000
	4th	85	Fixed	3000
	5th	85	Variable	Both in the range
	6th	85	Variable	from 4000 to 10,000
		Total 516		
$EQBI_a$		4		0
	1st	25	Fixed	500
	2nd	162	Fixed	1000
	3rd	162	Variable	Both in the range
	4th	162	Variable	from 2000 to 10,000
		Total 515		
MeEQBI		2		0
(hemispherical)	1st	240	Fixed	2000
	2nd	272	Variable	In the range from 1000 to 10,000
		Total 514		
QBI	1st	Total 514	Variable	In the range from 1000 to 10,000

ing the optimal experimental parameters that minimize (in average) this quantity.

Simulated Data Description: Experiment 1

The algorithm described in the above subsection was employed to run the first simulation. The q-space encoding schemes corresponding to each method are summarized in what follows. In EQBI we used sampling schemes comprised of concentric spherical shells, which are listed in Table 1. In order to test the effect of different measurement strategies, we simulated one type of scheme comprised of six shells that gives priority to the radial sampling denoted as $EQBI_r$, and another type of scheme comprised by four shells that gives priority to the angular sampling denoted as $EQBI_a$. This table also depicts the MeEQBI scheme comprised of two hemispherical shells.

In $EQBI_r$ the first four shells were fixed for all experiments to the following *b*-values: 500, 1000, 2000, and 3000 s/mm^2. The *b*-values of the two remaining shells were ranged from 4000 to 10,000 s/mm^2 in steps of 1000 s/mm^2, which gives a total number of 21 possible combinations of q-space sampling schemes. Similarly, in $EQBI_a$ the first two shells were fixed for all experiments to *b*-values: 500 and 1000 s/mm^2. The *b*-values of the two remaining shells were varied from 2000 to 10,000 s/mm^2 in intervals of 1000 s/mm^2, yielding a total number of 36 possible combinations of q-space sampling schemes. In MeEQBI the first shell was fixed for all experiments to the *b*-value 2000 s/mm^2 while the second shell was ranged from 1000 to 10,000 s/mm^2 in steps of 500 s/mm^2 to give a total of 19 possible sampling schemes.

Similarly, in QBI we employed 19 sampling schemes with a single spherical shell. The *b*-value corresponding to each particular shell was varied from 1000 to 10,000 s/mm^2 in intervals of 500 s/mm^2. In addition to the EQBI and QBI analysis, a standard DSI experiment was simulated (11). The q-space sampling points were obtained from a 3D Cartesian grid. The grid is comprised by points of a cubic lattice within the sphere of five lattice units in radius. These points were obtained from the following expression:

$$\vec{\mathbf{q}} = a\hat{\mathbf{q}}_x + b\hat{\mathbf{q}}_y + c\hat{\mathbf{q}}_z, \qquad [27]$$

with $a, b, c \in \{0, \pm1, \pm2, \pm3, \pm4, \pm5\}$, and $\hat{\mathbf{q}}_x$, $\hat{\mathbf{q}}_y$, $\hat{\mathbf{q}}_z$ denoting the q-space unit vectors along the x-, y-, and z-axis, respectively. Diffusion images were simulated via Eq. [24] for the $N = 515$ q-space points where $\sqrt{a^2 + b^2 + c^2} \leq 5$. For this experiment the maximum *b*-value was ranged from 1500 to 17,000 s/mm^2 in steps of 500 s/mm^2, which gives a total number of 32 sampling schemes. For each fiber configuration and SNR, diffusion signals were generated using all the above possible combinations of the sampling schemes relevant to each reconstruction method.

Simulated Data Description: Experiment 2

The above simulation was designed to evaluate the performance of different methodologies using moderate spatial resolution q-space data with encoding schemes of $N = 515$ measurements. In the present experiment we employ the same algorithm and fiber configurations generated in the above simulation, but using sampling schemes with a smaller number of measurements, i.e., $N = 252 - 258$. The q-space encoding schemes corresponding to EQBI and QBI are listed in Table 2. Again, $EQBI_r$ and $EQBI_a$ denote schemes that give priority to the radial and angular sam-

Table 2
EQBI and QBI q-Space Encoding Schemes

Method	Shell	No. of directions	Status	*b*-value (s/mm^2)
$EQBI_r$		6		0
	1st	42	Fixed	500
	2nd	42	Fixed	1000
	3rd	42	Fixed	2000
	4th	42	Fixed	3000
	5th	42	Variable	Both in the range
	6th	42	Variable	from 4000 to 10,000
		Total 258		
$EQBI_a$		3		0
	1st	85	Fixed	2000
	2nd	85	Variable	Both in the range
	3rd	85	Variable	from 3000 to 10,000
		Total 258		
MeEQBI		2		0
(hemispherical)	1st	125	Fixed	2000
	2nd	125	Variable	In the range from 1000 to 10,000
		Total 252		
QBI	1st	Total 252	Variable	In the range from 1000 to 10,000

pling, respectively. In particular, in this experiment $EQBI_r$ and $EQBI_a$ were comprised of six and three shells, respectively.

The only difference between the $EQBI_r$, MeEQBI, and QBI sampling schemes generated in the above experiment and employed in this simulation is the number of points corresponding to each spherical shell (see Table 2). For these sampling schemes the same configurations of *b*-values obtained in the above experiment were employed. In contrast, in $EQBI_a$ the first shell was fixed for all experiments to the *b*-value 2000 s/mm^2 and the *b*-values of the two remaining shells were varied from 3000 to 10,000 s/mm^2 in intervals of 1000 s/mm^2, which gives a total number of 28 possible combinations of sampling schemes.

DSI synthetic data were generated using a Cartesian grid comprised of points of a cubic lattice within the sphere of four lattice units in radius. These points were obtained from Eq. [27] with $a, b, c \in \{0, \pm1, \pm2, \pm3, \pm4\}$. Diffusion images were simulated through Eq. [24] for $N = 257$ points where $\sqrt{a^2 + b^2 + c^2} \leq 4$. Similarly, for this experiment the maximum *b*-value was ranged from 1500 to 17,000 s/mm^2 in steps of 500 s/mm^2 to give a total number of 32 sampling schemes. Again, for each fiber configuration and SNR, diffusion signals were generated using all above possible combinations of the sampling schemes corresponding to each reconstruction method.

Simulated Data Description: Experiment 3

The above experiments were devoted to extract the optimum sampling schemes (from the set of generated schemes) relevant to each q-space reconstruction methodology. The estimation of such optimum values is performed taking into account the observed experimental variability of diffusivities in white matter tissues. In contrast, this final experiment is proposed as an initial test to characterize the stability and dependence of these methods on diffusivities (in terms of fractional anisotropy) with both optimal and suboptimal sampling schemes. To do this, we perform a simulation in line with the general algorithm described in previous subsections. However, in this experiment we do not generate random values for the diffusivities; instead, they were generated as follows: The main diffusivity was fixed to $\lambda_1 = 1.5 \cdot 10^{-3}$ mm^2/s while λ_2 and λ_3 were varied from $\lambda_2 = \lambda_3 = 0.1 \cdot 10^{-3}$ mm^2/s to $\lambda_2 = \lambda_3 = 0.6 \cdot 10^{-3}$ mm^2/s in intervals of $0.1 \cdot 10^{-3}$ mm^2/s. Typically, these diffusivities are observed in human brain regions (26,27). Fractional anisotropy (FA) values corresponding to these diffusivities are FA $\approx$ 0.93, 0.85, 0.77, 0.69, 0.60, and 0.52, respectively. The sampling schemes employed for the different reconstruction methods are described below.

For each q-space method we used 19 different sampling schemes. In particular, in QBI and MeEQBI the same sampling schemes listed in Table 2 were employed. DSI synthetic data were generated following the same procedure described in the second experiment ($N = 257$). In this case the maximum *b*-value was varied from 1000 to 10,000 s/mm^2 in intervals of 500 s/mm^2. Model-free EQBI methods were tested using a subset of the sampling schemes generated in the second experiment (see Table 2). Specifically, in $EQBI_a$ the first two shells were fixed to 2000 and 3000 s/mm^2 while the third shell ranged from 1000 to 10,000 s/mm^2 in intervals of 500 s/mm^2. In $EQBI_r$ the first five shells were fixed for all experiments to the following *b*-values: 500, 1000, 2000, 3000, and 4000 s/mm^2. The *b*-value of the sixth shell was varied from 1000 to 10,000 s/mm^2 in steps of 500 s/mm^2. The SNR values used in this experiment were 10 and 20.

Simulated Data Description: EQBI, QBI, and DSI Reconstruction

All ODFs computed from the above experiments were reconstructed onto 2562 angular directions obtained from the "sphere_tri" function, "bioelectromagnetism" MatLab toolbox (MathWorks, Natick, MA; http://eeg.sourceforge.et/doc_m2html/bioelectromagnetism/sphere_tri.html). This function was also used to generate the spherical sampling schemes with $N = 514$, 162, and 42 measurements listed in Tables 1 and 2. Similarly, the spherical encoding schemes with $N = 85$ and 25 were selected from tables of spherical codes published electronically at http://www.research.att.com/~njas/electrons/dim3/, which are based on minimal energy approaches. In Table 1 the hemispherical MeEQBI schemes were obtained from the QBI scheme with $N = 514$ measurements. Likewise, the hemispherical MeEQBI schemes listed in Table 2 were obtained from the QBI scheme with $N = 252$ measurements, which was obtained from the vertices of a 5-fold regularly tessellated icosahedron projected onto the sphere. The methodologies behind the estimation of individual ODFs corresponding to each reconstruction method are summarized below.

All DSI ODFs were computed as follows. First, diffusion images obtained from Experiments 1, 2, and 3 ($N = 515$ and 257) are premultiplied by a Hanning window to ensure a smooth attenuation of the signal at high values of q (11). Second, we reconstructed the diffusion propagator at each voxel by taking the 3D FFT of the diffusion signals. The signal is zero-padded before the Fourier transformation in order to obtain interpolated diffusion propagators in real space. As the number of zeros increases, the FFT better represents the continuous Fourier transform of the signals (28). This methodology allows us to obtain a signal representation on a $100 \times 100 \times 100$ 3D Cartesian grid. Finally, from this map we compute an ODF using Eq. [6]. The integral is evaluated as a discrete sum (Simpson numerical integration) over the available range $\rho \in [0,100]$.

The approach used to compute QBI ODFs is similar to those previously described (8,29,30). The ODFs were computed through Eq. [18] using the spherical harmonic decomposition of the data (see Appendix C for a detailed description).

Model-free EQBI reconstructions (i.e., $EQBI_r$, and $EQBI_a$) were performed through the following steps:

- Computation of the radial projection of the signal along each direction by means of a Simpson numerical integration.
- Computation of the set of harmonic coefficients $\{s_{lm}\}$ using Eq. [16] (see Appendix C).
- ODF estimation using Eq. [18].

On the other hand, the estimation of model-based ODFs from MeEQBI involves the following steps:

Table 3
Optimal q-Space Encoding Schemes ($N = 515$)

Method	Shell	No. of directions	Optimal configuration of b-values (s/mm^2)				
			$SNR = 5$	$SNR = 8$	$SNR = 10$	$SNR = 15$	$SNR = 20$
$EQBI_r$		6	0	0	0	0	0
	1st	85	500	500	500	500	500
	2nd	85	1000	1000	1000	1000	1000
	3rd	85	2000	2000	2000	2000	2000
	4th	85	3000	3000	3000	3000	3000
	5th	85	4000	4000	4000	4000	5000
	6th	85	5000	5000	5000	6000	7000
		Total 516					
$EQBI_a$		4	0	0	0	0	0
	1st	25	500	500	500	500	500
	2nd	162	1000	1000	1000	1000	1000
	3rd	162	2000	3000	4000	2000	5000
	4th	162	4000	4000	5000	7000	8000
		Total 515					
MeEQBI		2	0	0	0	0	0
(hemispherical)	1st	240	2000	2000	2000	2000	2000
	2nd	272	2500	2500	3000	3500	6000
		Total 514					
QBI	1st	Total 514	2000	2500	2500	3000	3000
DSI		Total 515	3000	3500	4500	7500	8500

- Computation of the diffusivity profile (i.e., ADC_1 and ADC_2) corresponding to each different spherical shell by means of Eq. [19].
- Computation of a representative diffusivity profile $ADC = (ADC_1 + ADC_2)/2$.
- Computation of the set of harmonic coefficients $\{s_{lm}\}$ using Eq. [23] (see Appendix C).
- ODF estimation using Eq. [18].

The ODF reconstruction accuracy was measured using the KL divergence between the reference ODF given in Eq. [26] (i.e., ODF_T) and the estimated ODF (i.e., ODF). The KL divergence is a measure of the dissimilarity between two probability distributions that has previously been used to compare ODFs (17). The KL divergence between ODF and ODF_T is defined as:

$$KL(ODF_T \| ODF) = \sum_{i=1}^{N} ODF_T(\hat{\mathbf{r}}_i) \log \frac{ODF_T(\hat{\mathbf{r}}_i)}{ODF(\hat{\mathbf{r}}_i)}, \quad [28]$$

where $\{\hat{\mathbf{r}}_i,\ i = 1, \ldots N\}$ is the set of angular directions in which the ODFs are sampled or reconstructed (i.e., $N = 2562$). From the above experiments, the KL divergence was calculated for each synthetic data and reconstruction method. The synthetic diffusion signals were corrupted by Rician noise with different SNRs, i.e., $SNR = \{5, 8, 10, 15, 20\}$, which were related to the E_0 image by means of $SNR = E_0/\sigma$, where σ is the standard deviation of the Rician distribution.

RESULTS

Experiment 1

Table 3 lists the optimal sampling schemes obtained from the first experiment. These optimal q-space encoding schemes minimize the mean value of the KL divergence computed between the estimated and true ODFs. It is interesting to note how the optimal schemes depend on SNR. The maximum b-value increases with the increase of SNR for all methods. In particular, DSI exhibits the maximum b-value (8500 s/mm^2) for SNR = 20.

Figure 1 shows the mean values (upper bars) and standard deviations (lower bars) of the KL divergence relevant to each reconstruction method when the optimal sampling schemes listed in Table 3 are used. Based on these results we can draw several partial conclusions. First, the mean value of the KL divergence increases with the decrease of SNR for all methods, as expected. Second, the MeEQBI method provides better ODF estimation for all SNRs (in terms of mean value). Note that the main differences between the MeEQBI and QBI reconstructions arise for $SNR \geq 15$. Third, although DSI presents better stability (in terms of variance), it provides worse ODF reconstruction (in terms of mean value). Fourth, the accuracy of model-free EQBI reconstruction depends on the sampling scheme; for instance, $EQBI_a$ gives in general better output ODFs than $EQBI_r$. In the Discussion section we shall provide some practical implications of these results.

Experiment 2

Table 4 lists the optimal q-space encoding schemes for each reconstruction method. These optimal sampling schemes minimize the mean value of the KL divergence estimated in the second experiment. As can be seen, the maximum b-value increases with the improvement of SNR for all methods. Again, the maximum b-value corresponds to the DSI method, which requires a value of 7500 s/mm^2 for $SNR = 20$. Note that the $EQBI_r$, $EQBI_a$, and MeEQBI optimal sampling schemes do not show differences for cases of $SNR = 5$, 8, and 10.

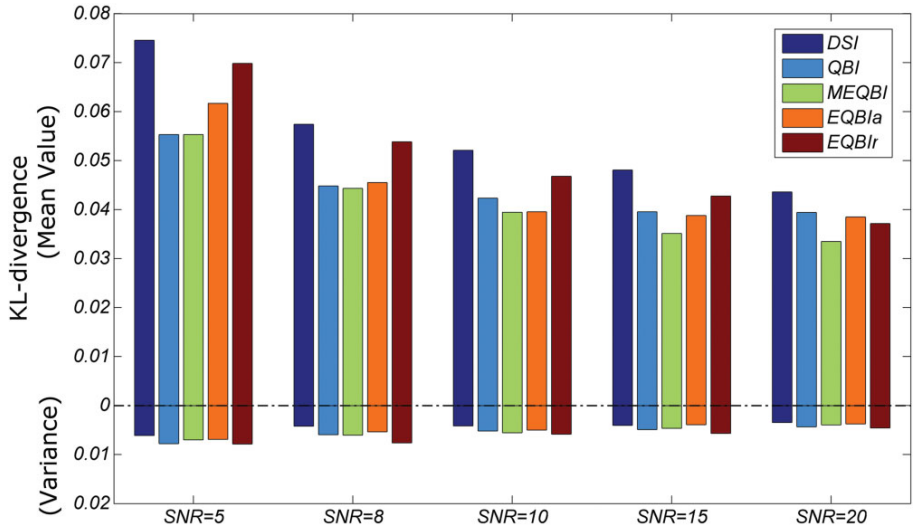

FIG. 1. Reconstruction accuracy of ODF reconstruction methods for a diffusion synthetic dataset with 200 fiber configurations, which were generated with two and three fiber populations and the optimal sampling schemes listed in Table 3. For each SNR and fiber configuration 20 repetitions of Rician random noise were generated to corrupt the synthetic diffusion signals. The x- and y-axis denote respectively the SNR and KL divergence between the reference and estimated ODFs. The upper and lower bars represent the mean value and the variance of the KL divergence computed for each SNR respectively.

Figure 2 depicts the mean values (upper bars) and standard deviations (lower bars) of the KL divergence relevant to each reconstruction method when the optimal sampling schemes listed in Table 4 are used. From this study we draw the following partial conclusions. First, the mean value of the KL divergence increases with the decrease of SNR for all methods, as expected. Second, MeEQBI outperforms all remaining methods for all SNRs (in terms of mean value). Finally, $EQBI_a$ performs better than DSI and $EQBI_r$.

The above experiments (Tables 3 and 4; Figs. 1 and 2) have similar results in some aspects. Most of these results are robust with respect to the two q-space sampling resolutions employed in the experiments. The major difference resides only in the reconstruction accuracy of $EQBI_r$, which showed a decline for the lower spatial resolution (i.e., $N \approx 258$). In addition, the difference between the KL divergences computed with MeEQBI and QBI has decreased in the second experiment with respect to the first one.

Experiment 3

Figures 3 and 4 show the mean values and standard deviations of the KL divergence corresponding to MeEQBI, $EQBI_r$, $EQBI_a$, QBI, and DSI as function of the anisotropy (i.e., FA) of the diffusion process within each fiber compartment. Figure 3 corresponds to the case $SNR = 10$, and Fig. 4 to $SNR = 20$.

As can be seen in Fig. 3, the performance of QBI, $EQBI_a$, and $EQBI_r$ highly depends on FA for b-values larger than 4000, 5000, and 8000 s/mm^2, respectively. It is important

Table 4
Optimal q-Space Encoding schemes ($N = 258$)

Method	Shell	No. of directions	Optimal configuration of b-values (s/mm^2)				
			$SNR = 5$	$SNR = 8$	$SNR = 10$	$SNR = 15$	$SNR = 20$
$EQBI_r$		6	0	0	0	0	0
	1st	42	500	500	500	500	500
	2nd	42	1000	1000	1000	1000	1000
	3rd	42	2000	2000	2000	2000	2000
	4th	42	3000	3000	3000	3000	3000
	5th	42	4000	4000	4000	4000	5000
	6th	42	5000	5000	5000	6000	7000
		Total 258					
$EQBI_a$		3	0	0	0	0	0
	1st	85	2000	2000	2000	2000	2000
	2nd	85	3000	3000	3000	3000	3000
	3rd	85	4000	4000	4000	4000	5000
		Total 258					
MeEQBI		2	0	0	0	0	0
(hemispherical)	1st	125	2000	2000	2000	2000	2000
	2nd	125	2500	2500	2500	3000	3500
		Total 252					
QBI	1st	Total 252	1500	2000	2500	3000	3000
DSI		Total 258	2500	3000	4500	6500	7500

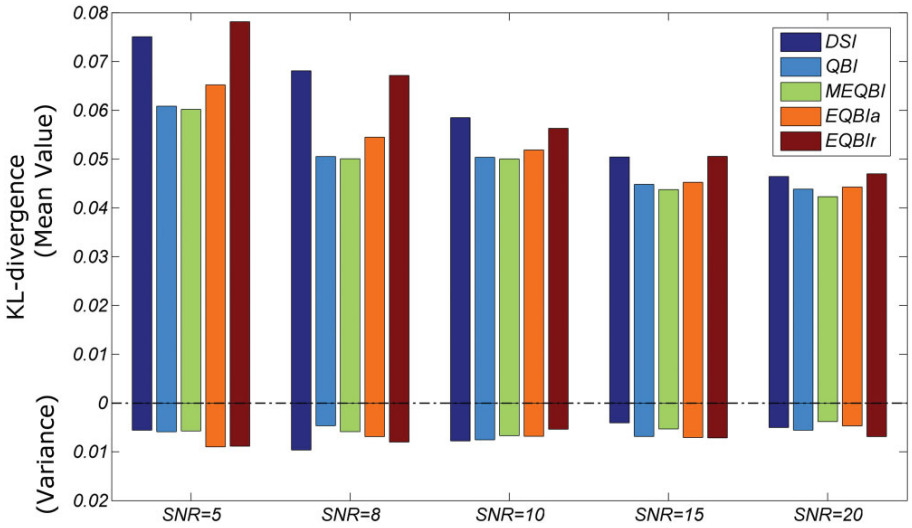

FIG. 2. Reconstruction accuracy of ODF reconstruction methods for a diffusion synthetic dataset with 200 fiber configurations, which were generated with two and three fiber populations and the optimal sampling schemes listed in Table 4. For each SNR and fiber configuration 20 repetitions of Rician random noise were generated to corrupt the synthetic diffusion signals. The x- and y-axis denote respectively the SNR and KL divergence between the reference and estimated ODFs. The upper and lower bars represent the mean value and the variance of the KL divergence computed for each SNR.

to notice that KL divergences computed from QBI using optimal and nonoptimal sampling schemes differ by one order of magnitude. In contrast, MeEQBI and DSI showed a stable behavior with respect to the FA value over the entire range of *b*-values. MeEQBI was slightly more accurate than DSI.

In Fig. 4 a decrease in the dependence of q-space methods on FA can be appreciated in comparison with Fig. 3. Specifically, the performance of QBI and $EQBI_a$ depends more on FA for *b*-values larger than 5000 and 8000 s/mm^2, respectively. In this experiment MeEQBI, DSI, and $EQBI_r$ behave stably in the whole range of *b*-values (in the case of $EQBI_r$ for *b*-values lower than 9500 s/mm^2). Here QBI was the most unstable method as well.

The above experiment supports the hypothesis that, in general, q-space methods based on sampling schemes with a large variety of *b*-values (i.e., EQBI, DSI) are more stable for describing the orientational structure of diffusion processes with a moderate value of the anisotropy (FA). This issue will be explored in the following section.

DISCUSSION

Error Sources and Practical Implications

Ideally, if the ODF corresponding to DSI is calculated by means of the radial projection given by Eq. [4] then, in theory, the ODFs predicted by DSI and EQBI should be identical. However, in practice these ODFs are different as a result of numerical errors introduced by different reconstruction approaches.

In DSI the mapping between Cartesian and spherical coordinates systems can introduce artifacts in the ODF. These artifacts, known as Cartesian artifacts, may be a problem at the low (or moderate) spatial resolution typically used for DSI (4). In addition, the ODF only can be computed through the Fourier formalism (i.e., FFT), which requires large experimental diffusion-sensitizing gradients to satisfy the Nyquist condition. Also, in FFTs the noise interacts with the signal in a complex way. In particular, since the FFT is done on magnitude data, it introduces a Rician bias effect into the reconstruction, which will have a considerable effect given the very low SNR of many of the measurements at higher *b*-values. This is revealed in our experiments by the fact that the better DSI ODF reconstructions were achieved for moderate values of the maximum *b*-value; for example *b*max = 7500 s/mm^2 for N = 515, and *b*max = 6500 s/mm^2 for N = 257, with SNR = 15 (see Tables 3, 4). Although previous studies have employed a maximum *b*-value in the range from 12,000–18,000 s/mm^2 (11), a recent study with real data in a 3T MRI system (31) showed that lower *b*-values can produce better ODF reconstructions (e.g., *b*max = 6500 s/mm^2 for N = 515, and *b*max = 4000 s/mm^2 for N = 203), which support our results. Unfortunately, the SNR inherent to this clinical MRI system was not reported, and therefore we cannot perform a rigorous comparison between the optimal *b*-values obtained in this article and the one forecasted in our work.

On the other hand, EQBI inherits some benefits of QBI: 1) the measurements and the reconstructions are both performed on the sphere, so the reconstructions are immune to Cartesian artifacts; 2) spherical sampling provides a more natural framework for describing angular resolution (16); and 3) it provides a simplified and flexible framework that can be implemented using a number of well-characterized spherical functions, for example: spherical harmonics, spherical radial basis functions, and spherical wavelets. However, this type of implementation also introduces artifacts. The two main error sources are the truncation effects on the spherical functions, which will be the topic of a separate discussion in this section, and the fact that Eq. [10] is approximated by a discrete sum. In principle, these error sources depend on the q-space sampling scheme. Therefore, different sampling schemes with a constant number of measurements N can provide different reconstruction quality. This effect is tested in our simulations by considering two different types of schemes that give priority to the angular ($EQBI_a$) and radial ($EQBI_r$) sampling. Notice that the experiments do not account for T_2 effects as q increases. Incorporating this effect will give

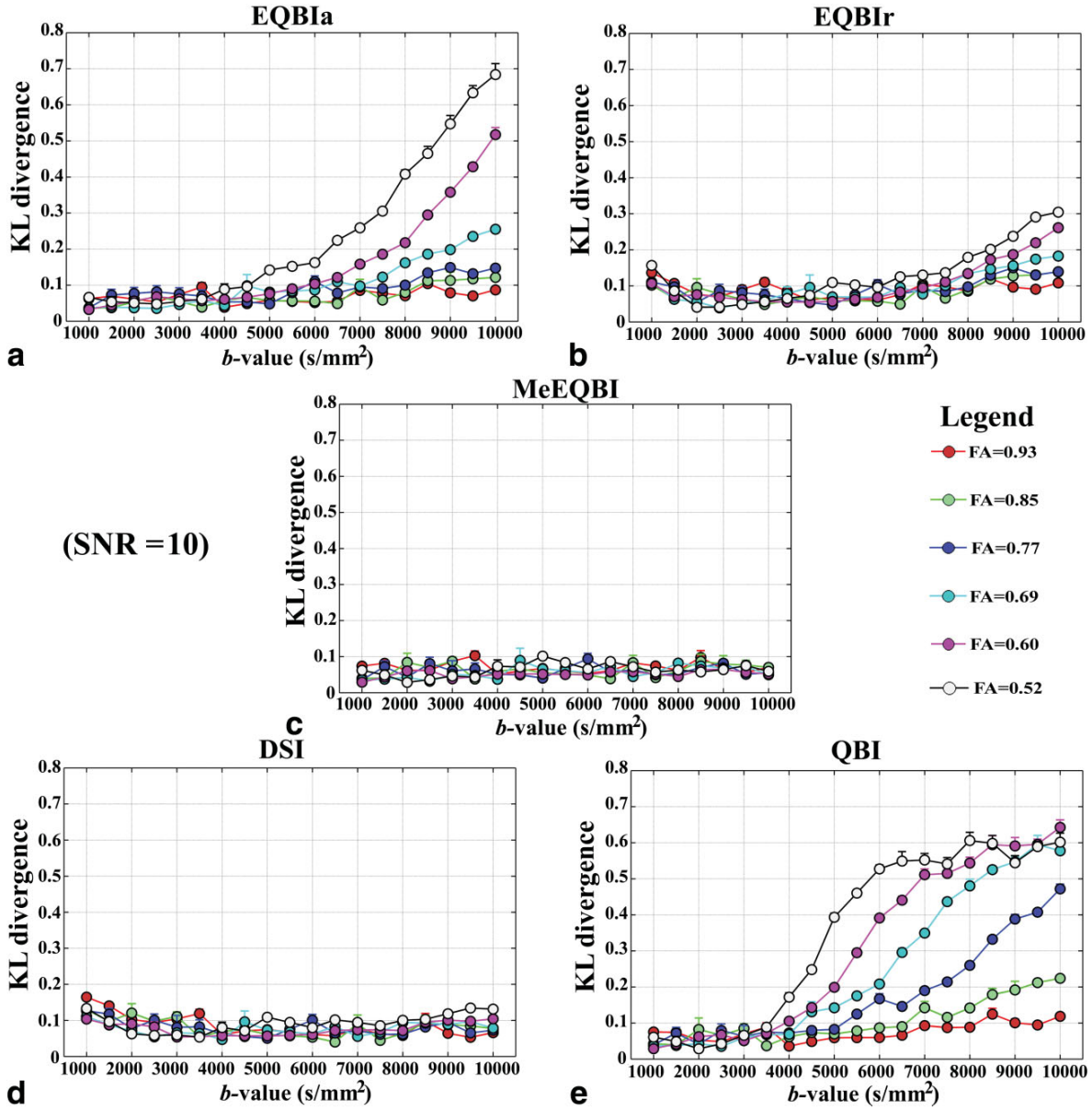

FIG. 3. Reconstruction accuracy of ODF reconstruction methods for a diffusion synthetic dataset with 200 fiber configurations, which were generated with two and three fiber populations, sampling schemes with $N = 252 - 258$ measurements, and different FA values. For each fiber configuration 20 repetitions of Rician random noise with SNR = 10 were generated to corrupt the synthetic diffusion signals. The y-axis of the individual subfigures denotes the KL divergence, i.e., mean value and variance, between the reference and estimated ODFs. **a,b:** The x-axis denotes *b*-values corresponding to the third ($EQBI_a$) and sixth ($EQBI_r$) shell of the sampling schemes of model-free EQBI methods. For $EQBI_a$ the first two shells were fixed to the *b*-values 2000 and 3000 s/mm^2. For $EQBI_r$ the first five shells were fixed to the following *b*-values: 500, 1000, 2000, 3000, and 4000 s/mm^2. **c:** The x-axis indicates the *b*-value corresponding to the second shell of the sampling scheme used in MeEQBI (the first shell was fixed to $b = 2000$ s/mm^2). **d:** The x-axis denotes the maximum *b*-value employed in the DSI sampling scheme. Similarly, in **(e)** the x-axis represents the *b*-value of the sampling scheme utilized in QBI.

better estimates of the best settings for diffusion MRI experiments (32). Nevertheless, the sampling schemes employed in this work allow us to illustrate the features of different EQBI encoding strategies. It is important to mention that the estimation of the optimal EQBI sampling schemes can be performed using a larger set of possible combinations of *b*-values (see Tables 1, 2) and a spherical lattice with a finer resolution. Since the analysis of all such possible combinations is a very demanding task from the computational point of view, in this work we employed a reasonable reduced set of sampling schemes.

In theory, it is far from clear which of the above source of artifacts is more severe. Hence, in this work we examined, via numerical simulations, the ODF reconstruction

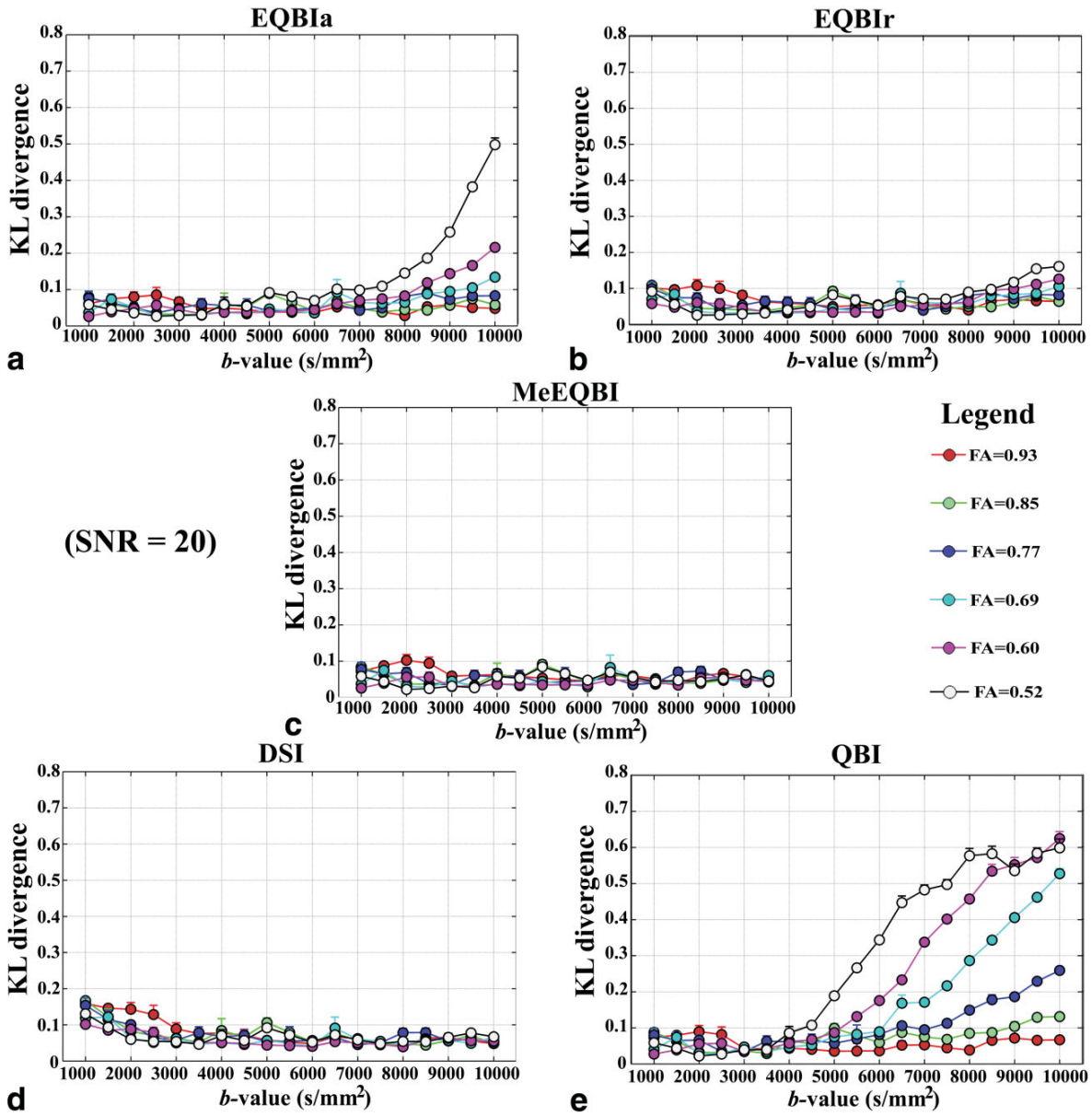

FIG. 4. Reconstruction accuracy of ODF reconstruction methods for a diffusion synthetic dataset with 200 fiber configurations, which were generated with two and three fiber populations, sampling schemes with $N = 252 - 258$ measurements, and different FA values. For each fiber configuration 20 repetitions of Rician random noise with SNR = 20 were generated to corrupt the synthetic diffusion signals. The y-axis of the individual subfigures denotes the KL divergence, i.e., mean value and variance, between the reference and estimated ODFs. **a,b:** The x-axis denotes *b*-values corresponding to the third ($EQBI_a$) and sixth ($EQBI_r$) shell of the sampling schemes of model-free EQBI methods, respectively. For $EQBI_a$ the first two shells were fixed to the *b*-values 2000 and 3000 s/mm^2. For $EQBI_r$ the first five shells were fixed to the following *b*-values: 500, 1000, 2000, 3000, and 4000 s/mm^2. **c:** The x-axis indicates the *b*-value corresponding to the second shell of the sampling scheme used in MeEQBI (the first shell was fixed to $b = 2000$ s/mm^2). **d:** The x-axis denotes the maximum *b*-value employed in the DSI sampling scheme. Similarly, in **(e)** the x-axis represents the *b*-value of the sampling scheme utilized in QBI.

accuracy for some methods, sampling schemes, fiber configurations, and SNRs. These studies allowed extracting the optimal sampling schemes of each method (see Tables 3, 4) and comparing their performance using these optimal protocols. Results from the first and second experiments (Figs. 1, 2) reveal some interesting aspects. In the typical DSI q-space resolution (i.e., $N = 515$) $EQBI_a$ and $EQBI_r$ give better output ODFs than DSI. On the other hand, in a lower q-space resolution with $N = 257$ $EQBI_a$ outperforms DSI; however, DSI gives similar output ODFs than $EQBI_r$.

The relative superiority of $EQBI_a$ with respect to $EQBI_r$ in both experiments suggests that, for these optimal sampling schemes, the numerical errors arising from the radial projection of the diffusion signal, which are produced by a

low radial resolution of the sampling scheme, are less important than the loss of information due to a sampling scheme with low angular resolution. Therefore, in practice one should concentrate the measurements on a q-space frequency band with a high angular resolution. Nevertheless, this idea cannot be necessarily extrapolated to the limit case of sampling in a single shell. The MeEQBI method, which was implemented with two shells, provides better ODF estimation for all SNRs.

The third experiment (Figs. 3, 4) reveals that MeEQBI is more stable than QBI for arbitrary (nonoptimal) sampling schemes, especially at high *b*-values. This result implies that in practice MeEQBI (as well as DSI) may provides stable solutions for a higher number of voxels, due to the dependence of the optimal sampling scheme on SNR and FA, and the lack of a priori information about the values of these magnitudes at each voxel.

This result suggests that q-space methods like EQBI and DSI, which are based on sampling schemes with a large variety of *b*-values, are more stable for describing the orientational structure of diffusion processes with moderate anisotropy. From a theoretical point of view this fact can be explained by considering that different *b*-values allow exploring the real space (i.e., the space where take place the diffusion process) at different length scales. So, q-space methods based on these schemes are able to characterize a broad range of molecular displacement lengths, and hence, a broad range of pore microstructure shapes. Reconstruction methods based on the combination of low and high *b*-values in the same experiment are more stable and robust than those based on sampling schemes with a single spherical shell. Particularly in voxels with moderate anisotropy, where high *b*-values are required to characterize the angular structure of the diffusion profile. In practice, ODF reconstruction techniques based on methods that take into account only the information coming from high *b*-values will be unstable due to the low SNR of the measurements.

It is important to mention that the concept of sampling on several concentric shells is not new. It was recently proposed (33) to study the human central nervous system. This methodology, termed hybrid diffusion imaging (HYDI), facilitates the application of multiple data-analysis strategies including DTI, DSI, QBI, and biexponential diffusion from a single dataset in a moderate scan time on a clinical MRI scanner. The methodology introduced in this article can be easily incorporated within the HYDI framework.

Model-Based Reconstructions and Image Fusion Techniques

Although model-free EQBI reconstructions can be performed with sampling schemes with low or moderate relative density, the best theoretical performance is obtained for dense sampling schemes (i.e., schemes with a high spatial coverage in q-space). Nevertheless, one of the most important advantages of EQBI is its versatility to compute model-based ODFs. This type of reconstruction provides some benefits that can be enumerated as follows: 1) the radial projection of the signal can be computed over the continuous q-space, 2) the upper limit of integration can be extended to infinity, and 3) the measurements can be collected using a smaller sampling scheme.

To illustrate this, we derived an analytical expression for the ODF under the assumption that dMRI signal attenuates monoexponentially (i.e., MeEQBI), which is the more elementary diffusion model for characterizing multimodal diffusion processes. Even so, as can be seen in Figs. 1–4, it provides the best ODF reconstruction in terms of accuracy and stability for both optimal and nonoptimal sampling schemes. In principle, this approach can be implemented using a sampling scheme with only one spherical shell. However, in this work we use a sampling scheme formed by two hemispherical shells. This procedure allows computing an ADC profile more representative of the voxel that allows a better interpolation of the signal in the whole q-space. The output ADC relevant to the MeEQBI technique was computed as the average of the ADCs acquired (or estimated) using low and moderate *b*-values (Tables 3, 4). Lower *b*-values provide lower angular resolution but higher SNRs and vice versa. Nevertheless, it may be possible to obtain the best predictions by combining these ADCs in a nonlinear way. For instance, by using the new reconstruction algorithm termed multiple wavevector fusion (MWF), which has been used to boost the SNR of QBI (17). This algorithm operates by nonlinearly fusing the diffusion signals collected on separate spherical shells using low and moderate *b*-values. The MWF methodology merges the wavelets coefficients obtained from the spherical wavelet transform of the signals. These coefficients are used to reconstruct a final composite image (or ODF). The fusion rule is based on the assumption that the final image contains the salient features that are best described at each different spherical shell. Unfortunately, a direct comparison of MWF and MeEQBI was not possible in this work since MWF is developed in terms of spherical wavelets and MeEQBI in terms of spherical harmonics. A future implementation using the same spherical basis is required to test the ODF reconstruction accuracy of both methodologies.

In the research fields of image fusion, data compression, and pattern recognition, a large variety of empirical fusion rules have been proposed (34,35). However, there is no consensus about which of them is the best theoretical alternative because the best criterion is tied to the specific application. Although the search for the best image fusion criterion is encouraging, in our opinion the best results may be obtained with the use of more realistic diffusion models, such as the biexponential model (36), the generalized diffusion tensor model (18), or the stretched-exponential model (37), which have been shown in numerous articles to provide a very accurate characterization of the radial behavior of the diffusion signal (19,33,34). The presented formulation can be easily extended to these models. However, we leave the details of these model-based reconstructions as well as the investigation of the effects of different interpolation strategies to future work.

Truncation Effects

In practice, both model-free and model-based ODFs are computed approximately by limiting the series in Eq. [18] to a particular l_{max}-term. In this way, we obtain a hierar-

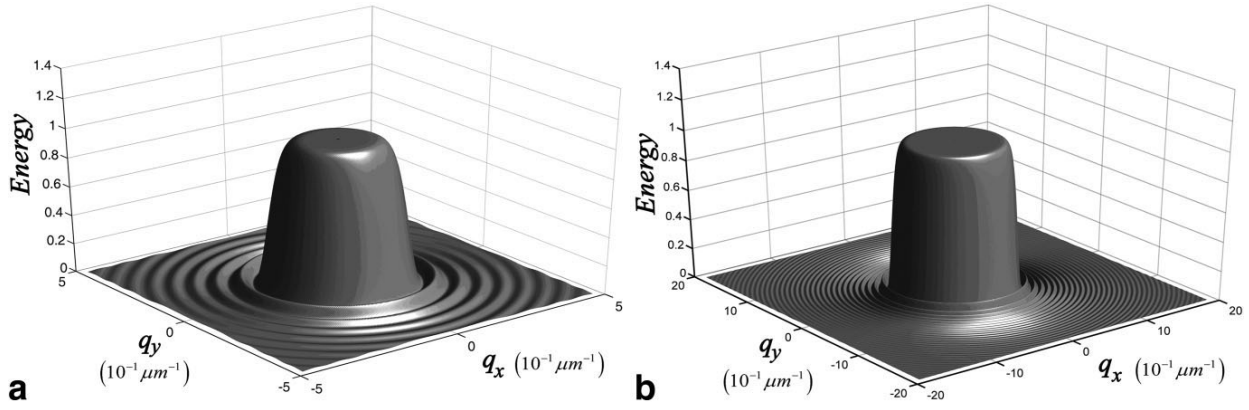

FIG. 5. Energy of the truncated plane wave, defined as the square of the magnitude of the wave computed using Eq. [29]. The direction of **r** was assumed along the z-axis. **a:** Energy pattern corresponding to the case $\rho = 10$ μm and $l_{max} = 10$, which gives rise to a low-pass filter in the range from 0 to $q_{max} = 1.6 \cdot 10^{-1}$ μm^{-1}. **b:** Energy pattern corresponding to the case $\rho = 10$ μm and $l_{max} = 40$, which gives rise to a low-pass filter in the range from 0 to $q_{max} = 6.4 \cdot 10^{-1}$ μm^{-1}. Notice that in the limit as $l_{max} \to \infty$, Eq. [29] produces a perfect plane wave with constant energy (i.e., equal to 1) within a circle of radius infinity.

chical surface description that includes further details when more coefficients are considered. This subsection focuses precisely on a theoretical examination of errors introduced due to truncation effects in Eq. [18]. To this end, let us return to the analysis of Eq. [2]. The plane wave given by the exponential term in Eq. [2] can be expanded in terms of spherical wavefunctions:

$$\exp(-2\pi i\vec{\mathbf{r}}\vec{\mathbf{q}}) \equiv \frac{2\pi}{(\rho q)^{1/2}} \lim_{l_{max}\to\infty} \sum_{l=0}^{l_{max}} \sum_{m=-l}^{l} \times (-i)^l J_{l+1/2}(2\pi\rho q) Y_{lm}(\hat{\mathbf{r}}) \bar{Y}_{lm}(\hat{\mathbf{q}}), \quad [29]$$

where J_l is the Bessel function of order l. This expansion was discovered by Bauer as early as 1859 (38). Making use of Eq. [29], Eq. [2], and Eq. [6], we obtain

$$ODF(\hat{\mathbf{r}}) = \frac{2\pi}{Z} \sum_{l=0}^{\infty} \sum_{m=-l}^{l} (-i)^l Y_{lm}(\hat{\mathbf{r}}) \times \int \left(\int J_{l+1/2}(2\pi\rho q)\rho^{-1/2}\, d\rho \right) E(\vec{\mathbf{q}}) \bar{Y}_{lm}(\hat{\mathbf{q}}) q^{-1/2}\, d\vec{\mathbf{q}}. \quad [30]$$

The above integrals can be evaluated with the use of the Weber's infinity integral given by Eq. [58] in Appendix D, and the relationships in Eqs. [16] and [45]. After some tedious algebra, and taking into account the result in Eq. [51], Eq. [30] becomes:

$$ODF(\hat{\mathbf{r}}) = \frac{1}{2\pi^{1/2} s_{00}} \sum_{l=0}^{\infty} \sum_{m=-l}^{l} s_{lm} P_l(0) Y_{lm}(\hat{\mathbf{r}}) \quad [31]$$

Notice that this expression is equal to Eq. [18]. Therefore, the above analysis provides an alternative way to arrive at the ODF inversion via spherical harmonics derived in previous subsections, and more important, provides a framework for the physical interpretation of errors due to truncation effects. In fact, truncation of series in Eq. [18] (or Eq. [31]) to a certain order of l_{max} is equivalent to approximate the plane wave in Eq. [2] (or Eq. [29]) to a particular value of l_{max}. Because only the plane orthogonal to $\hat{\mathbf{r}}$ in q-space contributes to the ODF evaluation in that direction, we restrict our analysis of the wave to this plane.

Theoretically, in the limit as $l_{max} \to \infty$, Eq. [29] produces a perfect plane wave within a sphere of radius infinity. However, because a Bessel function $J_n(u)$ has a value very close to zero for $u < n$ (39), $J_{l_{max}+1/2}(2\pi q\rho)$ likewise is very close to zero for $2\pi q t\rho < l_{max}$, where it was considered that $l_{max} \approx l_{max} + 1/2$. We can thus infer that for a finite value of l_{max} and outside the sphere of radius $l_{max}/2\pi\rho$ (in the plane perpendicular to the direction of propagation in q-space) the wave field decays quite rapidly. This implies that the truncated representation of the plane wave is accurate only for $q \le l_{max}/2\pi\rho$. To illustrate this, Fig. 5 shows the energy of the truncated plane wave given by Eq. [29] for two particular values of l_{max}.

This analysis shows that the truncated plane wave acts as a low-pass filter in q-space, which is the frequency space for the propagator. Therefore, limiting the series in Eq. [18] to a certain order of l_{max} is equivalent to compute the ODF from the following filtered propagator:

$$P_F(\vec{\mathbf{r}}) \cong \int E(\vec{\mathbf{q}}) \exp(-2\pi i\vec{r}q) \Pi(|\vec{\mathbf{q}}|) d\vec{\mathbf{q}}, \quad [32]$$

where $\Pi(|\vec{\mathbf{q}}|)$ is the filter, with $\Pi(|\vec{\mathbf{q}}|) \equiv 1$ for $|\vec{\mathbf{q}}| \le l_{max}/2\pi\rho$ and $\Pi(|\vec{\mathbf{q}}|) \equiv 0$ for $|\vec{\mathbf{q}}| \le l_{max}/2\pi\rho$. Hence, the truncated diffusion ODF can be considered as a low-pass filtering of the exact ODF. For short displacements, or large series orders, the above propagator resembles the true propagator:

$$\lim_{|\vec{\mathbf{r}}|\to 0} P_F(\vec{\mathbf{r}}) = P(\vec{\mathbf{r}}), \qquad [33]$$

$$\lim_{l_{\max}\to\infty} P_F(\vec{\mathbf{r}}) = P(\vec{\mathbf{r}}).$$

The filter in q-space introduces a low-pass threshold given by $q_{\max} = l_{\max}/2\pi\rho$ that can be rewritten as $q_{\max} = k/\rho$, with $k > 1$ for $l_{\max} > 6$. It is important to remember that a standard DSI reconstruction with a nominal isotropic spatial resolution ρ requires an experimental q-value given by $q'_{\max} = 1/\rho$ (11). This implies that (for $l_{\max} > 6$) $q'_{\max}$ is below the low-pass threshold $q_{\max}$ imposed by the filter. Therefore, in this case the low-pass filtering has no consequence in the spatial resolution of the reconstructed diffusion propagator. This analysis provides a way to chose adequately the optimum series order $l_{\max}$. A standard practice in ODF (or ADC) representations using spherical harmonics is to choose a series order in the range from $l_{\max} = 6–10$. A higher value of $l_{\max}$ provides a higher angular resolution but, simultaneously, it is capable of representing the high-frequency components introduced by measurement noise (30). Therefore, the most plausible approach is to choose a moderate series order to achieve a moderate angular resolution where fluctuations in the data are effectively removed.

CONCLUSIONS

In summary, we have presented a detailed mathematical description of q-space in spherical coordinates that helps to highlight the differences and similarities between various related q-space methodologies proposed to date. This formulation allows us to obtain a theoretical relationship between the ODF and diffusion MRI data without using any approximation. Under this relationship, the exact ODF can be computed by means of the Radon transform of the radial projection (in q-space) of the diffusion signal. The new methodology, termed *exact q-ball imaging (EQBI)*, is capable of mapping ODF to a high accuracy and provides a new perspective for interpreting and designing diffusion MRI experiments. Although the EQBI formalism uses only the information contained in the modulus of the measured signal, the proposed methodology has a straightforward extension to complex data and can potentially be used to image asymmetric microstructures. We leave the details of this generalization to future research.

In this article we have introduced a new framework for combining information coming from diffusion data recorded on multiple spherical shells in q-space (i.e., HYDI encoding schemes). This represents an important step toward a more efficient development of diffusion MRI experiments for obtaining better ODF estimates. In particular, we have reported optimal q-space sampling schemes for QBI, DSI, and model-free and model-based EQBI methods (Tables 3, 4) that were obtained from exhaustive numerical simulations.

Ideally, EQBI has a major advantage over the standard QBI method: the exact ODF does not depend on a particular value of q. This advantage is crucial, since the diffusion ODF should describe physical properties of the fluid-filled pore space and hence must depend on experimental parameters as little as possible. However, as it is not possible to do an infinite number of signal attenuation measurements, in practice the exact ODF can only be computed approximately. This technical limitation introduces error sources that have been pointed out in this article from a theoretical and practical point of view.

The new technique has potential applications in materials science and biomedicine. It can be used to map complex fiber architectures in tissues such as the brain, skeletal muscle, and heart. EQBI may improve the existing fiber-tracking algorithms to obtain more reliable estimates of neural anatomical connections. This can be used to study how different diseases affect the water diffusion process in the brain, including schizophrenia and other neuropsychiatric disorders. Further work should be undertaken to find the optimal interpolation strategies as well as the development of more accurate model-based solutions. In particular, the estimation of the optimal sampling scheme corresponding to each method should be performed using a larger set of possible combinations of spherical shells. The possibility of including sampling schemes with a different number of diffusion gradient directions per shell is another interesting fact that will be explored in a future work.

ACKNOWLEDGMENTS

We thank to Luis Rodríguez-Gil (from the "Oscar Lucero Moya" University, Holguín, Cuba) and Eduardo Martínez-Montes (from the Neurostatistic Department, Cuban Neuroscience Center) for the final revision of the article and helpful comments. Finally, we thank the anonymous reviewers for suggestions that have considerably improved the article.

APPENDIX A

Derivation of the Exact ODF in Spherical Coordinates

In spherical coordinates, Eq. [8] becomes:

$$ODF(\hat{\mathbf{r}}) = \frac{1}{Z}\int E(q,\alpha,\beta)\delta(q\cos w)q^2\sin\alpha\, dq\, d\alpha\, d\beta, \qquad [34]$$

where w is the angle enclosed between $\hat{\mathbf{r}}$ and $\hat{\mathbf{q}}$ (i.e., $\hat{\mathbf{r}}\hat{\mathbf{q}} = \cos w$). The value of the above integral is invariant to any rotation of the laboratory coordinate system. Therefore, if we introduce a new rotated system with spherical coordinates labeled α' and β', Eq. [34] can be rewritten as:

$$ODF(\hat{\mathbf{r}}) = \frac{1}{Z}\int E(q,\alpha',\beta')\delta(q\cos w')q^2\sin\alpha'\, dq\, d\alpha'\, d\beta', \qquad [35]$$

where now w' is the angle enclosed between $\hat{\mathbf{r}}$ and $\hat{\mathbf{q}}'$ (the q-space unit vector in the rotated coordinate system).

The above expression acquires a simpler form in the rotated system whose z'-axis is parallel to $\hat{\mathbf{r}}$. In such a

system $w' = \alpha'$. Consequently, making the change of variables $t = \cos w'$, Eq. [35] can be computed:

$$ODF(\hat{\mathbf{r}}) = \frac{1}{Z}\int E(q, w', \beta')\delta(q\cos w')q^2\, dq\, d\cos w'\, d\beta'$$
$$= \frac{1}{Z}\int E(q, \cos^{-1}t, \beta')\delta(qt)q^2\, dq\, dt\, d\beta'. \quad [36]$$

Where was considered that $\sin\alpha' d\cos\alpha'$. Taking into account that (22):

$$\delta(qt) = \frac{\delta(q) + \delta(t)}{\sqrt{q^2 + t^2}}. \quad [37]$$

Equation [36] becomes:

$$ODF(\hat{\mathbf{r}}) = \frac{1}{Z}\int \frac{E(q, \cos^{-1}t, \beta')}{\sqrt{q^2 + t^2}} q^2\delta(q)\, dq\, dt\, d\beta'$$
$$+ \frac{1}{Z}\int \frac{E(q, \cos^{-1}t, \beta')}{\sqrt{q^2 + t^2}} q^2\delta(t)\, dq\, dt\, d\beta'. \quad [38]$$

Note that the first integral is zero. Therefore,

$$ODF(\hat{\mathbf{r}}) = \frac{1}{Z}\int E(q, \pi/2, \beta')q\, dq\, d\beta' \quad [39]$$

where it was considered that $\cos^{-1}0 = \pi/2$. This equation can be rewritten in the nonrotated coordinate system as:

$$ODF(\hat{\mathbf{r}}) = \frac{1}{Z}\int_{\hat{\mathbf{r}}\perp\hat{\mathbf{q}}} d\hat{\mathbf{q}}\int E(q, \hat{\mathbf{q}})q\, dq. \quad [40]$$

APPENDIX B

Relationship between the Spherical Harmonic Coefficients

The Radon transform given by Eq. [9] can be rewritten in terms of the delta function as:

$$ODF(\hat{\mathbf{r}}) = \frac{1}{Z}\int S(\hat{\mathbf{q}})\delta(\hat{\mathbf{r}}\hat{\mathbf{q}})\, d\hat{\mathbf{q}} \quad [41]$$

Therefore, making use of the above equation and the spherical harmonic expansions given by Eqs. [15] and [16], we obtain:

$$\sum_{l=0}^{\infty}\sum_{m=-l}^{l} o_{lm}Y_{lm}(\hat{\mathbf{r}}) = \frac{1}{Z}\sum_{l=0}^{\infty}\sum_{m=-l}^{l} s_{lm}\int Y_{lm}(\hat{\mathbf{q}})\delta(\hat{\mathbf{r}}\hat{\mathbf{q}})\, d\hat{\mathbf{q}}. \quad [42]$$

The relationship between the harmonic coefficients o_{lm} and s_{lm} can be proven using the Legendre polynomial expansion of the delta function:

$$\delta(\hat{\mathbf{r}}\hat{\mathbf{q}}) = \frac{1}{2}\sum_{l'=0}^{\infty}(2l' + 1)P_{l'}(0)P_{l'}(\hat{\mathbf{r}}\hat{\mathbf{q}}), \quad [43]$$

the well-known addition theorem for spherical harmonics:

$$P_{l'}(\hat{\mathbf{r}}\hat{\mathbf{q}}) = \frac{4\pi}{2l' + 1}\sum_{m'=-l'}^{l'} Y_{l'm'}(\hat{\mathbf{r}})\bar{Y}_{l'm'}(\hat{\mathbf{q}}), \quad [44]$$

and the orthogonality property of the spherical harmonics:

$$\int Y_{l'm'}(\hat{\mathbf{q}})\bar{Y}_{lm}(\hat{\mathbf{q}})\, d\hat{\mathbf{q}} = \delta_{ll'}\delta_{mm'}, \quad [45]$$

where $\delta_{ll'}$ and $\delta_{mm'}$ are Kronecker deltas, which lead to the relation:

$$\sum_{l=0}^{\infty}\sum_{m=-l}^{l} o_{lm}Y_{lm}(\hat{\mathbf{r}}) = \frac{2\pi}{Z}\sum_{l=0}^{\infty}\sum_{m=-l}^{l} s_{lm}P_l(0)Y_{lm}(\hat{\mathbf{r}}). \quad [46]$$

Therefore,

$$o_{lm} = \frac{2\pi}{Z}s_{lm}P_l(0). \quad [47]$$

The normalization constant Z can be obtained in practice from the ODF normalization condition:

$$\int ODF(\hat{\mathbf{r}})\, d\hat{\mathbf{r}} = 1. \quad [48]$$

Inserting Eqs. [15] and [47] into Eq. [48], we obtain:

$$Z = 2\pi\sum_{l=0}^{\infty}\sum_{m=-l}^{l} s_{lm}P_l(0)\int Y_{lm}(\hat{\mathbf{r}})\, d\hat{\mathbf{r}}. \quad [49]$$

Considering that $1 = 2\pi^{1/2}\bar{Y}_{00}(\Omega_r)$, and taking into account the orthogonality property of the spherical harmonics (see Eq. [45]), the integral in the previous equation can be evaluated:

$$\int Y_{lm}(\hat{\mathbf{r}})\, d\hat{\mathbf{r}} = 2\pi^{1/2}\int Y_{lm}(\hat{\mathbf{r}})\bar{Y}_{00}(\Omega_r)\, d\hat{\mathbf{r}}$$
$$= 2\pi^{1/2}\delta_{l0}\delta_{m0}. \quad [50]$$

Hence, Eq. [49] becomes

$$Z = 4\pi^{3/2}s_{00}. \quad [51]$$

Therefore, the set of coefficients $\{o_{lm}\}$ can be computed by means of the set $\{s_{lm}\}$ through the following relationship (see Eqs. [47] and [51]):

$$o_{lm} = \frac{1}{2\pi^{1/2}} \frac{s_{lm}}{s_{00}} P_l(0). \quad [52]$$

APPENDIX C

Mathematical Formulation for the Spherical Harmonic Inversion

The ODF estimation requires the computation of harmonic coefficients corresponding to a function that depends on diffusion data (e.g., the measured signal, the inverse of the ADC profile, or the radial projection of the signal). The purpose of this appendix is to describe the mathematical aspects related to the accurate estimation of these coefficients.

Let us first consider that F is an antipodal symmetric function that depends on diffusion data. In addition, suppose that the experiment is performed with diffusion-sensitizing gradients applied along the direction set $\{\hat{\mathbf{q}}_i,\ i = 1, \ldots N\}$. Also, let us consider that F can be expanded accurately in terms of spherical harmonics as:

$$F(\hat{\mathbf{q}}_i) \approx \sum_{l=0}^{l_{\max}} \sum_{m=-l}^{l} s_{lm} Y_{lm}(\hat{\mathbf{q}}_i) \quad [53]$$

where l runs through all even integer values from zero to $l_{\max}$. Now, let $\mathbf{F} = (F_1,\ldots,F_N)^{\mathrm{T}}$ be the Nx1 observations vector, where $F_i \equiv F(\hat{\mathbf{q}}_i)$. In this case, the harmonic coefficients $\{s_{lm}\}$ can be obtained in practice by solving the following linear regression model:

$$\mathbf{F} = \mathbf{YC} + \mathbf{e}, \quad [54]$$

where $\mathbf{Y}$ is a Nxp design matrix of explanatory variables with $p = (l_{\max}+1)(l_{\max}+2)/2$, $\mathbf{C}$ is the px1 column vector of unknown regression coefficients, and $\mathbf{e}$ is the Nx1 vector of residuals.

The design matrix and the regression coefficients vector are obtained by concatenating $\mathbf{Y} = (\mathbf{Y}_0,\ldots,\mathbf{Y}_{l\max})$ and $\mathbf{C} = (\mathbf{C}_0,\ldots,\mathbf{C}_{l\max})^{\mathrm{T}}$ respectively, where the Nx$(2l+1)$ submatrix $\mathbf{Y}_l$ is constructed as:

$$\mathbf{Y}_l = \begin{bmatrix} Y_{l(-l)}(\hat{\mathbf{q}}_1) & \cdots & Y_{l0}(\hat{\mathbf{q}}_1) & \cdots & Y_{ll}(\hat{\mathbf{q}}_1) \\ \vdots & \vdots & \vdots & \vdots & \vdots \\ Y_{l(-l)}(\hat{\mathbf{q}}_N) & \cdots & Y_{l0}(\hat{\mathbf{q}}_N) & \cdots & Y_{ll}(\hat{\mathbf{q}}_N) \end{bmatrix}, \quad [55]$$

and the $(2l+1)$x1 subvector $\mathbf{C}_l$ is formed as $\mathbf{C}_l = (s_{l(-l)},\ldots,s_{l0},\ldots,s_{ll})^{\mathrm{T}}$.

Assuming statistical independence between elements of the residuals vector, the linear regression model given by Eq. [54] can be solved by minimizing the following expression:

$$\min_{\mathbf{C}} \{\|\mathbf{F} - \mathbf{YC}\|^2 + \tau^2\|\mathbf{LC}\|^2\} \quad [56]$$

where $\|\mathbf{x}\|^2$ is the square of the Frobenius norm given by $\|\mathbf{x}\|^2 = Trace(\mathbf{x}\cdot\tilde{\mathbf{x}}^{\mathrm{T}})$, with $\tilde{\mathbf{x}}$ denoting the complex conjugate of the vector $\mathbf{x}$. The regularization parameter τ represents the relative weight between the data fitting error term $\|\mathbf{F}-\mathbf{YC}\|^2$ and constrains given by the choice of the pxp matrix $\mathbf{L}$ in the term $\|\mathbf{LC}\|^2$.

The explicit solution for Eq. [56] is:

$$\mathbf{C}(\tau) = (\mathbf{Y}^{\mathrm{T}}\mathbf{Y} + \tau^2\mathbf{H})^{-1}\mathbf{Y}^{\mathrm{T}}\mathbf{F}, \quad [57]$$

where $\mathbf{H} = \mathbf{L}^{\mathrm{T}}\mathbf{L}$.

In our case, the Generalized Cross-Validation (GCV) method is used to estimate the optimal regularization parameter. In addition, $\mathbf{H}$ is a pxp diagonal matrix with elements $\mathbf{H}_{ij} = 0$, $\forall i \neq j$, and $\mathbf{H}_{ii} = l_i^2(l_i+1)^2$ where l_i is the order l corresponding to the harmonic coefficient s_{lm} in the vector $\mathbf{C}$ at row i. This matrix is based on the Laplace–Beltrami operator, which has previously been used to obtain smooth ODF profiles (29). This regularization approach reduces the undesirable effect (observed in Ref. 8) of producing false spikes around the origin that the harmonic series exhibit when the SNR is very low or when the series is prematurely truncated.

APPENDIX D

Weber's Infinity Integral

The Weber's infinity integral (40) states that:

$$\int_0^{\infty} J_v(x)x^{-(v-u+1)}\,dx = \frac{\Gamma\left(\frac{u}{2}\right)}{2^{v-u+1}\Gamma\left(v-\frac{u}{2}+1\right)}. \quad [58]$$

By setting $v = l + 1/2$ and $u = l + 1$, we obtain:

$$\int_0^{\infty} J_{l+1/2}(x)x^{-1/2}\,dx = \frac{\Gamma\left(\frac{l+1}{2}\right)}{2^{1/2}\Gamma\left(\frac{l}{2}+1\right)}. \quad [59]$$

It is important to note that the integral in brackets in Eq. [30] can be rewritten, under a simple change of variables, in the form given by Eq. [59].

A useful relationship used in our derivation (between the Gamma function Γ and the Legendre polynomial for even-l terms) is:

$$P_l(0) = (-1)^{l/2} \frac{\Gamma\left(\frac{l+1}{2}\right)}{\Gamma\left(\frac{l}{2}+1\right)} \pi^{-1/2} \quad [60]$$

REFERENCES

1. Callaghan PT. Principles of nuclear magnetic resonance microscopy. Oxford: Clarendon Press. 1991.
2. Price WS, Stilbs P, Soderman O. Determination of pore space shape and size in porous systems using NMR diffusometry. Beyond the short gradient pulse approximation. J Magn Reson 2003;160:139–143.
3. Basser PJ, Mattiello J, LeBihan D. Estimation of the effective self-diffusion tensor from the NMR spin echo. J Magn Reson B 1994;103: 247–254.
4. Tuch DS. Q-ball imaging. Magn Reson Med 2004;52:1358–1372.

5. Tuch DS, Reese TG, Wiegell MR, Makris N, Belliveau JW, Wedeen VJ. High angular resolution diffusion imaging reveals intravoxel white matter fiber heterogeneity. Magn Reson Med 2002;48:577–582.
6. Assaf Y, Basser PJ. Composite hindered and restricted model of diffusion (CHARMED) MR imaging of the human brain. Neuroimage 2005; 27:48–58.
7. Alexander DC. Multiple-fiber reconstruction algorithms for diffusion MRI. Ann N Y Acad Sci 2005;1064:113–133.
8. Anderson AW. Measurement of fiber orientation distributions using high angular resolution diffusion imaging. Magn Reson Med 2005;54: 1194–1206.
9. Behrens TE, Berg HJ, Jbabdi S, Rushworth MF, Woolrich MW. Probabilistic diffusion tractography with multiple fibre orientations: what can we gain? Neuroimage 2007;34:144–155.
10. Tournier JD, Calamante F, Gadian DG, Connelly A. Direct estimation of the fiber orientation density function from diffusion-weighted MRI data using spherical deconvolution. Neuroimage 2004;23:1176–1185.
11. Wedeen VJ, Hagmann P, Tseng WY, Reese TG, Weisskoff RM. Mapping complex tissue architecture with diffusion spectrum magnetic resonance imaging. Magn Reson Med 2005;54:1377–1386.
12. Ozarslan E, Shepherd TM, Vemuri BC, Blackband SJ, Mareci TH. Resolution of complex tissue microarchitecture using the diffusion orientation transform (DOT). Neuroimage 2006;31:1086–1103.
13. Jansons KM, Alexander DC. Persistent angular structure: new insights from diffusion MRI data. Inverse Probl 2003;19:1031–1046.
14. Melie-García L, Canales-Rodríguez EJ, Alemán-Gómez Y, Lin CP, Iturria-Medina Y, Valdés-Hernández PA. A Bayesian framework to identify principal intravoxel diffusion profiles based on diffusion-weighted MR imaging. Neuroimage 2008;42:750–770.
15. Canales-Rodríguez EJ, Melie-García L, Iturria-Medina Y, Martínez-Montes E, Alemán-Gómez Y, Lin CP. Inferring multiple maxima in intravoxel white matter fiber distribution. Magn Reson Med 2008;60: 616–630.
16. Tuch DS. MRI of complex tissue structure. PhD Thesis . 2002.
17. Khachaturian MH, Wisco JJ, Tuch DS. Boosting the sampling efficiency of q-ball imaging using multiple wavevector fusion. Magn Reson Med 2007;57:289–296.
18. Liu C, Bammer R, Acar B, Moseley ME. Characterizing non-Gaussian diffusion by using generalized diffusion tensors. Magn Reson Med 2004;51:924–937.
19. Mitra PP, Halperin BI. Effects of finite gradient-pulse widths in pulsed-field-gradient diffusion measurements. J Magn Reson Ser A 1995;113: 94–101.
20. Lin CP, Wedeen VJ, Chen JH, Yao C, Tseng WY. Validation of diffusion spectrum magnetic resonance imaging with manganese-enhanced rat optic tracts and ex vivo phantoms. Neuroimage 2003;19:482–495.
21. Perrin M, Poupon C, Rieul B, Leroux P, Constantinesco A, Mangin JF, LeBihan D. Validation of q-ball imaging with a diffusion fibre-crossing phantom on a clinical scanner. Philos Trans R Soc Lond B Biol Sci 2005;360:881–891.
22. Bracewell RN. The Fourier transform and its applications. New York: McGraw-Hill, 1965, 2nd ed. 1978, revised 1986.
23. Apostol TM. Mathematical analysis. Menlo Park, CA: Addison-Wesley; 1957.
24. Spiegel MR, Liu J. Mathematical handbook of formulas and tables. New York: McGraw-Hill, Schaum's Outlines; 1968.
25. Basser P, Mattielo J, LeBihan D. MR diffusion tensor spectroscopy and imaging. Biophys J 1994;66:259–267.
26. Pierpaoli C, Basser PJ. Toward a quantitative assessment of diffusion anisotropy. Magn Reson Med 1996;36:893–906.
27. Beaulieu C. The basis of anisotropic water diffusion in the nervous system — a technical review. NMR Biomed 2002;15:435–455.
28. Donnelly D, Rust B. The fast Fourier transform for experimentalists. Part I. Concepts. Comput Sci Eng 2005;7:80–88.
29. Descoteaux M, Angelino E, Fitzgibbons S, Deriche R. A fast and robust ODF estimation algorithm in q-ball imaging. Int Symp Biomed Imaging: From Nano to Macro (ISBI'06) 2006:81–84.
30. Hess CP, Mukherjee P, Han ET, Xu D, Vigneron DB. Q-ball reconstruction of multimodal fiber orientations using the spherical harmonic basis. Magn Reson Med 2006;56:104–117.
31. Kuo LW, Chen JH, Wedeen VJ, Tseng WY. Optimization of diffusion spectrum imaging and q-ball imaging on clinical MRI system. Neuroimage 2008;41:7–18.
32. Alexander DC, Barker GJ. Optimal imaging parameters for fiber-orientation estimation in diffusion MRI. Neuroimage 2005;27:357–367.
33. Wu YC, Alexander AL. Hybrid diffusion imaging. Neuroimage 2007; 36:617–629.
34. Burt P, Adelson E. The Laplacian pyramid as a compact image code. IEEE Trans Commun 1983;532–540.
35. Li H, Manjunath B, Mitra S. Multisensor image fusion using the wavelet transform. Graph Models Image Process 1995;57:235–245.
36. Niendorf T, Dijkhuizen RM, Norris DG, van Lookeren CM, Nicolay K. Biexponential diffusion attenuation in various states of brain tissue: implications for diffusion-weighted imaging. Magn Reson Med 1996; 36:847–857.
37. Bennett KM, Schmainda KM, Bennett RT, Rowe DB, Lu H, Hyde JS. Characterization of continuously distributed cortical water diffusion rates with a stretched-exponential model. Magn Reson Med 2003;50: 727–734.
38. Bauer GVd. Coefficienten der Reihen von Kugelfunctionen einer Variablen. J Math 1859;LVI:101–121.
39. Coggins BE, Zhou P. Polar Fourier transforms of radially sampled NMR data. J Magn Reson 2006;182:84–95.
40. Weber H. Ueber einige bestimmte Integrale. J Math 1869;LXIX:222–237.

5.2 Diffusion orientation transform revisited

Autores: Erick J Canales-Rodríguez, Ching-Po Lin, Yasser Iturria-Medina, CH Yeh, KH Cho, Lester Melie-García

Título: *Diffusion orientation transform revisited*

Revista: *Neuroimage*

Año y volumen: 2010, Vol 49, 2, 1326-1339

Factor de impacto (en el año de publicación): 5.93

NeuroImage 49 (2010) 1326–1339

Contents lists available at ScienceDirect

NeuroImage

journal homepage: www.elsevier.com/locate/ynimg

Diffusion orientation transform revisited

Erick Jorge Canales-Rodríguez [a,b,1], Ching-Po Lin [c,d,1], Yasser Iturria-Medina [e], Chun-Hung Yeh [c,d], Kuan-Hung Cho [c], Lester Melie-García [e,*]

[a] Benito Menni Complex Assistencial en Salut Mental, Barcelona, Spain
[b] Centro de Investigación Biomédica en Red de Salud Mental (CIBERSam), Spain
[c] Laboratory for Brain Connectivity, Institute of Neuroscience, National Yang-Ming University, Taipei, Taiwan
[d] Department of Biomedical Imaging and Radiological Sciences, National Yang-Ming University, Taipei, Taiwan
[e] Neuroimaging Department, Cuban Neuroscience Center. Ave 25, Esq. 158, #15202, P.O. Box 6412/6414, Cubanacan, Playa, Havana, Cuba

ARTICLE INFO

Article history:
Received 13 May 2009
Revised 27 July 2009
Accepted 29 September 2009
Available online 6 October 2009

Keywords:
Diffusion orientation transform (DOT)
Diffusion spectrum imaging (DSI)
Q-ball imaging (QBI)
High angular resolution diffusion imaging (HARDI)
Orientational distribution function (ODF)

ABSTRACT

Diffusion orientation transform (DOT) is a powerful imaging technique that allows the reconstruction of the microgeometry of fibrous tissues based on diffusion MRI data. The three main error sources involving this methodology are the finite sampling of the q-space, the practical truncation of the series of spherical harmonics and the use of a mono-exponential model for the attenuation of the measured signal. In this work, a detailed mathematical description that provides an extension to the DOT methodology is presented. In particular, the limitations implied by the use of measurements with a finite support in q-space are investigated and clarified as well as the impact of the harmonic series truncation. Near- and far-field analytical patterns for the diffusion propagator are examined. The near-field pattern makes available the direct computation of the probability of return to the origin. The far-field pattern allows probing the limitations of the mono-exponential model, which suggests the existence of a limit of validity for DOT. In the regimen from moderate to large displacement lengths the isosurfaces of the diffusion propagator reveal aberrations in form of artifactual peaks. Finally, the major contribution of this work is the derivation of analytical equations that facilitate the accurate reconstruction of some orientational distribution functions (ODFs) and skewness ODFs that are relatively immune to these artifacts. The new formalism was tested using synthetic and real data from a phantom of intersecting capillaries. The results support the hypothesis that the revisited DOT methodology could enhance the estimation of the microgeometry of fiber tissues.

Introduction

In recent years, water diffusion magnetic resonance imaging (dMRI) has played an increasingly important role in the investigation of the architectural features of fibrous tissues and porous media. This technique provides a new dimension of MRI contrast based on water mobility, because of the different cellular environment experienced by different water molecules (Basser et al., 1994; Callaghan, 1991; LeBihan, 2003). The study of this phenomenon has made possible a deeper knowledge of the microanatomy of the living brain, and others complex tissues, due to its noninvasive nature (Behrens et al., 2003; Iturria-Medina et al., 2008; Parker et al., 2003).

Conceptually, the anisotropy of the water self-diffusion process is fully characterized by means of the displacement probability density function of water molecules. This probability density function, termed diffusion propagator, contains valuable information about the microgeometry of the medium where the diffusion process occurs. In dMRI the observed (or measured) signal can be modeled directly as a function of the diffusion propagator. Typically, it is computed at each voxel by taking the discrete or fast Fourier transform (FFT) of the modulus of the normalized signal measured on a 3D Cartesian grid in q-space. This methodology, known as q-space imaging or diffusion spectrum imaging (DSI) (Wedeen et al., 2005), allows the estimation of the diffusion propagator in a straightforward way. Nevertheless, the FFT formalism requires large experimental diffusion-sensitizing magnetic field gradients to satisfy the Nyquist condition (Tuch, 2004), and therefore, it requires large amount of experimental data for its practical implementation. As a consequence, DSI is time-intensive. The three main error sources involving this reconstruction algorithm are (1) the mapping between Cartesian and spherical coordinates systems that give rise to Cartesian artifacts (Tuch, 2004), (2) the complex interaction between signal and noise, and (3) the moderate spatial resolution of DSI sampling schemes. Points (1) and (2) affect the quality of the reconstruction in terms of signal-to-noise ratio, whereas point (3) determines its angular resolution.

Alternatively, a novel approach termed diffusion orientation transform (DOT) has been introduced to compute analytically the diffusion propagator (Ozarslan et al., 2006). DOT uses a generative

* Corresponding author. Fax: +53 7 208 6707.
E-mail address: lester@cneuro.edu.cu (L. Melie-García).
[1] The first two authors contributed equally.

1053-8119/$ – see front matter © 2009 Elsevier Inc. All rights reserved.
doi:10.1016/j.neuroimage.2009.09.067

model for the modulus of the measured signal, in particular, a mono-exponential decay model along each radial line in q-space. Also, to evaluate the Fourier integral this technique employs a plane wave expansion in terms of spherical harmonics. Under this approximation DOT is able to transform water diffusivity profiles into displacement probability profiles. The motivation for computing the diffusion propagator from DOT is three-fold. First, the Fourier integral can be computed over the continuous q-space. Second, the upper limit of integration can be extended to infinity. Third, the measurements can be collected using a less dense sampling scheme, which is a critical parameter in clinical applications. Specifically, this formalism allows computing the diffusion propagator using high angular resolution diffusion images (HARDI) that are sampled on a single spherical shell in q-space. This type of measurement strategy is the basis of a family of methods and algorithms previously developed for the reconstruction of oriented fibers in white matter tissues of human and other animal brains (see for example Alexander, 2005; Anderson, 2005; Assaf and Basser, 2005; Behrens et al., 2007; Canales-Rodríguez et al., 2008; Frank, 2001; Frank, 2002; Hess et al., 2006; Hosey et al., 2005; Jansons and Alexander, 2003; Melie-García et al., 2008; Ramírez-Manzanares et al., 2007; Tournier et al., 2007; Tuch, 2004; Tuch et al., 2002). In DOT, the intravoxel orientational heterogeneity of fibers is measured (or quantified) by evaluating the diffusion propagator at a fixed random-walk displacement length (Ozarslan et al., 2006), that is, using a single contour or isosurface of the diffusion propagator.

The three main error sources involving the DOT method are the finite experimental sampling of q-space, the practical truncation of the spherical harmonic series, and the use of a mono-exponential model for the attenuation of the measured signal, which is inaccurate to predict the signal behavior under some experimental conditions such as long diffusion times and strong magnetic field gradients (i.e., high *b*-values). These approximations may introduce significant aberrations or artifacts in the reconstructed diffusion propagator. However, to date, these aspects remain unstudied.

On the other hand, the orientational distribution function (ODF) formalism, which has been used extensively to characterize the underlying angular structure of fiber tissues (Tuch, 2004), has not been adapted to be included in the DOT method. The straightforward way to compute the ODF corresponding to DOT is to evaluate the diffusion propagator at several displacement lengths and then to perform (numerically) the radial projection. The caveat with this approach would be that it is time-intensive and introduces new error sources from the numerical integration process. A way of circumventing this problem is to compute the ODF analytically, bypassing the computation of the diffusion propagator. However, closed-form analytical solutions for this calculation are not yet available.

In order to address both theoretically and practically the above limitations, in this work we will focus on a detailed mathematical description of the DOT methodology that is rooted in basic concepts of q-space. The rest of the manuscript has the following structure. The "Theory" section is ordered in three main different parts. The first one is dedicated to summarize the mathematical basis of the DOT formalism. Some of the equations described here will be used as starting point for the development of the subsequent sections. The second part is devoted to study the theoretical aspects regarding the effects of the potential sources of error mentioned above concerning the DOT methodology. In the third part analytical expressions that facilitate the fast and accurate reconstructions of ODF and skewness ODF maps will be derived. Details of the synthetic data generation process will be presented in Material and methods, as well as the data acquisition protocol corresponding to water-filled capillaries. The performance of the new formalism both in synthetic and real data will be evaluated in Results. Finally, in Discussion and conclusions the relevant findings and contributions of this work will be succinctly described. The Appendices present detailed mathematical derivations pertinent to the developed theory.

Theory

Diffusion orientation transform: Mathematical basis

This subsection is devoted to review the mathematical basis behind DOT methodology. In spherical coordinates, the fundamental relationship between the modulus E of the normalized dMRI complex signal and the diffusion propagator P is given by the following 3D Fourier transform (Callaghan, 1991)

$$P(\rho,\hat{\mathbf{r}}) = \oint_{\Omega}\int_{0}^{\infty} E(q,\hat{\mathbf{q}})\exp(-2\pi i\rho q\hat{\mathbf{r}}\hat{\mathbf{q}})q^2 dq d\hat{\mathbf{q}}, \tag{1}$$

where $q = \gamma G\tau / 2\pi$ represents the length of the q-space vector $\vec{\mathbf{q}}$(i.e., $\vec{\mathbf{q}} = q\hat{\mathbf{q}}$) γ is the gyromagnetic ratio for the diffusing species (i.e., hydrogen proton in water molecules); G and τ are respectively the intensity and the duration of the diffusion-sensitizing magnetic field gradient vector; ρ and $\hat{\mathbf{r}}$ are the length and unit vector of the real-space vector $\vec{\mathbf{r}}$(i.e., $\vec{\mathbf{r}} = \rho\hat{\mathbf{r}}$).

The set of all possible directions of $\hat{\mathbf{q}}$ corresponds to the unit sphere Ω in q-space, i.e., $\Omega \equiv (\theta,\phi)$ with elevation angle $\theta \in [0, \pi]$, and azimuthal angle $\phi \in [0, 2\pi]$. The integral over the surface of the unit sphere (or over all possible directions of $\hat{\mathbf{q}}$) is denoted by

$$\oint_{\Omega} d\hat{\mathbf{q}} = \int_{0}^{2\pi}\int_{0}^{\pi} \sin\theta d\theta d\phi. \tag{2}$$

In DOT the Fourier integral is computed under the assumption that E attenuates mono-exponentially as follows (Ozarslan et al., 2006)

$$E(q,\hat{\mathbf{q}}) = \exp\left[-4\pi^2 t q^2 D(\hat{\mathbf{q}})\right], \tag{3}$$

where D is the apparent diffusion coefficient or diffusivity profile and t is the effective experimental diffusion time.

In addition, DOT uses the following expansion of the plane wave in terms of spherical wave functions

$$\exp(-2\pi i\rho q\hat{\mathbf{r}}\hat{\mathbf{q}}) = lim_{N\to\infty} 4\pi \sum_{l=0}^{N}\sum_{m=-l}^{l} (-i)^l j_l(2\pi q\rho) Y_{lm}(\hat{\mathbf{r}}) Y^*_{lm}(\hat{\mathbf{q}}), \tag{4}$$

where j_l and Y_{lm} are respectively the spherical Bessel function of the first kind and the spherical harmonic of order l, Y^*_{lm} denotes the complex conjugate of Y_{lm}.

Inserting Eqs. (3) and(4) into Eq. (1) the diffusion propagator can be written as (Ozarslan et al., 2006):

$$P(\rho,\hat{\mathbf{r}}) = lim_{N\to\infty} \sum_{l=0}^{N}\sum_{m=-l}^{l} (-1)^{l/2} Y_{lm}(\hat{\mathbf{r}}) \oint_{\Omega} Y^*_{lm}(\hat{\mathbf{q}}) I_l(\rho,\hat{\mathbf{q}}) d\hat{\mathbf{q}}, \tag{5}$$

with

$$I_l(\rho,\hat{\mathbf{q}}) = \frac{\rho^l \Gamma\left(\frac{l+3}{2}\right)}{2^{l+3}\pi^{3/2}\Gamma\left(l+\frac{3}{2}\right)[D(\hat{\mathbf{q}})t]^{\frac{l+3}{2}}} \times {}_1F_1\left(\frac{l+3}{2}; l+\frac{3}{2}; -\frac{\rho^2}{4D(\hat{\mathbf{q}})t}\right), \tag{6}$$

where ${}_1F_1$ denotes the confluent hypergeometric function of the first kind and Γ is the gamma function. Notice that has been used the fact

that l is even (i.e., $(-i)^l=(-1)^{1/2}$) due to the inherent symmetry of the diffusion propagator, $P(\rho, \hat{\mathbf{r}})=P(\rho, -\hat{\mathbf{r}})$.

Since $I_l(\rho, \hat{\mathbf{q}})$ is a function of orientation, it can be expanded in terms of spherical harmonics

$$I_l(\rho, \hat{\mathbf{q}}) = lim_{N\to\infty}\sum_{l'=0}^{N}\sum_{m'=-l'}^{l'} a^l_{l'm'}Y_{l'm'}(\hat{\mathbf{q}}). \quad (7)$$

Inserting Eq. (7) into Eq. (5) the diffusion propagator becomes (Ozarslan et al., 2006)

$$P(\rho, \hat{\mathbf{r}}) = lim_{N\to\infty}\sum_{l=0}^{N}\sum_{m=-l}^{l}(-1)^{l/2}a^l_{lm}Y_{lm}(\hat{\mathbf{r}}), \quad (8)$$

where was considered the well-known orthogonality condition of the spherical harmonics:

$$\oint_{\Omega} Y^*_{lm}(\hat{\mathbf{q}})Y_{l'm'}(\hat{\mathbf{q}})d\hat{\mathbf{q}} = \delta_{ll'}\delta_{mm'}, \quad (9)$$

δ_{ij} represents the Kronecker delta.

In summary, the local probability that a molecule travel a distance ρ during the experimental time can be estimated as follows (Ozarslan et al., 2006):

(1) Compute the diffusivity $D(\hat{\mathbf{q}})$ profile using the diffusion model given by Eq. (3).
(2) Then, compute $I_l(\rho,\hat{\mathbf{q}})$ using Eq. (6).
(3) For each l, compute the set of harmonic coefficients $\{a^l_{lm}\}$ using Eq. (7).
(4) Then, evaluate Eq. (8).

Theoretical aspects regarding finite sampling schemes, truncated harmonic series and the mono-exponential attenuation

The next three subsections are devoted to study, from a theoretical point of view, the effects of the three main potential sources of error involving the DOT formalism. To do this, we first analyze the influence of HARDI sampling schemes with a finite support in q-space on the estimation of the diffusion propagator using a Fourier transform model defined on the whole q-space. In this part it is introduced the "diffusion point spread function." Next, a second subsection is dedicated to investigate and clarify the effect of the practical truncation of the spherical harmonic series on the diffusion point spread function. Finally, a third subsection is devoted to consider the limitations of the mono-exponential model. In this last part it is examined the diffusion pattern in the far-field limit of displacement.

Diffusion point spread function

In practice the HARDI measurements have a finite support in q-space. Hence, the model-free propagator (see Eq. (1)) that we are able to compute has the following form:

$$P_F(\rho, \hat{\mathbf{r}}) = \oint_{\Omega}\int_0^{\infty} E(q, \hat{\mathbf{q}})\prod\left(\frac{q}{q_{max}}\right)\exp(-2\pi i\rho\hat{\mathbf{r}}\hat{\mathbf{q}})q^2dqd\hat{\mathbf{q}} \quad (10)$$

where Π represents a filter in q-space with spherical symmetry defined as:

$$\prod\left(\frac{q}{q_{max}}\right) = \begin{cases} 1, & \forall q \le q_{max} \\ 0, & \forall q > q_{max} \end{cases} \quad (11)$$

Note that this filter corresponds to a signal measured within a 3D spherical lattice, where $q_{\max}$ is the maximum experimental value of q.

Taking into account the convolution theorem (Bracewell, 1986), the resulting filtered diffusion propagator can be written in terms of the true diffusion propagator (Eq. (1)) by means of the following relationship (see Appendix A for full details):

$$P_F = P \otimes \mathbb{F}\left\{\prod\right\}, \quad (12)$$

where $\otimes$ is a convolution operator and $\mathbb{F}\{\Pi\}$ is the 3D continuous Fourier transform of the filter that can be evaluated as:

$$\mathbb{F}\{\Pi\} = 4\pi\frac{\sin(2\pi q_{max}R) - 2\pi q_{max}R\cos(2\pi q_{max}R)}{(2\pi R)^3}, \quad (13)$$

As a consequence, the true diffusion propagator interacts with the Fourier transform of the filter, which can be regarded as the point spread function (PSF) of the convolution process, to give the filtered or convolved diffusion propagator. Eq. (12) can be interpreted as follows: the estimated intensity for the diffusion propagator at a particular point $\vec{\mathbf{r}}$ arises from the contributions of all points of the space, their real intensities weighted by the PSF $\mathbb{F}\{\Pi\}$ depending on the distance R to the considered point.

In this manner, it is obtained the precise relationship that allows quantifying the accuracy of the reconstruction as function of HARDI q-space sampling schemes. The convolution between the true propagator and the diffusion PSF give rise to a blurred propagator with decreased contrast and angular resolution. Removing the effect of the PSF from the estimated propagator requires the use of some sort of deconvolution algorithm. The implementation and design of this deconvolution operation, however, is beyond the scope of this work. Notice that the results derived here are not confined only to the DOT methodology; they have valid connotation for the general q-space theory.

The truncated plane wave and the diffusion PSF

In this subsection will be investigated the behaviour of the truncated plane wave and its repercussion on the diffusion point spread function and the truncated diffusion propagator. Eq. (4) is a rigorous solution of the plane wave within the sphere of radius infinite. However, in practice it is necessary to use a truncate representation of this expression. That is, an expansion with a finite order of N. Note that the order of N used in the plane wave expansion is the same order that can be used for the calculation of the diffusion propagator given by Eq. (8). Interestingly enough, the truncate representation is still a rigorous solution of the plane wave, but within the sphere of radius $\rho=N/2\pi q$. For a radius larger than ρ the wave field decays quite rapidly (Canales-Rodríguez et al., 2009).

The above properties allow us to clarify from a theoretical point of view the implications of truncating the harmonic series. As we demonstrated in a previous work (Canales-Rodríguez et al., 2009) the truncated plane wave acts as a low-pass filter in q-space, where the resulting diffusion propagator can be computed by means of Eq. (10) but with a different maximum value for the filter that is given by $q_{\max}=N/2\pi\rho$. The main implication of the above result is that for a truncation order $N>2\pi$ the truncated propagator is able to map fine details at a spectral resolution not lower than the resolution provided by the FFT methodology (Canales-Rodríguez et al., 2009).

In such case the PSF given in Eq. (13) becomes:

$$\mathbb{F}\{\Pi\} = \frac{1}{2\pi^2R^3}\left[\sin\left(\frac{NR}{\rho}\right) - \frac{NR}{\rho}\cos\left(\frac{NR}{\rho}\right)\right] = \left(\frac{N}{2\pi R\rho}\right)^{3/2}J_{3/2}\left(\frac{NR}{\rho}\right) \quad (14)$$

where was considered the following property

$$j_1(x) = \frac{\sin x}{x^2} - \frac{\cos x}{x}, \quad (15)$$

and the relationship given by Eq. (71) (see Appendix B). $J_{3/2}$ is the Bessel function of the first kind with order 3/2. Notice that in the limit

as $N\to\infty$ or $\rho\to 0$ (i.e., $q_{max}\to\infty$) the PSF $\mathbb{F}\{\Pi\}$ resembles a Dirac's delta function; only in this limit the computed diffusion propagator resembles the true propagator.

In Fig. 1 we depict the profile of $\mathbb{F}\{\Pi\}$ (Eq. (14)) for some values of ρ as function of R. In order to quantify the degradation of spatial resolution that produces the convolution given by Eq. (12), we define an effective radius R_c for $\mathbb{F}\{\Pi\}$, which can be considered as a measure for the PFS resolution. In this definition we are assuming that for a distance R longer that this radius the effect of the convolution can be neglected with a high degree of accuracy. We define R_c as the value of R at which $\mathbb{F}\{\Pi\}$ achieves its second root. The nth root of Eq. (14) can be computed approximately as $\pi\rho(2n+1)/2N$. This approximation is more valid insofar as n increase. For $n=2$ we obtain $R_c\approx 5\pi\rho/2N$.

The above analysis facilitates the evaluation of the effect of the convolution operation at different length scales. As can be seen, the estimated diffusion propagator is less affected by the PSF $\mathbb{F}\{\Pi\}$ for small displacement lengths (near-field limit), e.g., $R_c\approx 3.9$ μm for $\rho=5$ μm. In contrast, for large displacement lengths (far-field limit) the PSF $\mathbb{F}\{\Pi\}$ interacts over a larger spatial extension, e.g., $R_c\approx 31.4$ μm for $\rho=40$ μm.

The original DOT method (Ozarslan et al., 2006) was implemented using the same value of ρ to evaluate the diffusion propagator in all voxels, which was selected empirically from the experiments. Optimum results may be obtained by using optimum values of ρ that in general can be different in diverse white matter regions. The estimation process of optimum contours must consider that, in theory, the true diffusion propagator evaluated at large displacement lengths provides isosurfaces with high angular contrast. However, in this regimen of displacement the convolution operation causes a higher spatial interaction (or averaging) between the diffusion propagator values. This negative effect may give rise to a global decrement of spatial resolution in the estimated propagator. The estimation process of optimum contours, however, is beyond the scope of this work.

Far-field pattern and the mono-exponential model

In this subsection the far-field analytic pattern for the diffusion propagator will be considered. This type of mathematical description is well-known in the physics literature for expressing electromagnetic field data (Arnoldus et al., 2008; Brehm et al., 2008). To do this, we define the far-field limit by $\rho q \gg (N+1)/2\pi$. This limit was defined in view of the well-known asymptotic expressions (seeAppendix E) for the spherical Bessel function that appears in the expansion of the plane wave given in Eq. (4).

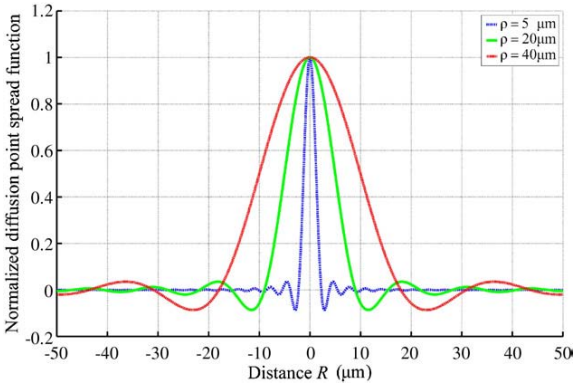

Fig. 1. Normalized point spread function (PSF) profiles for different displacement lengths $\rho=5$, 20, and 40 μm, with a maximum series order $N=10$. The effective radius corresponding to these parameters are $R_c=3.9$, 15.7, and 31.4 μm, respectively. The normalized PSF was defined as the PSF given by Eq. (17) divided by its maximum value that is achieved at the origin. This normalized function permits a clearer visual comparison among the different curves depicted here.

In Appendix B we demonstrated that the far-field pattern P_{FF} of the diffusion propagator forecasted by the DOT model is given by:

$$P_{FF}(\rho,\hat{\mathbf{r}})\approx\frac{1}{[4\pi D(\hat{\mathbf{r}})t]^{3/2}}\exp\left[-\frac{\rho^2}{4D(\hat{\mathbf{r}})t}\right]. \tag{16}$$

It is important to note that the exponential term of Eq. (16) becomes the exponential term of a 3D Gaussian propagator when $1/2D(\hat{\mathbf{r}})t=\hat{\mathbf{r}}^{T}\sum^{-1}\hat{\mathbf{r}}$, where $\sum$ is the covariance matrix of the random variable $\vec{r}$ that represents the natural displacement vector of water molecules. However, the resulting distribution presents a normalization constant that depends on $\hat{\mathbf{r}}$. This property is unusual because in statistic the normalization constant of a Gaussian distribution does not depend on the sample direction. The only case in which Eq. (16) represents strictly a 3D Gaussian propagator is obtained when $D(\hat{\mathbf{r}})$ does not depend on $\hat{\mathbf{r}}$, i.e., $D(\hat{\mathbf{r}})=D=cte$; in this case the diffusion profile is isotropic.

Notice also that Eq. (16) cannot be interpreted as the propagator of a 1D Gaussian diffusion process along each radial line $\hat{\mathbf{r}}$ where in general each radial line possesses a different diffusion coefficient. The breakdown of this possible interpretation takes root in the fact that the normalization constant of a 1D Gaussian propagator contains a power term of 1/2, whereas the power term of Eq. (16) is 3/2.

The above inconsistencies are consequence of the assumptions behind the mono-exponential model (Eq. (3)). In the far-field limit these assumptions give rise to a diffusion propagator that is unable to characterize the correct microgeometry due to the maxima of the diffusivity profile in general do not coincide with the main axes of the media. Therefore, although the mono-exponential model assumed in DOT allows computing accurate diffusion patterns at relatively small or moderate displacement lengths, it is not convenient to characterize the diffusion propagator in the far-field limit. This result implies that there may be a transition point or critical radius in real-space for which the estimated diffusion propagator will be biased (e.g., in the limit from moderate to large displacements). The existence of such critical radius will be studied in the Result section in simulated and real capillary systems. For completeness, the analysis of the near-field pattern of displacement is provided in Appendix D, which is used to deduce the analytical expression for the probability of return to the origin.

Average descriptors for fiber tissues

In order to reconstruct the 3D microgeometry of fiber tissues, some measures derived from the diffusion propagator can be employed. Between these ones, the ODF is the descriptor most used in the literature. It provides a very efficient approach to summarize the angular information from the propagator. This quantity is known under the name of "texture" in the materials science community. The next subsection is dedicated to obtaining the ODF analytical expressions corresponding to the DOT model. Additionally, a last subsection is devoted to provide analytical equations of the skewness ODF corresponding to the discrepancy between the ODF assuming a non-Gaussian model and the ODF assuming a Gaussian model.

Orientational distribution function

In practice, the ODF can be written in the following general form:

$$\mathrm{ODF}_n(\hat{\mathbf{r}})=\frac{1}{Z_n}\int_0^{\infty}P(\hat{\mathbf{r}},\rho)\rho^n d\rho, \tag{17}$$

where n is the order of the radial projection and Z_n is a normalization constant. In this work we shall focus on obtaining the zero-, first-, and second-order radial projections, which corresponds to the cases $n=0$, 1, and 2, respectively.

The zero-order radial projection will be denoted as ODF_0, and it represents the classical ODF definition used in the QBI method (Tuch, 2004). The first- and second-order radial projections will be denoted as ODF_I and ODF_{II}, respectively. They have been employed in previous DSI reconstructions (Gilbert et al., 2006; Lin et al., 2003; Wedeen et al., 2005).

The above ODF definitions capture the relevant information contained in the diffusion propagator, however, in the integration process each one assigns a different weight to the probabilities of a given displacement length. Making use of Eq. (5), Eq. (6), and Eq. (17) we obtain the general ODF expression:

$$\mathrm{ODF}_n(\hat{\mathbf{r}}) = \frac{1}{Z_n}\sum_{l=0}^{\infty}\sum_{m=-l}^{l}(-1)^{l/2}Y_{lm}(\hat{\mathbf{r}})\oint_{\Omega}Y_{lm}^{*}(\hat{\mathbf{q}})\Phi_{l,n}(\hat{\mathbf{q}})d\hat{\mathbf{q}}, \tag{18}$$

where

$$\Phi_{l,n}(\hat{\mathbf{q}}) = \frac{\Gamma\left(\frac{l+3}{2}\right)}{2^{l+3}\pi^{3/2}\Gamma\left(l+\frac{3}{2}\right)[D(\hat{\mathbf{q}})t]^{\frac{l+3}{2}}}\int_0^{\infty}\rho^{l+n} \times {}_1F^1\left(\frac{l+3}{2};l+\frac{3}{2};-\frac{\rho^2}{4D(\hat{\mathbf{q}})t}\right)d\rho. \tag{19}$$

Eq. (19) admits a general analytic solution that is valid for $n=0$ and $n=1$ (seeAppendix C for a detailed description). Inserting the result given by Eq. (59) into Eq. (18) we obtain:

$$\mathrm{ODF}_0(\hat{\mathbf{r}}) \propto \sum_{l=0}^{\infty}\sum_{m=-l}^{l}(-1)^{l/2}\frac{\Gamma\left(\frac{l+1}{2}\right)}{\Gamma\left(\frac{l}{2}+1\right)} \times Y_{lm}(\hat{\mathbf{r}})\oint_{\Omega}Y_{lm}^{*}(\hat{\mathbf{q}})\frac{1}{D(\hat{\mathbf{q}})}d\hat{\mathbf{q}} \tag{20}$$

where the irrelevant numerical constants were neglected.

The inverse of the diffusion profile can be expanded in terms of spherical harmonics as follows:

$$\frac{1}{D(\hat{\mathbf{q}})} = \sum_{l'=0}^{\infty}\sum_{m'=-l'}^{l'}d_{l'm'}Y_{l'm'}(\hat{\mathbf{q}}). \tag{21}$$

Inserting the above expansion into Eq. (20), taking into account the orthogonally condition of the spherical harmonics given by Eq. (9), and considering the following relationship between the Gamma function and the Legendre polynomials P_l for even-l terms

$$P_l(0) = (-1)^{l/2}\frac{\Gamma\left(\frac{l+1}{2}\right)}{\Gamma\left(\frac{l}{2}+1\right)}, \tag{22}$$

the zero-order radial projection can be computed

$$\mathrm{ODF}_0(\hat{\mathbf{r}}) \propto \sum_{l=0}^{\infty}\sum_{m=-l}^{l}P_l(0)d_{lm}Y_{lm}(\hat{\mathbf{r}}). \tag{23}$$

This result agrees with a previous derivation of our group (Canales-Rodríguez et al., 2009). It is interesting to note that the above expression is similar to the QBI spherical harmonic reconstruction developed in Anderson (2005), Descoteaux et al. (2006a,b) and Hess et al. (2006). The only difference comes from the harmonic coefficients d_{lm} in the series. In QBI these coefficients are estimated from the spherical harmonic transform of the measured signal, whereas in Eq. (23) are computed from the spherical harmonic transform of the inverse of the diffusivity profile by means of Eq. (21).

In summary, the zero-order ODF_0 can be computed in the following steps:

(1) Compute the diffusivity $D(\hat{\mathbf{q}})$ profile using the diffusion model given by Eq. (3).
(2) Compute the set of harmonic coefficients $\{d_{lm}\}$ using Eq. (21).
(3) Then evaluate Eq. (23).

Similarly, inserting the result given by Eq. (60) (see Appendix C) into Eq. (18) we obtain:

$$\mathrm{ODF}_I(\hat{\mathbf{r}}) \propto \sum_{l=0}^{\infty}\sum_{m=-l}^{l}(-1)^{l/2}\frac{\Gamma\left(\frac{l}{2}+1\right)}{\Gamma\left(\frac{l+1}{2}\right)}Y_{lm}(\hat{\mathbf{r}})\oint_{\Omega}D(\hat{\mathbf{q}})^{-1/2}Y_{lm}^{*}(\hat{\mathbf{q}})d\hat{\mathbf{q}} \tag{24}$$

The inverse of the square root of the diffusion profile can be expanded in terms of spherical harmonics as follows:

$$D(\hat{\mathbf{q}})^{-1/2} = \sum_{l'=0}^{\infty}\sum_{m'=-l'}^{l'}e_{l'm'}Y_{l'm'}(\hat{\mathbf{q}}). \tag{25}$$

Inserting the above expansion into Eq. (24) and considering the orthogonally condition of the spherical harmonics (Eq. (9)), we obtain the following final expression:

$$\mathrm{ODF}_I(\hat{\mathbf{r}}) \propto \sum_{l=0}^{\infty}\sum_{m=-l}^{l}(-1)^{l/2}\frac{\Gamma\left(\frac{l}{2}+1\right)}{\Gamma\left(\frac{l+1}{2}\right)}e_{lm}Y_{lm}(\hat{\mathbf{r}}). \tag{26}$$

Therefore, the first-order ODF_I can be computed as follows:

(1) Compute the diffusivity $D(\hat{\mathbf{q}})$ profile using the diffusion model given by Eq. (3).
(2) Compute the set of harmonic coefficients $\{e_{lm}\}$ using Eq. (25).
(3) Then evaluate Eq. (26).

The analytical solution of Eq. (19) for the case $n=2$ is developed in Appendix C. The expression inside square brackets in Eq. (61) can be expanded in terms of spherical harmonics as follows:

$$\kappa + \log\left(\frac{1}{D(\hat{\mathbf{q}})t}\right) = \sum_{l'=0}^{\infty}\sum_{m'=-l'}^{l'}f_{l'm'}Y_{l'm'}(\hat{\mathbf{q}}), \tag{27}$$

where $\kappa \approx 0.577216$ is the Euler's constant. Making use of Eq. (27) and Eq. (61), Eq. (18) becomes

$$\mathrm{ODF}_{II}(\hat{\mathbf{r}}) = \frac{4}{\pi}\sum_{l=0}^{\infty}\sum_{m=-l}^{l}(-1)^{l/2}\chi_l f_{lm}Y_{lm}(\hat{\mathbf{r}}), \tag{28}$$

where

$$\chi_l = \begin{cases} g_l, & \forall l \neq 0 \\ \dfrac{2\pi^{1/2}|h_0|}{f_{00}}, & l = 0 \end{cases} \tag{29}$$

In the above derivation we have considered the results given in Eq. (47) and Eq. (9) (see Table 1). (Note that $Z_2=1$.) In summary, the second-order radial projection (ODF_{II}) can be computed via the following algorithm:

(1) Compute the diffusivity $D(\hat{\mathbf{q}})$ profile using the diffusion model given by Eq. (3).
(2) Compute the set of harmonic coefficients $\{f_{lm}\}$ using Eq. (27).
(3) Then evaluate Eq. (28) using the estimated harmonic coefficients $\{f_{lm}\}$ and the coefficients χ_l defined by Eq. (29) and Table 1.

Skewness orientation distribution function

In statistics, skewness and kurtosis are measures of whether the data are peaked or flat relative to a normal distribution. Recently, this idea has been extended to diffusion MRI data to visualize isosurfaces (on the sphere) of the deviation of the diffusion propagator from the Gaussian propagator (Liu et al., 2004; Liu et al., 2005). The later was

Table 1
Coefficients obtained from the evaluation of Eq. (19) with $n=2$ for the specific values of $l=0, 2, 4, \ldots, 14$.

l	0	2	4	6	8	10	12	14
h_l	$-\frac{1}{16}$	$\frac{8}{32}$	$\frac{61}{64}$	$\frac{1019}{512}$	$\frac{3407}{1024}$	$\frac{80939}{16384}$	$\frac{1115963}{163840}$	$\frac{1170017}{131072}$
g_l	0	$\frac{3}{32}$	$\frac{15}{64}$	$\frac{210}{512}$	$\frac{630}{1024}$	$\frac{13860}{16384}$	$\frac{180180}{163840}$	$\frac{180180}{131072}$

called the skewness map, which is determined by means of the relationship:

$$\Delta P(\hat{\mathbf{r}},\rho) = P(\hat{\mathbf{r}},\rho) - P_G(\hat{\mathbf{r}},\rho), \tag{30}$$

where $P_G(\hat{\mathbf{r}},\rho)$ is the Gaussian propagator that depends on the second-order self-diffusion tensor estimated from the data. The strength of this descriptor to delineate the cytoarchitectonics of fiber tissues was discussed in Liu et al. (2004).

In analogy, this concept can be extended to compute the skewness orientation distribution function (sODF), which we introduce in this work via the following equation:

$$\mathrm{sODF}_n(\hat{\mathbf{r}}) = \mathrm{ODF}_n(\hat{\mathbf{r}}) - \mathrm{gODF}_n(\hat{\mathbf{r}}), \tag{31}$$

where $\mathrm{gODF}_n(\hat{\mathbf{r}})$ is the orientation distribution function corresponding to the Gaussian model (see Eq. (17))

$$\mathrm{gODF}_n(\hat{\mathbf{r}}) = \frac{1}{Z_{Gn}} \int_0^\infty P_G(\hat{\mathbf{r}},\rho)\rho^n d\rho, \tag{32}$$

and Z_{Gn} is a normalization constant.

In principle, the Gaussian $g\mathrm{ODF}_n$ given by Eq. (32) admits analytical solutions for our cases of interest, i.e., $n=0$, 1 and 2. However, due to the zero-, first-, and second-order ODF radial projections are computed as truncated versions of the true ODFs (see Eqs. (23), (26) and (28)), the Gaussian $g\mathrm{ODF}_n$ must be estimated under the same level of approximation. This can be done by computing $g\mathrm{ODF}_n$ with the same equations employed for estimating $\mathrm{ODF}_n(\hat{\mathbf{r}})$, but replacing the observed diffusivity profile $D(\hat{\mathbf{q}})$ by the Gaussian diffusivity profile $D(\hat{\mathbf{q}}) = \hat{\mathbf{q}}\mathbf{D}\hat{\mathbf{q}}^T$, where $\mathbf{D}$ is the second-order self-diffusion tensor estimated from the data. As with the skewness map, only positive values of Eq. (31) should be considered. In voxels where $\mathrm{sODF}_n = 0$. $\forall \hat{\mathbf{r}}$, the diffusion process is purely Gaussian and the main orientation of the media can be determined from the diffusion tensor model.

Materials and methods

Synthetic data generation

We have applied the simulation protocol described in Ozarslan et al. (2006) to generate the data corresponding to a fiber crossing system. This scheme provides a suitable test bed to study our models. The diffusion MR signal attenuation from molecules, with free diffusion coefficient given by D_0, restricted inside a cylinder of radius r and length L is given by (Soderman and Jonsson, 1995):

$$\begin{aligned} E(q,\hat{\mathbf{q}},\hat{\nu},r,L) = & \sum_{n=0}^{\infty}\sum_{k=1}^{\infty}\sum_{m=0}^{\infty} \frac{2K_{nm}r^2(2\pi qr)^4\sin^2(2\psi)\gamma_{km}^2}{\left[(n\pi r/L)^2-(2\pi qr\cos\psi)^2\right]^2} \\ & \times \frac{\left[1-(-1)^n\cos(2\pi qL\cos\psi)\right]\left[J'_m(2\pi qr\sin\psi)\right]^2}{L^2\left[\gamma_{km}^2-(2\pi qr\sin\psi)^2\right]^2(\gamma_{km}^2-m^2)} \\ & \times \exp\left(-\left[\left(\frac{\gamma_{km}}{r}\right)^2+\left(\frac{n\pi}{L}\right)^2\right]D_0\Delta\right). \end{aligned} \tag{33}$$

In the above expression, γ_{km} is the kth solution of the equation $J'_m(\gamma)=0$, with the convention $\gamma_{10}=0$; $K_{nm}=\delta_{n0}\delta_{m0}+2[(1-\delta_{n0})+(1-\delta_{m0})]$, and ψ is the angle between the unit vector $\hat{\mathbf{q}}$ and the main axis of the cylinder $\hat{\mathbf{v}}$ (i.e., $\psi=\mathrm{acos}(\hat{\mathbf{q}}\hat{\mathbf{v}})$).

The net signal E_T corresponding to the presence of two identical cylinders inside a voxel can be computed as:

$$E_T = E(q,\hat{\mathbf{q}},\hat{\mathbf{v}}_1,r,L) + E(q,\hat{\mathbf{q}},\hat{\mathbf{v}}_2,r,L) \tag{34}$$

This expression assumes that there is no molecular exchange between the cylinders. All diffusion processes are restricted inside the cylinders, thus no extracylinder diffusion is considered. In our experiments we will choose the same experimental values employed in Ozarslan et al. (2006). That is, $L=5$ mm, $D_0=2.02\ 10^{-3}$ mm^2/s, $\Delta=20.8$ ms and $\tau=2.4$ (where $t=\Delta-\tau/3$). Similarly, we terminated the infinite series in Eq. (33) at $n=1000$, and $k=m=10$, which ensures a high degree of convergence to the expansion (Ozarslan et al., 2006). The net signal was generate for a configuration of two perpendicular cylinders (i.e., $\hat{\mathbf{v}}_1\perp\hat{\mathbf{v}}_2$), for b-values of 1500 and 3000 s/mm^2, and two different radius $r=5$, 20 μm. The signal was measured onto 642 angular directions obtained from the "sphere_tri" function, "bioelectromagnetism" Matlab toolbox (online: http://eeg.sourceforge.net/doc_m2html/bioelectromagnetism/sphere_tri.html) that provides high angular resolution diffusion images.

Phantom model generation

The model was constructed from plastic capillaries with inner and outer diameters of 20 and 90 μm respectively (flexible fused silica capillary tubing, Polymicro Technologies, Phoenix, Arizona, USA). A large number of these capillaries were compactly arranged along the same direction in a flat placeholder. Two such placeholders were stacked on top of each other, and the angle between the two fiber orientations was adjusted to 45°. The whole phantom was then immersed in water and vibrated for a long time prior to the experiment to ensure adequate filling of the capillaries. Temperature was maintained at 20 °C throughout the imaging experiment.

Data were collected using a 9.4 T spectrometer (Bruker Companies, Ettlingen, Germany). A 2D-FT stimulated-echo HARDI sequence was used with the following parameters: TR/TE/TM = 1900/13.8/92.3 ms, matrix size = 32×32, FOV = 25×25 mm, slice thickness = 3.6 mm, diffusion gradient pulse separation and duration $\Delta=100$ ms and $\tau=3$ ms respectively, maximum diffusion gradient pulse amplitude $G_{\max}=354.2$ mT/m, and 160 gradient directions. This sequence permits relatively narrow diffusion gradient pulses and large diffusion times, which satisfies the narrow pulse approximation inherent to DSI and DOT methodologies. The gradient directions were calculated using an electrostatic repulsion model (Jones et al., 1999). The diffusion gradient scheme consisted of 2×80 noncollinear orientations: for each of the 80 orientations, the opposite direction was also measured. The b-value dependence was investigated by varying $G_{\max}$ from 88.6 to 354.2 mT/m to produce the set of b-values = {500, 1000, 2000, 4000, 8000, s/mm^2}. The signal to noise ratio (SNR) corrupting the $b=0$ images of these measurements is SNR = 35 (for more details, see Tournier et al., 2008).

Results

The spherical harmonic inversion of all the harmonic series used in this work was implemented using the formalism described in Appendix C in Canales-Rodríguez et al. (2009). This formalism is similar to the one previously presented in Descoteaux et al. (2006a,b), which produces accurate spherical inversions. In particular, all the reconstructions were performed with a maximum series order $N=8$.

Synthetic data

Fig. 2 and 3 show the evolution of the isosurfaces of the diffusion propagator forecasted by DOT for several displacement lengths (in the range $r/4\leq\rho\leq5r$). These propagators were computed from the signals generated for the system of two perpendicular cylinders (see Eq.(34)) with radius $r=5$ μm and b-values of 1500 s/mm^2 (Fig. 2) and 3000 s/mm^2 (Fig. 3). As can be seen, for small displacement lengths (i.e., $\rho<r$) the diffusion propagator does not capture the relevant 3D structure of the system of cylinders, as expected. In the range of moderate displacement lengths (i.e., $\rho\sim10$, 15 μm) the propagator successfully represents the true orientation of the cylinders. Moreover, in the range from moderate to large displacement lengths (i.e., $\rho\geq20$ μm), the isosurfaces show aberrations in form of artifactual peaks that gradually increase its intensity.

In Fig. 4 are shown the ODF and skewness ODF maps reconstructed using the same signals employed to compute the above diffusion propagators. Specifically, panels (a) and (b) designate the ODFs and skewness ODFs corresponding to the propagators depicted in Figs. 2 and 3 respectively. Notice that the angular resolution of the ODFs increases with the order of the radial projection. Nevertheless, in this simulation the best compromise between angular resolution and accuracy, for both b-values, is obtained for the first-order radial projection $\mathrm{ODF_I}$. Note that the second-order radial projection $\mathrm{ODF_{II}}$ presents artifactual peaks near the origin, which become significant especially in panel (b). On the other hand, the angular resolution of the three skewness ODFs were similar, however, the second-order radial projection $\mathrm{sODF_{II}}$ presents small artifacts near the origin, which are the result of the artifacts in $\mathrm{ODF_{II}}$.

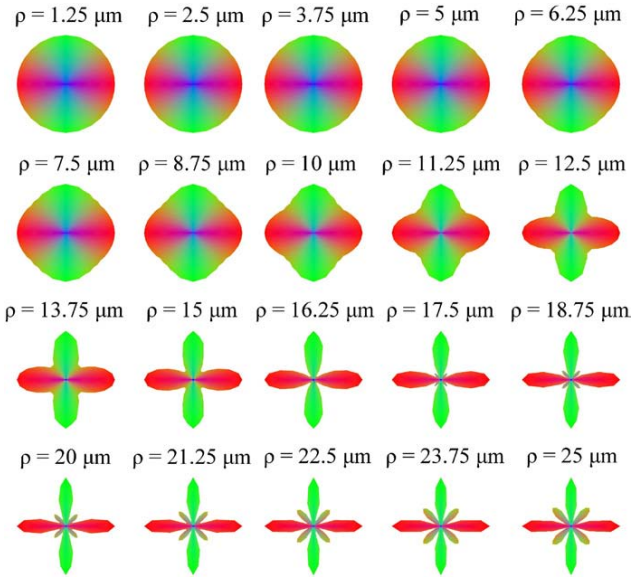

Fig. 2. Isosurfaces of the diffusion propagator reconstructed by DOT evaluated at different displacement lengths (in the range $r/4\leq\rho\leq5r$). The propagator was computed from the signal generated for the system of two perpendicular cylinders with radius $r=5$ μm and b-value of 1500 s/mm^2.

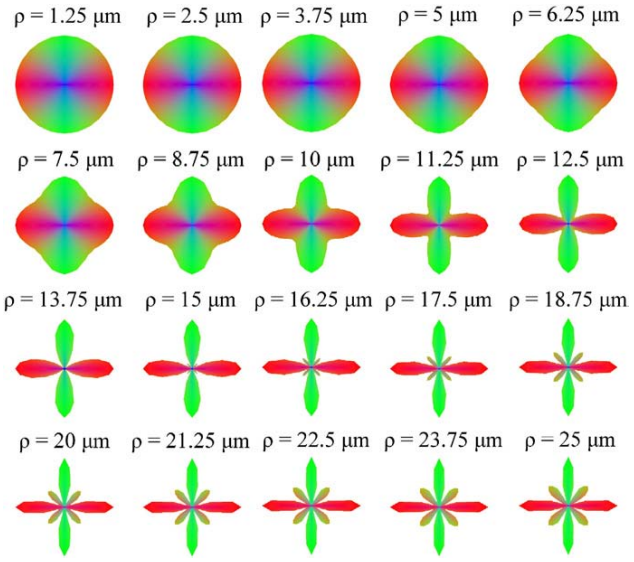

Fig. 3. Isosurfaces of the diffusion propagator reconstructed by DOT evaluated at different displacement lengths (in the range $r/4\leq\rho\leq5r$). The propagator was computed from the signal generated for the system of two perpendicular cylinders with radius $r=5$ μm and b-value of 3000 s/mm^2.

Figs. 5 and 6 depict the progression of the isosurfaces of the propagator forecasted by DOT for several displacement lengths (in the range $r/4\leq\rho\leq5r$). These reconstructions were computed from the signals generated for the system of two perpendicular cylinders (see Eq. (34)) with radius $r=20$ μm and b-values of 1500 s/mm^2 (Fig. 5) and 3000 s/mm^2 (Fig. 6).

In both figures the propagator is able to predict the orientation of the cylinders for displacement lengths in the order of the radius of the cylinders. The best solution is obtained for $\rho=25$ μm; however, for displacement lengths larger than 30 μm the propagator presents significant artifactual peaks.

In Fig. 7 are shown the ODF and skewness ODF maps reconstructed using the same signals employed to calculate the above diffusion propagators. Particularly, panels (a) and (b) illustrate the ODFs and skewness ODFs corresponding to the propagators depicted in Figs. 5 and 6 respectively. In this simulation the artifactual peaks in the ODFs and the skewness ODF maps are insignificant. This result supports the hypothesis that the contribution of the propagator to the radial projections given by Eq. (17) is unimportant for large displacement lengths. Therefore, although the radial projections take into account the information from all displacement lengths, in practice they are more sensitive to the diffusion propagator values in the range from low to moderate displacement lengths, which is the regimen in which the propagator predicted by DOT potentially presents a reduced amount of artifacts.

From these simulations we can formulate the following partial conclusions. First, the diffusion propagator reconstructed by DOT presents artifactual peaks that appear incrementally from a certain critical value of the displacement length. Second, this critical value depends on the dimension of the media where the diffusion process takes place, e.g., in our simulation it depends on the radius of the cylinders. Third, the appearance of the artifactual peaks is a phenomenon inherent to the method, due to the synthetic signals were created without experimental noise and with a dense HARDI scheme. Four, the isosurface of the propagator that best represents the microgeometry of the media is different for systems with different

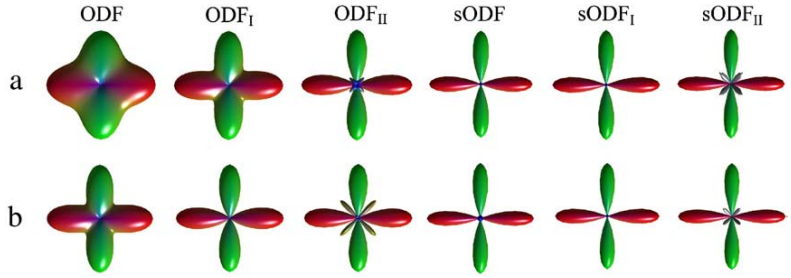

Fig. 4. Panel (a) designates the ODF and skewness ODF maps corresponding to the diffusion propagator showed in Fig. 2. Panel (b) illustrates the ODF and skewness ODF maps corresponding to the diffusion propagator depicted in Fig. 3.

physical dimensions. For instance, for the cylinders with radius 5 and 20 μm the optimum isosurfaces are obtained for displacement lengths near of 15 and 25 μm, respectively. This implies that if we use a single isosurface to characterize heterogeneous fiber tissues, like the brain white matter where fiber bundles can have a large variety of radius, each region may be characterized with a significant different degree of accuracy.

Phantom model

The phantom data analysis was performed using only two sets of 80 directions from the two hemispherical shells measured with *b*-values of 4000 and 8000 s/mm^2, which corresponds to a more clinically realistic sampling scheme. The diffusivity profile corresponding to each hemispherical shell (i.e., $D_1(\hat{\mathbf{q}})$ and $D_2(\hat{\mathbf{q}})$) was computed by means of Eq. (3). The net diffusivity profile was computed as the average of the individual diffusivities, i.e., $D_1(\hat{\mathbf{q}}) = (D_1(\hat{\mathbf{q}}) + D_2(\hat{\mathbf{q}}))/2$. This procedure was employed in Canales-Rodríguez et al. (2009) to obtain a diffusivity profile more representative of the voxel that makes available a better interpolation of the signal in the whole q-space. The accuracy of the method in defining local fiber orientations was defined as the average deviation angle between the reconstructed and true principal orientations. The average deviation angle was computed as

$$\Delta\varphi = \frac{1}{2}\sum_{i=1}^{2} \min\left\{\left|\arccos\left(\hat{\boldsymbol{\nu}}_i^T \hat{\mathbf{e}}_1\right)\right|, \left|\arccos\left(\hat{\boldsymbol{\nu}}_i^T \hat{\mathbf{e}}_2\right)\right|\right\}, \tag{35}$$

where, $\hat{\mathbf{v}}_1$ and $\hat{\mathbf{v}}_2$ are the unit vectors along the true fibers of the phantom; $\hat{\mathbf{e}}_1$ and $\hat{\mathbf{e}}_2$ are the unit vectors along the two main maxima extracted from the angular profiles. In addition, to quantify the occurrence of false peaks we compute the number of main maxima from the reconstructions. At each voxel the number of main maxima was defined specifically as

$$\text{n-fiber} = \sum_{i=1}^{k} I(I_i, I_{max}), \tag{36}$$

where $I(I_i, I_{max}) = 1$ for $I_i > 0.3\ I_{max}$ and $I(I_i, I_{max}) = 0$ for $I_i \leq 0.3\ I_{max}$; I_i denotes the intensity of the *i-th* maximum, I_{max} is the intensity of the main maximum (i.e., $I_{max} = \max\{I_i | i = 1, \ldots, k\}$), and k is the number of maxima extracted from the local angular profiles.

Fig. 8 shows the diffusion propagator predicted by DOT evaluated at different displacement lengths in a region of interest (ROI) within

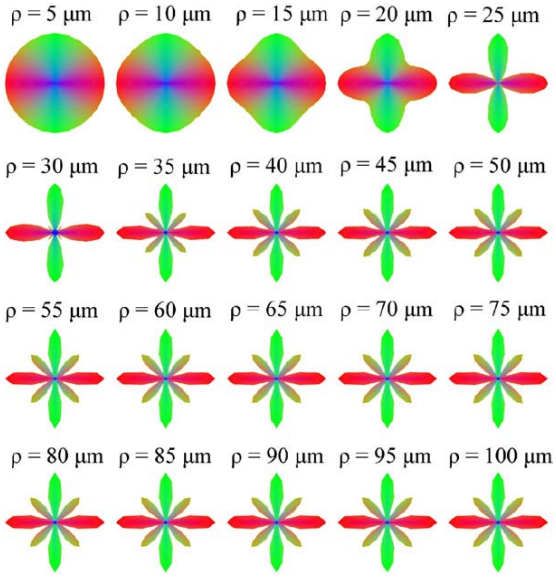

Fig. 5. Isosurfaces of the diffusion propagator reconstructed by DOT evaluated at different displacement lengths (in the range $r/4 \leq \rho \leq 5r$). The propagator was computed from the signal generated for the system of two perpendicular cylinders with radius $r = 20$ μm and *b*-value of 1500 s/mm^2.

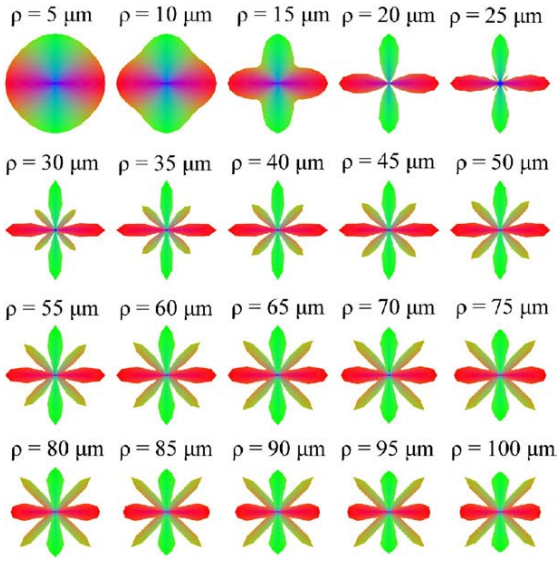

Fig. 6. Isosurfaces of the diffusion propagator reconstructed by DOT evaluated at different displacement lengths (in the range $r/4 \leq \rho \leq 5r$). The propagator was computed from the signal generated for the system of two perpendicular cylinders with radius $r = 20$ μm and *b*-value of 3000 s/mm^2.

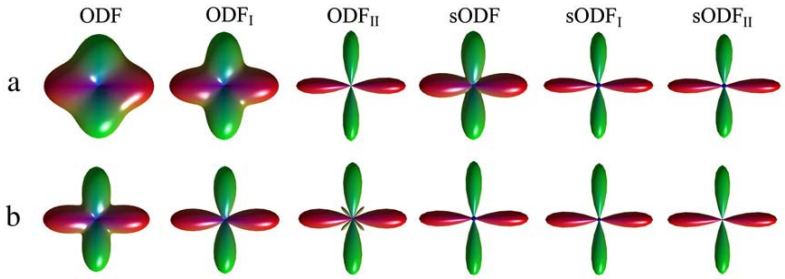

Fig. 7. Panel (a) designates the ODF and skewness ODF maps corresponding to the diffusion propagator showed in Fig. 5. Panel (b) illustrates the ODF and skewness ODF maps corresponding to the diffusion propagator depicted in Fig. 6.

the plane of intersection of the capillaries. The isosurfaces of the propagator at 20 μm does not allow inferring the true direction of the cylinders. The average deviation angle of these contours is $\Delta\tilde{\varphi}=22.8^\circ\pm0.14^\circ$. The large value of this angle and its small standard deviation are due to the contours only present (in all voxels within the ROI) a single maximum. This is reflected in the number of peaks detected per voxel n-fiber $=1\pm0$. At 30 μm it is possible to distinguish the orientation of the capillaries that coincides with the two main maxima of the isosurfaces, i.e., $\Delta\tilde{\varphi}=8.7^\circ\pm7.9^\circ$. The average number of fibers is n-fiber $=2.8\pm0.5$. This result confirms that in some voxels the contours present three main peaks. For larger displacement lengths, i.e., 50 μm, the two main maxima of the angular profiles exhibit the best alignment with the capillaries system, i.e., $\Delta\tilde{\varphi}=4.8^\circ\pm1.2^\circ$. However, these profiles are corrupted and shown many artifactual peaks, i.e., n-fiber $=10\pm1.7$.

Fig. 9 depicts the ODFs in the same ROI of 5×5 voxels where was computed the diffusion propagator illustrated in Fig. 8. As can be seen, the angular resolution of the method as well as the intensity of the artifactual peaks increases with the order of the radial projection. The average deviation angle of the zero-order radial projections (ODF$_0$) is $\Delta\tilde{\varphi}=19.7^\circ\pm7^\circ$. The average number of peaks is n-fiber $=1.2\pm0.4$. These results reveal that in most of voxels only one maximum is detected. Nevertheless, the uncertainty inherent to this main maximum allows forecasting a high probability of fibers along the true orientations. On the other hand, the first-order radial projections (ODF$_I$) present the more accurate reconstructions, i.e., $\Delta\tilde{\varphi}=4.9^\circ\pm2.9^\circ$ and n-fiber $=2\pm0$. The second-order radial projections (ODF$_{II}$) also provide a small average deviation angle $\Delta\tilde{\varphi}=4.2^\circ\pm1.3^\circ$. However, the profiles have some artifactual fibers: n-fiber $=4.4\pm1.7$.

In Fig. 10 are presented the skewness ODF maps for the same ROI tested in the above experiments. In general, these profiles have higher angular resolution than the ODF maps (see Fig. 9). However, in some voxels, the small peaks near the origin that appear in the ODFs were amplified to the skewness ODFs. In particular, the second-order skewness ODF$_{II}$ map is very corrupted and is not useful to infer the microgeometry of the capillaries system. The average deviation angle for the skewness ODF maps is $7.5^\circ\pm1.6^\circ$ (for sODF$_0$), $6.7^\circ\pm1.4^\circ$ (for sODF$_I$) and $17.1^\circ\pm11.6^\circ$ (for sODF$_{II}$). The average number of fibers detected per voxel is 2.8 ± 0.8 for (sODF$_0$), 3.4 ± 0.5 (for sODF$_I$) and 5.8 ± 0.8 (for sODF$_{II}$). As can be appreciated, the sODF$_0$ profiles provide the most appropriated skewness map.

From these experiments we can infer the following partial conclusions. First, the accuracy of the propagator reconstructed by DOT heavily depends on the displacement length. The DOT isosurfaces have shown strong artifactual peaks for displacement lengths larger than its optimum value, which is unknown a priori. On the other hand, for displacement lengths smaller than the optimum value the DOT isosurfaces were very smooth, and hence they cannot be employed to determine the main axis of each capillary sheet. Second, the radial projection ODFs have shown the potential to delineate the structure of the cylinders, which provide spherical shapes that are comparable to the isosurfaces forecasted by DOT evaluated near of its optimal displacement lengths. Third, caution must be taken to interpret the results derived from the second-order skewness ODF$_{II}$ map in real data; they showed a high number of artifactual peaks. However, the zero- and first-order skewness ODFs (i.e., sODF$_0$, sODF$_I$) had depicted a great potential to infer the main orientations of the capillaries with a high angular resolution, and relatively few artifacts for the case of sODF$_0$ maps.

Discussion and conclusions

In this work, a mathematical description that provides an extension to the DOT methodology is presented, which helps to analyse and mitigate the DOT model limitations. The main theoretical

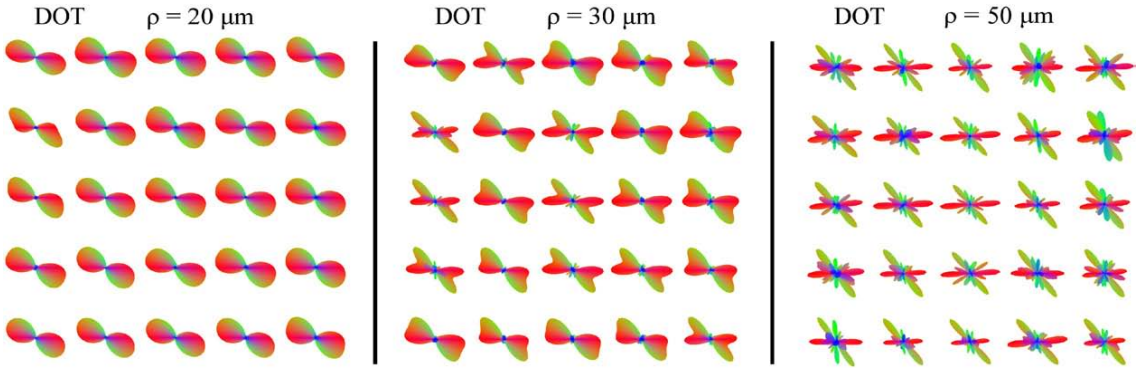

Fig. 8. Diffusion propagator predicted by DOT evaluated at different displacement lengths (i.e., $\rho=20$, 30 and 50 μm) in a region of interest (ROI) within the plane of intersection of the capillaries.

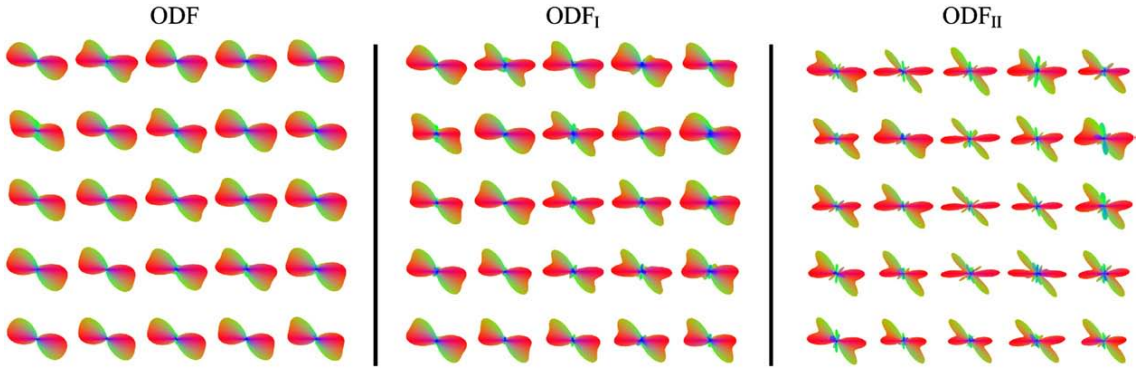

Fig. 9. ODF maps (i.e., ODF_0, ODF_I and ODF_{II}) computed in the same region of interest (ROI) of 5×5 voxels where was computed the diffusion propagator illustrated in Fig. 8.

contributions of this paper can be enumerated as follows. First, it is studied the effects of the use of signals with a finite support in q-space to analyze Fourier transform models defined on the whole q-space. The above analysis reveals that the resulting diffusion propagator is the convolution of the true propagator by a point spread function. Second, it is investigated the impact of the truncation of the spherical harmonic series on the point spread function and its repercussion on the diffusion propagator. This analysis facilitated the evaluation of the effect of the convolution operation at different length scales. Third, the diffusion propagator is examined in two opposite limits, termed the near- and far-field pattern of displacement. The near-field pattern makes available the direct computation of the probability of return to the origin corresponding to the DOT model. The far-field pattern analysis allows probing the limitations of the mono-exponential model, which suggest the existence of a limit of validity for DOT. The existence of this range of validity was corroborated in simulated and real data through simple examples of fiber crossing. Fourth, new analytical equations to compute the zero-, first- and second-order radial projection ODFs were derived. The main advantage of this extension is that the ODFs can be calculated directly from the data, without the calculus of the diffusion propagator, which allows the fast ODF estimation. Results from simulated and real data suggest that these ODFs can be relatively immune to the artifactual peaks observed in the propagator. Finally, a direct way to compute skewness ODF maps was derived. In practice these maps showed sharper shapes than the ODF profiles.

The analysis of synthetic and real data reveals that the isosurfaces predicted by DOT present significant artifactual peaks in the regimen from moderate to large displacement lengths. This regimen of displacements was not investigated in the original DOT article (Ozarslan et al., 2006). It is important to notice that the concept of moderate or large displacement length is relative to experimental parameters like the local physical dimensions of the media and the experimental diffusion time. Therefore, the methodology proposed in DOT of using a single displacement length to characterize all voxels in heterogeneous media is far to be an optimal criteria, due to some regions may be processed with a significant inaccuracy. In this work it is demonstrated that the ODF and skewness ODF maps are more robust descriptors of the media. In accordance with our results, the skewness ODFs are more appropriated to represent geometries with a high angular resolution. In contrast, the ODF maps are more adequate descriptors to represent profiles free of artifactual peaks near the origin with a relatively high angular resolution. Particularly, the first-order radial projection ODF_I and the zero-order skewness map $sODF_0$ have depicted the optimal reconstructions, and hence, they may be more appropriated for brain connectivity analysis using fiber tracking methods. Even so, this issue needs to be investigated in additional experiments. For example, the use of phantom data with different sizes could be appropriated to test the robustness of these functions for a wide range of physical dimensions. Nevertheless, the use of simulated data does not suggest a significant different behavior for capillaries with radius between 5 and 20 μm, which are typical dimensions in human fiber tissues (Schröder et al., 1988); although the squid giant axons reach diameters of 600–1000 μm (Haydon and Urban, 1985).

It is important to mention that although the DOT method was primarily developed under the assumption of a mono-exponential signal decay, the methodology is flexible and also allows the use of more complex models like the bi- or multiexponential model

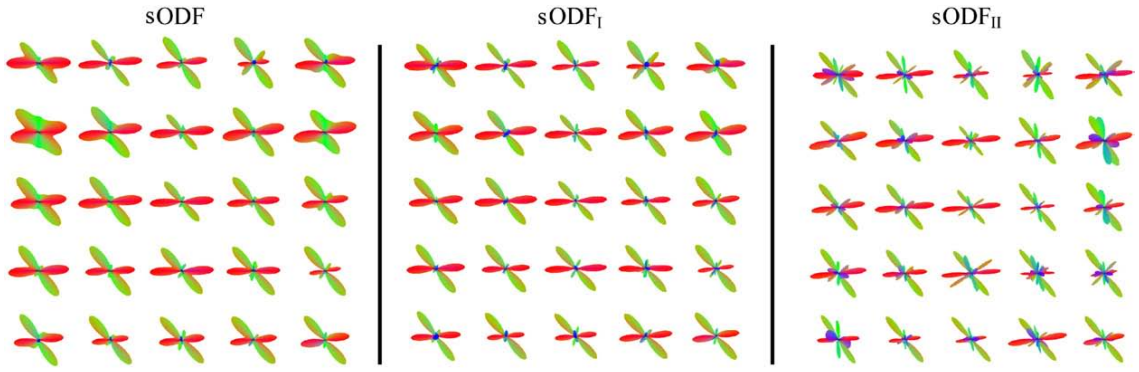

Fig. 10. Skewness ODF maps (i.e., $sODF_0$, $sODF_I$ and $sODF_{II}$) computed in the same region of interest of 5×5 voxels where was computed the diffusion propagator depicted in Fig. 8.

(Ozarslan et al., 2006). The use of more realistic biophysical models surely can improve the accuracy and robustness of the method. However, the parameter estimation process of these complex models requires the use of time-intensive experimental sampling schemes. For instance, using a biexponential attenuation fit would necessitate collecting about three times the number of data points when compared with the case in which the mono-exponentiality assumption is made (Ozarslan et al., 2006). For this reason, in this work we focused on the mono-exponential model that is the most popular model used in the DOT methodology.

An issue of special interest is that the diffusion propagator was computed here using a mathematical method different to the one previously developed in Ozarslan et al. (2006). To compute the confluent hypergeometric function of the first kind given in Eq. (6), in Ozarslan et al. (2006) an approximated expansion approach was developed. This approach was based on recurrence properties that yield an expansion in terms of the error and Gaussian functions. In contrast, in our implementation we used the method described in Zhang and Jin (1996), which allows a more exact evaluation of this function. In particular, we employed the converted version from FORTRAN program to Matlab codes that is provided by f2matlab open source project (online: https://sourceforge.net/projects/f2matlab/). Therefore, the propagators reconstructed from both approaches are not necessarily identical. In addition, the spherical harmonic inversions were computed using a robust methodology based on linear regularization techniques and the Laplace-Beltrami operator, which have previously been used to obtain smooth profiles on the sphere (Descoteaux et al., 2006a,b). This implementation reduces the undesirable effect of producing false spikes around the origin that the harmonic series exhibit when the SNR is very low or when the series is prematurely truncated.

In the last years the reconstruction of the three-dimensional structure of the fluid-filled tissue space has captured the attention of the Neuroimage community, due to the applications that these methods provide to study fiber tissue properties and in special the living brain. The results obtained in this work support the hypothesis that the revisited DOT methodology could improve the estimation of the local fiber microgeometry and, as a consequence, the enhancement in the estimation of anatomical connections between distant voxels in the brain by means of tractography algorithms.

Acknowledgments

This work was supported in part by the Instituto de Salud Carlos III, Centro de Investigación Biomédica en Red de Salud Mental (CIBERSAM, Spain), the Cuban Neuroscience Center, the National Science Council, Taiwan (NSC 98-2923-B-010-001-MY3), and the National Health Research Institute, Taiwan (NHRI-EX98- 9813EC). The authors acknowledge support from Laboratory of MRI Core Facility at National Yang-Ming University, Taiwan.

Appendix A. Convolution theorem and the Fourier transform of the filter

The Convolution theorem can be analyzed more compactly in Cartesian coordinates, in which Eq. (10) can be written as

$$P_F(\vec{\mathbf{r}}) = \int E\left(\vec{\mathbf{q}}\right)\Pi\left(\frac{|\vec{\mathbf{q}}|}{q_{max}}\right)\exp\left(-2\pi i\vec{\mathbf{r}}\,\vec{\mathbf{q}}\right)d\vec{\mathbf{q}}. \tag{37}$$

Similarly, the diffusion signal can be written as the inverse Fourier Transform of the diffusion propagator as follows:

$$E\left(\vec{\mathbf{q}}\right) = \int P\left(\vec{\mathbf{r}}'\right)\exp\left(2\pi i\vec{\mathbf{r}}'\,\vec{\mathbf{q}}\right)d\vec{\mathbf{r}}'. \tag{38}$$

Notice that without loss of generality we have written the above expression in terms of an auxiliary vector $\vec{\mathbf{r}}'$ in real-space. Inserting Eq. (38) into Eq. (37) we obtain

$$P_F\left(\vec{\mathbf{r}}\right) = \int\left[\int P\left(\vec{\mathbf{r}}'\right)\exp\left(2\pi i\vec{\mathbf{r}}'\,\vec{\mathbf{q}}\right)d\vec{\mathbf{r}}'\right]\Pi\left(\frac{|\vec{\mathbf{q}}|}{q_{\max}}\right) \times\exp\left(-2\pi i\vec{\mathbf{r}}\,\vec{\mathbf{q}}\right)d\vec{\mathbf{q}}. \tag{39}$$

Reordering terms, the above equation becomes:

$$P_F\left(\vec{\mathbf{r}}\right) = \int P\left(\vec{\mathbf{r}}'\right)\mathbb{F}\left\{\Pi\left\{\vec{\mathbf{r}}-\vec{\mathbf{r}}'\right\}\right\}d\vec{\mathbf{r}}', \tag{40}$$

where $\mathbb{F}\left\{\Pi\left\{\vec{\mathbf{r}}-\vec{\mathbf{r}}'\right\}\right\}$ is the Fourier transform of the filter with respect to the relative vector $\vec{\mathbf{r}}-\vec{\mathbf{r}}'$:

$$\mathbb{F}\left\{\Pi\left\{\vec{\mathbf{r}}-\vec{\mathbf{r}}'\right\}\right\} = \int\Pi\left(\frac{|\vec{\mathbf{q}}|}{q_{max}}\right)\exp\left[-2\pi i\left(\vec{\mathbf{r}}-\vec{\mathbf{r}}'\right)\vec{\mathbf{q}}\right]d\vec{\mathbf{q}}. \tag{41}$$

It is important to note that Eq. (40) is the 3D convolution (in real-space) of the true diffusion propagator with the Fourier transform of the filter, which can be rewritten in the compact notation:

$$P_F\left(\vec{\mathbf{r}}\right) = P\left(\vec{\mathbf{r}}'\right)\otimes\mathbb{F}\left\{\Pi\left\{\vec{\mathbf{r}}-\vec{\mathbf{r}}'\right\}\right\}. \tag{42}$$

In order to compute $\mathbb{F}\{\Pi\}$ it is convenient to return to the spherical coordinates, in which Eq. (41) can be written as

$$\mathbb{F}\left\{\Pi\left\{\vec{\mathbf{R}}\right\}\right\} = \oint_{\Omega}\int_{0}^{\infty}\Pi\left(\frac{q}{q_{max}}\right)\exp\left[-2\pi iqR\hat{\mathbf{R}}\hat{\mathbf{q}}\right]q^2dqd\hat{\mathbf{q}}, \tag{43}$$

where R and $\hat{\mathbf{R}}$ are the length and unit vector of the relative vector $\vec{\mathbf{R}}=\vec{\mathbf{r}}-\vec{\mathbf{r}}'$. In view of the plane wave expansion

$$\exp(-2\pi iqR\hat{\mathbf{R}}\hat{\mathbf{q}}) = 4\pi\sum_{l=0}^{\infty}\sum_{m=-l}^{l}(-i)^l j_l(2\pi qR)Y_{lm}(\hat{\mathbf{R}})Y_{lm}^*(\hat{\mathbf{q}}), \tag{44}$$

Eq. (43) becomes

$$\mathbb{F}\left\{\Pi\left\{\vec{\mathbf{R}}\right\}\right\} = 4\pi\sum_{l=0}^{\infty}\sum_{m=-l}^{l}(-i)^l Y_{lm}\left(\hat{\mathbf{R}}\right)I_l(\mathrm{R})\left[\oint_{\Omega}Y_{lm}^*(\hat{\mathbf{q}})d\hat{\mathbf{q}}\right] \tag{45}$$

where,

$$I_l(R) = \int_0^{q_{max}} j_l(2\pi qR)q^2dq. \tag{46}$$

Taking into account the orthogonality condition of the spherical harmonic basis (see Eq. (9)) and considering that $1=2\pi^{1/2}Y_{00}(\hat{\mathbf{q}})$, the integral in brackets in Eq. (45) can be evaluated as:

$$\oint_{\Omega}Y_{lm}^*(\hat{\mathbf{q}})d\hat{\mathbf{q}} = 2\pi^{1/2}\delta_{l0}\delta_{m0}, \tag{47}$$

The above result give rise to a massive reduction of calculus in Eq. 45 due to the fact that only the term $l=0$ persists in the series.

As a result, inserting Eq. 47 into Eq. 45 we obtain:

$$\mathbb{F}\left\{\Pi\left\{\vec{\mathbf{R}}\right\}\right\} = 4\pi I_0(R) = 4\pi\int_0^{q_{max}} j_0(2\pi qR)q^2dq. \tag{48}$$

The above integral can be evaluated and it is given by

$$\mathbb{F}\left\{\Pi\left\{\vec{\mathbf{R}}\right\}\right\} = 4\pi\frac{\sin(2\pi q_{max}R) - 2\pi q_{max}R\cos(2\pi q_{max}R)}{(2\pi R)^3}. \quad (49)$$

Appendix B. Far-field pattern

The truncated wave equation in the far-field limit becomes (see Appendix E for full details):

$$\exp(-2\pi i\rho q\hat{\mathbf{r}}\,\hat{\mathbf{q}}) \approx \frac{2}{q\rho}\sum_{l=0}^{N}\sum_{m=-l}^{l}(-i)^l\sin\left(2\pi q\rho - \frac{\pi l}{2}\right)Y_{lm}(\hat{\mathbf{r}})Y_{lm}^*(\hat{\mathbf{q}}). \quad (50)$$

The far-field limit was defined by means of the following relationship $\rho q \gg N(N+1)/2\pi$. So, insofar as $q\to 0+$ the above expansion is valid only for $\rho\to\infty$. The integral in q-space given by Eq. 1 is defined from 0 to infinity, therefore, we can only accurately compute its far-field pattern in the limit $\rho\to\infty$. Inserting Eq. 50 into Eq. 1 the far-field diffusion propagator P_{FF} can be written as:

$$P_{FF}(\rho,\hat{\mathbf{r}}) \approx \sum_{l=0}^{N}\sum_{m=-l}^{l}Y_{lm}(\hat{\mathbf{r}})\oint_{\Omega}Y_{lm}^*(\hat{\mathbf{q}})I(\rho,\hat{\mathbf{q}})d\hat{\mathbf{q}}, \quad (51)$$

with

$$I(\rho,\hat{\mathbf{q}}) = \lim_{\Delta q\to 0+}\frac{2}{\rho}\int_{\Delta q}^{\infty}E(q,\hat{\mathbf{q}})\sin(2\pi q\rho)qdq. \quad (52)$$

In the last step we have used the fact that $\sin(2\pi q\rho - \pi l/2) = (-1)^{1/2}\sin(2\pi q\rho)$ and $(-\mathrm{i})^l = (-1)^{1/2}$ for even values of l.

Inserting Eq. (3) into Eq. (52), it can be evaluated as

$$I(\rho,\hat{\mathbf{q}}) = \frac{1}{[4\pi D(\hat{\mathbf{q}})t]^{3/2}}\exp\left[-\frac{\rho^2}{4D(\hat{\mathbf{q}})t}\right]. \quad (53)$$

This equation can be expanded in terms of spherical harmonics as follows:

$$I(\rho,\hat{\mathbf{q}}) \approx \sum_{l'=0}^{N}\sum_{m'=-l'}^{l'}c_{l'm'}Y_{l'm'}(\hat{\mathbf{q}}), \quad (54)$$

where in general the coefficients $c_{l'm'}$ depend on ρ and t. Inserting the above expansion into Eq. (51), and considering the orthogonality condition of the spherical harmonics given by Eq. (9), the far-field propagator becomes

$$P_{FF}(\rho,\hat{\mathbf{r}}) \approx \sum_{l=0}^{N}\sum_{m=-l}^{l}c_{lm}Y_{lm}(\hat{\mathbf{r}}). \quad (55)$$

From this result can be inferred that the effect of the spherical harmonic inversion given by Eq. (51) is to transform the function I from q-space to real-space, i.e., $P_{FF}(\rho,\hat{\mathbf{r}}) = I(\rho,\hat{\mathbf{r}})$. Consequently, we obtain

$$P_{FF}(\rho,\hat{\mathbf{r}}) \approx \frac{1}{[4\pi D(\hat{\mathbf{r}})t]^{3/2}}\exp\left[-\frac{\rho^2}{4D(\hat{\mathbf{r}})t}\right]. \quad (56)$$

Appendix C. Evaluation of the radial integrals

The radial integral in Eq. (19) can be analytically evaluated and it is given by

$$\int_0^{\infty}\rho^{l+n}{}_1F_1\left(\frac{l+3}{2};l+\frac{3}{2};-\frac{\rho^2}{4D(\hat{\mathbf{q}})t}\right)d\rho = \frac{2^{l+n}(D(\hat{\mathbf{q}})t)^{\frac{1}{2}(l+n+1)}\Gamma(l+\frac{3}{2})\Gamma(1-\frac{n}{2})\Gamma[\frac{1}{2}(l+n+1)]}{\Gamma(\frac{l+3}{2})\Gamma[\frac{1}{2}(l-n+2)]}$$

This result is general and valid for $n=0, 1$. Inserting the above result into Eq. (19) we obtain:

$$\Phi_{l,n}(\hat{\mathbf{q}}) = \frac{\Gamma(1-\frac{n}{2})\Gamma[\frac{1}{2}(l+n+1)]}{2^{3-n}\pi^{3/2}\Gamma[\frac{1}{2}(l-n+2)][D(\hat{\mathbf{q}})t]^{1-\frac{n}{2}}}, \quad (58)$$

with the following particular solutions

$$\Phi_{l,0}(\hat{\mathbf{q}}) = \frac{\Gamma(\frac{l+1}{2})}{2^3\pi^{3/2}\Gamma(\frac{l}{2}+1)D(\hat{\mathbf{q}})t}, \ (for\, n=0), \quad (59)$$

and

$$\Phi_{l,1}(\hat{\mathbf{q}}) = \frac{\Gamma(\frac{1}{2})\Gamma(\frac{l}{2}+1)}{4\pi^{3/2}\Gamma(\frac{l+1}{2})[D(\hat{\mathbf{q}})t]^{1/2}}, \ (for\, n=1). \quad (60)$$

A different type of solution is obtained for the case $n=2$. In such a situation we cannot obtain a general solution to Eq. (19) as a function of l. However, for each particular value of l it admits a solution with the following general form:

$$\Phi_{l,2}(\hat{\mathbf{q}}) = \frac{4}{\pi}\left\{g_l\left[\kappa + \log\left(\frac{1}{D(\hat{\mathbf{q}})t}\right)\right] - h_l\right\} \quad (61)$$

where κ denotes the Euler's constant, $\kappa \approx 0.577216$. The values obtained for the coefficients g_l and h_l for the specific values of $l=0$, 2, 4, ..., 14 are listed in Table 1.

Appendix D. Near-field pattern and the return to the origin probability

In previous subsections the far-field pattern of the diffusion propagator was derived; to complete the developed theory in this appendix we study the near-field pattern. The diffusion propagator evaluated at infinitesimal values of ρ does not provides sufficient information to infer the 3D tissue microstructure because in this limit it is "quasi-isotropic." In contrast, a useful quantity derived from the near-field limit can be computed, namely the return-to-the-origin (RTO) probability (Mitra et al., 1995), which is defined by the following limit $\mathrm{RTO} = \lim_{\rho\to 0}P\left(\rho,\vec{\mathbf{r}}\right)$. This quantity measures the degree of restriction for the diffusing species and it has been employed as a scalar index for mapping and characterizing the anisotropy of the diffusion process in different fibrous tissues (Helmer et al., 2003; Meiler et al., 1998).

The RTO probability can be computed from Eq. (1), and it is given by

$$\mathrm{RTO} = \lim_{\rho\to 0}\oint_{\Omega}\int_0^{\infty}E(q,\hat{\mathbf{q}})\exp(-2\pi i\rho q\hat{\mathbf{r}}\hat{\mathbf{q}})q^2dqd\hat{\mathbf{q}} \quad (62)$$

In the near-field limit the wave equation term becomes:

$$\lim_{\rho\to 0}\exp(-2\pi i\rho q\hat{\mathbf{r}}\hat{\mathbf{q}}) = 2\pi^{1/2}Y_{00}^*(\hat{\mathbf{q}}) = 1. \quad (63)$$

The notation used in the above equation is convenient to evaluate the integral given by Eq. (62) in a direct way. Inserting Eq. (63) into Eq. (62) we obtain

$$\mathrm{RTO} = 2\pi^{1/2} \oint_{\Omega} S(\hat{\mathbf{q}}) Y_{00}^{*}(\hat{\mathbf{q}}) d\hat{\mathbf{q}}, \tag{64}$$

where

$$S(\hat{\mathbf{q}}) = \int_{0}^{\infty} E(q, \hat{\mathbf{q}}) q^2 dq. \tag{65}$$

In line with the DOT formalism that assumes a mono-exponential model (see Eq. (3)), Eq. (65) can be evaluated as

$$S(\hat{\mathbf{q}}) = \int_{0}^{\infty} \exp\left[-4\pi^2 t D(\hat{\mathbf{q}}) q^2\right] q^2 dq = \frac{1}{32\pi^{5/2}[tD(\hat{\mathbf{q}})]^{3/2}} \tag{66}$$

Inserting the above result into Eq. (64) we get

$$\mathrm{RTO} = \frac{1}{(4\pi)^2 t^{3/2}} \oint_{\Omega} D(\hat{\mathbf{q}})^{-3/2} Y_{00}^{*}(\hat{\mathbf{q}}) d\hat{\mathbf{q}} \tag{67}$$

Considering the following spherical harmonic expansion

$$D(\hat{\mathbf{q}})^{-3/2} = \sum_{l'=0}^{\infty} \sum_{m'=-l'}^{l'} b_{l'm'} Y_{l'm'}(\hat{\mathbf{q}}), \tag{68}$$

and taking into account the result given in Eq. (9), Eq. (67) becomes

$$\mathrm{RTO} = \frac{b_{00}}{(4\pi)^2 t^{3/2}}. \tag{69}$$

Notice that RTO only depends on the first term of the expansion given in Eq. (68). This term describes the isotropic component of the $D(\hat{\mathbf{q}})^{-3/2}$ profile, which depends on the minimum value of the profile. In the limit case of isotropic free diffusion we obtain $D = b_{00} Y_{00} = b_{00}/2\pi^{1/2}$. Hence, Eq. (69) becomes

$$\mathrm{RTO} \approx \frac{1}{(4\pi t D)^{3/2}}, \tag{70}$$

which agrees with the result previously developed by (Mitra et al., 1995).

The rotationally invariant measure given by Eq. (69) could be incorporated as a new parameter derived from DOT to quantify the structural changes occurring in several pathologies. In the original DOT article, other measures such as the anisotropy from variance and entropy (Ozarslan et al., 2006) were proposed that will not be analyzed in this work.

Appendix E. Near- and far-field limits of the plane wave

The spherical Bessel function of the first kind is defined by (Spiegel and Liu, 1968)

$$j_l(x) = \sqrt{\frac{\pi}{2x}} J_{l+1/2}(x), \tag{71}$$

where J_l is a Bessel function of the first kind. Asymptotic forms for the Bessel functions are

$$J_k(x) \cong \frac{1}{\Gamma(k+1)} \left(\frac{x}{2}\right)^k, \; x \ll \sqrt{k+1}$$
$$J_k(x) \cong \sqrt{\frac{2}{\pi x}} \cos(x - k\pi/2 - \pi/4), \; x \gg |k^2 - 1/4| \tag{72}$$

From the above expressions can be inferred the asymptotic behaviour for the spherical Bessel function as follows:

$$j_l(x) \cong \frac{1}{\Gamma\left(l + \frac{3}{2}\right)} \frac{\pi^{1/2}}{2} \left(\frac{x}{2}\right)^l, \; x \ll \sqrt{l + 3/2}$$
$$j_l(x) \cong \frac{1}{x} \sin\left(x - \frac{\pi l}{2}\right), \; x \gg l(l+1) \tag{73}$$

where was considered that $k = l + 1/2$. Therefore, it is possible to infer the behaviour of the truncated plane wave (see Eq. (4)) in the near-field limit (i.e., $\rho q \ll \sqrt{N + 3/2}/2\pi$):

$$\exp(-2\pi i \rho q \hat{\mathbf{r}}\hat{\mathbf{q}}) \approx 2\pi^{3/2} \sum_{l=0}^{N} \sum_{m=-l}^{l} (-i)^l \frac{(\pi q \rho)^l}{\Gamma\left(l + \frac{3}{2}\right)} Y_{lm}(\hat{\mathbf{r}}) Y_{lm}^{*}(\hat{\mathbf{q}}). \tag{74}$$

Similarly, in the far-field limit (i.e., $\rho q \gg N(N+1)/2\pi$) the plane wave becomes

$$\exp(-2\pi i \rho q \hat{\mathbf{r}}\hat{\mathbf{q}}) \approx \frac{2}{q\rho} \sum_{l=0}^{N} \sum_{m=-l}^{l} (-i)^l \sin\left(2\pi q\rho - \frac{\pi l}{2}\right) Y_{lm}(\hat{\mathbf{r}}) Y_{lm}^{*}(\hat{\mathbf{q}}). \tag{75}$$

Appendix F. Supplementary data

Supplementary data associated with this article can be found, in the online version, at doi:10.1016/j.neuroimage.2009.09.067.

References

Alexander, D.C., 2005. Multiple-fiber reconstruction algorithms for diffusion MRI. Ann. N.Y. Acad. Sci. 1064, 113–133.

Anderson, A.W., 2005. Measurement of fiber orientation distributions using high angular resolution diffusion imaging. Magn. Reson. Med. 54, 1194–1206.

Arnoldus, H.F., Li, X., Shu, J., 2008. Subwavelength displacement of the far-field image of a radiating dipole. Opt. Lett. 33, 1446–1448.

Assaf, Y., Basser, P.J., 2005. Composite hindered and restricted model of diffusion (CHARMED) MR imaging of the human brain. Neuroimage 27, 48–58.

Basser, P.J., Mattiello, J., LeBihan, D., 1994. MR diffusion tensor spectroscopy and imaging. Biophys. J. 66, 259–267.

Behrens, T.E., Johansen-Berg, H., Woolrich, M.W., Smith, S.M., Wheeler-Kingshott, C.A., Boulby, P.A., Barker, G.J., Sillery, E.L., Sheehan, K., Ciccarelli, O., Thompson, A.J., Brady, J.M., Matthews, P.M., 2003. Non-invasive mapping of connections between human thalamus and cortex using diffusion imaging. Nat. Neurosci. 6, 750–757.

Behrens, T.E., Berg, H.J., Jbabdi, S., Rushworth, M.F., Woolrich, M.W., 2007. Probabilistic diffusion tractography with multiple fibre orientations: what can we gain? Neuroimage 34, 144–155.

Bracewell, R.N., 1986. The Fourier Transform and Its Applications. (McGraw-Hill, 1965, 2nd ed. 1978, revised 1986).

Brehm, M., Schliesser, A., Cajko, F., Tsukerman, I., Keilmann, F., 2008. Antenna-mediated back-scattering efficiency in infrared near-field microscopy. Opt. Express 16, 11203–11215.

Callaghan, P.T., 1991. Principles of Nuclear Magnetic Resonance Microscopy. Clarendon Press, Oxford.

Canales-Rodríguez, E.J., Melie-García, L., Iturria-Medina, Y., Martínez-Montes, E., Alemán-Gómez, Y., Lin, C.P., 2008. Inferring multiple maxima in intravoxel white matter fiber distribution. Magn. Reson. Med. 60, 616–630.

Canales-Rodríguez, E.J., Melie-García, L., Iturria-Medina, Y, 2009. Mathematical description of q-space in spherical coordinates: exact q-Ball imaging. Magn. Reson. Med. 61 (6), 1350–1367 2009 Jun.

Descoteaux, M., Angelino, E., Fitzgibbons, S., Deriche, R., 2006a. A Fast and Robust ODF Estimation Algorithm in Q-Ball Imaging. International Symposium on Biomedical Imaging: From Nano to Macro (ISBI'06), pp. 81–84. April.

Descoteaux, M., Angelino, E., Fitzgibbons, S., Deriche, R., 2006b. Apparent diffusion coefficients from high angular resolution diffusion imaging: estimation and applications. Magn. Reson. Med. 56, 395–410.

Frank, L.R., 2001. Anisotropy in high angular resolution diffusion-weighted MRI. Magn. Reson. Med. 45, 935–939.

Frank, L.R., 2002. Characterization of anisotropy in high angular resolution diffusion-weighted MRI. Magn. Reson. Med. 47, 1083–1099.

Gilbert, R.J., Magnusson, L.H., Napadow, V.J., Benner, T., Wang, R., Wedeen, V.J., 2006. Mapping complex myoarchitecture in the bovine tongue with diffusion-spectrum magnetic resonance imaging. Biophys. J. 91, 1014–1022.

Haydon, DA, Urban, BW., 1985. The admittance of the squid giant axon at radio frequencies and its relation to membrane structure. J. Physiol. 360, 275–291 Mar.

Helmer, K.G., Meiler, M.R., Sotak, C.H., Petruccelli, J.D., 2003. Comparison of the return-to-the-origin probability and the apparent diffusion coefficient of water as indicators of necrosis in RIF-1 tumors. Magn. Reson. Med. 49, 468–478.
Hess, C.P., Mukherjee, P., Han, E.T., Xu, D., Vigneron, D.B., 2006. Q-ball reconstruction of multimodal fiber orientations using the spherical harmonic basis. Magn. Reson. Med. 56, 104–117.
Hosey, T., Williams, G., Ansorge, R., 2005. Inference of multiple fiber orientations in high angular resolution diffusion imaging. Magn. Reson. Med. 54, 1480–1489.
Iturria-Medina, Y., Sotero, R.C., Canales-Rodríguez, E.J., Alemán-Gómez, Y., Melie-García, L., 2008. Studying the human brain anatomical network via diffusion-weighted MRI and graph theory. Neuroimage 40, 1064–1076.
Jansons, K.M., Alexander, D.C., 2003. Persistent angular structure: new insights from diffusion MRI data. Inverse Problems 19, 1031–1046.
Jones, D.K., Horsfield, M.A., Simmons, A., 1999. Optimal strategies for measuring diffusion in anisotropic systems by magnetic resonance imaging. Magn. Reson. Med. 42, 515–525.
LeBihan, D., 2003. Looking into the functional architecture of the brain with diffusion MRI. Nat. Rev. Neurosci. 4, 469–480.
Lin, C.P., Wedeen, V.J., Chen, J.H., Yao, C., Tseng, W.Y., 2003. Validation of diffusion spectrum magnetic resonance imaging with manganese-enhanced rat optic tracts and ex vivo phantoms. Neuroimage 19, 482–495.
Liu, C., Bammer, R., Acar, B., Moseley, M.E., 2004. Characterizing non-Gaussian diffusion by using generalized diffusion tensors. Magn. Reson. Med. 51, 924–937.
Liu, C., Bammer, R., Moseley, M.E., 2005. Limitations of apparent diffusion coefficient-based models in characterizing non-gaussian diffusion. Magn. Reson. Med. 54, 419–428.
Meiler, M., Helmer, K.G., Sotak, C.H., 1998. Return-to-the-origin probability imaging as indicator of localnecrosis. Bioengineering Conference. Proceedings of the IEEE 24th Annual Northeast; Hershey, PA, USA, pp. 72–73.
Melie-García, L., Canales-Rodríguez, E.J., Alemán-Gómez, Y., Lin, C.P., Iturria-Medina, Y., Valdés-Hernández, P.A., 2008. A Bayesian framework to identify principal intravoxel diffusion profiles based on diffusion-weighted MR imaging. Neuroimage 42, 750–770.
Mitra, P.P., Latour, L.L., Kleinberg, R.L., Sotak, C.H., 1995. Pulsed-field-gradient NMR measurements of restricted diffusion and the return-to-the-origin probability. J. Magn. Reson., Series A 114, 47–58.
Ozarslan, E., Shepherd, T.M., Vemuri, B.C., Blackband, S.J., Mareci, T.H., 2006. Resolution of complex tissue microarchitecture using the diffusion orientation transform (DOT). Neuroimage 31, 1086–1103.
Parker, G.J., Haroon, H.A., Wheeler-Kingshott, C.A., 2003. A framework for a streamline-based probabilistic index of connectivity (PICo) using a structural interpretation of MRI diffusion measurements. J. Magn. Reson. Imaging 18, 242–254.
Ramírez-Manzanares, A., Rivera, M., Vemuri, B.C., Carney, P., Mareci, T., 2007. Diffusion basis functions decomposition for estimating white matter intravoxel fiber geometry. IEEE Trans. Med. Imaging 26, 1091–1102.
Schröder, JM, Bohl, J, von Bardeleben, U., 1988. Changes of the ratio between myelin thickness and axon diameter in human developing sural, femoral, ulnar, facial, and trochlear nerves. Acta Neuropathol. 76 (5), 471–483.
Soderman, O., Jonsson, B., 1995. Restricted diffusion in cylindrical geometry. J. Magn. Reson., Series A 117, 94–97.
Spiegel, M.R. and Liu, J., 1968. Mathematical Handbook of Formulas and Tables. Schaum's Outlines.
Tournier, J.D., Calamante, F., Connelly, A., 2007. Robust determination of the fibre orientation distribution in diffusion MRI: non-negativity constrained super-resolved spherical deconvolution. Neuroimage 35, 1459–1472.
Tournier, J.D., Yeh, C.H., Calamante, F., Cho, K.H., Connelly, A., Lin, C.P., 2008. Resolving crossing fibres using constrained spherical deconvolution: validation using diffusion-weighted imaging phantom data. Neuroimage 42, 617–625.
Tuch, D.S., 2004. Q-ball imaging. Magn. Reson. Med. 52, 1358–1372.
Tuch, D.S., Reese, T.G., Wiegell, M.R., Makris, N., Belliveau, J.W., Wedeen, V.J., 2002. High angular resolution diffusion imaging reveals intravoxel white matter fiber heterogeneity. Magn. Reson. Med. 48, 577–582.
Wedeen, V.J., Hagmann, P., Tseng, W.Y., Reese, T.G., Weisskoff, R.M., 2005. Mapping complex tissue architecture with diffusion spectrum magnetic resonance imaging. Magn. Reson. Med. 54, 1377–1386.
Zhang, S., Jin, J., 1996. Computation of Special Functions, Har/Dis edition. Wiley-Interscience. (July 12, 1996).

5.3 Deconvolution in diffusion spectrum imaging

Autores: Erick J Canales-Rodríguez, Yasser Iturria-Medina, Yasser Alemán-Gómez, Lester Melie-García

Título: *Deconvolution in diffusion spectrum imaging*.

Revista: *Neuroimage*

Año y volumen: 2010, Vol 50, 1, 136-149

Factor de impacto (en el año de publicación): 5.93

La técnica propuesta también se presentó y se extendió en trabajos presentados en los siguientes congresos internacionales:

Autores: Erick J Canales-Rodríguez, Yasser Iturria-Medina, Yasser Alemán-Gómez, Lester Melie-García

Título: *The deconvolution of finite q-space sampling effects in diffusion spectrum imaging*

Conferencia (Póster): 16th Annual Meeting of the Organization for Human Brain Mapping, June 6-10, 2010, Barcelona, Spain.

Autores: Erick J Canales-Rodríguez, Lester Melie-García, Yasser Iturria-Medina, Yasser Alemán-Gómez.

Título: *Evaluation of the Deconvolved Diffusion Spectrum Imaging Technique.*

Conferencia (Presentación oral y abstract): IEEE International Symposium on Biomedical Imaging (ISBI 2012), workshop on High Angular Resolution Diffusion MRI Reconstruction Techniques, 2-5 May 2012, Barcelona, Spain.

NeuroImage 50 (2010) 136–149

Contents lists available at ScienceDirect

NeuroImage

journal homepage: www.elsevier.com/locate/ynimg

Deconvolution in diffusion spectrum imaging

Erick Jorge Canales-Rodríguez [a,b,*], Yasser Iturria-Medina [c], Yasser Alemán-Gómez [b,d], Lester Melie-García [c]

[a] Benito Menni Complex Assistencial en Salut Mental, Barcelona, Spain
[b] Centro de Investigación Biomédica en Red de Salud Mental (CIBERSam), Spain
[c] Neuroimaging Department, Cuban Neuroscience Center, Havana, Cuba
[d] Laboratorio de Imagen Médica, Unidad de Medicina y Cirugía Experimental, Hospital General Universitario Gregorio Marañon, Madrid, Spain

ARTICLE INFO

Article history:
Received 3 September 2009
Revised 19 November 2009
Accepted 24 November 2009
Available online 3 December 2009

Keywords:
Diffusion spectrum imaging (DSI)
Diffusion MRI
Orientational distribution function (ODF)
Brain tissues

ABSTRACT

Diffusion spectrum magnetic resonance imaging (DSI) allows the estimation of the displacement probability density function (*pdf*) of water molecules, which contain valuable information about the microgeometry of the medium where the diffusion process occurs. It provides a more general approach to disentangle complex fiber structures in biological tissues because it does not assume any particular model of diffusion; even so, it has a number of limitations that remain unstudied. For instance, the theoretical model used to compute the displacement *pdf* is based on a Fourier transformation defined in the whole measurement space; however, in practice, it is computed using discrete signals with a finite support. As a consequence, the displacement *pdf* obtained from the experiments is the convolution between the true *pdf* and a point spread function (PSF) that completely depends on the experimental sampling scheme. In this work, a general framework to rectify and decontaminate the displacement *pdf* reconstructed from DSI is introduced. This framework is based on model-free deconvolution techniques that allow obtaining clearer and sharper DSI estimates. The method was tested in synthetic data as well as in real data measured from a healthy human volunteer. The results demonstrated that the angular resolution of DSI can be increased, potentially revealing new real fiber components and reducing both the artefactual peaks and the uncertainty of the local diffusion orientational distribution. Furthermore, the deconvolution process provides scalar maps of quantities derived from the propagator, such as the zero displacement probability, with higher tissue contrast.

Introduction

Diffusion magnetic resonance imaging (dMRI) is a relatively new MRI modality that is sensitive to the natural random motion of water molecules. Owing to the microscopic length scale of diffusion in biological tissues, dMRI can reveal histological architecture irresolvable by previous imaging methods (Basser et al., 1994; Callaghan, 1991; LeBihan, 2003). In the last years, this noninvasive technique has provided the main tool to study the spatial order in living organs such as spine, skeletal muscle, heart, tongue, and the white matter of the brain (Basser and Pierpaoli, 1996; Tuch et al., 2003; Wedeen et al., 2005).

The cerebral white matter consists of densely packed nerve fibers called axons. Usually, the axons are surrounded by an electrically insulating material composed of lipids and proteins that form a layer known as the myelin sheath. These packed axons form barriers that restrict the molecular motion. As a result, water diffusion within the white matter is highly anisotropic, i.e., it diffuses preferentially along axonal fiber directions (Frank, 2002).

The imaging modality most used to study this phenomenon is diffusion tensor imaging (DTI), a dMRI technique that reconstructs at each voxel of the brain a second-rank self-diffusion tensor (Basser et al., 1994; Pierpaoli et al., 1996). The main advantage of this model is its easy implementation and interpretation. The principal eigenvector of the reconstructed tensor is oriented along the average direction of fibers (Basser, 1997). The diffusion tensor model has been used to reconstruct connectivity pathways within the central nervous system (Behrens et al., 2003, 2007; Iturria-Medina et al., 2007; Parker et al., 2002b, 2003), which has important implications for many aspects of neuroscience (for more details, see Behrens and Johansen-Berg, 2005; Ciccarelli et al., 2003; Hagmann et al., 2008; Iturria-Medina et al., 2008; Johansen-Berg and Behrens, 2006; Parker et al., 2002a). However, there are many brain regions where the tensor model is inadequate. In areas where many fibers converge, diverge, or cross, many voxels can contain two or more distinct fiber directions. In this situation, the fiber direction predicted by the tensor model will not correspond to any of the true fiber directions. Nevertheless, it has been showed that, if the tensor model is constrained to have a cylindrical symmetry, the predicted fiber direction will be oriented along the dominant fiber (Canales-Rodríguez et al., 2008).

* Corresponding author. Benito Menni, Complex Assistencial en Salut Mental; C/ Dr. Antoni Pujadas, 38, 08830 Sant Boi de Llobregat, Barcelona, Spain. Fax: +94 93 640 02 68.
E-mail addresses: ejcanalesr@gmail.com, ecanales@hospitalbenitomenni.org (E.J. Canales-Rodríguez).

1053-8119/$ – see front matter © 2009 Elsevier Inc. All rights reserved.
doi:10.1016/j.neuroimage.2009.11.066

To avoid the limitations of DTI, new physical models and reconstruction techniques for estimating multiple fibers configurations have been developed (Alexander, 2005; Anderson, 2005; Behrens et al., 2007; Canales-Rodríguez et al., 2009; Descoteaux et al., 2007; Liu et al., 2004; Melie-García et al., 2008; Özarslan et al., 2006; Ramírez-Manzanares et al., 2007; Tournier et al., 2004; Tuch et al., 2002; Tuch, 2004; Wedeen et al., 2005). The use of these methods becomes important in white matter regions with fiber crossings and, in particular, in areas where major fiber pathways obscure the presence of the smaller ones, for example, the lateral motor pathway is obscured by the third (lateral) branch of the superior longitudinal fasciculus (SLF), and the first portion of SLF is obscured by the medial corticospinal fibers (Behrens et al., 2007).

Among the above techniques, diffusion spectrum imaging (DSI) (also called q-space imaging) provides the more general approach to disentangle complex fiber structures because it does not assume any particular model for the diffusion process (Wedeen et al., 2005). DSI computes the displacement probability density function of water molecules (also termed diffusion spectrum, or diffusion propagator) that provide valuable information about the microgeometry of the medium where the diffusion process occurs. In practice, the diffusion propagator is computed at each voxel by taking the discrete or fast Fourier transform (FFT) of the modulus of the normalized signal measured on a three-dimensional (3D) Cartesian grid in q-space (Tuch, 2002; Wedeen et al., 2005).

DSI has demonstrated the capability to resolve fiber crossings within neural structures (Habas and Cabanis, 2007; Wedeen et al., 2005) and structurally complex muscular tissues (Gilbert et al., 2008, 2006). This is exemplified by the reconstruction of long association fiber pathways in monkey cerebral hemispheres, observations that have been supported by comparing with the results of tract-tracing studies using autoradiographic techniques (Schmahmann et al., 2007). Further, it has been used to map regions of fiber crossing not only in cerebral white matter but also in the basis pontis and cerebellar cortices in monkey and human brains, which have been demonstrated in postmortem (Wedeen et al., 2008) and in vivo studies (Granziera et al., 2009). In addition, this technique has been validated in rat optic tracts and capillary phantom models under different configurations (Lin et al., 2003).

Despite its popularity, DSI has some practical limitations. The obstacles include contamination to the phase of the echo signal from biological motion and eddy current distortions caused by the high gradients required to obtain a sufficiently high spatial resolution. Thus, it requires a large amount of experimental data for its practical implementation (Tuch, 2004). In addition, although DSI is based on a 3D Fourier transform defined in the whole q-space, in practice, the propagator is reconstructed using discrete data with a finite support. This fact can considerably affect the quality of the reconstruction in terms of angular resolution. However, to date, this effect remains unstudied.

In this work, we aimed to study the influence of computing the diffusion propagator with the use of signals with a finite support in q-space. To do this, in the Theory section, we will express the reconstructed propagator by means of the convolution between the true propagator and a point spread function (PSF) that completely depends on the experimental sampling scheme. Also, in this part, the PSF corresponding to a typical DSI Cartesian sampling scheme will be derived. This result will allow us to address the problem for estimating clearer and sharper propagators by means of deconvolution methods. Details of the synthetic data generation process will be described in the "Materials and methods" section as well as the data acquisition protocol applied to a healthy human subject. The performance of the deblurring formalism will be evaluated in the Results section. Finally, in the Discussion and Summary sections, the relevant findings, open problems, and contributions of this work will be succinctly described.

Theory

The diffusion propagator $P(\mathbf{r})$ of a normalized dMRI signal $E(\mathbf{q})$, as measured with a standard Stejskal–Tanner (ST) spin-echo pulse sequence (Tanner and Stejskal, 1968), can be recovered via the 3D Fourier transform (Callaghan, 1991)

$$P(\mathbf{r}) = \int_{-\infty}^{\infty} E(\mathbf{q})\exp(-2\pi i\mathbf{r}\mathbf{q})d\mathbf{q}, \tag{1}$$

where $\mathbf{r}$ is the real space vector of molecular displacements, $\mathbf{q}$ is the q-space vector (measurement space) defined as $\mathbf{q}=(\gamma\tau/2\pi)\mathbf{g}$, γ represents the gyromagnetic ratio for the diffusing species (i.e., hydrogen proton in water molecules), $\mathbf{g}$ is the diffusion gradient pulse vector, and τ is the diffusion pulse duration.

In practice, diffusion signals can only be measured out to the maximum experimental q-value ($q_{\max}$) that is determined by the physical properties of the MRI scanner. Therefore, in the typical case of identical symmetrical limits of $\pm q_{\max}$ along each Cartesian axis (Wedeen et al., 2005), Eq. (1) becomes

$$P_M(r_x,r_y,r_z) = \int_{-qmax}^{qmax}\int_{-qmax}^{qmax}\int_{-qmax}^{qmax} E(q_x,q_y,q_z) \exp\left[-2\pi i\left(r_xq_x + r_yq_y + r_zq_z\right)\right]dq_xdq_ydq_z, \tag{2}$$

where $[r_x,r_y,r_z]$ and $[q_x,q_y,q_z]$ are the Cartesian components of the real- and q-space vectors respectively. Note that we introduced the "modified" diffusion propagator P_M to differentiate it from the exact propagator, which was defined in Eq. (1) in the whole q-space.

The above expression is equivalent to multiplying the diffusion signal in Eq. (1) by the following 3D boxcar (or uniform) filter:

$$\begin{aligned}\Pi(q_x,q_y,q_z) &= \Pi(q_x)\Pi(q_y)\Pi(q_z)\\ &= \begin{cases} 1, & |q_x|\le q_{max},\ |q_y|\le q_{max},\ |q_z|\le q_{max},\\ 0, & |q_x| > q_{max},\ |q_y| > q_{max},\ |q_z| > q_{max}.\end{cases}\end{aligned} \tag{3}$$

In a recent work (Canales-Rodríguez et al., 2010), we showed that the effect of computing the diffusion spectrum out to finite q-values is equivalent to convolve the true spectrum with the Fourier transform of the corresponding filter $\mathbb{F}\{\Pi\}$, which can be considered as the point spread function (PSF) of the convolution process (see Appendix A for a detailed demonstration). According to this property, the modified and true propagators are related by

$$P_M = P \otimes \mathbb{F}\{\Pi\{\mathbf{R}\}\}, \tag{4}$$

where $\otimes$ is a convolution operator. The above equation can be interpreted as follows: the modified propagator at a particular point arises from the contribution of the true propagator in all points of the space, their real intensities multiplied by the PSF function $\mathbb{F}\{\Pi\{\mathbf{R}\}\}$ that depends on the distance R and direction $\mathbf{R}$ to the considered point ($\mathbf{R} = R\hat{\mathbf{R}}$).

For the Cartesian boxcar function defined in Eq. (3), the resulting PSF is proportional to the product of three sinc functions (see Appendix B for a detailed description)

$$\mathbb{F}\{\Pi\{\mathbf{R}\}\} = (2q_{max})^3\mathrm{sinc}(2\pi R_xq_{max})\mathrm{sinc}\left(2\pi R_yq_{max}\right)\mathrm{sinc}(2\pi R_zq_{max}), \tag{5}$$

where $[R_x,R_y,R_z]$ are the Cartesian components of $\mathbf{R}$, i.e., $\mathbf{R} = R_x\hat{\mathbf{i}} + R_y\hat{\mathbf{j}} + R_z\hat{\mathbf{k}}$ with $\hat{\mathbf{i}},\hat{\mathbf{j}},\hat{\mathbf{k}}$ denoting the Cartesian unit vectors in real space along the x-, y-, and z-axes, respectively.

The convolution between the true propagator and the PSF produces a blurred propagator with a decreased contrast and a lower angular resolution. Removing the effect of the PSF from the

modified diffusion propagator requires the use of a deconvolution algorithm. The goal of deconvolution is to recreate the image as it existed before the convolution took place, thus creating clearer and sharper images. Thus, our objective was to find the true propagator from the following equation:

$$P_M = P \otimes \mathbb{F}\{\Pi\{\mathbf{R}\}\} + \varepsilon, \tag{6}$$

where ε is the unknown error component due to the experimental noise in our recorded diffusion signal. In the literature there are some well-known algorithms to solve this type of equation. In this work, the accelerated Lucy–Richardson (L–R) method (Biggs and Andrews, 1997; Lucy, 1974; Richardson, 1972) will be used. This algorithm, which derives from Bayes' theorem on conditional probabilities, conserves the constraints on frequency distributions such as normalization and non-negativeness. This iterative method, at each step, increases the likelihood of the observed sample. It is effective when one know the PSF but know little about the additive noise in the image (Hanisch et al., 1997), which is just our case. This algorithm has previously been applied to solve fiber crossing in the human brain using high angular resolution diffusion imaging (HARDI) (Dell'Acqua et al., 2007, 2009). Alternatively, we will also use a blind deconvolution (B-D) algorithm (Stockham et al., 1975), which can be used effectively when no information about the distortion (blurring and noise) is known. This method restores the exact propagator and the PSF simultaneously using an iterative process similar to the L–R algorithm (Biggs and Andrews, 1997).

Materials and methods

Simulated data: local diffusion model

Synthetic data were generated using the multitensor model (Tuch et al., 2002), which allows to consider the presence of several fiber populations inside the voxel. Assuming this model, the expression for the normalized diffusion signal can be expressed by:

$$E(\mathbf{q}) = S(\mathbf{q})/S_0 = \sum_{i=1}^{M} \mathrm{f}_i \exp\left(-b\hat{\mathbf{q}}^{\mathrm{T}}\mathbf{D}^{(i)}\hat{\mathbf{q}}\right), \tag{7}$$

where M is the number of fiber compartments, the diffusion weighting factor b (also known as b-value) is defined as $b = 4\pi^2 tq^2$ with $\mathbf{q} = q\hat{\mathbf{q}}$, the volume fraction of the ith compartment is denoted by f_i, so that $\sum_{i=1}^{M} \mathrm{f}_i = 1$, $\mathbf{D}^{(i)}$ represents the second-order self-diffusion tensor of the ith compartment, S is the measured signal, and S_0 is the signal amplitude in the absence of magnetic field gradients (i.e., $b = 0$). It is assumed that the compartments have equal relaxation rates and water density. In addition, the molecular exchange between compartments is neglected.

The eigenvectors (i.e., $[\mathbf{e}_1,\mathbf{e}_2,\mathbf{e}_3]$) and eigenvalues (i.e., $[\lambda_1,\lambda_2,\lambda_3]$) of each self-diffusion tensor contain information about the fiber orientation and the anisotropy of the diffusion process within each fiber compartment. In this work, we will use the values $\lambda_1 = 1.7\times10^{-3}$ mm^2/s and $\lambda_2 = \lambda_3 = 0.3\times10^{-3}$ mm^2/s, which are typically observed (or estimated) in human brain regions (Pierpaoli and Basser, 1996).

Simulated data generation

To evaluate the effects of the deconvolution in DSI, several synthetic data sets were generated. The diffusion signal was computed from Eq. (7) for different signal-to-noise (SNR) levels. The noise was assumed as Rician distributed (Andersson, 2008) with a standard deviation defined by $\sigma = S_0/\mathrm{SNR}$.

The signals were generated using several fiber geometries. Specifically, the simulation considers two fiber populations with identical volume fractions, where the interfiber angle varies from 30° to 90° in steps of 15°. For each SNR value (i.e., SNR = {10, 15, 20, 30, 50}) and fiber configuration, 100 trials of signals were generated. An additional experiment without noise was also implemented.

All synthetic data were generated using a DSI sampling scheme (Wedeen et al., 2005), which consisted of a keyhole Cartesian acquisition to include the set of points in q-space lying on a $7\times7\times7$ Cartesian grid within a sphere of radius 3.6, for a total of $N = 203$ sampling points. This sampling scheme is equal to the one used in the real data acquisition (see the next subsection). Two experiments were implemented using two different values for the maximum b-value ($b_{\max}$): 9000 and 4000 s/mm^2.

Human brain data

MR experiments were performed on a healthy 24-year-old male volunteer in a 3-T MRI system with a maximum gradient strength of 40 mT/m (Trio, Siemens, Erlangen, Germany). A Siemens eight-channel head array coil was used as a receiver. To reduce the eddy current effect, a twice-refocused balanced spin-echo diffusion echo-planar imaging (EPI) sequence was used. Diffusion images were acquired with the following acquisition parameters: matrix size = 64×64×40; field of view (FOV) = 185×185 mm; pixel spacing = 2.890625/2.890625 mm; slice thickness = 2.9 mm; TR/TE = 6200/118 ms; diffusion time (Δ) and diffusion pulse duration (τ) $\Delta/\tau = 80/35$ ms; maximum b-value = 4000 s/mm^2. The images were measured using 203 diffusion encodings. These encodings are comprised of isotropic 3D grid points in the q-space contained within a sphere with radius 3.6. These data are part of a public database (free for testing) provided by the Advanced Biomedical MRI Lab, National Taiwan University Hospital (for more technical details see: http://dsi-studio.labsolver.org/download-images).

DSI reconstructions

All DSI reconstructions were computed as follows. First, the blurred or modified diffusion propagator was reconstructed at each voxel by taking the 3D FFT of the diffusion signals. The signal is zero-padded before the Fourier transformation to obtain interpolated propagators in real space, which is a commonly used technique associated with FFT (Donnelly and Rust, 2005). This methodology allows computing the propagator on a $35\times35\times35$ 3D Cartesian grid. Second, we denoised the obtained propagator using a statistical thresholding technique. In particular, a gamma distribution was fitted to the resulting 3D image intensities. Only were considered those values within 95% percent confidence intervals. This process allows neglecting all intensities near the noise floor. Third, we computed two different versions of the exact propagator using two different image deconvolution techniques: (1) the L–R method and (2) the B-D method. Finally, from the resulting deconvolved maps, the diffusion orientational distribution function (ODF) was computed via the following line integral (Wedeen et al., 2005):

$$\mathrm{ODF}(\hat{\mathbf{r}}) = \int_0^{\infty} P(\rho,\hat{\mathbf{r}})\rho^2 d\rho, \tag{8}$$

Fig. 1. Evaluation of deconvolution methods in synthetic data generated for two different fiber configurations using a maximum b-value of 9000 s/mm^2. Upper and lower panels show diffusion propagators and their corresponding ODFs computed for two fiber crossings with interfiber angles of 90° and 45°, respectively. (A) Propagator reconstructed using the standard DSI technique. (B) and (C) Deblurred propagators by means of the L–R and B-D deconvolution algorithms, respectively. (D) ODF corresponding to the standard DSI technique (see panel A). (E) and (F) ODFs corresponding to the deconvolved propagators depicted in panels B and C, respectively.

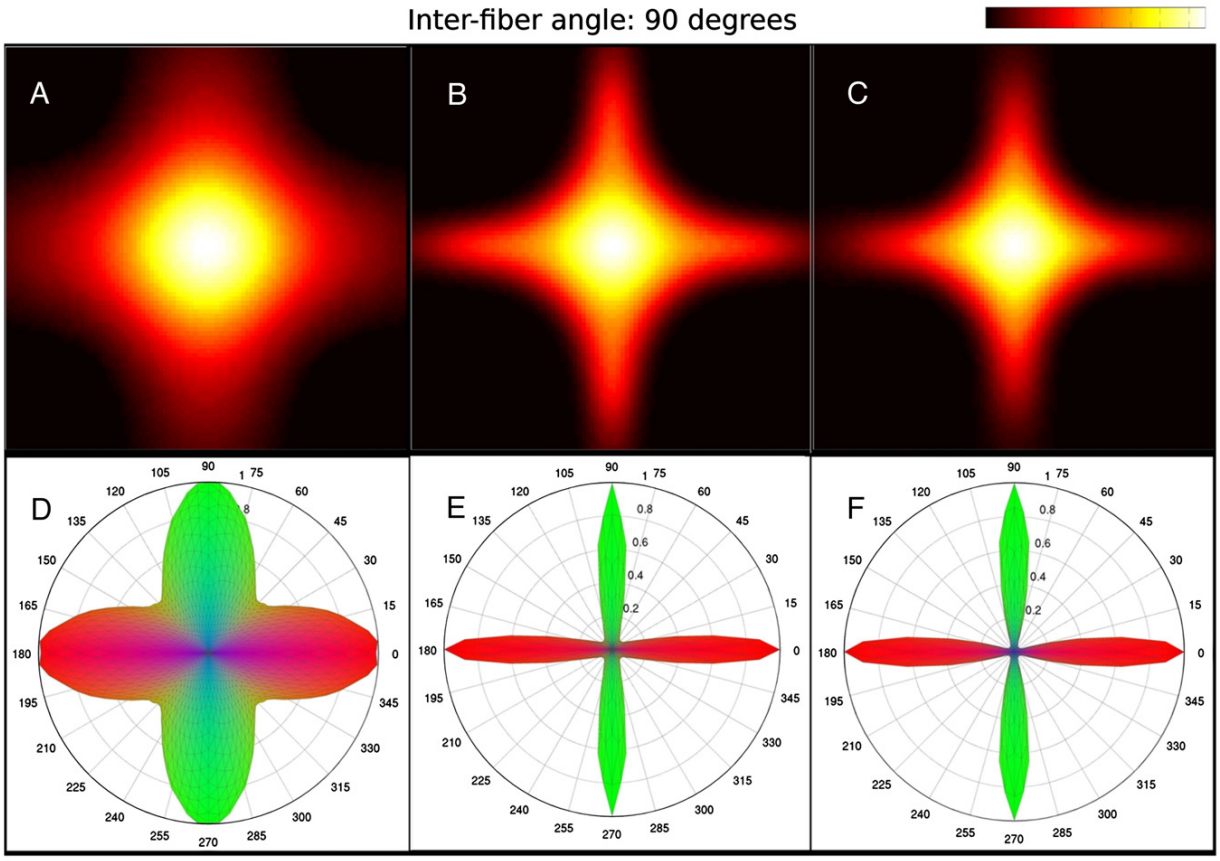
Inter-fiber angle: 90 degrees
A
B
C
D
E
F

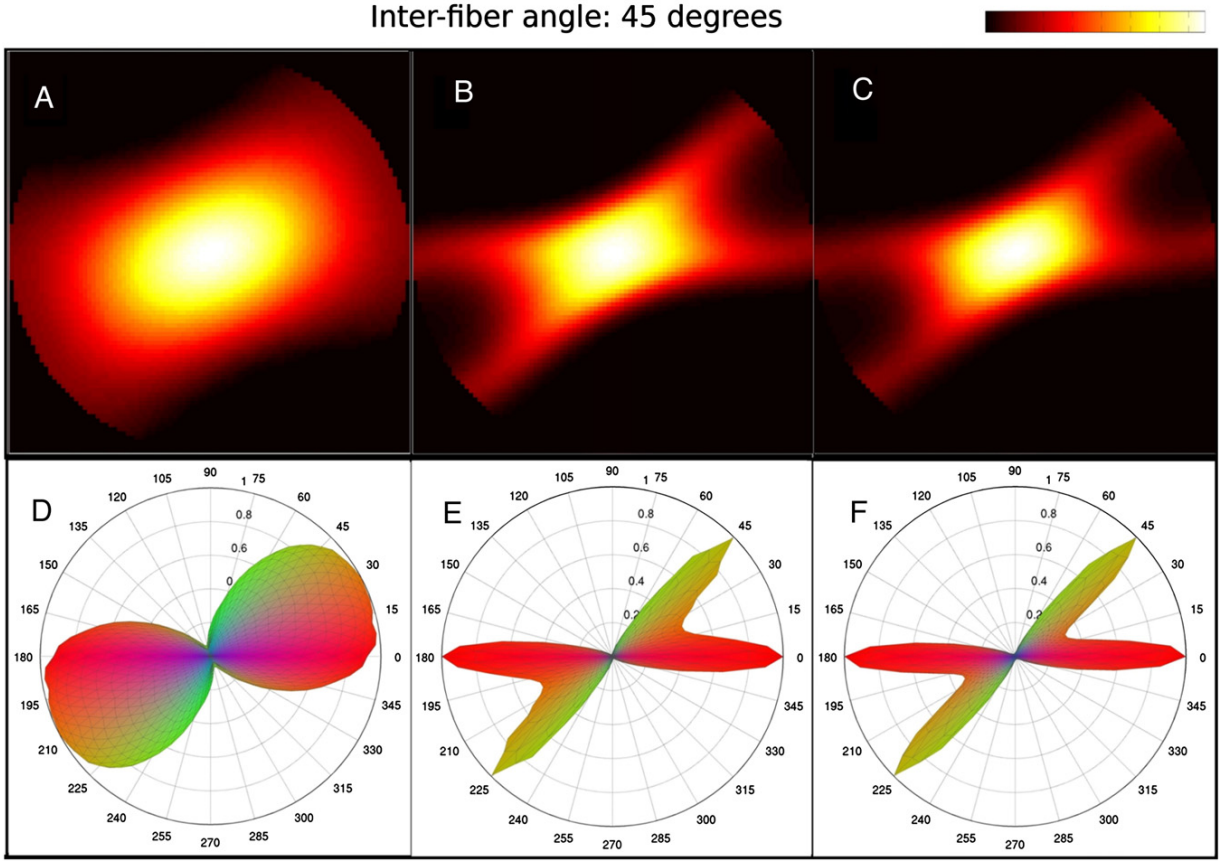
Inter-fiber angle: 45 degrees
A
B
C
D
E
F

where ρ and $\hat{\mathbf{r}}$ are the length and unit vector of $\mathbf{r}$, respectively, i.e., $\mathbf{r} = \rho\hat{\mathbf{r}}$. The ODF sacrifices the radial information in the diffusion propagator but retains, in average, relevant angular contrast (Tuch, 2004). Before the ODF calculation, each propagator is interpolated to a spherical lattice using a trilinear method. To obtain ODFs with high angular resolution, the interpolation parameters were chosen to obtain 50 radial points along each one of the 642 equidistant spatial directions on the sphere. The integral was then evaluated, at each spatial direction, over the resulting spherical lattice (i.e., $\rho \in [0, 50]$) using a Simpson numerical method.

To test the enhancement in the angular resolution that produces the introduction of the deconvolution process, the ODFs corresponding to standard DSI reconstructions were computed. It employs the above algorithm without applying the deconvolution step.

Similarly, to test the effect of the deconvolution in rotationally invariant scalar quantities derived from the propagator, in this work the zero displacement probability (P_o) and the mean squared displacement (MSD) maps were computed. In line with (Yu-Chien et al., 2008), these quantities were evaluated by means of the following equations:

$$P_0 = P(\mathbf{r} \equiv 0),$$
$$\mathrm{MSD} = \int_{-\infty}^{\infty} P(\mathbf{r})\mathbf{r}^2 d\mathbf{r}. \tag{9}$$

Definition of quantitative measures

The accuracy of the methods to reconstruct local fiber orientations was quantified by the average deviation angle between the reconstructed and true principal orientations. The average deviation angle was computed as:

$$\Delta\varphi = \frac{1}{2}\sum_{i=1}^{2} \min\left\{ \left|\mathrm{acos}\left(\hat{\mathbf{v}}_i^T \hat{\mathbf{e}}_1\right)\right|, \left|\mathrm{acos}\left(\hat{\mathbf{v}}_i^T \hat{\mathbf{e}}_2\right)\right| \right\}, \tag{10}$$

where $\hat{\mathbf{v}}_1$ and $\hat{\mathbf{v}}_2$ are the unit vectors along the true generated fibers and $\hat{\mathbf{e}}_1$ and $\hat{\mathbf{e}}_2$ are the unit vectors along the two main maxima extracted from the ODFs. Furthermore, to quantify the occurrence of false peaks, the local number of main maxima from the reconstructions was also computed as:

$$\mathrm{n-fiber} = \sum_{i=1}^{k} \mathrm{I}(I_i, I_{max}), \tag{11}$$

where $\mathrm{I}(I_i, I_{\max}) = 1$ for $I_i > 0.3I_{\max}$ and $\mathrm{I}(I_i, I_{\max}) = 0$ for $I_i \leq 0.3I_{\max}$, I_i denotes the intensity of the ith maximum, $I_{\max}$ is the intensity of the main maximum (i.e., $I_{\max} = \max\{I_i | i = 1, ..., k\}$), and k is the number of maxima extracted from the local angular ODF profiles. These measures have been previously used to quantify the reconstruction accuracy of some diffusion imaging techniques (Behrens et al., 2007; Lin et al., 2003; Melie-García et al., 2008; Tuch et al., 2002).

Results

Synthetic data

Fig. 1 shows the comparison of propagators and ODFs obtained by the standard DSI method and the new deconvolved reconstructions (B-D and L–R) for two particular fiber configurations. This result was obtained for synthetic data generated with a maximum b-value of 9000 s/mm^2. This example allows visualizing the effect of the deconvolution operation on the diffusion propagator and its repercussion on the ODF.

As can be seen in Fig. 1, the deconvolution operations give rise to sharper and clearer diffusion propagators. As a result, the ODF maps depict sharper profiles that potentially increase the angular resolution of the method. This is exemplified by the reconstruction of two crossing fibers with a separation angle of 45°. For this fiber configuration, the standard DSI method predicts only one diffusion maximum at an intermediate orientation between the true ODF maxima (Fig. 1, lower panel D). In contrast, the ODFs computed from deconvolved propagators were capable to solve the two fiber directions (Fig. 1, lower panels E and F). This result can be compared with the true ODF profiles depicted in Fig. 2, which are the theoretical ODFs predicted by the standard DSI method using continuous data in the whole infinite q-space (see Appendix C for a detailed description). Perceive that the ODFs obtained from the deconvolution methods are quite similar to those predicted from theory.

The above result illustrates the accuracy of the new approach in synthetic signals generated without considering the presence of experimental noise, which is, however, a limiting factor in diffusion MRI experiments. An exhaustive study about the effect of different noise levels, interfiber angles, and b-values on the reconstructed ODF fields is presented in Figs. 3 and 4.

Fig. 3 shows the results obtained from the simulation of two crossing fibers for different separation angles and SNR values using a maximum b-value of 9000 s/mm^2 (see the Simulated data generation subsection). As can be observed, the standard DSI method was not capable of disentangling fiber geometries with interfiber angles lower than 45° (i.e., average deviation angle = 20°), revealing its better performance for fiber configurations with separation angles higher than 60°. In contrast, the ODF fields computed from deconvolved propagators were more accurate. In particular, L–R DSI was the most stable and precise method under the range of values tested in this experiment. It was able to reconstruct fiber crossings with a separation angle of 30°. Notice the inaccuracy of B-D DSI to determine both the average deviation angle and the number of fibers for the higher noise level (SNR = 10). Nevertheless, the performance of the blind deconvolution approach increased considerably with the SNR value.

Fig. 4 depicts the results obtained from the simulation of two crossing fibers with different interfiber angles and SNR values using a maximum b-value of 4000 s/mm^2. As can be seen, the standard DSI method was not capable to reconstruct fiber crossings with separation angles lower than 60° (i.e., average deviation angle >20°). In contrast with results showed at Fig. 3, the B-D approach was very unstable. Although the deviation angle (panel A: B-D DSI) was considerably affected only for the higher noise level (SNR = 10), some spurious peaks appeared for moderate noise levels (SNR = 15 and 20), which can be visualized in the pie map (panel B: B-D DSI) that shows the proportions for the estimated number of fibers. On the other hand, the L–R method provides the more accurate reconstructions. For this experiment, the L–R method increased the angular resolution of DSI in approximately 15°. Notice also the ability of the method for detecting the correct number of fibers in most of the tested situations.

From these simulations, we can formulate the following partial conclusions. First, the L–R deconvolution provides the more accurate and stable method under the range of values tested in the experiments. Second, this superiority was more pronounced for the sampling scheme with higher diffusion weighting ($b_{\max} = 9000$ s/mm^2). Third, the standard DSI reconstructions present nondominant spurious peaks, which occurrence was observed in both experiments. Finally, although the B-D approach provides accurate results for the sampling scheme with higher diffusion weighting (and SNR ≥ 15), the results derived from the sampling scheme with lower diffusion weighting ($b_{\max} = 4000$ s/mm^2) showed a high number of artefactual peaks. This result allows us suggesting the application of the B-D algorithm only for data measured with relatively high b-values.

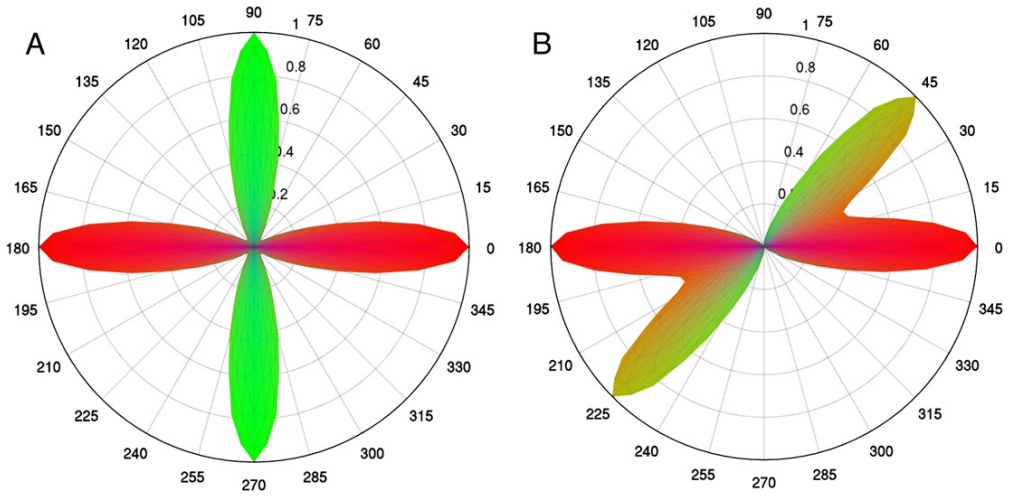

Fig. 2. Theoretical ODFs predicted for the fiber geometries displayed at Fig. 1. These ODFs were obtained assuming a continuous DSI sampling scheme in the whole infinite q-space. (A) and (B) Fiber crossings with interfiber angles of 90° and 45°, respectively. This figure allows the comparison among the theoretical ODFs, the ODFs estimated from DSI using finite data, and the ODFs obtained from deconvolution processes (Fig. 1).

Brain data

Figs. 5 and 6 show the effect of the deconvolution transform on the ODF reconstructions in regions of interest (ROIs) located in coronal (Fig. 5) and sagittal (Fig. 6) slices, respectively. These ROIs depict two- and three-way axonal crossings between the superior corona radiata (scr) (i.e., descending and ascending axons from and to the cerebral cortex), superior longitudinal fasciculus (slf) (i.e., a pair of long bidirectional bundles of neurons connecting the front and the back of the cerebrum), and the lateral projections of the corpus callosum (cc) (i.e., fiber bundles that connect the left and right cerebral hemispheres). In these figures, the ODF maps are colored according to their directions with red indicating mediolateral, green anteroposterior, and blue superoinferior. Thus, red, green and blue ODF peaks correspond to cc, slf, and scr tracts, respectively.

It is important to note how the B-D process (in both figures) gives rise to spurious peaks. This expected result is consistent with the results obtained from simulated data using the same experimental sampling scheme with $b_{max}=4000$ s/mm^2 (Fig. 4). This finding supports the hypothesis that, for real data measured with moderate values of b_{max}, the typical DSI reconstructions are more accurate than the obtained from B-D algorithms. In this situation, the B-D method was not able to concurrently determine, in an effective way, both the real propagator and the blurring function.

On the other hand, the L–R deconvolution operation gives rise to different effects. From both figures, we can summarize the following general results. First, it diminishes the angular uncertainty of the fiber orientations by sharpening the diffusion ODFs in a majority of voxels. Second, in some cases, the L–R deconvolution transforms the fiber crossings that are formed by dominant and nondominant components, in single sharp peaks. It is difficult to evaluate the impact of the above result as positive or negative because in real data, there is no ground truth. However, the obtained results in the synthetic data (Figs. 3 and 4) demonstrate that the standard DSI reconstructions can produce nondominant spurious peaks, which, in general, are not obtained by means of L–R deconvolution. Hence, some of the above small angular crossings predicted by the standard DSI method, which were not obtained using the L–R algorithm, may be artefactual patterns in the unrectified propagator due to noise and the finite sampling scheme.

Fig. 7 depicts the scalar P_o and MSD maps derived from the propagator obtained with the standard DSI method (upper row) and the L–R deconvolution algorithm (bottom row) in an axial slice. As can be seen, the deconvolution operation increased the tissue contrast between white and grey matter. This effect is mainly observed in the P_o map (panel (a)). This result agrees with the hypothesis that the white matter exhibits the most consistently high P_o (Yu-Chien et al., 2008). Recently, it has been demonstrated that the P_o value, at each voxel, depends on the apparent diffusivity value measured along the direction in which the diffusion process is more restricted (Canales-Rodríguez et al., 2010). In the brain, the diffusion process is especially restricted just in the plane perpendicular to the white mater tract orientations. On the other hand, the maximum intensities of the MDS maps were located in the cerebrospinal fluid (CSF) where the diffusion process is unrestricted. In line with Yu-Chien et al. (2008), the MSD maps provide low tissue contrast images.

Discussion

Implementation details and open problems

Deconvolution error sources

Even when the unwanted convolution is "perfectly" understood, there are still factors that limit the performance of deconvolution: (1) the inherent noise, (2) the truncation effects, and (3) the loss of information due to discretization. For instance, most unwanted convolutions take the form of a low-pass filter, reducing the amplitude of the high-frequency components in the image. Deconvolution corrects this effect by amplifying these frequencies. However, if the amplitude of these components falls below the inherent noise of the system, the information contained in these frequencies is lost. On the other hand, the PSF (Eq. (5)) continues to both negative and positive infinity without dropping to zero amplitude, which is determined by the oscillatory properties of the sinc function (see http://mathworld.wolfram.com/SincFunction.html). In practice, the PSF must be truncated; however, the abrupt discontinuity at the ends of the truncated PSF can produce several artifacts in form of ripples on the deconvolved image (for a more detailed discussion about this matter, please see: http://www.dspguide.com/pdfbook.htm). The practical solution to this problem is to design a less aggressive deconvolution filter. For this reason, in this work, a truncated version of the PSF was used, in which only the positive main lobe of the PSF was considered. The results support the hypothesis that this level of truncation is sufficient to produce accurate and stable results that are comparable or better than those provided by blind deconvolution methods, which are computationally more demanding.

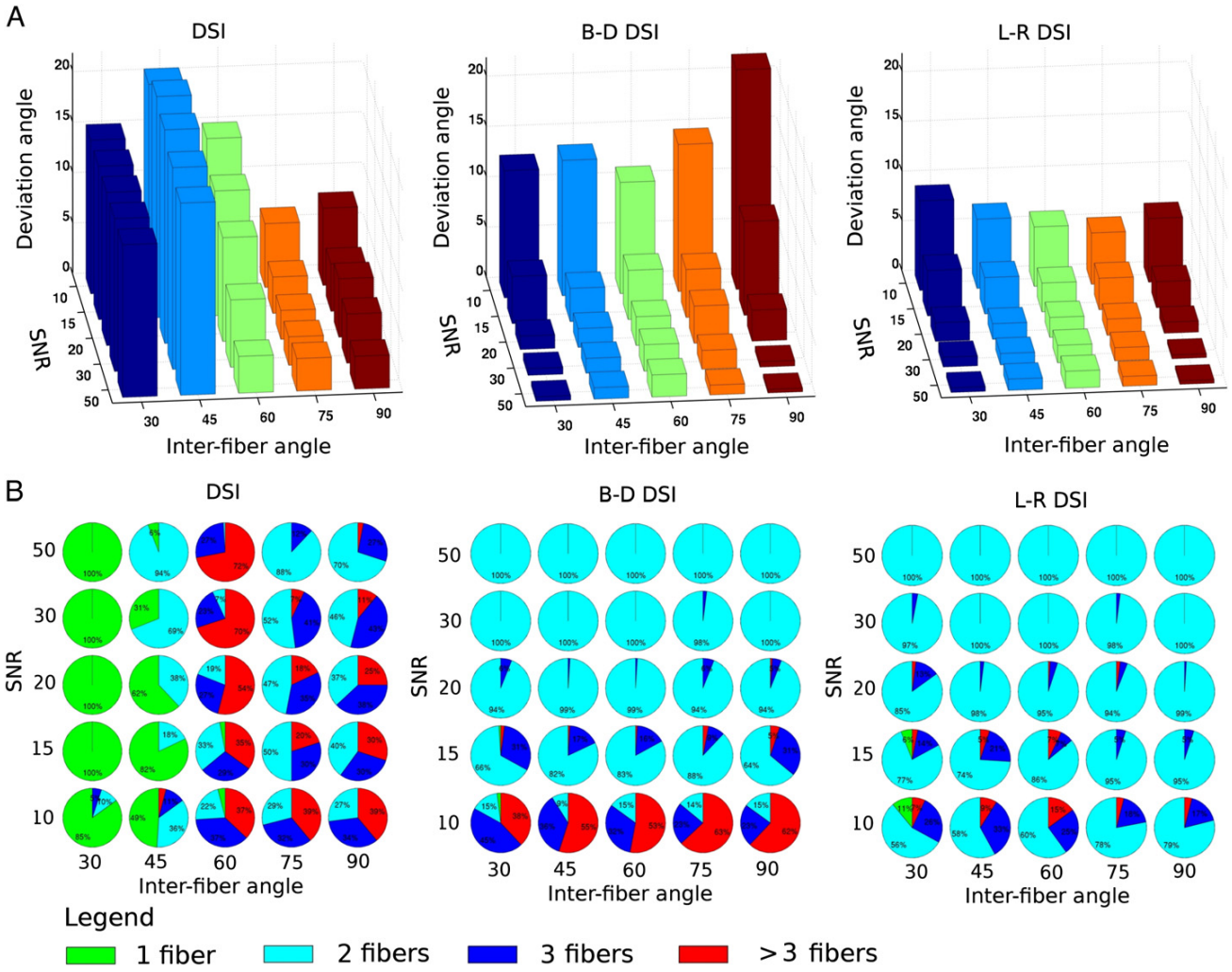

Fig. 3. Simulations of fiber crossings with different separation angles (individual *x*-axes) and SNR values (individual *y*-axis) using a sampling scheme with 203 q-space points and a maximum *b*-value of 9000 s/mm^2. Simulations were repeated 100 times. (A) Three-dimensional vertical bars of the average deviation angle (individual *z*-axis) between the simulated and reconstructed fibers using three different estimation techniques. (B) Pie maps where the area of each slice is proportional to the number of main fibers recovered by the estimation approaches. The green, cyan, and blue colors correspond to one, two, and three fibers, respectively, whereas red corresponds to cases in which more than three fibers were estimated. In both panels, the standard DSI reconstruction is denoted by DSI, whereas B-D DSI and L–R DSI designate the reconstructions from the blind deconvolution and Lucy–Richardson methods, respectively.

Prefiltering techniques

In the DSI community, there is no consensus on what preprocessing and prefiltering steps are really necessary before the FFT computation. To date, several approaches have been adopted. For example, in Yu-Chien and Alexander (2007), a new sampling strategy, called hybrid diffusion imaging (HYDI), was proposed. The HYDI encoding scheme is composed of multiple concentric shells of constant diffusion weighting. In a first step, to minimize overestimation of signals near the noise floor, diffusion signals were set to zero if smaller than two times of the mean signal in air. In a second step, the resulting data were regridded to a Cartesian lattice using a linear hypersurface fitting algorithm.

On the other hand, in some FFT applications, it is usual to multiply the signal by an apodization function (also called a tapering function) (Donnelly and Rust, 2005). The most common tapering functions are smooth non-negative curves with a finite support, which are used to bring the signal smoothly down to zero at the edges of the sampled region. This mitigates the effects of spectral leakage, at the expense of decreasing the resolution (Naylor and Tahic, 2007), by suppressing side lobes which would be produced. An example of this methodology applied to DSI analysis can be found in (Wedeen et al., 2005), which employed a Hanning window. It is important to note that the use of tapering functions will modify the PSF expressed by Eq. (4). For a detailed list of one-dimensional apodization functions and their corresponding PSFs, see: http://mathworld.wolfram.com/ApodizationFunction.html. The extension to three dimensions is straightforward.

In this work, we employed a different strategy. A statistical thresholding technique was applied to the propagator computed with the full data set, which was fitted to a gamma distribution (see the DSI reconstructions section). Because the propagator is reconstructed on a finer grid ($35\times35\times35$), the thresholding analysis may be more robust. However, we have little reason to prefer any of the above possibilities over the others. Future studies will be performed to compare all the available prefiltering techniques in DSI, which will consider the inclusion of some new procedures, such as wavelet thresholding (for more details, see: http://taco.poly.edu/WaveletSoftware/denoise.html) and dMRI denoising techniques (Aja-Fernández et al., 2009; Wiest-Daessle et al., 2008).

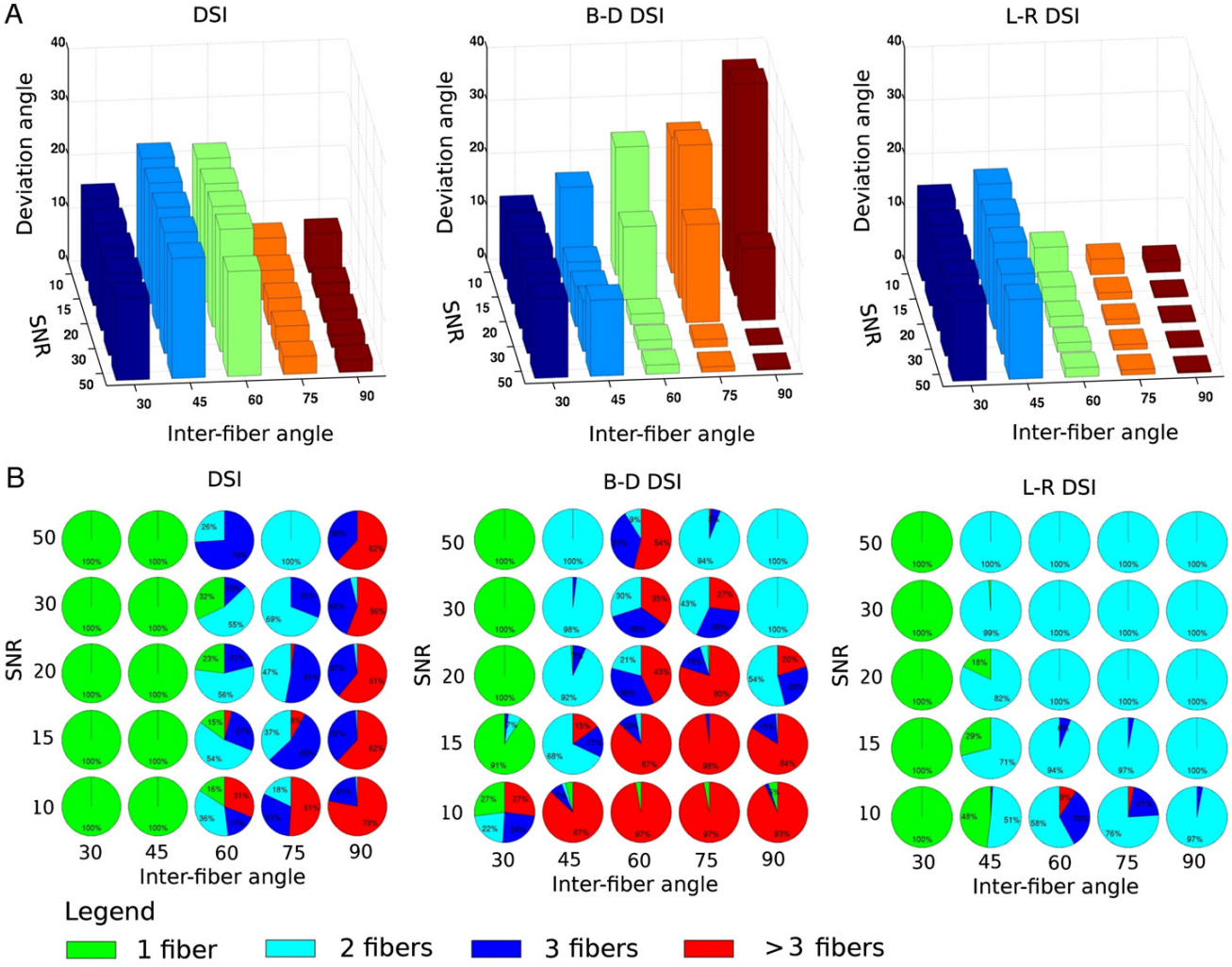

Fig. 4. Simulations of fiber crossings with different separation angles (individual *x*-axes) and SNR values (individual *y*-axis) using a sampling scheme with 203 q-space points and a maximum *b*-value of 4000 s/mm^2. Simulations were repeated 100 times. (A) Three-dimensional vertical bars of the average deviation angle (individual *z*-axis) between the simulated and reconstructed fibers using the three studied techniques. (B) Pie maps where the area of each slice is proportional to the number of main fibers recovered by the estimation algorithms. The green, cyan, and blue colors correspond to one, two, and three fibers, respectively, whereas red corresponds to cases in which more than three fibers were estimated. In both panels, the standard DSI reconstruction is denoted by DSI, whereas B-D DSI and L–R DSI designate the reconstructions from the blind deconvolution and Lucy–Richardson methods, respectively.

Reconstruction grid: resolution issues

Another technical aspect involving DSI is the reconstruction grid resolution. The FFT formalism allows computing the diffusion propagator on a Cartesian grid. However, to compute the ODF, the propagator must be interpolated to a spherical lattice. This transformation gives rise to Cartesian artifacts (Tuch, 2004), which are more pronounced for low-resolution grids. Hence, the ODF calculus will be less sensitive to these artifacts for high-resolution grids. Conversely, the computational cost of nonlinear interpolation techniques from Cartesian to spherical grids highly depends on the resolution. Therefore, in practice, it is necessary to establish a standard resolution level to produce accurate results in acceptable computation times. However, to date, there are no reports on this issue.

Previous studies have been conducted using different levels of resolution. For example, in Yu-Chien and Alexander (2007), a low-resolution Cartesian grid was employed ($9\times9\times9$). In the novel DSI paper (Wedeen et al., 2005), a reconstruction grid with moderate resolution ($17\times17\times17$) was used. Similarly, in Tuch (2002), a moderate resolution grid was also employed ($17\times17\times17$), which was interpolated to a spherical lattice using a cubic interpolation method. In contrast, in this work, we employed a different strategy that was motivated by the introduction of the deconvolution process. In general, the deconvolution algorithms increase their performance for high-resolution images. Once again, however, their computational cost increase with the resolution. An exploratory analysis (result not reported) suggested that the $35\times35\times35$ grid used in this work provides a good tradeoff between accuracy and deconvolution time. After FFT analysis, a fast trilinear interpolation method to resample the propagator on a high-resolution spherical lattice was then employed, which allows computing ODFs with a high degree of accuracy. This specific resolution level is not necessarily optimal from an accuracy standpoint but does adequately illustrate the benefits of the deconvolution process. Future studies will be performed to optimize the specific resolution of the reconstruction grid. In what follows, we report the expected (mean) computational time at each voxel of our procedures: FFT analysis with zero-padding plus thresholding analysis 2×10^{-2} s; B-D/L–R algorithms 0.6/0.2 s, respectively; trilinear interpolation plus ODF calculus 7×10^{-2} seconds. As can be appreciated, the

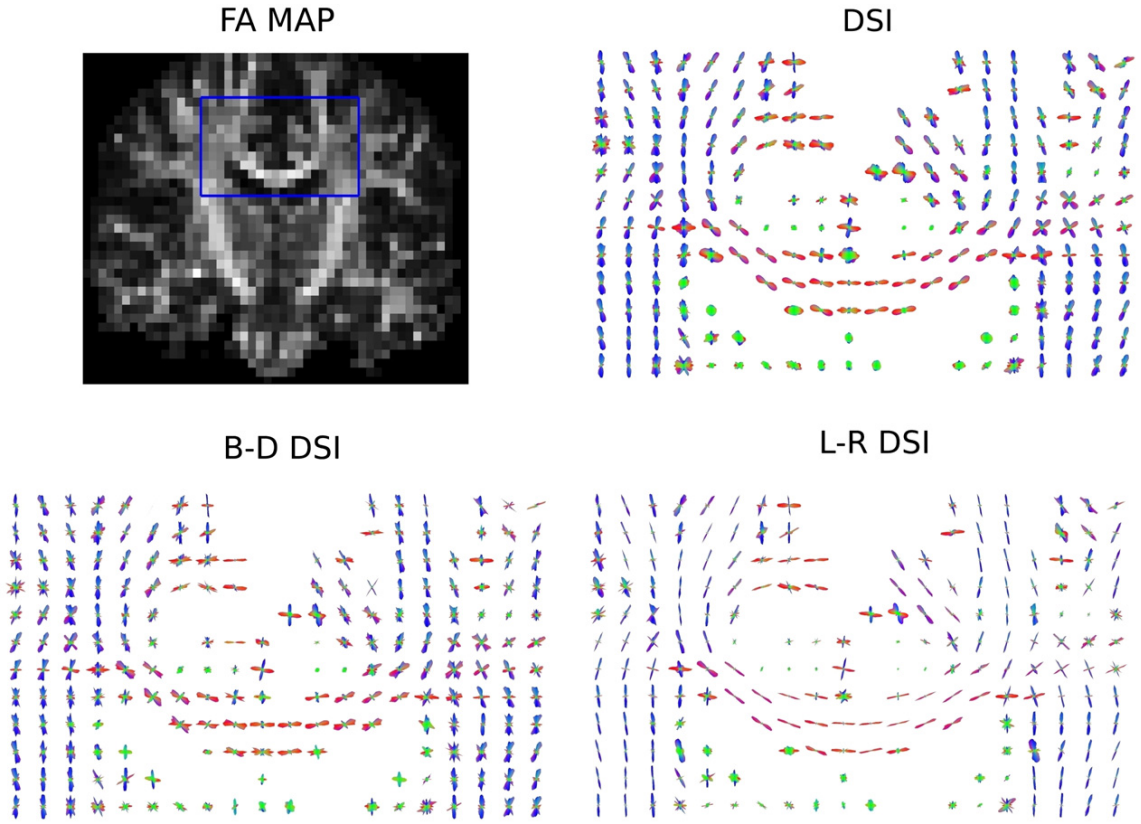

Fig. 5. Comparison of DSI reconstructions in a region of interest (ROI) located in the coronal plane of a human brain. The fractional anisotropy (FA) map of the whole slice is depicted for illustrative purposes. In this ROI (blue rectangle in the FA map), some important tracts can be identified: the superior longitudinal fasciculus, the superior corona radiata, and the corpus callosum. The standard DSI reconstruction is denoted by DSI, whereas B-D DSI and L–R DSI designate the reconstructions from the blind deconvolution and Lucy–Richardson methods, respectively. The ODF maps are colored according to their direction (RGB code) with red indicating mediolateral, green indicating anteroposterior, and blue indicating superoinferior.

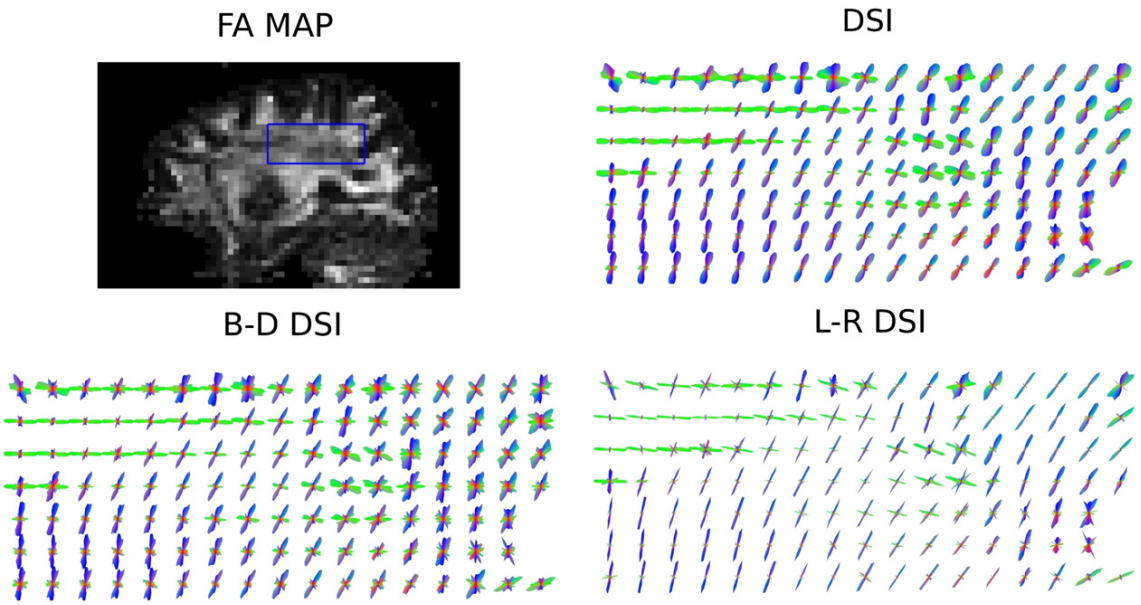

Fig. 6. Comparison of DSI reconstructions in a region of interest (ROI) located in the sagittal plane of a human brain. The fractional anisotropy (FA) map of the whole slice is depicted for illustrative purposes. In this ROI (blue rectangle in the FA map), two- and three-way crossing of the striations from the corpus callosum, the corona radiata, and the superior longitudinal fasciculus can be identified. The standard DSI reconstruction is denoted by DSI, whereas B-D DSI and L–R DSI designate the reconstructions from the blind deconvolution and Lucy–Richardson methods, respectively. The ODF maps are colored according to their direction (RGB code) with red indicating mediolateral, green indicating anteroposterior, and blue indicating superoinferior.

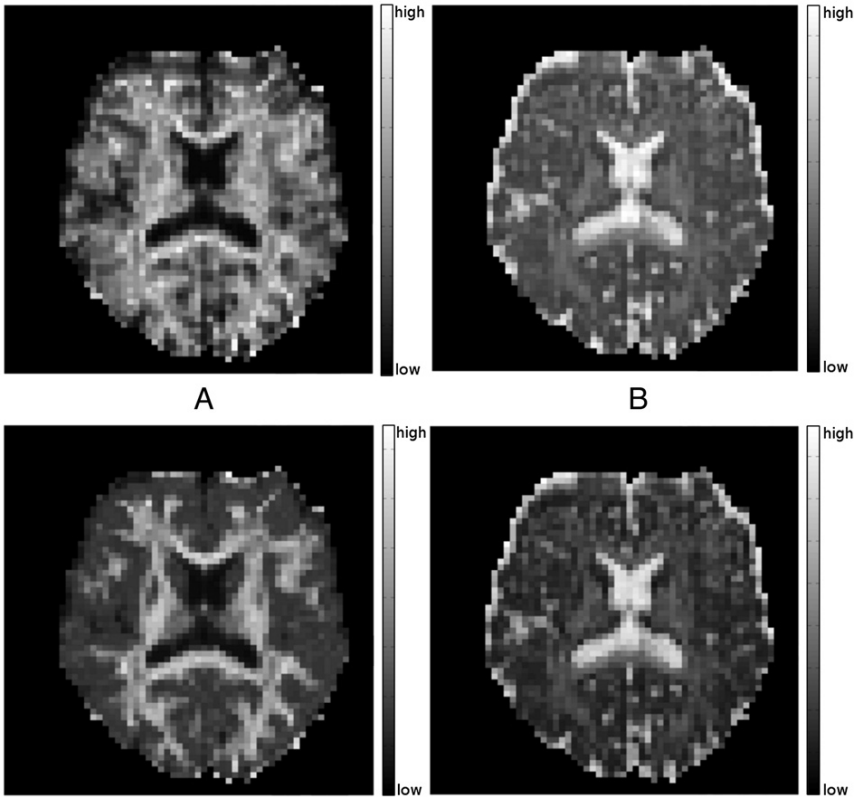

Fig. 7. Comparison of the scalar invariant maps derived from the propagator obtained with the standard DSI method (upper row) and the L–R deconvolution algorithm (bottom row) in an axial slice of a human brain. Panel A depicts the zero displacement (P_o) maps. Panel B shows the mean squared displacement (MSD) maps.

computational time is dominated by the deconvolution algorithms. However, these times are acceptable for practical applications.

Sampling schemes in DSI

The DSI sampling schemes commonly used in practice are comprised by 256 or 515 q-space points (Wedeen et al., 2005). Usually, such schemes are measured using extremely high *b*-values (from 12,000 to 18,000 s/mm^2). However, these typical schemes limit the practical use of the technique due to their long data acquisition times. Recently, an interesting study that quantifies the effects of sparser sampling schemes and lower *b*-values was reported (Kuo et al., 2008). The main result is that a DSI sampling scheme with 203 points can produce accurate and stable results that are comparable to those obtained with denser schemes. The optimal maximum *b*-value reported for this sampling scheme was $b_{max}=$ 4000 s/mm^2, which is just the experimental value employed to measure the real data used in this work. However, although this *b*-value is optimum for standard DSI experiments, the results obtained in simulated data suggest that the deconvolution operation introduced in this work will benefit from the use of higher *b*-values, e.g., $b_{max}=$ 9000 s/mm^2. In this regimen, the advantages of deconvolution methods are more evident. Future studies will be performed to validate this hypothesis in real data.

To explore the performance of the deconvolution with a sparser sampling scheme, further exploratory analysis with synthetic data was implemented. In particular, a DSI sampling scheme with 123 q-space points and a maximum *b*-value of 9000 s/mm^2 were considered. The analysis was developed in line with the synthetic data processing presented in the above subsections (see the Simulated data generation subsection). Fig. 8 shows the results obtained from the simulation of two crossing fibers with different separation angles and SNR values. As can be observed, for this sparse sampling scheme, there are no significant differences between the three methods, which are not capable of separating fiber crossings with interfiber angles lower than 75°. This result allows suggesting that the number of DSI q-space points cannot be drastically reduced to below 203 points.

It is important to note that the voxel size employed in the real data acquisition (i.e., $2.9\times2.9\times2.9$ mm^3) is slightly higher than that typically employed for fiber tracking analysis (e.g., $2\times2\times2$ mm^3). The use of this resolution was motivated only by illustrative reasons. It allows a clear visualization and recognition of fiber crossing regions. Nevertheless, an exploratory analysis (result not reported) using real data with lower voxel size shows similar results.

Effects of finite pulse widths

The relationship given by Eq. (1) is based on the assumption that the temporal shape of the diffusion-sensitizing gradient vector is infinitely narrow (i.e., $\tau\rightarrow0, \Delta\gg\tau$). In this situation, the molecules do not diffuse significantly during its application. This criterion is usually known as the *narrow pulse approximation*. However, acquisition methods cannot currently meet this condition; especially on clinical systems (see the Human brain data section). Any deviations to this criterion will have an impact on the diffusion propagator that is estimated, regardless of particular sampling strategy or reconstruction algorithm, since for finite diffusion gradient pulses, the diffusion propagator becomes the center-of-mass propagator (see Mitra and Halperin, 1995 for a detailed description). Although previous experimental results suggest that the breakdown of the narrow pulse approximation does not have a significant impact on the orientational structure of the propagator (Lin et al., 2003; Perrin et al., 2005), the resulting propagator is a blurred version of the real propagator. Future work will be performed to try to include, in the deconvolution process, the effect of finite pulse widths.

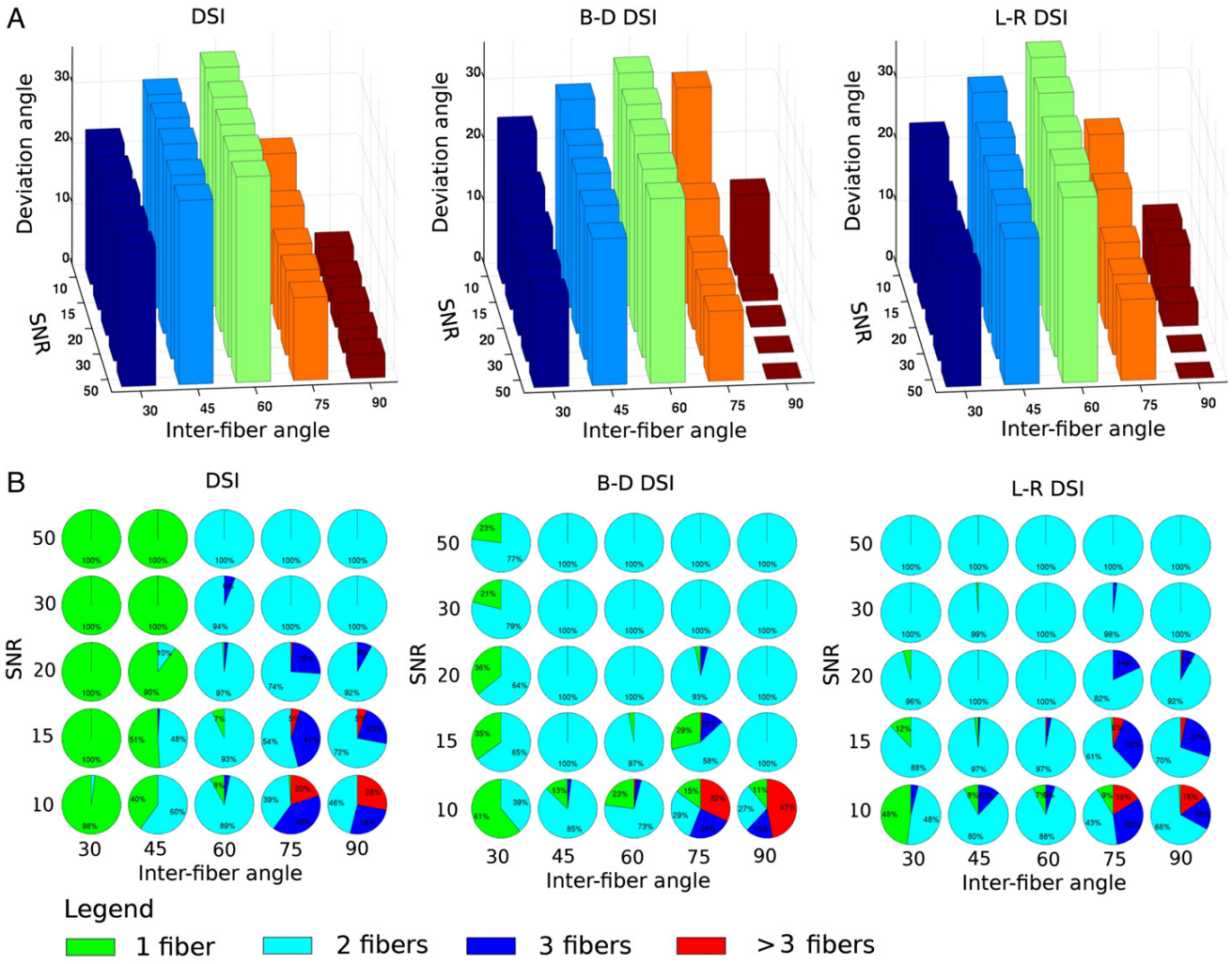

Fig. 8. Simulations of fiber crossings with different separation angles (individual *x*-axes) and SNR values (individual *y*-axis) using a DSI sampling scheme with 123 q-space points and $b_{max} = 9000$ s/mm^2. Simulations were repeated 100 times. (A) Three-dimensional vertical bars of the average deviation angle (individual *z*-axis) between the simulated and reconstructed fibers using three different estimation techniques. (B) Pie maps where the area of each slice is proportional to the number of main fibers recovered by the estimation approaches. The green, cyan, and blue colors correspond to one, two, and three fibers, respectively, whereas red involves the cases in which more than three fibers were estimated. In both panels, the standard DSI reconstruction is denoted by DSI, whereas B-D DSI and L–R DSI designate the reconstructions from the blind deconvolution and Lucy–Richardson methods, respectively.

ODF deconvolution versus PDF deconvolution

A central assumption in dMRI techniques is that brain water diffuses preferentially along fiber bundles. Therefore, although the theoretical relationship between diffusion ODF and fiber ODF is unknown (Tuch, 2004), it is natural to assume that the maxima in the diffusion ODF correspond to the "true" fiber directions. In practice, the diffusion ODF has a large part not aligned with the principal fiber directions, which reduces the angular resolution of the methods. It means that the diffusion ODF maxima do not correspond to the true fiber directions for nearly oriented fibers. Recently, different approaches to deal with this limitation were proposed. A particular solution to this problem was introduced by Descoteaux et al. (2009), which employs a deconvolution operation that aims to transform the diffusion ODF, obtained from QBI (Tuch, 2004), into a sharp fiber ODF. This idea was inspired by the original spherical deconvolution approach (Tournier et al., 2004, 2007, 2008). Both methods allow obtaining sharper diffusion ODFs that are more representative of the local fiber distribution. These approaches are based on the assumption that all fiber bundles in the brain have the same typical diffusion anisotropy, i.e., identical diffusivity values. However, this hypothesis may be violated in some brain areas. As a consequence, different regions may be processed with different degree of accuracy. A previous study has suggested that the use of incorrect diffusivities produces incorrect estimates in the intensities of the ODF peaks (Anderson, 2005).

In contrast, in this work, the deblurring operation was applied directly on the displacement probability density function (*pdf*) in a model-free way, which does not require prior knowledge of intravoxel diffusion model parameters, e.g., diffusivity values. The resulting blurring function only depends on the experimental sampling scheme. Hence, from this method, one can expect to obtain similar levels of accuracy in the different brain regions. Going further, from a theoretical point of view, it is possible to expect similar levels of accuracy in different subjects, which will depend only on the experimental noise but not on the inaccurate modeling. The latter may have a positive impact on the identification of brain structural abnormalities by means of statistical group comparison of quantities derived from the propagator. It is just another further advantage of the presented method over the above techniques based on HARDI

data. DSI can be used to obtain additional maps of scalar invariant quantities to characterize the anisotropy of the diffusion process, such as the zero displacement probability and the mean squared displacement computed in this work.

The obtained results in both synthetic and real data demonstrated that the angular resolution of DSI can be increased by means of the L–R deconvolution, potentially revealing new real fiber components and reducing both the artefactual peaks and the angular uncertainty in the ODF profiles. For instance, in simulated data, the L–R method was capable of resolving fiber components with separation angles of 30° for SNR≥15 with a maximum *b*-value 9000 s/mm^2 (Fig. 3). To the best of our knowledge, this resolution power has not been achieved by any previous model-independent q-space reconstruction method. In contrast, the benefits of the blind deconvolution method are only effective for sampling schemes with relatively high *b*-values.

An area of future research will be the implementation of new alternative deconvolution approaches (see Högbom, 1974; Narayan and Nityananda, 1986; Segalovitz and Frieden, 1978) as well as their validation using experimental data measured with a variety of DSI sampling schemes. Another interesting issue is the rectification, or deblurring, of diffusion propagators computed from models based on HARDI sampling schemes like the diffusion orientation transform method (Özarslan et al., 2006).

Summary

In this work, a new framework for obtaining clearer and sharper diffusion propagators was introduced. The approach is based on deconvolution methods, which are supported from a theoretical point of view by the use of signals with a finite support in q-space. The diffusion propagator obtained by the standard DSI technique is a convolution between the true propagator and a point spread function that depends on the experimental sampling scheme. Thus, the deconvolution between these functions gives rise to the exact diffusion propagator, which contains decontaminated information about the underlying diffusion process.

The orientational resolution achieved due to the deconvolution process in DSI should extend the viability of cerebral fiber tracking methods. The new methodology introduced in this work enhances the DSI capability for the noninvasive analysis of fiber tissue architecture on the microscopic scale.

Conflict of interest
None of the authors declare any conflicts of interest.

Acknowledgments

This work was supported in part by the Instituto de Salud Carlos III, Centro de Investigación Biomédica en Red de Salud Mental (CIBERSAM, Spain), and the Cuban Neuroscience Center. We thank the Advanced Biomedical MRI Laboratory, National Taiwan University Hospital, for providing the human brain data used in this work, which is part of a public database. Finally, we thank our anonymous reviewers for their comments and suggestions that have considerably improved the manuscript.

Appendix A. Convolution theorem

In Cartesian coordinates, the modified propagator can be written as (see Eqs. (1) and (2))

$$P_M(\mathbf{r}) = \int_{-\infty}^{\infty} E(\mathbf{q})\Pi(\mathbf{q})\exp(-2\pi i\mathbf{rq})d\mathbf{q}, \tag{12}$$

where $\Pi(\mathbf{q})$ is the q-space filter (see for one example, Eq. (3)).

Similarly, the diffusion signal can be written as the inverse Fourier transform of the true, or exact, diffusion propagator as follows:

$$E(\mathbf{q}) = \int_{-\infty}^{\infty} P(\mathbf{r}')\exp(2\pi i\mathbf{r}'\mathbf{q})d\mathbf{r}'. \tag{13}$$

Notice that without loss of generality we have written the above expression in terms of an auxiliary vector $\mathbf{r}'$ in real space. Inserting Eq. (13) into Eq. (12), we obtain

$$P_M(\mathbf{r}) = \int_{-\infty}^{\infty}\left[\int_{-\infty}^{\infty} P(\mathbf{r}')\exp(2\pi i\mathbf{r}'\mathbf{q})d\mathbf{r}'\right]\Pi(\mathbf{q})\exp(-2\pi i\mathbf{rq})d\mathbf{q}. \tag{14}$$

Reordering terms, the above equation becomes:

$$P_M(\mathbf{r}) = \int_{-\infty}^{\infty} P(\mathbf{r}')\mathbb{F}\{\Pi\{\mathbf{r}-\mathbf{r}'\}\}d\mathbf{r}', \tag{15}$$

where $\mathbb{F}\{\Pi\{\mathbf{r}-\mathbf{r}'\}\}$ is the Fourier transform of the filter with respect to the relative vector $\mathbf{R}=\mathbf{r}-\mathbf{r}'$:

$$\mathbb{F}\{\Pi\{\mathbf{r}-\mathbf{r}'\}\} = \int_{-\infty}^{\infty}\Pi(\mathbf{q})\exp[-2\pi i(\mathbf{r}-\mathbf{r}')\mathbf{q}]d\mathbf{q}. \tag{16}$$

It is important to note that Eq. (15) is the 3D convolution (in real space) of the true diffusion propagator with the Fourier transform of the filter, which can be rewritten in the compact notation:

$$P_M = P\otimes\mathbb{F}\{\Pi\{\mathbf{R}\}\}. \tag{17}$$

Appendix B. Point spread function of a Cartesian 3D boxcar filter

The Fourier transform of the boxcar function defined in Eq. (3) is given by the following integral (see Eq. (16))

$$\mathbb{F}\{\Pi\{\mathbf{R}\}\} = \int_{-\infty}^{\infty}\int_{-\infty}^{\infty}\int_{-\infty}^{\infty}\Pi\left(q_x,q_y,q_z\right)\exp\left[-2\pi i\left(R_xq_x+R_yq_y+R_zq_z\right)\right]dq_xdq_ydq_z, \tag{18}$$

which can be separated into three one-dimensional independent parts

$$\mathbb{F}\{\Pi\{\mathbf{R}\}\} = I(x)I(y)I(z), \tag{19}$$

where I is defined by the functional

$$I(k) = \int_{-qmax}^{qmax}\exp[-2\pi iR_kq_k]dq_k,\ k=x,y,z. \tag{20}$$

The above integral can be evaluated as

$$\begin{aligned} I(k) &= \frac{2q_{max}\sin(2\pi R_kq_{\max})}{2\pi R_kq_{\max}} \\ &= 2q_{max}sinc(2\pi R_kq_{\max}). \end{aligned} \tag{21}$$

Therefore, the PSF becomes

$$\mathbb{F}\{\Pi\{\mathbf{R}\}\} = (2q_{max})^3\mathrm{sinc}(2\pi R_xq_{\max})\mathrm{sinc}\left(2\pi R_yq_{\max}\right)\mathrm{sinc}(2\pi R_zq_{\max}). \tag{22}$$

Appendix C. Orientational distribution function

The diffusion propagator obtained by the Fourier transform (in the whole q-space) of the multitensor signal defined in Eq. (7) is given by the following integral

$$P(\mathbf{r}) = \sum_{i=1}^{M} f_i \int_{-\infty}^{\infty} \exp(-b\hat{\mathbf{q}}^T D^{(i)} \hat{\mathbf{q}}) \exp(-2\pi i \mathbf{q}\mathbf{r}) d\mathbf{q} = \sum_{i=1}^{M} f_i \mathbf{I}_i, \tag{23}$$

where

$$I_i = \int_{-\infty}^{\infty} \exp\Big(- 4\pi^2 t \mathbf{q}^{\mathrm{T}} \mathbf{D}^{(i)} \mathbf{q} - 2\pi i \mathbf{q}\mathbf{r} \Big) d\mathbf{q}. \tag{24}$$

To solve the above integral, we will consider the following identity:

$$\begin{aligned} &-4\pi^2 t \mathbf{q}^T \mathbf{D}^{(i)} \mathbf{q} + 8\pi^2 t \mathbf{q}^T \mathbf{D}^{(i)} \mathbf{q}_0 \\ &= \; - 4\pi^2 t (\mathbf{q} - \mathbf{q}_0)^{\mathrm{T}} \mathbf{D}^{(i)} (\mathbf{q} - \mathbf{q}_0) + 4\pi^2 t \mathbf{q}_0{}^T \mathbf{D}^{(i)} \mathbf{q}_0. \end{aligned} \tag{25}$$

Making the change of variable, $\mathbf{q}_0 = -i\mathbf{D}^{(i)^{-1}} \mathbf{r}/4\pi t$, the above equation becomes:

$$\begin{aligned} -4\pi^2 t \mathbf{q}^T \mathbf{D}^{(i)} \mathbf{q} - i2\pi \mathbf{q}\mathbf{r} = &- 4\pi^2 t \Big(\mathbf{q} + i\mathbf{D}^{(i)^{-1}} \mathbf{r}/4\pi t \Big)^T \mathbf{D}^{(i)} \Big(\mathbf{q} + i\mathbf{D}^{(i)^{-1}} \mathbf{r}/4\pi t \Big) \\ &- \frac{1}{4t} r^T \mathbf{D}^{(i)^{-1}} \mathbf{r}. \end{aligned} \tag{26}$$

It is important to notice that the left term of the above equation is equal to the exponential term in Eq. (24). Hence, inserting Eq. (26) into Eq. (24), we obtain:

$$I_i = \exp\Big(-\frac{1}{4t} \mathbf{r}^T \mathbf{D}^{(i)^{-1}} \mathbf{r} \Big) \int_{-\infty}^{\infty} \exp\Big(-\mathbf{u}^{\mathrm{T}} \mathbf{u} \Big) d\mathbf{q}, \tag{27}$$

where $\mathbf{u} = (4\pi^2 t)^{1/2} \mathbf{A}(\mathbf{q} + i\mathbf{D}^{(i)^{-1}} \mathbf{r}/4\pi t)$. In the above transformation, the following Cholesky decomposition $\mathbf{D}^{(i)} = \mathbf{A}^{(i)T} \mathbf{A}^{(i)}$ was employed, where $\mathbf{A}^{(i)}$ is a triangular matrix. At this point, it is possible to show that $d\mathbf{u} = Jd\mathbf{q}$, where $J = |(4\pi^2 t)^{1/2} \mathbf{A}^{(i)}| = (4\pi^2 t)^{3/2} |\mathbf{A}^{(i)}|$ is the Jacobian determinant of the transformation. Hence, the above integral can be evaluated as:

$$\begin{aligned} \int_{-\infty}^{\infty} \exp\Big(-\mathbf{u}^{\mathrm{T}} \mathbf{u} \Big) d\mathbf{q} &= \frac{1}{(4\pi^2 t)^{3/2} |\mathbf{A}^{(i)}|} \int_{-\infty}^{\infty} \exp\Big(-\mathbf{u}^{\mathrm{T}} \mathbf{u} \Big) d\mathbf{u}, \\ &= \frac{1}{(4\pi t)^{3/2} |\mathbf{A}^{(i)}|}. \end{aligned} \tag{28}$$

Therefore, the final expression for the propagator is:

$$P(\mathbf{r}) = \frac{1}{(4\pi t)^{3/2}} \sum_{i=1}^{M} \mathrm{f}_i |\mathbf{D}^{(i)}|^{-1/2} \exp\Big(-\frac{1}{4t} \mathbf{r}^T \mathbf{D}^{(i)^{-1}} \mathbf{r} \Big), \tag{29}$$

where it was considered that $|\mathbf{A}^{(i)}| = |\mathbf{D}^{(i)}|^{-1/2} (|\mathbf{D}^{(i)}| = |\mathbf{A}^{(i)T} \mathbf{A}^{(i)}| = |\mathbf{A}^{(i)T}||\mathbf{A}^{(i)}| = |\mathbf{A}^{(i)}|^2)$.

Notice that the determinant of $\mathbf{D}^{(i)}$ can be computed as $|\mathbf{D}^{(i)}| = \lambda_1 \lambda_2 \lambda_3$. Hence, substituting Eq. (29) in Eq. (8) and using the identity:

$$\int_0^{\infty} x^m \exp\Big(ax^2 \Big) dx = \frac{\Gamma\Big(\frac{m+1}{2}\Big)}{2a^{\frac{m+1}{2}}}, \tag{30}$$

where Γ is the Gamma function, we can obtain the ODF as:

$$\mathrm{ODF}(\hat{\mathbf{r}}) = \frac{1}{Z} \sum_{i=1}^{M} \mathrm{f}_i \Big(\hat{\mathbf{r}}^{\mathrm{T}} \mathbf{D}^{(i)^{-1}} \hat{\mathbf{r}} \Big)^{-\frac{3}{2}}. \tag{31}$$

Here, Z is a normalization constant which ensures that the ODF is properly normalized to unit mass. The ODF given by Eq. (31) is the exact analytical ODF corresponding to a diffusion signal generated in the whole q-space by means of the multitensor model. In this work, this expression was used to generate Fig. 2.

References

Aja-Fernández, S., Tristán-Vega, A., Alberola-López, C., 2009. Noise estimation in single- and multiple-coil magnetic resonance data based on statistical models. Magn. Reson. Imaging 27 (10), 1397–1409.

Alexander, D.C., 2005. Multiple-fiber reconstruction algorithms for diffusion MRI. Ann. N.Y. Acad. Sci. 1064, 113–133.

Anderson, A.W., 2005. Measurement of fiber orientation distributions using high angular resolution diffusion imaging. Magn. Reson. Med. 54, 1194–1206.

Andersson, J.L., 2008. Maximum a posteriori estimation of diffusion tensor parameters using a Rician noise model: why, how and but. Neuroimage 42, 1340–1356.

Basser, P., 1997. New histological and physiological stains derived from diffusion tensor MR images. Ann N.Y. Acad. Sci. 820.

Basser, P.J., Mattiello, J., LeBihan, D., 1994. Estimation of the effective self-diffusion tensor from the NMR spin echo. J. Magn. Reson. B. 103, 247–254.

Basser, P.J., Pierpaoli, C., 1996. Microstructural and physiological features of tissues elucidated by quantitative-diffusion-tensor MRI. J. Magn. Reson. B. 111, 209–219.

Behrens, T.E., Berg, H.J., Jbabdi, S., Rushworth, M.F., Woolrich, M.W., 2007. Probabilistic diffusion tractography with multiple fiber orientations: what can we gain? Neuroimage 34, 144–155.

Behrens, T.E., Johansen-Berg, H., 2005. Relating connectional architecture to grey matter function using diffusion imaging. Philos. Trans. R. Soc. Lond., B Biol. Sci. 360, 903–911.

Behrens, T.E., Woolrich, M.W., Jenkinson, M., Johansen-Berg, H., Nunes, R.G., Clare, S., Matthews, P.M., Brady, J.M., Smith, S.M., 2003. Characterization and propagation of uncertainty in diffusion-weighted MR imaging. Magn. Reson.Med. 50, 1077–1088.

Biggs, D.S., Andrews, M., 1997. Acceleration of iterative image restoration algorithms. Appl. Opt. 36, 1766–1775.

Callaghan, P.T., 1991. Principles of Nuclear Magnetic Resonance Microscopy. Clarendon Press, Oxford.

Canales-Rodríguez, E.J., Melie-García, L., Iturria-Medina, Y., Martínez-Montes, E., Alemán-Gómez, Y., Lin, C.P., 2008. Inferring multiple maxima in intravoxel white matter fiber distribution. Magn. Reson. Med. 60, 616–630.

Canales-Rodríguez, E.J., Lin, C.P., Iturria-Medina, Y., Yeh, C.H., Cho, K.H., Melie-García, L., 2010. Diffusion orientation transform revisited. Neuroimage 49 (2), 1326–1339.

Canales-Rodríguez, E.J., Melie-Garcia, L., Iturria-Medina, Y., 2009. Mathematical description of q-space in spherical coordinates: exact q-ball imaging. Magn. Reson. Med. 61, 1350–1367.

Ciccarelli, O., Toosy, A.T., Parker, G.J., Wheeler-Kingshott, C.A., Barker, G.J., Miller, D.H., Thompson, A.J., 2003. Diffusion tractography based group mapping of major white-matter pathways in the human brain. Neuroimage 19, 1545–1555.

Descoteaux, M., Angelino, E., Fitzgibbons, S., Deriche, R., 2007. Regularized, fast, and robust analytical Q-ball imaging. Magn. Reson. Med 58, 497–510.

Descoteaux, M., Deriche, R., Knosche, T.R., Anwander, A., 2009. Deterministic and probabilistic tractography based on complex fiber orientation distributions. IEEE Trans. Med. Imaging 28, 269–286.

Dell'Acqua, F., Rizzo, G., Scifo, P., Clarke, R.A., Scotti, G., Fazio, F., 2007. A model-based deconvolution approach to solve fiber crossing in diffusion-weighted MR imaging. IEEE Trans. Biomed. Eng. 54, 462–472.

Dell'Acqua, F., Scifo, P., Rizzo, G., Catani, M., Simmons, A., Scotti, G., Fazio, F., 2009. A modified damped Richardson Lucy algorithm to reduce isotropic background effects in spherical deconvolution. Neuroimage 49 (2), 1446–1458.

Donnelly, D., Rust, B., 2005. The fast Fourier transform for experimentalists: Part I: Concepts. Comput. Sci. Eng. 7 (2), 80–88.

Frank, L.R., 2002. Characterization of anisotropy in high angular resolution diffusion-weighted MRI. Magn. Reson. Med. 47, 1083–1099.

Gilbert, R.J., Magnusson, L.H., Napadow, V.J., Benner, T., Wang, R., Wedeen, V.J., 2006. Mapping complex myoarchitecture in the bovine tongue with diffusion–spectrum magnetic resonance imaging. Biophys. J. 91, 1014–1022.

Gilbert, R.J., Gaige, T.A., Wang, R., Benner, T., Dai, G., Glickman, J.N., Wedeen, V.J., 2008. Resolving the three-dimensional myoarchitecture of bovine esophageal wall with diffusion spectrum imaging and tractography. Cell Tissue Res. 332, 461–468.

Granziera, C., Schmahmann, J.D., Hadjikhani, N., Meyer, H., Meuli, R., Wedeen, V., Krueger, G., 2009. Diffusion spectrum imaging shows the structural basis of functional cerebellar circuits in the human cerebellum in vivo. PLoS One 4, e5101.

Habas, C., Cabanis, E.A., 2007. Anatomical parcellation of the brainstem and cerebellar white matter: a preliminary probabilistic tractography study at 3 T. Neuroradiology 49, 849–863.

Hagmann, P., Cammoun, L., Gigandet, X., Meuli, R., Honey, C.J., Wedeen, V.J., Sporns, O., 2008. Mapping the structural core of human cerebral cortex. PloS Biol. e159, 6.

Hanisch, R.J., White, R.L., Gilliland, R.L., 1997. Deconvolution of Hubble Space Telescope images and spectra. In: Jansson, P.A. (Ed.), Deconvolution of Images and Spectra. Academic Press, Boston, MA, pp. 310–356.

Högbom, J., 1974. Aperture synthesis with a non-regular distribution of interferometer baselines. Astrophys. J. Suppl. Ser. 15, 417–426.
Iturria-Medina, Y., Canales-Rodríguez, E.J., Melie-García, L., Valdés-Hernández, P.A., Martínez-Montes, E., Alemán-Gómez, Y., Sánchez-Bornot, J.M., 2007. Characterizing brain anatomical connections using diffusion weighted MRI and graph theory. Neuroimage 36, 645–660.
Iturria-Medina, Y., Sotero, R.C., Canales-Rodríguez, E.J., Aemán-Gómez, Y., Melie-García, L., 2008. Studying the human brain anatomical network via diffusion-weighted MRI and graph theory. Neuroimage 40, 1064–1076.
Johansen-Berg, H., Behrens, T.E., 2006. Just pretty pictures? What diffusion tractography can add in clinical neuroscience. Curr. Opin. Neurol. 19, 379–385.
Kuo, L.W., Chen, J.H., Wedeen, V.J., Tseng, W.Y., 2008. Optimization of diffusion spectrum imaging and q-ball imaging on clinical MRI system. Neuroimage 41, 7–18.
LeBihan, D., 2003. Looking into the functional architecture of the brain with diffusion MRI. Nat. Rev. Neurosci. 4, 469–480.
Lin, C.P., Wedeen, V.J., Chen, J.H., Yao, C., Tseng, W.Y., 2003. Validation of diffusion spectrum magnetic resonance imaging with manganese-enhanced rat optic tracts and ex vivo phantoms. Neuroimage 19, 482–495.
Liu, C., Bammer, R., Acar, B., Moseley, M.E., 2004. Characterizing non-Gaussian diffusion by using generalized diffusion tensors. Magn. Reson. Med. 51, 924–937.
Lucy, L.B., 1974. An iterative technique for the rectification of observed distributions. Astron. J. 79, 745–754.
Melie-García, L., Canales-Rodríguez, E.J., Aemán-Gómez, Y., Lin, C.P., Iturria-Medina, Y., Valdés-Hernández, P.A., 2008. A Bayesian framework to identify principal intravoxel diffusion profiles based on diffusion-weighted MR imaging. Neuroimage 42, 750–770.
Mitra, P.P., Halperin, B.I., 1995. Effects of finite gradient-pulse widths in pulsed-field-gradient diffusion measurements. J. Magn. Reson. 113, 94–101.
Narayan, R., Nityananda, R., 1986. Maximum entropy image restoration in astronomy. Ann. Rev. Astron. Astrophys. 24, 127–170.
Naylor, D.A., Tahic, M.K., 2007. Apodizing functions for Fourier transform spectroscopy. J. Opt. Soc. Am. A Opt. Image Sci. Vis. 24, 3644–3648.
Özarslan, E., Shepherd, T.M., Vemuri, B.C., Blackband, S.J., Mareci, T.H., 2006. Resolution of complex tissue microarchitecture using the diffusion orientation transform (DOT). Neuroimage 31, 1086–1103.
Parker, G.J., Stephan, K.E., Barker, G.J., Rowe, J.B., MacManus, D.G., Wheeler-Kingshott, C.A., Ciccarelli, O., Passingham, R.E., Spinks, R.L., Lemon, R.N., Turner, R., 2002a. Initial demonstration of in vivo tracing of axonal projections in the macaque brain and comparison with the human brain using diffusion tensor imaging and fast marching tractography. Neuroimage 15, 797–809.
Parker, G.J., Wheeler-Kingshott, C.A., Barker, G.J., 2002b. Estimating distributed anatomical connectivity using fast marching methods and diffusion tensor imaging. IEEE Trans. Med. Imaging 21, 505–512.
Parker, G.J., Haroon, H.A., Wheeler-Kingshott, C.A., 2003. A framework for a streamline-based probabilistic index of connectivity (PICo) using a structural interpretation of MRI diffusion measurements. J. Magn. Reson. Imaging 18, 242–254.
Perrin, M., Poupon, C., Rieul, B., Leroux, P., Constantinesco, A., Mangin, J.F., LeBihan, D., 2005. Validation of q-ball imaging with a diffusion fiber-crossing phantom on a clinical scanner. Philos. Trans. R. Soc. Lond., B Biol. Sci. 360 (1457), 881–891.
Pierpaoli, C., Basser, P.J., 1996. Toward a quantitative assessment of diffusion anisotropy. Magn. Reson. Med. 36, 893–906.
Pierpaoli, C., Jezzard, P., Basser, P.J., Barnett, A., Di, C.G., 1996. Diffusion tensor MR imaging of the human brain. Radiology 201, 637–648.
Ramírez-Manzanares, A., Rivera, M., Vemuri, B.C., Carney, P., Mareci, T., 2007. Diffusion basis functions decomposition for estimating white matter intravoxel fiber geometry. IEEE Trans. Med. Imaging 26, 1091–1102.
Richardson, W.H., 1972. Bayesian-based iterative method of image restoration. J Opt. Soc. Am. 62, 55–59.
Schmahmann, J.D., Pandya, D.N., Wang, R., Dai, G., D'Arceuil, H.E., de Crespigny, A.J., Wedeen, V.J., 2007. Association fiber pathways of the brain: parallel observations from diffusion spectrum imaging and autoradiography. Brain 130, 630–653.
Segalovitz, A., Frieden, B.R., 1978. A 'CLEAN'-type deconvolution algorithm. Astron. Astrophys. 70, 335–343.
Stockham, T., Cannon, T., Ingebretsen, R., 1975. Blind deconvolution through digital signal processing. Proc. IEEE 63, 678–692.
Tanner, J.E., Stejskal, E.O., 1968. Restricted Self-diffusion of Protons in Colloidal System by the Pulse-Gradient, Spin Echoes Method, 49 ed., pp. 1768–1777.
Tournier, J.D., Calamante, F., Gadian, D.G., Connelly, A., 2004. Direct estimation of the fiber orientation density function from diffusion-weighted MRI data using spherical deconvolution. Neuroimage 23, 1176–1185.
Tournier, J.D., Calamante, F., Connelly, A., 2007. Robust determination of the fiber orientation distribution in diffusion MRI: non-negativity constrained super-resolved spherical deconvolution. Neuroimage 35, 1459–1472.
Tournier, J.D., Yeh, C.H., Calamante, F., Cho, K.H., Connelly, A., Lin, C.P., 2008. Resolving crossing fibres using constrained spherical deconvolution: validation using diffusion-weighted imaging phantom data. Neuroimage 42, 617–625.
Tuch, D.S., 2002. MRI of complex tissue structure. PhD Thesis.
Tuch, D.S., 2004. Q-ball imaging. Magn. Reson. Med. 52, 1358–1372.
Tuch, D.S., Reese, T.G., Wiegell, M.R., Makris, N., Belliveau, J.W., Wedeen, V.J., 2002. High angular resolution diffusion imaging reveals intravoxel white matter fiber heterogeneity. Magn. Reson. Med. 48, 577–582.
Tuch, D.S., Reese, T.G., Wiegell, M.R., Wedeen, V.J., 2003. Diffusion MRI of complex neural architecture. Neuron 40, 885–895.
Wedeen, V.J., Hagmann, P., Tseng, W.Y., Reese, T.G., Weisskoff, R.M., 2005. Mapping complex tissue architecture with diffusion spectrum magnetic resonance imaging. Magn. Reson. Med. 54, 1377–1386.
Wedeen, V.J., Wang, R.P., Schmahmann, J.D., Benner, T., Tseng, W.Y., Dai, G., Pandya, D.N., Hagmann, P., D'Arceuil, H., de Crespigny, A.J., 2008. Diffusion spectrum magnetic resonance imaging (DSI) tractography of crossing fibers. Neuroimage 41, 1267–1277.
Wiest-Daessle, N., Prima, S., Coupe, P., Morrissey, S.P., Barillot, C., 2008. Rician noise removal by non-local means filtering for low signal-to-noise ratio MRI: applications to DT–MRI. Med Image Comput. Comput. Assist. Interv. Int. Conf. Med Image Comput. Comput. Assist. Interv. 11, 171–179.
Yu-Chien, W.u., Alexander, A.L., 2007. Hybrid diffusion imaging. Neuroimage 36, 617–629.
Yu-Chien, W.u., Field, A.S., Alexander, A.L., 2008. Computation of diffusion function measures in q-space using magnetic resonance hybrid diffusion imaging. IEEE Trans. Med. Imaging 27 (6).

5.4 A Bayesian framework to identify principal intravoxel diffusion profiles based on diffusion-weighted MR imaging

Autores: Lester Melie-García, Erick J Canales-Rodríguez, Yasser Alemán-Gómez, Ching-Po Lin, Yasser Iturria-Medina, Pedro Valdés-Hernández

Título: *A Bayesian framework to identify principal intravoxel diffusion profiles based on Diffusion-Weighted MR Imaging*

Revista: *Neuroimage*

Año y volumen: 2008, Vol 42, 2, 750-770

Factor de impacto (en el año de publicación): 5.69

ELSEVIER

NeuroImage

www.elsevier.com/locate/ynimg
NeuroImage 42 (2008) 750–770

A Bayesian framework to identify principal intravoxel diffusion profiles based on diffusion-weighted MR imaging

Lester Melie-García,[a,*,1] Erick J. Canales-Rodríguez,[a,1] Yasser Alemán-Gómez,[a] Ching-Po Lin,[b] Yasser Iturria-Medina,[a] and Pedro A. Valdés-Hernández[a]

[a] *Neuroimaging Department, Cuban Neuroscience Center, Havana, Cuba*
[b] *Laboratory for Brain Connectivity, Institute of Neuroscience, National Yang-Ming University, Taipei, Taiwan*

Received 10 March 2007; revised 12 April 2008; accepted 16 April 2008
Available online 30 April 2008

In this paper we introduce a new method to characterize the intravoxel anisotropy based on diffusion-weighted imaging (DWI). The proposed solution, under a fully Bayesian formalism, deals with the problem of joint Bayesian Model selection and parameter estimation to reconstruct the principal diffusion profiles or primary fiber orientations in a voxel. We develop an efficient stochastic algorithm based on the reversible jump Markov chain Monte Carlo (RJMCMC) method in order to perform the Bayesian computation. RJMCMC is a good choice for this problem because of its ability to jump between models of different dimensionality. This methodology provides posterior estimates of the parameters of interest (fiber orientation, diffusivities etc) unconditional of the model assumed. It also gives an empirical posterior distribution of the number of primary nerve fiber orientations given the DWI data. Different probability maps can be assessed using this methodology: 1) the intravoxel fiber orientation map (or orientational distribution function) that gives the probability of finding a fiber in a particular spatial orientation; 2) a three-dimensional map of the probability of finding a particular number of fibers in each voxel; 3) a three-dimensional MaxPro (maximum probability) map that provides the most probable number of fibers for each voxel.

In order to study the performance and reliability of the presented approach, we tested it on synthetic data; an ex-vivo phantom of intersecting capillaries; and DWI data from a human subject.

Keywords: Diffusion-weighted imaging (DWI); Diffusion tensor imaging; Bayesian model selection; Anisotropy characterization; Reversible jump; RJMCMC

Introduction

Diffusion-weighted imaging (DWI) is a noninvasive neuroimaging modality that provides quantitative maps of the micro-structural organization and physiological features of living tissues. This technique uses molecular water (Le Bihan, 2003) as a probe to reveal the structure and dynamics of brain tissues in normal and abnormal states. The Diffusion Tensor (DT) formalism (Basser et al., 1994a,b; Basser and Pierpaoli, 1996) has been widely employed to model the anisotropic displacements of the water molecules in brain white matter. The DT method models the diffusion profile as a single three-dimensional ellipse. When fiber bundles cross, diverge or converge, the DT approximation fails. In order to overcome this difficulty multi-fiber reconstruction algorithms have been developed, based on high angular resolution (HARD) diffusion gradient schemes (Frank, 2001, 2002; Tuch et al., 2002). Multi-compartment methods assume that only small number of different particle packets (*diffusion profiles*) diffuse in the medium with low interchange. Thus, the translational displacement of each molecular packet provides meaningful information that allows inference on the spatial geometry and the principal orientations of the medium (Tuch et al., 2002). In this case, the magnetic resonance diffusion signal will be a weighted sum of the individual contributions of each packet of water molecules.

In practice, this type of formulation has two major problems. First, the nonlinear nature of the objective function leads to the use of fitting procedures that are unstable and depend on the starting point. Second, it leads to a model selection problem that arises when selecting the correct number of k compartments. Different strategies have been proposed for model selection. For example Parker et al. (2005) used the spherical-harmonic voxel classification algorithm proposed by Alexander et al. (2002). In a study by Tuch et al. (2002) a thresholded correlation function is employed to decide whether to use $k=1$, or $k=2$. In the study by Hosey et al. (2005), the modeling framework introduced by Behrens et al. (2003) is extended, allowing a probability density function for up to 2 intravoxel fiber orientations. In this case the model selection is achieved by a Bayes factor approach that calculates the relative

* Corresponding author. Neuroimaging Department, Cuban Neuroscience Center, Ave 25, Esq. 158, #15202, PO Box 6412/6414, Cubanacan, Playa, Havana, Cuba. Fax: +53 7 208 6707.
E-mail address: lester@cneuro.edu.cu (L. Melie-García).
[1] These authors contributed equally.
Available online on ScienceDirect (www.sciencedirect.com).

1053-8119/$ - see front matter © 2008 Published by Elsevier Inc.
doi:10.1016/j.neuroimage.2008.04.242

probabilities of $k=1$ and $k=2$ fiber models. One limitation of these methodologies is that they estimate a maximum of $k=2$ fiber bundles (Hosey et al., 2005; Tuch et al., 2002). Recently Behrens et al. (2007) proposed a Bayesian Automatic Relevance Determination (ARD) method to infer the number of fibers. This approach detects up to 3 orthogonal fibers for simulated data requiring b-values higher than 4000 s/mm^2 and a gradient encoding scheme with at least 60 directions.

This paper proposes a solution for the multi-fiber model selection problem based on the Bayesian reversible jump Markov chain Monte Carlo (RJMCMC) formalism. It follows a previous proposal (Melie-García et al., 2004). RJMCMC has been widely used in other research and application fields (Andrieu et al., 2001; Andrieu and Doucet, 1999; Bandyopadhyay, 2005; Bertrand et al., 2001; Brooks, 2001; Green, 1995; Larocque et al., 2002; Richardson and Green, 1997; Rue and Hurn, 1999; Stephens, 1998). RJMCMC is based on a Markov chain that jumps between models of different dimensionality in the Bayesian computation. RJMCMC provides: a) posterior estimates of diffusion model parameters (fiber orientations, diffusivities, fiber volume fractions, etc.); b) posterior expected values of model parameters unconditional on the model assumed; and a particularly novel feature c) the empirical marginal posterior of the number of diffusion profiles k (number of fibers) given the diffusion data.

The paper is organized as follows: the Methods section introduces a general Bayesian formalism for the identification of the principal diffusion profiles in a voxel. We then propose the RJMCMC algorithm based on the model introduced by Behrens et al. (2003, 2007). The Results section is devoted to the evaluation of the performance of our method on synthetic data, a capillary MRI phantom, and data from a human subject. The final section is dedicated to discussion of the main results and the unique contributions of this paper. Appendixes present mathematical details for completeness.

Methods

In this section we introduce a general Bayesian modeling framework to detect and describe the principal intravoxel diffusion profiles. Henceforth 'diffusion profile' and 'fiber' will be used interchangeably.

Problem statement

In order to formalize the problem of inferring the components in a multi-compartmental model we define a Cartesian coordinate system XYZ centered in one voxel where 'k' nerve fiber bundles reside. Fig. 1 represents a single fiber bundle, with orientation vector $\vec{p}_j$ parameterized by φ and θ as azimuthal and elevation angles respectively.

The number of fibers 'k' is a priori unknown, so the DWI signal S_i observed in a gradient direction $\vec{u}_i(\alpha,\beta)=\vec{g}_i/|\vec{g}_i|$, of N_g encoding diffusion gradients (see Fig. 1) could be expressed by one of the following models $M_0,\ldots,M_{k_{\max}}$:

$$\begin{cases} S_i=\mu_i+\varepsilon_i & \\ M_0:\mu_i=f_0\mathcal{K}_{i0}(\Theta_0,\wp_i) & \\ M_1:\mu_i=f_0\mathcal{K}_{i0}(\Theta_0,\wp_i)+f_1\mathcal{K}_{i1}(\Theta_1,\wp_i) & \\ \vdots & \vdots \\ M_k:\mu_i=f_0\mathcal{K}_{i0}(\Theta_0,\wp_i)+\ldots+f_k\mathcal{K}_{ik}(\Theta_k,\wp_i) & \\ \vdots & \vdots \\ M_{k_{\max}}:\mu_i=f_0\mathcal{K}_{i0}(\Theta_0,\wp_i)+\ldots+f_k\mathcal{K}_{ik}(\Theta_k,\wp_i)+\ldots+f_{k_{\max}}\mathcal{K}_{ik_{\max}}(\Theta_{k_{\max}},\wp_i) & \end{cases} \quad (1)$$

where μ_i is the predicted diffusion signal. The difference between models $M_0,\ldots,M_{k_{\max}}$ is the number of k diffusion profiles. Thus, k defines the order or dimension of the model M_k. Term f_j is the volume fraction for the profile j, so that $\sum_{j=0}^{k} f_j=1$. The term $\mathcal{K}_{ij}(\Theta_j,\wp_i)$ characterizes the generative model of the diffusion signal for profile j in the diffusion gradient orientation i where Θ_j represents the parameters of diffusion profile j (orientation, diffusivities etc). $\wp_i$ encloses the experimental parameters or/and MR pulse sequence setup, (e.g. b-value, diffusion gradient orientation). The experimental noise for the $\vec{u}_i$ direction of the diffusion gradient scheme is represented by ε_i. Model M_0 defines a single diffusion profile that is different from the other modeled profiles. The term $\mathcal{K}_{i0}(\Theta_0,\wp_i)$ describes a diffusion process dissimilar to every one of 'k' previous diffusion profiles and is parameterized by Θ_0. In our modeling framework this term plays the role of explaining the diffusion signal when none of the 'k' diffusion profiles is present. For example, this function could be regarded as an isotropic diffusion process in a mixture of 'k' anisotropic processes. Model M_0 could be also considered as measurement noise, where $\mathcal{K}_{i0}(\Theta_0,\wp_i)=0$ would specify the absence of water diffusion processes in the medium.

Eq. (1) can be generalized assuming different expressions for $\mathcal{K}_{ij}(\Theta_j,\wp_i)$ to model mixtures of diffusion profiles of different kinds (different diffusion properties). This provides the flexibility to model the complex micro-geometries of living tissue.

Having defined the general framework for the generative model of the diffusion signal, the main problem can be stated with the following questions: 1) Given the DWI data, how do we select the correct model M_k among $k_{\max}+1$ candidate models $M_0,\ldots,M_{k_{\max}}$? This corresponds to selecting the exact number of resident diffusion profiles 'k'; 2) Once the correct model M_k has been identified, how do we infer the principal orientations and other parameters that describe the k intravoxel diffusion profiles? In the following sections we will introduce a novel and efficient approach to tackle both the model selection problem (question 1) and the model estimation problem (question 2).

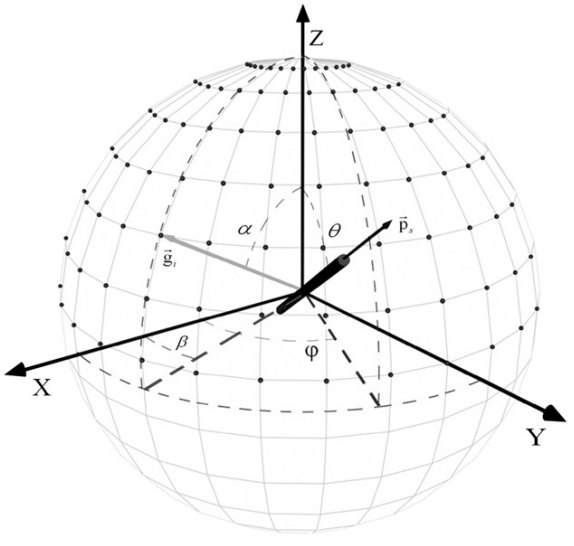

Fig. 1. This figure shows one of the 'k' fibers in a voxel and the experimental gradient scheme used for measuring the DWI signal. Black dots on the sphere represent the gradient encoding scheme. Vector $\vec{g}_i$ represents the ith gradient parameterized by the angles α and β. The vector $\vec{p}_s$ represents the principal orientation of the diffusion profile, where φ and θ are the azimuthal and elevation angles respectively.

A generative model for the predicted diffusion signal

We selected the degenerate diffusion multi-tensor model proposed by Behrens et al. (2007) in order to introduce the new methodology. The generative model of the predicted diffusion signal of a mixture of 'k' diffusion profiles is expressed as:

$$\mu_i = S_0\left(f_0\ \exp\left(-b_i\lambda\right) + \sum_{j=1}^{k} f_j\ \exp\left(-b_i\lambda\ \overrightarrow{u_i}^{\mathrm{T}}\mathbf{R}(\theta_j,\varphi_j)\mathbf{A}\mathbf{R}^{\mathrm{T}}(\theta_j,\varphi_j)\ \overrightarrow{u_i}\right)\right) \tag{2}$$

where $\mathbf{A} = \begin{pmatrix}1&0&0\\0&0&0\\0&0&0\end{pmatrix}$; $f_0 = \left(1 - \sum_{j=1}^{k} f_j\right)$, $\mathbf{R}(\theta_j, \varphi_j)$ is the rotation matrix that rotates $\mathbf{A}$ so that its only eigenvector aligns with the fiber orientation represented by (θ_j, φ_j); where φ_j and θ_j are the azimuthal and elevation angles respectively (see Fig. 1); λ represents the medium diffusivity and S_0 represents the diffusion signal value measured in the absence of a diffusion gradient pulse ($b=0$).

The diffusion profiles are defined as the anisotropic part of Eq. (2) given by $\mathcal{K}_{ij}(\Theta_j, \wp_i) = S_0\ \exp\left(-b_i\lambda\ \overrightarrow{u}_i^{\mathrm{T}}\mathbf{R}(\theta_j,\varphi_j)\mathbf{A}\mathbf{R}^{\mathrm{T}}(\theta_j,\varphi_j)\ \overrightarrow{u_i}\right)$, with parameters $\Theta_j=(\theta_j, \varphi_j, \lambda, S_0)$. In this case $\mathcal{K}_{ij}(\Theta_j, \wp_i)$ models the diffusion in and around axons where diffusion only occurs along the fiber direction (θ_j, φ_j) (Behrens et al., 2003). The experimental parameters $\wp_i$ are defined as $\wp_i = (b_i, \overrightarrow{u_i})$, where b_i is the b-value for the gradient direction $\overrightarrow{u_i}$. The term $\mathcal{K}_{i0}$ defines the isotropic diffusion profile expressed by $\mathcal{K}_{i0}(\Theta_0, \wp_i) = S_0\ \exp\left(-b_i\lambda\right)$. This models the free water diffusion process in the voxel, where $\Theta_0=(\lambda, S_0)$. As in Behrens et al. (2003, 2007), S_0 signal and diffusivity λ are assumed constant across the voxel.

Bayesian modeling: general aims

In this section we introduce a Bayesian formalism to detect the diffusion profiles that characterize the tissue heterogeneity in a voxel. We set out the forward probabilistic generative model in which we define the Likelihood function and priors for each parameter of the model including the number of diffusion profiles k. Through Bayes Theorem we can obtain posterior probabilities for the model parameters given the data. These combine Likelihood and prior probability distributions.

Likelihood

Assuming a Gaussian distribution for the noise $\boldsymbol{\varepsilon} = [\varepsilon_1, \ldots, \varepsilon_{N_g}]$ so that $\boldsymbol{\varepsilon} \sim N(\mathbf{0}, \boldsymbol{\Sigma})$, the Likelihood function for measured diffusion signal $S = [S_1, \ldots, S_{N_g}]$ of N_g encoding diffusion gradients, (see Eq. (1)) is given by:

$$p(\mathbf{S}|\boldsymbol{\varphi}_k, \boldsymbol{\theta}_k, \mathbf{f}_k, \lambda, S_0, k, \boldsymbol{\Sigma}) = \frac{1}{(2\pi)^{N_g/2}|\boldsymbol{\Sigma}|^{1/2}}\ \exp\left(-\frac{1}{2}(\mathbf{S}-\mathbf{S}_k)^{\mathrm{T}}\boldsymbol{\Sigma}^{-1}(\mathbf{S}-\mathbf{S}_k)\right) \tag{3}$$

where, $\mathbf{S}_k=[\mu_1,\ldots,\mu_{N_g}]$ is the predicted diffusion signal vector for model M_k (see Eqs. (1) and (2)), and $\boldsymbol{\varphi}_k=[\varphi_1,\ldots,\varphi_k]$, $\boldsymbol{\theta}_k=[\theta_1,\ldots,\theta_k]$, $\mathbf{f}_k=[f_1,\ldots f_k]$ are the orientation and volume fraction vectors respectively that characterize the k diffusion profiles.

Assuming that $\boldsymbol{\Sigma}=\sigma^2\mathbf{I}$, where σ is the noise standard deviation, the Likelihood becomes:

$$p(\mathbf{S}|\boldsymbol{\varphi}_k, \boldsymbol{\theta}_k, \mathbf{f}_k, \lambda, S_0, k, 1/\sigma^2) = \prod_{i=1}^{N_g} p(S_i|\boldsymbol{\varphi}_k, \boldsymbol{\theta}_k, \mathbf{f}_k, \lambda, S_0, k, 1/\sigma^2) \tag{4}$$

where,

$$p(S_i|\boldsymbol{\varphi}_k, \boldsymbol{\theta}_k, \mathbf{f}_k, \lambda, S_0, k, 1/\sigma^2) = \frac{1}{\sqrt{2\pi}\sigma}\ \exp\left(-\frac{1}{2\sigma^2}(S_i-\mu_i)^2\right) \tag{5}$$

Prior distributions

Fig. 2 defines the hierarchical structure for the prior distributions of the model parameters graphically.

The joint prior probability for the model parameters $p(\boldsymbol{\varphi}_k, \boldsymbol{\theta}_k, \mathbf{f}_k, \lambda, S_0, k, 1/\sigma^2)$ is given by:

$$p(\boldsymbol{\varphi}_k, \boldsymbol{\theta}_k, \mathbf{f}_k, \lambda, S_0, k, 1/\sigma^2) = p(\boldsymbol{\varphi}_k, \boldsymbol{\theta}_k|a_\varphi, b_\varphi, a_\theta, b_\theta, k)p(\mathbf{f}_k|k)p(S_0|a_{S_0}, b_{S_0}) \cdot \cdot\ p(\lambda|a_\lambda, b_\lambda)p(k|\Lambda)p(\Lambda|a_\Lambda, b_\Lambda)p(1/\sigma^2|a_\sigma, b_\sigma) \tag{6}$$

Each of the parameters $\boldsymbol{\varphi}_k$, $\boldsymbol{\theta}_k$, $\mathbf{f}_k$, λ, S_0, $1/\sigma^2$ is subject to a non-informative prior reflecting our lack of knowledge other than that the parameter must be positive:

- $p\left(\boldsymbol{\varphi}_k, \boldsymbol{\theta}_k|a_\varphi, b_\varphi, a_\theta, b_\theta, k\right) = \prod_{i=1}^{k} U_s(\varphi_i, \theta_i|a_\varphi, b_\varphi, a_\theta, b_\theta) = \frac{1}{(4\pi)^k}\ \prod_{i=1}^{k}\ \sin\theta_i$, where U_s is a uniform distribution on the sphere $a_\theta=a_\varphi=0$, $b_\varphi=2\pi$ and $b_\theta=\pi$. Parameters a_φ and b_φ are the lower and upper bound respectively of the azimuth angle, a_θ and b_θ correspond to the lower and upper bound of the elevation angle.
- $p(\mathbf{f}_k|k)=\mathrm{Di}_k(\mathbf{f}_k|\boldsymbol{\alpha})$: is a Dirichlet distribution, $\boldsymbol{\alpha}=(\alpha_1,\ldots,\ \alpha_{k+1})$ where $\alpha_i=1$, $i=1,\ldots,\ k$.
- $p(S_0|a_{S_0}, b_{S_0}) = U(a_{S_0}, b_{S_0})$, where U is the uniform distribution $a_{S_0} = 0$, $b_{S_0} = \infty$.
- $p(\lambda|a_\lambda,\ b_\lambda)=\mathrm{Ga}(a_\lambda,\ b_\lambda)$; $a_\lambda=1$, $b_\lambda \ll 1$.
- $p(1/\sigma^2|a_\sigma,\ b_\sigma)=\mathrm{Ga}(a_\sigma,\ b_\sigma)$, $a_\sigma=1$, $b_\sigma \ll 1$.

For the number of fiber parameter 'k' the prior we chose was:

- $p(k|\Lambda) = C\cdot\mathrm{Po}(k|\Lambda) = \frac{\Lambda^k/k!}{\sum_{j=1}^{k_{\max}}\Lambda^j/j!}$, $k = 0, \ldots, k_{\max}$;

$$C = 1\Big/\sum_{j=1}^{k_{\max}}\Lambda^j\frac{\exp(-\Lambda)}{j!}.$$

The mean value Λ of the truncated Poisson distribution Po provides the expected number of fibers in a voxel. Apriori this is assumed to be a random variable with a gamma probability distribution function $p(\Lambda|a_\Lambda,b_\Lambda)=\mathrm{Ga}(1/2+a_\Lambda,b_\Lambda)$. Hyperparameters a_Λ,b_Λ depend on the anisotropy linear coefficient CL (Westin et al., 1997). This coefficient provides information about the linear shape of the diffusion

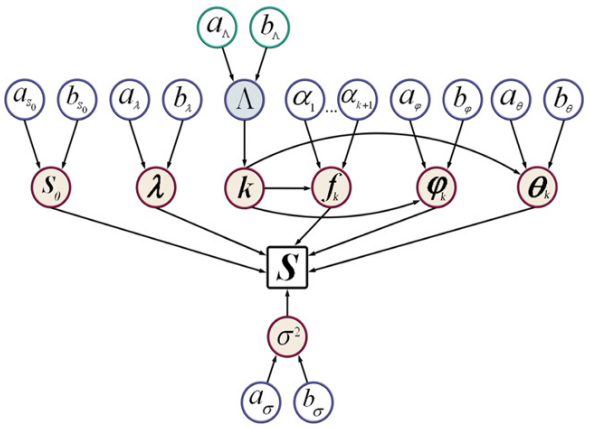

Fig. 2. Hierarchical structure for the prior distribution of the parameters. (A color version of this figure is available in the online issue.)

tensor calculated using the DWI data. Based on experimental findings, there is a strong evidence for CL≥0.8 in the presence of a single fiber inside the voxel, for example, in major white matter tracts such as corpus callosum. Thus, for CL≥0.8 we selected $a_\Lambda, b_\Lambda \gg 1$ so that $p(\Lambda|a_\Lambda, b_\Lambda)$ will have a mean value close to 1 and very small variance. Otherwise, when CL<0.8, a_Λ, b_Λ we chose $a_\Lambda, b_\Lambda \ll 1$ so that $p(\Lambda|a_\Lambda, b_\Lambda)$ yields an uninformative prior. Thus all Λ values are equiprobable which reflects our lack of apriori knowledge about the number of diffusion profiles. We suggest this is an appropriate and relatively unconstrained method of introducing prior information about the number of profiles 'k' based on the same DWI data.

Posterior distributions

We obtain the posterior probabilities of the model parameters using Bayes Theorem combining Likelihood function and prior probability functions obtained in Eqs. (4) and (6) respectively. This is:

$$p\left(\boldsymbol{\varphi}_k, \boldsymbol{\theta}_k, \mathbf{f}_k, \lambda, S_0, k, 1/\sigma^2|\mathbf{S}\right) \propto p\left(\mathbf{S}|\boldsymbol{\varphi}_k, \boldsymbol{\theta}_k, \mathbf{f}_k, \lambda, S_0, k, 1/\sigma^2\right) \cdot p\left(\boldsymbol{\varphi}_k, \boldsymbol{\theta}_k, \mathbf{f}_k, \lambda, S_0, k, 1/\sigma^2\right). \quad (7)$$

We are interested only in the posterior pdf on a subset of model parameters describing the number of diffusion profiles and their properties. Obtaining these *marginal* distributions involves performing large integrals:

$$p(\Omega_i|\mathbf{S}) = \int p(\Omega|\mathbf{S}) \mathrm{d}\Omega_{-i} \quad (8)$$

where $\Omega=[\lambda, S_0, \boldsymbol{\varphi}_k, \boldsymbol{\theta}_k, \mathbf{f}_k, \Lambda]$ is the set of parameters, Ω_i is the parameter of interest and Ω_{-i} represents all other parameters. These integrals are seldom tractable analytically.

Bayesian modeling: inference algorithm

RJMCMC algorithm: general aims

It is obvious that estimation using Eq. (8) cannot be performed analytically due to the combination of nonlinear dependences of the parameters of interest and high multidimensional integrals. Markov chain Monte Carlo (MCMC) techniques (Gilks, 1995) are efficient in this situation due to their simulation of probability distributions that cannot be derived analytically. In our problem it is necessary to construct a Markov chain able to sample the joint posterior distribution of the model order 'k' and model parameters and the chain must be able to move across subspaces of different dimensions defined by models $M_0, \ldots, M_{k_{\max}}$. However, standard MCMC techniques are not able to jump between subspaces of different dimensions. We therefore employed an efficient MCMC sampler referred to as reversible jump MCMC (RJMCMC). This is designed to jump between subspaces (Green, 1995). RJMCMC allows for dimensional changes in the probability distribution being simulated and can be used for model selection in cases where dimensionality may change. In general the algorithm is composed of the following steps:

– A set of moves are selected.
– RJMCMC randomly "walks around" the space of candidate models $M_0, \ldots, M_{k_{\max}}$ by changing one fiber at a time (adding or deleting one fiber). Each move is chosen with a particular probability.
– At each move in its "walk", all model parameters are updated.
– At the end, we have a list of all visited models at each move and their corresponding set of parameters.
– We can calculate different outcome measures: the most probable model (most visited model), the mean and variance for parameters belonging to a particular model M_k, the probability of visiting a specific model M_k given the data, etc.

The following sections will adapt the RJMCMC algorithm to our specific problem and will give details of the implementation of RJMCMC outcome measures.

RJMCMC algorithm for a diffusion model with unknown number of fibers

In order to set up our RJMCMC algorithm we selected the following reversible jumps: 1) Birth of a new fiber, 2) Death of an existing fiber. 3) Merging of two fibers, 4) Splitting of one fiber into two fibers; 5) Updating of the parameters for all fibers and the nuisance parameter. Moves from 1 to 4 implies changes from 'k' to 'k'+1 or $k-1$. A brief description of moves from 1 to 4 can be found below:

1. Birth/death moves are given by:
   a) Proposing a new fiber at random on the sphere.
   b) Removing one of the existing fibers chosen at random.
2. Split/merge moves consist of:
   a) Splitting a fiber into two new fibers;
   b) Merging two fibers into one.

We summarize the main procedure of the RJMCMC algorithm in Table 1.

We develop a detailed description of different moves including their acceptance probabilities in Appendix B.

So, at each iteration of the RJMCMC algorithm, one of the 5 candidate moves – birth; death; split; merge; or update – is randomly selected with particular probabilities b_k, d_k, s_k, m_k, u_k respectively, so that $b_k+d_k+s_k+m_k+u_k=1$ for all $0 \le k \le k_{\max}$. For $k=0$, death, merge and split moves are not permitted so that $d_0=m_0=s_0=0$. A merge move is not allowed for $k=1$ so, $m_1=0$. For $k=k_{\max}$ birth and split moves are not permitted, therefore $b_{k_{\max}} = s_{k_{\max}} = 0$. We have introduced a heuristic term f_{thres} that is useful to avoid the birth of diffusion profiles with very low contributions to the diffusion signal to reduce the possibility of overfitting. In consequence, when the condition $\sum_{j=1}^{k} f_j > 1 - f_{\text{thres}}$ is met, the birth move is not allowed so $b_k=0$. The split move will not be allowed when the fiber to be divided into two has a volume fraction f_{split} such that $f_{\text{split}} < 2f_{\text{thres}}$. As in the previous case, this restriction penalizes the birth of fibers with low contributions as well. Excepting the aforementioned cases the move probabilities are defined as:

$$\begin{aligned} b_k &= s_k = c\ \min\{1, p(k+1|\Lambda)/p(k|\Lambda)\} \\ d_{k+1} &= m_{k+1} = c\ \min\{1, p(k|\Lambda)/p(k+1|\Lambda)\} \end{aligned} \quad (9)$$

where $p(k|\Lambda)$ is the model M_k prior probability and 'c' is a parameter that tunes the proportion of dimension and update moves. In our case as in other applications (Andrieu et al., 2001) we took $c=0.4$, so that $b_k+d_k+s_k+m_k \in [0.4,1]$ for all k. Therefore, the update step will have a proportion of $u_k=1-b_k-d_k-s_k-m_k=0.4$.

In our algorithm the update move is chosen to be the most probable. This facilitates reaching a stable state in the Markov chain (MC) and therefore the parameter estimates once a particular move type is accepted. As we can see in Eq. (9) the probability of the different move types depends on the prior for the number of fibers. This prior has direct implications for models with higher

Table 1
Main procedure of the reversible jump Markov chain Monte Carlo (RJMCMC) algorithm

Reversible MCMC algorithm (main procedure)
1. Initialization: set initial values for the model parameters ($k^{(0)}$, $\boldsymbol{\varphi}_k^{(0)}$, $\boldsymbol{\theta}_k^{(0)}$, $\mathbf{f}_k^{(0)}$, $\lambda^{(0)}$, $S_0^{(0)}$, $1/\sigma^{2(0)}$, $\Lambda^{(0)}$) belonging to the support of the posterior distribution in Eq. (7).
2. Iteration i
• Draw $u \sim U(0,1)$
• If $(u \le b_{k^{(i)}})$
– then 'birth' (see Birth/death section in Appendix B.1)
– else if $(u \le b_{k^{(i)}} + d_{k^{(i)}})$ then 'death' a fiber (see Birth/death section in Appendix B.1)
– else if $(u \le b_{k^{(i)}} + d_{k^{(i)}} + s_{k^{(i)}})$ then 'split' a fiber into two (see Merge/split section in Appendix B.2)
– else if $(u \le b_{k^{(i)}} + d_{k^{(i)}} + s_{k^{(i)}} + m_{k^{(i)}})$ then 'merge' two fiber into one (see Merge/split section in Appendix B.2)
– else update the parameters (see Update section in Appendix B.3)
End if
3. $i=i+1$ and go to 2

number of fibers in different ways: a) the moves related to model order reduction (like death: $M_{k+1} \rightarrow M_k$) are favored with higher acceptance probabilities (see Appendix B) as k increases, conversely birth move acceptance probability is penalized by the model order (see Appendix B, Eq. (34)); b) the RJMCMC move probabilities b_k, d_k, s_k, m_k are modulated by the current number of fibers. In this way, we reduce RJMCMC overfitting and MC convergence is improved.

RJMCMC outcomes — probability maps

The estimates of the model parameters are obtained by drawing N_s samples after the burn-in period of the Markov chain. Model selection (number of fibers) is determined by choosing the model order through $\arg\max_{k\in\{0,\dots,k_{\max}\}} p(k|\mathbf{S})$, which is the most visited model by the RJMCMC algorithm that has the highest probability among the candidates $M_0, \dots, M_{k_{\max}}$.

The probability of finding a particular number of diffusion profiles j in a voxel can be calculated by:

$$p(k=j|\mathbf{S}) = \frac{N_j}{N_s} \tag{10}$$

where N_j is the number of times the model M_j was visited by the RJMCMC algorithm in N_s samples. On the other hand, the expected values of the parameters that describe the diffusion profiles for a particular number of k fibers are calculated by:

$$E(\Omega_k|\mathbf{S}, k=j) = \frac{1}{N_j}\sum_{i=1}^{N_s} \Omega_{k^{(i)}}^{(i)} \mathrm{I}_{\{j\}}\left(k^{(i)}\right) \tag{11}$$

where Ω_k as before encloses $\Omega_k=[\lambda, S_0, \boldsymbol{\varphi}_k, \boldsymbol{\theta}_k, \mathbf{f}_k]$ and $\mathrm{I}_{\{j\}}(k^{(i)})$ is an indicator function so that $\mathrm{I}_{\{j\}}(k^{(i)})=1$ if at iteration i of the RJMCMC algorithm we have $k^{(i)}=j$, $\mathrm{I}_{\{j\}}(k^{(i)})=0$ otherwise.

Eq. (10) gives the marginal posterior distribution of the models $M_0, \dots, M_{k_{\max}}$. Hence, the posterior expected values $\widetilde{\Omega}$ of the parameters that describe the diffusion profiles unconditional on the competing generative models $M_0, \dots, M_{k_{\max}}$ can be achieved combining Eqs. (10) and (11) resulting in:

$$E\left(\widetilde{\Omega}|\mathbf{S}\right) = \sum_{k=0}^{k_{\max}} E(\Omega_k|\mathbf{S}, k)p(k|\mathbf{S}). \tag{12}$$

This is the third level of inference in the Bayesian formalism known as *Bayesian model averaging* (BMA) that accounts for the uncertainty inherent in the model selection process (Hoeting et al., 1999). By averaging over different competing models $M_0, \dots, M_{k_{\max}}$, BMA incorporates model uncertainty into conclusions about diffusion profile parameters. Hence, the expression for obtaining posterior expected values of the parameters is obtained by substituting Eqs. (10) and (11) into (12):

$$E\left(\widetilde{\Omega}|\mathbf{S}\right) = \frac{1}{N_s}\sum_{i=1}^{N_s} \Omega_{k^{(i)}}^{(i)} \tag{13}$$

Note that sum in Eq. (13) is taken independently of model M_k.

Orientation distribution of nerve fibers

The volume fraction that occupies a fiber in a unit volume gives the probability of finding a particular fiber in a voxel. Thus, for the special case of the fiber volume fraction f the evaluation of Eq. (13) yields a fiber orientation distribution function. Hence, the probability of finding a fiber in a specific angular position (φ, θ), unconditional on the model assumed, can be calculated by:

$$P_f\left(f^{(\varphi,\theta)}|\mathbf{S}\right) = \frac{1}{N_s}\sum_{i=1}^{N_s} f_i^{(\varphi,\theta)} \tag{14}$$

where $f_i^{(\varphi,\theta)}$ is the volume fraction for iteration i at the spatial orientation (φ, θ). Intuitively, this type of map reveals the number of times the RJMCMC algorithm has visited each spatial position (φ, θ) weighted by the volume fraction for all models $M_0, \dots, M_{k_{\max}}$.

Probability map of number of fibers

The RJMCMC methodology provides a way to assess the map of the probabilities of finding a specific number of fibers in a particular brain region. This is a three-dimensional map P_k where for a particular voxel at location x, y, z is obtained with:

$$P_k(x,y,z) = p(k=j|\mathbf{S}) \tag{15}$$

for $j=0,\dots, k_{\max}$. Therefore we can obtain $P_0, \dots, P_{k_{\max}}$ three-dimensional fiber probability images. The term $p(k=j|\mathbf{S})$ is computed using Eq. (11). This type of map has not been reported before and may provide a measure to evaluate the anisotropy of the white matter in a single subject and in subject populations.

Map of the most probable number of fibers

The three-dimensional map of the number of fibers $P_{\max}$ is another outcome of the RJMCMC method. This map gives the most likely number of fibers at each voxel. For a particular voxel at location x, y, z of the $P_{\max}$ map is calculated by:

$$P_{\max}(x,y,z) = \arg\max_{k\in\{0,\dots,k_{\max}\}} p(k|\mathbf{S}). \tag{16}$$

Results

Evaluation of the method using synthetic data

General setup

We generated a set of synthetic data in order to test the performance of the method introduced in this paper. We used the model defined in Eq. (2) to create the simulated diffusion signal with the following

experimental parameters: $S_0=100$, a diffusivity value of $\lambda=1.5$ mm^2/s, a set of b-values=1000, 2000, 3000, 4000, 5000, 6000 s/mm^2, and gradient encoding schemes of $N=42$, 60, 122 directions uniformly distributed over the sphere. Different fiber configurations were simulated from 1 to 5 fibers (fiber=[φ, θ, f]) as follows: *1 fiber*: fiber1=[90°, 45°, 0.5]; *2 fibers*: fiber1=[90°, 45°, 0.35], fiber2=[90°, 135°, 0.35]; *3 fibers*: fiber1=[90°, 45°, 0.25] , fiber2=[90°, 135°, 0.25], fiber3=[45°, 90°, 0.25]; *4 fibers*: fiber1=[90°, 45°, 0.2] , fiber2=[90°, 135°, 0.2], fiber3=[45°, 90°, 0.2], fiber4=[135°, 90°, 0.2]; *5 fibers*: fiber1=[90°, 45°, 0.15] , fiber2=[90°, 135°, 0.15], fiber3=[45°, 90°, 0.15], fiber4=[135°, 90°, 0.15], fiber5=[80°, 80°, 0.15].

The diffusion signal for each of the preceding fiber configurations was corrupted by Rician noise with different signal to noise ratios (SNR). The SNR was related to the S_0 image with SNR=S_0/σ. The selected SNRs were 5, 8, 15, 20 and 30. Note that our methodology has been developed assuming Gaussian noise, but we generated the simulated data using Rician noise to test our methodology under this modeling misspecification. However, for the selected SNRs>4 the Rician distribution function approximates a Gaussian distribution (Salvador et al., 2005).

For each SNR value, gradient encoding schemes N, set of b-values and fiber configurations, we created 15 repetitions of the diffusion signal. For the RJMCMC algorithm setup, we ran a Markov chain of 30,000 samples. The burn-in period was 10,000 samples and the remainder (N_s=20,000) were used to calculate the diffusion profile parameters and their statistics. The maximum number of fibers allowed was $k_{max}=7$.

We used two measures to evaluate the performance of the RJMCMC methodology: 1) fiber localization error and 2) blurring or dispersion around the mean of the fiber orientation.

The localization error measures the accuracy of the spatial fiber configuration reconstruction defined as the average minimum angle between the estimated and the 'true' fiber orientations (Tuch et al., 2002). Each sample of the N_s in the MC is forced to belong to one of the n clusters corresponding to the n simulated fibers. If the minimum angle between a particular orientation sample 'j' and the n true fiber populations correspond to the 'c' fiber, then the sample 'j' is classified as belonging to the 'c' cluster. The mean orientation value $\overline{\boldsymbol{e}}_c$ and the blurring β^c_{blurr} for each cluster are calculated with:

$$\overline{\boldsymbol{e}}_c = \frac{1}{N_c}\sum_{k=1}^{N_c}\boldsymbol{e}_{ck} \tag{17}$$

$$\beta^c_{\text{blurr}} = \frac{1}{N_c}\sum_{k=1}^{N_c} \text{acos}\left[\text{abs}\left(\overline{\boldsymbol{e}}_c^{\text{T}}\cdot\boldsymbol{e}_{ck}\right)\right] \tag{18}$$

where $\boldsymbol{e}_{ck}$ is a unit vector in Cartesian coordinates that represents the orientation of the 'k' sample of N_c points that belong to the cluster 'c'.

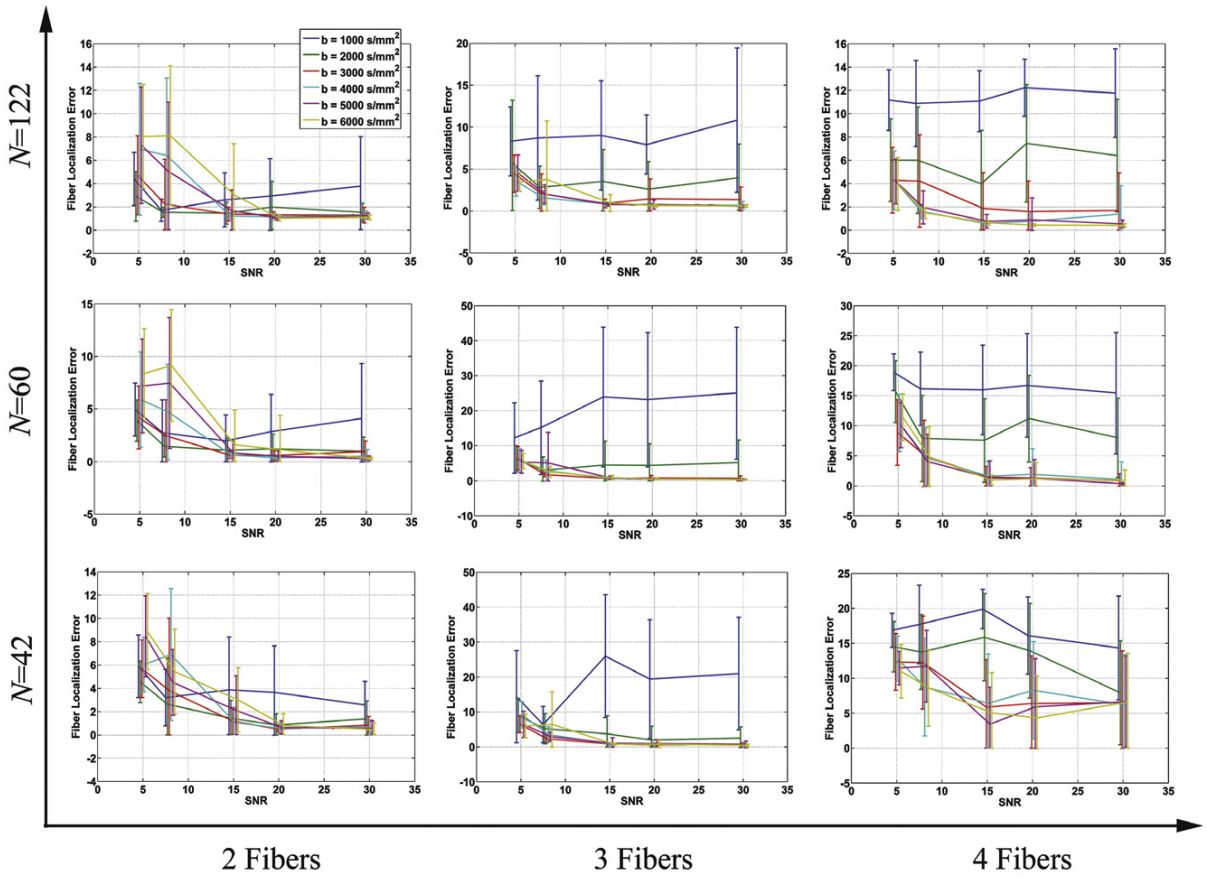

Fig. 3. Results of performance evaluation of the RJMCMC method on simulated data. The calculated localization error using Eq. (19) is shown for different numbers of gradient encoding directions N=42, 60, 122; different signal to noise ratios SNR=5, 8, 15, 20, 30, b-values=1000, 2000, 3000, 4000, 5000, 6000 s/mm^2 and configurations of 2, 3, 4 and 5 fibers. (A color figure is available in the online issue.)

The localization error of the fiber configuration is computed as:

$$\beta_{\text{err}} = \frac{1}{n}\sum_{c=1}^{n} \text{acos}\left[\text{abs}\left(\overline{\boldsymbol{e}}_c^{\text{T}} \cdot \boldsymbol{v}_c\right)\right] \tag{19}$$

where $\boldsymbol{v}_c$ is the unit vector representing the true fiber orientations. Blurring is defined as:

$$\beta_{\text{blurr}} = \frac{1}{n}\sum_{c=1}^{n} \beta_{\text{blurr}}^{c}. \tag{20}$$

Influence of SNR, b-value and gradient encoding schemes

Figs. 3 and 4 depict the influence of noise on the spatial localization accuracy of the diffusion profiles, and the associated blurring given by Eqs. (19) and (20). As expected, the spatial dispersion (blurring) around the mean fiber localization as well as the localization error (LE) increases as SNR decreases.

Blurring and LE increase with the number of diffusion profiles. This increase can be explained by the greater uncertainty in the parameters when the number of estimated parameters increases.

The LE decreases when the *b*-value increases for a specific gradient encoding scheme and a particular fiber configuration. In the case of the configuration of 2 fibers the LE doesn't change significantly, and ranges between 2 and 8°. For the 3 fiber configuration the LE decreases when SNR increases (except for *b*-value = 1000 s/mm^2). The major LE was 30° obtained for the 4 fiber configuration. The estimation of this configuration was the most affected by *b*-value and the number of gradient encoding variations. The maximum blurring (20° approximately) was attained for a *b*-value = 1000 s/mm^2, 3 and 4 fiber configurations and a gradient encoding scheme of 42 directions. In general, the blurring measure increases as *b*-value decreases.

Figs. 5–7 show the average fiber orientation probability maps (defined by the normalized version of the Eq. (14)) over 15 repetitions of the simulation. Only maps corresponding to *b*-values = 2000 and 4000 s/mm^2 and configurations of 2, 3, 4 and 5 fibers are shown.

For the case of the 4 fiber configuration a blurred fiber appears with orientation ($\varphi = 90°$, $\theta = 90°$) that coincides with the center of mass of the input fiber orientations. This result is most prominent for the case of 42 encoding gradients and *b*-value = 2000 s/mm^2. The underestimation this represents can be explained by the fact that the experimental parameters (*b*-value and number of gradients) provide insufficient information to resolve configurations with 4 fibers. The most probable number of fibers estimated was two for all SNRs in the case of the 5 fiber simulation (Fig. 5). Further analysis of these 5 fiber results showed that the RJMCMC algorithm spent most time in two different configurations, each of two fibers. The first configuration consisted of two fibers in the vertical plane, approximately localized around: fiber1 = [45°, 90°] and fiber2 = [135°, 90°]. The second configuration consisted of two fibers in the horizontal plane around the locations of fiber1 = [90°, 45°] and fiber2 = [90°, 135°].

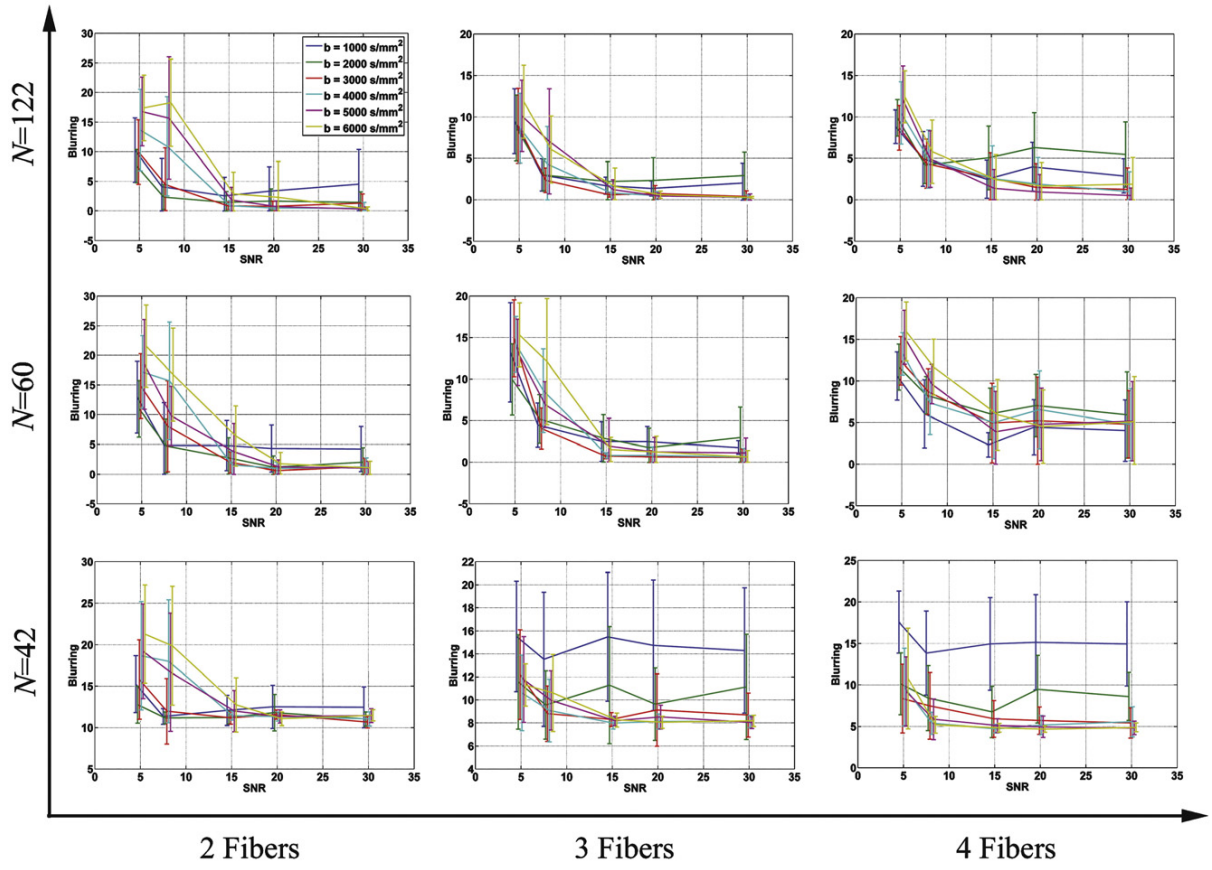

Fig. 4. Results of the RJMCMC performance evaluation in simulated data. The calculated spatial blurring using Eq. (20) is shown for different gradient encoding directions $N = 42, 60, 122$; signal to noise ratios SNR = 5, 8, 15, 20, 30, *b*-values = 1000, 2000, 3000, 4000, 5000, 6000 s/mm^2 and configurations of 2, 3, 4 and 5 fibers. (A color figure is available in the online issue.)

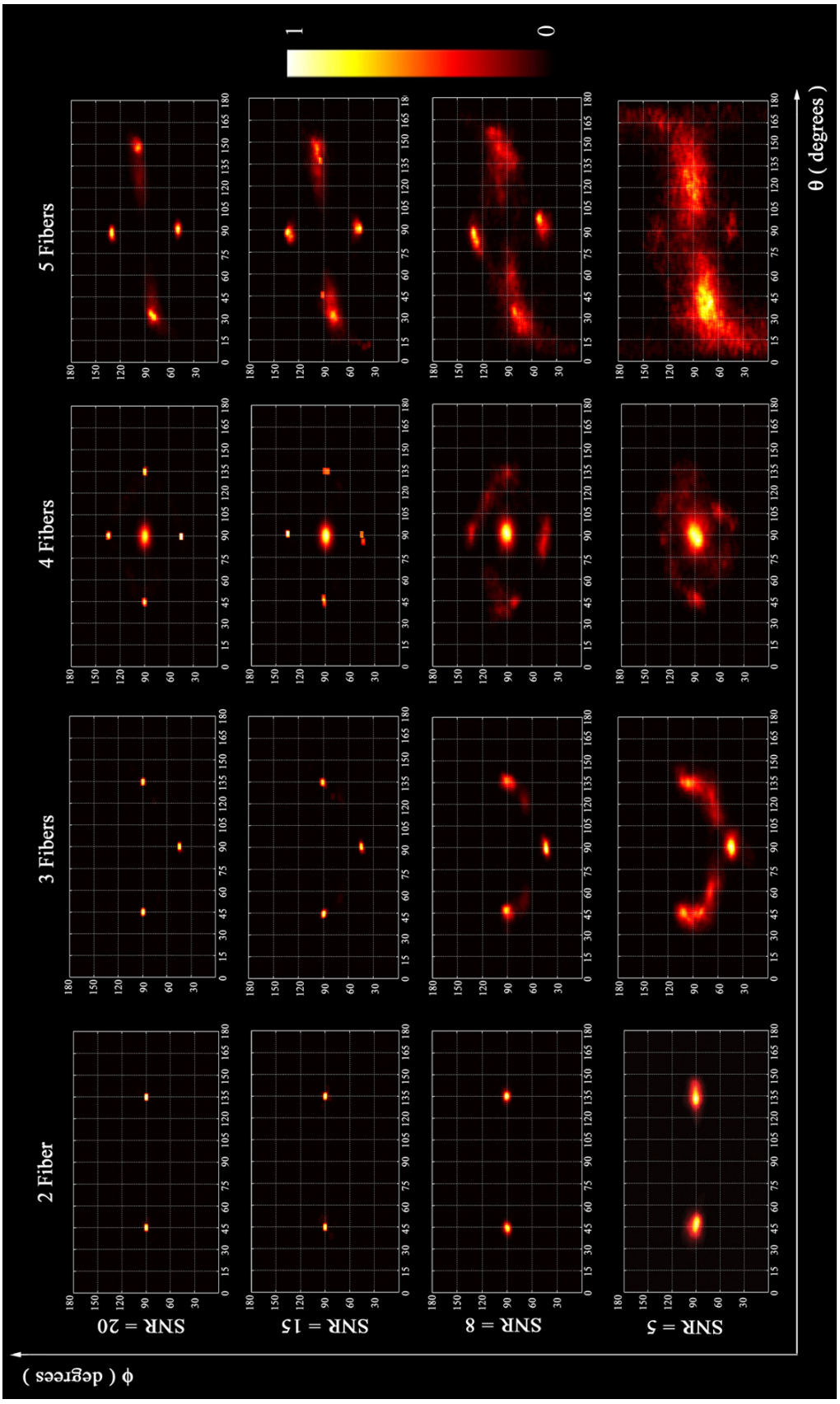

Fig. 5. Average probability maps of the fiber orientations computed (Eq. (14)) over 15 repetitions for: 2, 3 4, and 5 fiber configurations, different SNR values (SNR = 5, 8, 15, 20), *b*-value = 2000 s/mm^2 and 42 directions of a gradient encoding scheme. (A color figure is available in the online issue.)

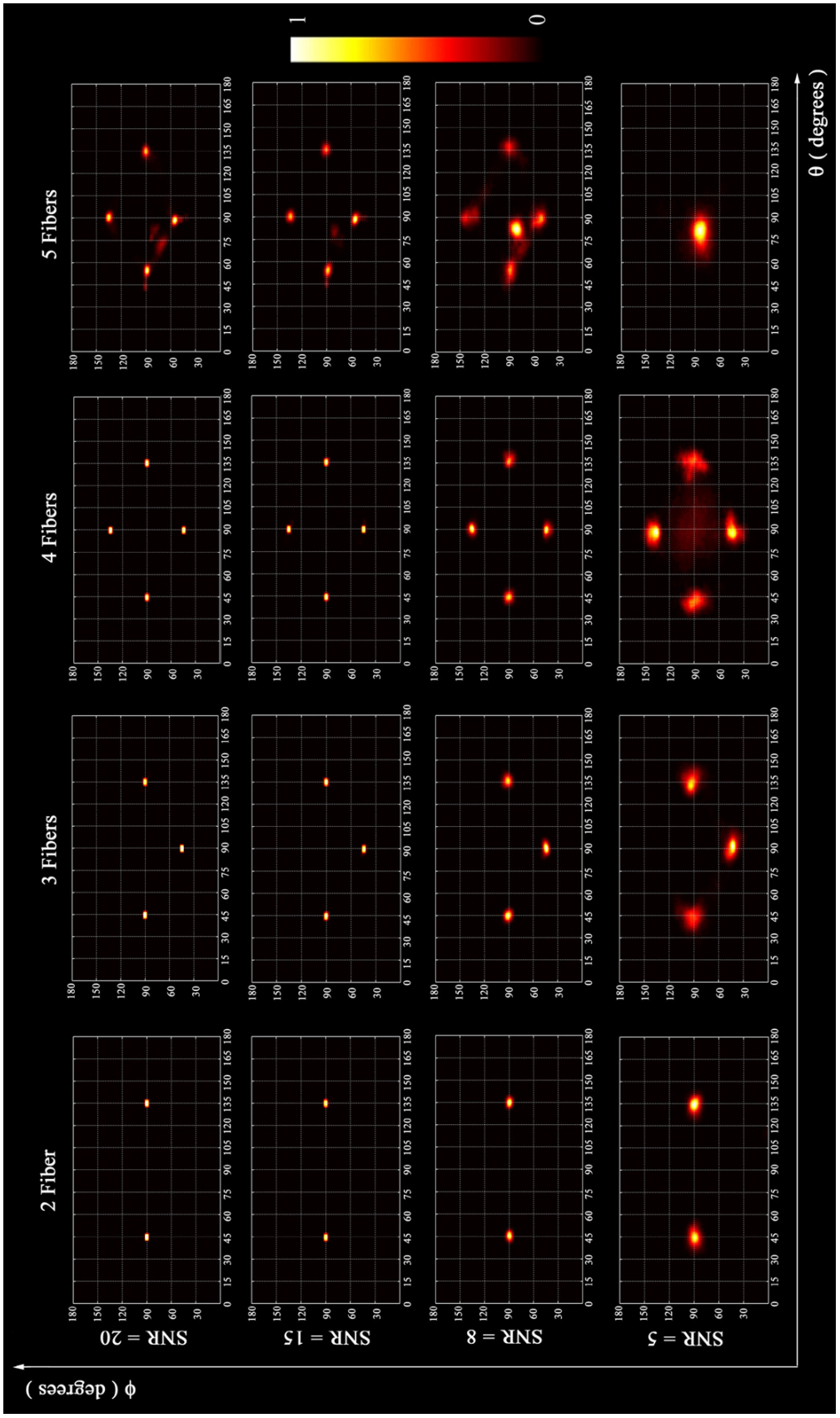

Fig. 6. Average probability maps of fiber orientation (Eq. (14)) over 15 repetitions for: 2, 3 4, and 5 fiber configurations, different SNR values (SNR = 5, 8, 15, 20), *b*-value = 4000 s/mm^2 and 60 directions of a gradient encoding scheme. (A color figure is available in the online issue.)

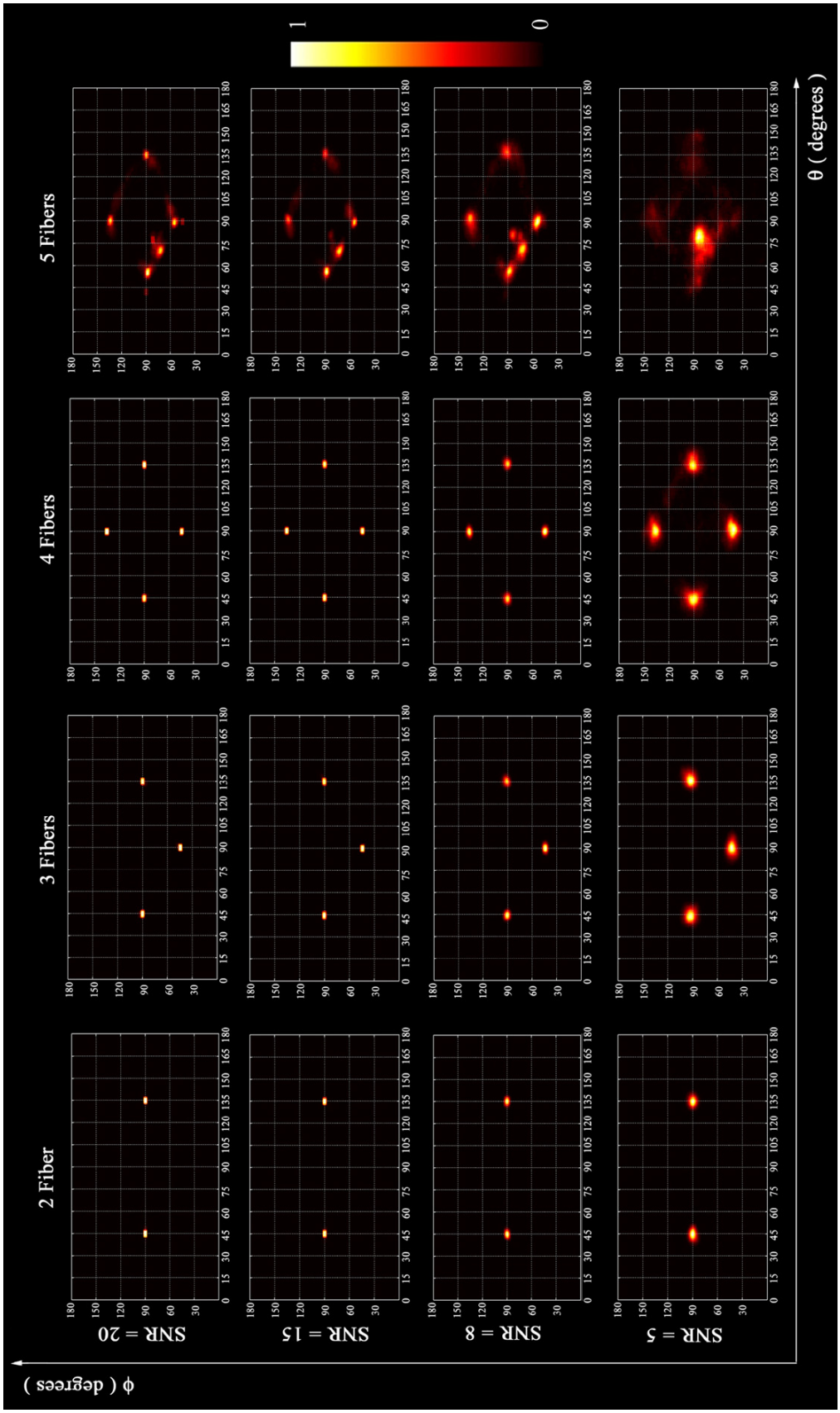

Fig. 7. Average probability maps of fiber orientations (Eq. (14)) over 15 repetitions for: 2, 3 4, and 5 fiber configurations, different SNR values (SNR=5, 8, 15, 20), *b*-value=4000 s/mm^2 and 122 directions of a gradient encoding scheme. (A color figure is available in the online issue.)

As the number of gradient encodings increases blurring improves, especially for 4 and 5 fiber configurations. For all fiber configurations blurring decreases with b-value increments as was described previously. The 4 and 5 fiber configurations are estimated correctly for b-value = 4000 s/mm^2 and a gradient encoding $N = 60$ directions when SNR ≥ 8. The best estimation of the 5 fiber configuration was attained for a gradient encoding of $N = 122$ directions and b-value = 4000 s/mm^2 even for low signal to noise ratios.

Studying model inference

Here we investigated the detection power of our methodology. We did this by evaluating the ability of the RJMCMC to detect the correct number of fibers in the voxel, given by the marginal probability of the number of fibers given the data $p(k=j|\mathbf{S})$ (Eq. (10)). To do this we used the fiber configurations estimated in the previous sections.

Fig. 8 shows the results. The gray color maps illustrate the mean value of $p(k=j|\mathbf{S})$ over 15 repetitions. When SNR increases, the estimation of the probability of finding the correct number of fibers $p(k=j|\mathbf{S})$ improves. As b-value increases the detection power of our method improves, especially when SNR > 15. The mean of $p(k=j|\mathbf{S})$ decreases as the fiber configuration complexity (from 3 to 5 fibers) increases. For larger gradient encoding schemes our methodology yields better estimates of the probability of finding a particular number of fibers due to higher spherical coverage.

Performance evaluation in a diffusion phantom

Phantom model description and MRI experiment

We used a phantom model designed by Lin et al. (2003) that simulates intersecting fibers. It consisted of sheets of parallel plastic capillaries filled with water. Sheets of two different orientations were stacked on top of each other in an interleaved fashion intersecting at 90° (see Fig. 9). We performed the MRI experiment in a 3T Medspec/Biospec MRI system (Bruker Companies, Ettlingen, Germany). We acquired DSI data with a stimulated echo-pulsed gradient sequence. The diffusion-encoding scheme consisted of 515 diffusion-encoding directions. We used only a shell of 30 gradient directions from the DSI encoding gradient scheme corresponding to a b-value = 2 880 s/mm^2.

The RJMCMC analysis used a Markov chain of 30,000 samples long. The burn-in period was 10,000 samples and the remaining 20,000 were employed to compute the diffusion profile parameters and their statistics.

Phantom analysis results

Fig. 9 panel a) shows a T2 image of the phantom sheets. Panel b) shows the orientation of the principal eigenvectors from a standard diffusion tensor analysis. In all voxels at the center of the phantom (where the capillaries intersect) the diffusion tensor eigenvectors pointed to an intermediate orientation between intersecting capillaries (45°). (See Fig. 2 page 484 in Lin et al. (2003)).

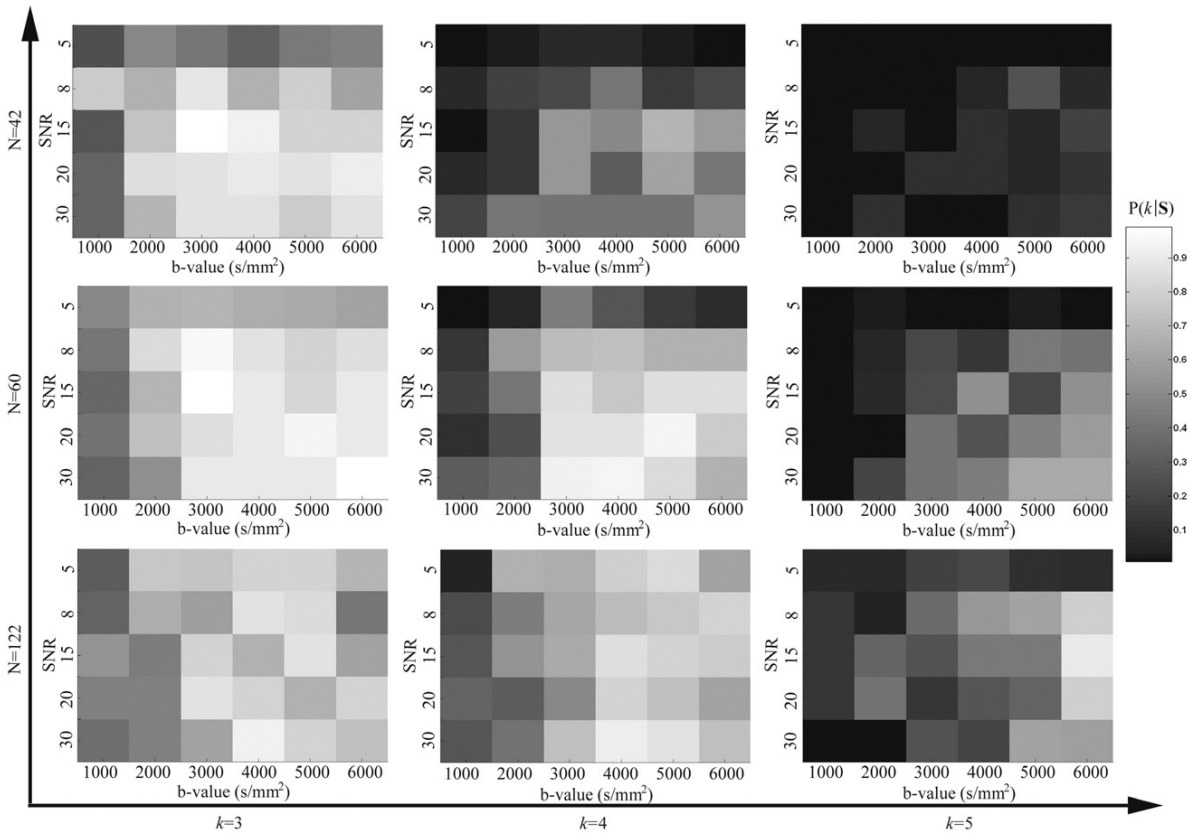

Fig. 8. Marginal probability of the number of fibers given the data $p(k=j|\mathbf{S})$ averaged over 15 repetitions. This is a measure of the detection power of our methodology in different experimental conditions. In the gray color bar, white denotes $p(k=j|\mathbf{S})=1$ and black $p(k=j|\mathbf{S})=0$ respectively.

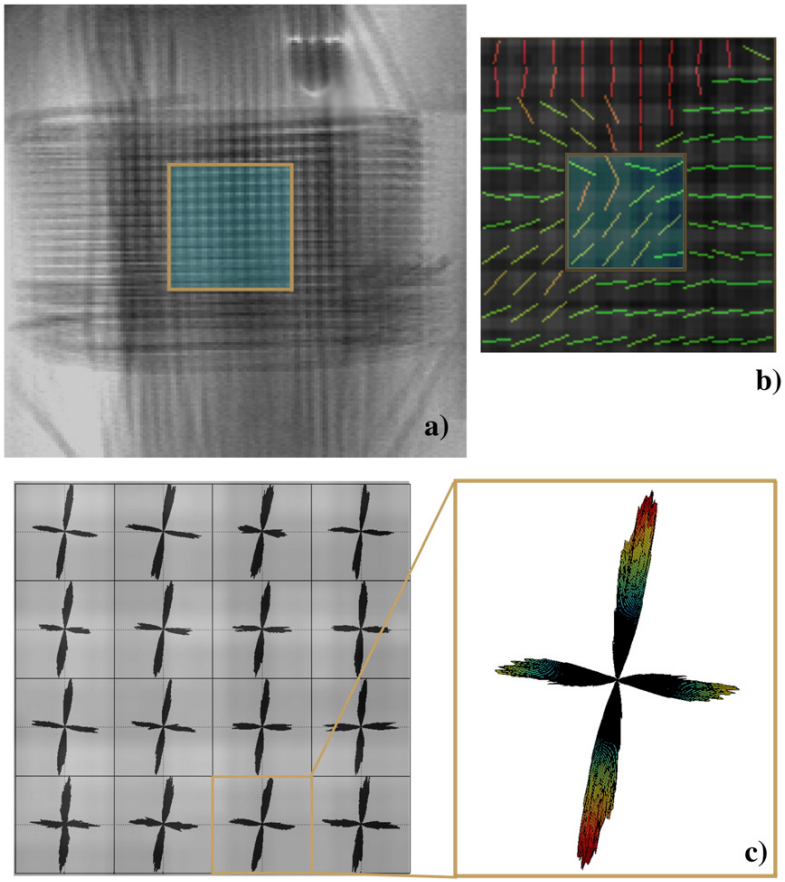

Fig. 9. RJMCMC performance evaluation in an MRI phantom containing capillaries intersecting at 90°. Panel a) T_2 image of the phantom sheets. Panel b) orientations of the principal eigenvectors of the estimated diffusion tensors. Panel c) Three-dimensional fiber probability maps (Eq. (21)) in the highlighted region of 4×4 voxels (see panel b)) using the RJMCMC methodology. (A color figure is available in the online issue.)

Fig. 9 panel c) shows the RJMCMC estimation of the capillary orientation in the same region of 4×4 voxels. RJMCMC detects that each voxel contains two diffusion profiles. The figure also shows the computed fiber orientation probability map (using Eq. (14)). There was good correspondence between the orientation of the intersecting capillaries and the estimated fibers. These results agree with the ODF (orientational distribution function) estimated using the full DSI gradient scheme reported by Lin et al. (2003).

Fig. 10 shows 3D probability maps of finding $k=1$, 2, and 3 fibers in panels a), b) and c) respectively. Panel d) shows the maximum probability map P_{max} (see Eq. (16)), showing regions where 1, 2 or 3 fibers in each voxel are the most probable given the data. The hot color bar gives the scale for the probability values in panel a), b) and c). The rainbow color bar gives the scale for the maximum probability map values. The maps reveal the presence and location of crossing fiber and single fiber voxels.

Evaluation in human brain DWI data

Data acquisition

The data was acquired from a 24 year old healthy male volunteer using a Siemens 1.5T Sonata Vision MR Scanner (Erlagen, Germany) with a quadrature birdcage head coil for RF transmission and reception.

Anatomical MRI

We acquired a 3D FLASH T1 weighted anatomical MRI. A field of view of FOV=224 mm×256 mm gave us a whole head coverage. This FOV provided a matrix size of 224×256 and 160 sagittal contiguous slices, with a voxel resolution of $1\times1\times1$ mm^3. The echo, repetition, and inversion times were (TE/TR/TI) 3.93 ms/2000 ms/710 ms respectively. The flip angle was 15°.

DWI study

The DWI dataset was recorded using an echo planar imaging (EPI) sequence consisting of 42 diffusion-weighted images with a b-value=3000 s/mm^2 and one non-diffusion-weighted image ($b=0$). The diffusion gradients were uniformly distributed on the sphere. The acquired volume covered the whole brain using 32 axial slices of 4 mm with a field of view (FOV) of 230 mm×230 mm and a matrix size of 128×128, yielding a voxel size of $1.8\times1.8\times4.0$ mm^3. The repetition time and echo time were (TR/TE) 7000 ms/150 ms. Flip angle was 90°.

RJMCMC algorithm setup

We used our RJMCMC methodology with a Markov chain of 30,000 samples long. The burn-in period was 10,000 samples and we used the remaining 20,000 samples to calculate the diffusion

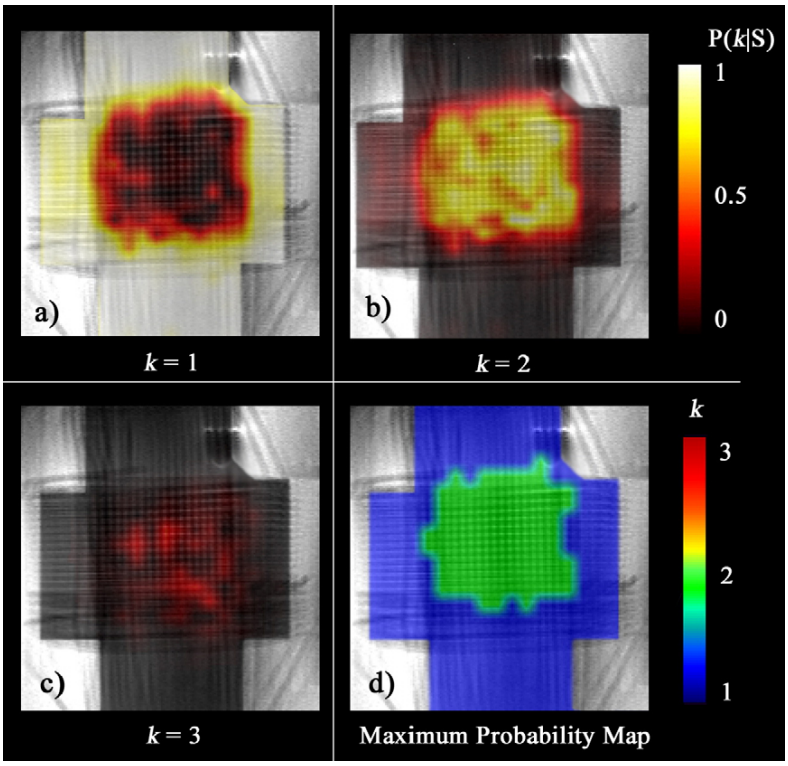

Fig. 10. 3D probability maps of finding $k=1$, 2, and 3 fibers in panels a), b) and c) respectively are depicted for the MRI phantom. Panel d) shows the maximum probability map, and therefore regions where 1, 2 or 3 fibers are most probable. (A color figure is available in the online issue.)

profile parameters and their statistics. The initial model for the Markov chain was selected at random to be 1, 2 or 3 fibers for each voxel. The maximum number of fibers permitted was $k_{max}=7$.

Results for human DWI data

We computed the fiber orientation probability maps (normalized version of the Eq. (14)) for voxels belonging to the white matter only. We also calculated maps for the probability of finding a specific number of fibers expressed by Eq. (15), and fractional anisotropy (FA). We co-registered the FA map to the high resolution T1 image.

In the following descriptions we have used the nomenclature and fiber tract localization from the recent atlas of Mori et al. (2005).

Fig. 11 shows an axial slice in which there are two fiber crossings. The middle of the figure shows the FA map and the three-dimensional probability map of finding 2 fibers $p(k=2|\mathbf{S})$. We selected two symmetrical points located in the right and left external capsules (ec) that are thin layers of white matter lateral to the lentiform nuclei. The external capsule contains association fibers such as the superior longitudinal fasciculus (slf), inferior fronto-occipital fasciculus (ifo) and the uncinate fasciculus (unc). The location of the fibers in the probability maps (bottom of the figure) shows symmetry in the sense that the fiber oriented to $\varphi=30°$, $\theta=30°$ in the left hemisphere voxel corresponds to a fiber oriented to $\varphi=45°$, $\theta=120°$ in the right hemisphere voxel, as expected.

The history of the instantaneous model probabilities is shown in the upper part of the Fig. 11, for both points. This is calculated as the percentage of steps in which a particular model has been visited, up to a given iteration. After the burn-in period of the MC, the probability of the model of two fibers continues as the maximum for both points $p(k=2|\mathbf{S})\geq 0.8$.

The middle part of Fig. 12 is an axial slice from: the FA map; the 3D probability map of finding 3 fibers $p(k=3|\mathbf{S})$; and the maximum probability map P_{max} (the most probable number of fibers residing in each voxel) (see Eq. (16)). The upper and lower parts of the figure show the fiber orientation probability maps. The voxel represented in blue is part of the retrolenticular (rlic) part of the internal capsule. The rlic is limited by the sagittal stratum (ss), which contains corticofugal fibers as well as association fibers, most notably the inferior fronto-occipital fasciculus (ifo) and the inferior longitudinal fasciculus (ilf). The internal capsule is the region where the corona radiata converges and it contains the thalamocortical and long corticofugal tracts (corticospinal tracts, corticobulbar tracts, corticopontine tract, corticoreticular tract and corticothalamic tract).

The voxel represented in cyan is anatomically located between the retrolenticular (rlic) part and the posterior limb (plic) of the internal capsule (ic). The white voxel is located nearby the posterior limb (plic) and the retrolenticular (rlic) part of the internal capsule. Both voxels have two estimated fiber bundles located at $\varphi=130°$, $\theta=115°$ and $\varphi=115°$, $\theta=75°$ approximately, that represent the same real fiber bundles. The green voxel is located in the external capsule (ec). The ec contains association fibers: superior longitudinal fasciculus (slf), inferior fronto-occipital fasciculus (ifo) and the uncinate fasciculus (unc). In all cases the final probability of finding a crossing of 3 fibers was $p(k=3|\mathbf{S})\geq 0.92$.

Fig. 13 shows a coronal slice where three fiber crossings are present. As in Fig. 12 the middle part depicts: FA map, 3D

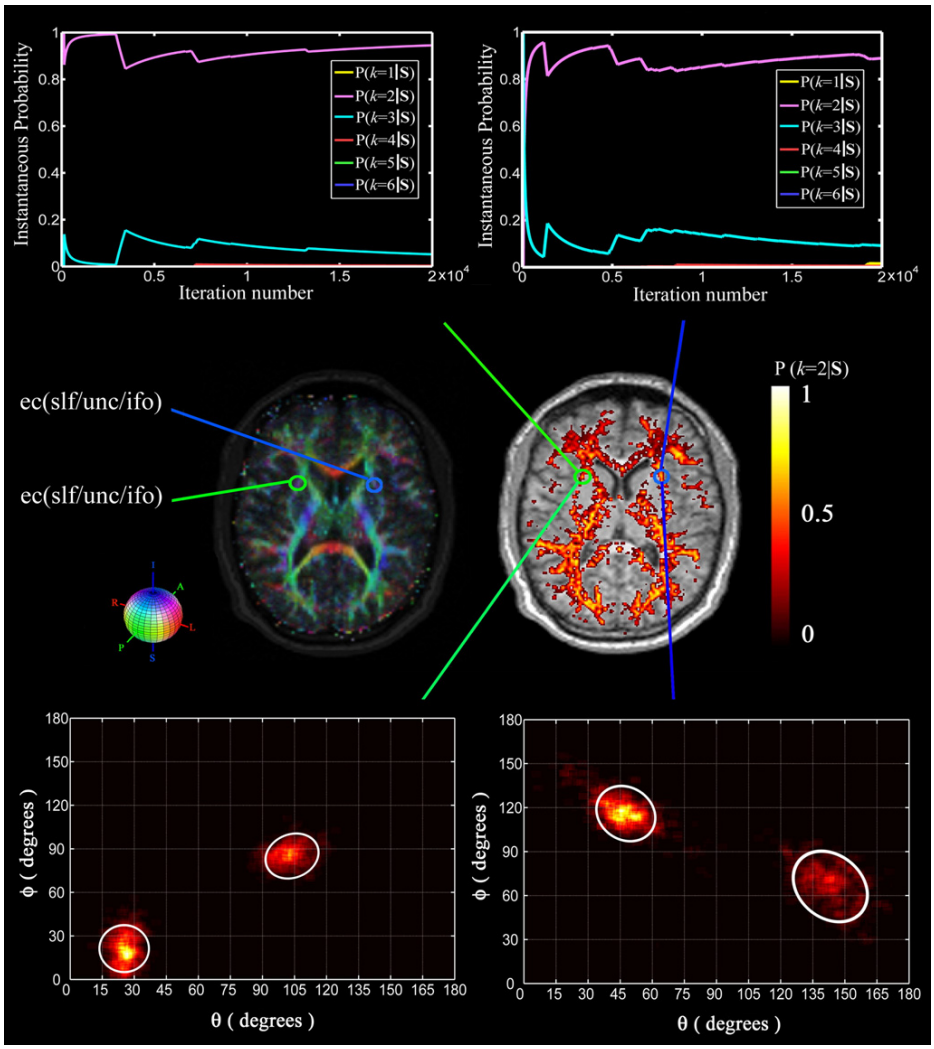

Fig. 11. Axial slice showing white matter areas with two fiber crossings. Two symmetrical voxels located in the right and left external capsule are shown. Top of figure: history of the instantaneous probability of the number of fibers. Middle: FA and probability map for finding 2 fibers $p(k=2|\mathbf{S})$. Bottom: probability maps of the intravoxel fiber orientations. Note the symmetry in the orientation of the fiber of the largest volume fraction with respect to elevation angle θ: left hemisphere voxel with $\varphi=30°$, $\theta=30°$, right hemisphere voxel $\varphi=45°$ and $\theta=120°$. Abbreviations: superior longitudinal fasciculus (slf), inferior fronto-occipital fasciculus (ifo), uncinate fasciculus (unc). (A color figure is available in the online issue.)

probability map of finding 3 fibers $p(k=3|\mathbf{S})$; and the maximum probability map $P_{\max}$ (see Eq. (16)). We selected two corresponding voxels (green and blue) from the left and right hemisphere, belonging to the well-known crossing area of the corona radiata (cr), corpus callosum (cc) and superior longitudinal fasciculus (slf). The cyan voxel belongs to the posterior limb of the internal capsule (plic). This region contains the superior thalamic radiation (str), the corticopontine tract (cpt) and the corticospinal tract (cst) as part of the corona radiata (cr). In the upper left part of the figure we show the histogram of the number of fibers. This histogram illustrates the marginal distribution probability of the models for the green voxel (in the left hemisphere). The maximum probability is for a model of three fibers with a value of $p(k=3|\mathbf{S})=0.73$. The four fiber model was the second most probable with a probability value of $p(k=4|\mathbf{S})\approx 0.1$.

Fig. 14 shows an enlarged image of the crossing area region of the corona radiata (cr), corpus callosum (cc) and superior longitudinal fasciculus (slf). There is a correspondence between the probability map of finding 3 fibers $p(k=3|\mathbf{S})$ in Fig. 13 and the fiber crossing area shown in panel b).

We computed the most likely number of fibers for voxels belonging to cerebral spinal fluid (CSF) and gray matter (GM). We found that isotropic models M_0 were favored in CSF voxels. However, there was a tendency to fit models with high complexity (more than 4 fibers) in GM voxels.

Discussion and conclusions

This paper presents a method based on a multi-compartment model that can identify more than 3 principal diffusion profiles in a voxel based on DWI data.

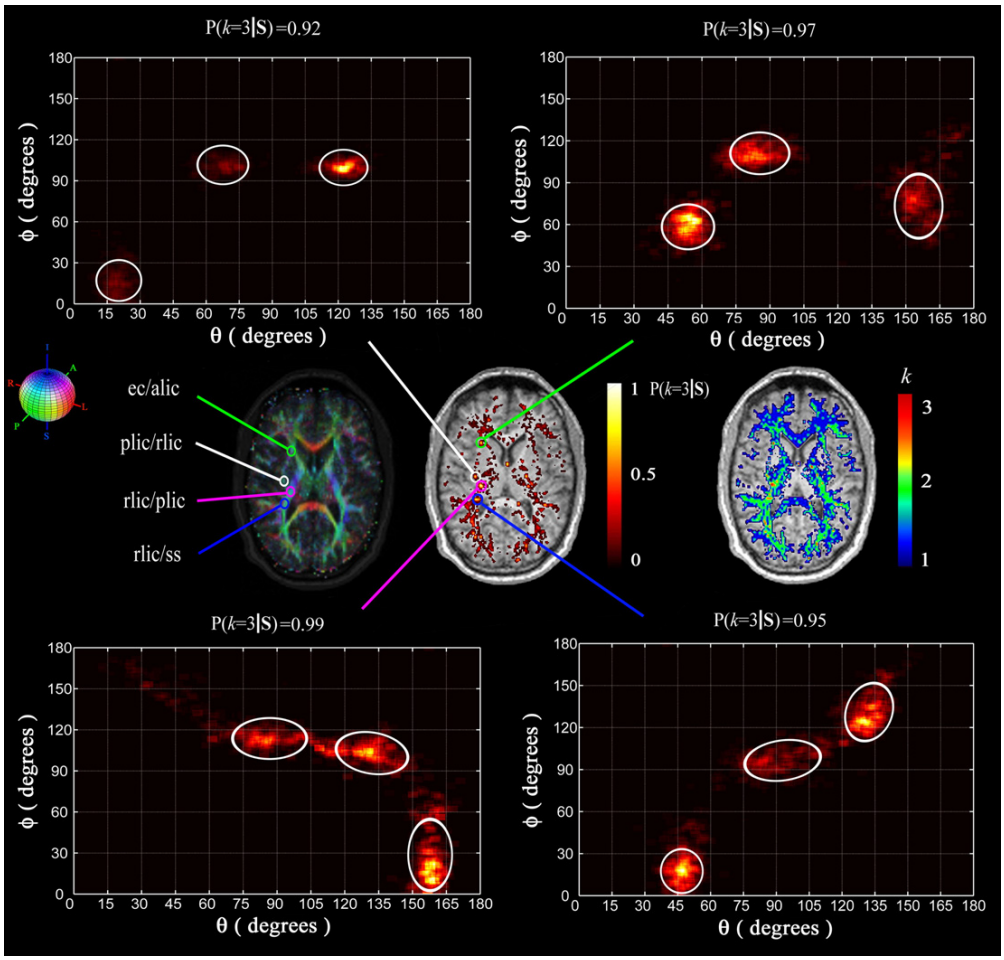

Fig. 12. Axial slice showing white matter regions with three fiber crossings. Middle: FA map co-registered with a T1 high resolution anatomic image and the probability map of finding 3 fibers $p(k=3|\mathbf{S})$. Bottom and top: probability maps of the intravoxel fiber orientations (Eq. (14)). Abbreviations: retrolenticular (rlic) part of the internal capsule (ic), sagittal stratum (ss), posterior limb (plic) part of the ic, anterior limb (alic) of the ic, external capsule (ec). (A color figure is available in the online issue.)

Multi-compartment models like ours have to overcome two main difficulties: 1) the nonlinear nature of the objective function. This requires the use of nonlinear fitting procedures that are unstable and starting point dependent, and can be trapped in local maxima or minima, and 2) the model selection problem, which is the problem of choosing the correct number of k compartments or number of diffusion profiles in the voxel.

Here we introduce a general modeling framework to tackle both problems. The Bayesian formalism is well-matched for these type of problems — in particular, the reversible jump Markov chain Monte Carlo (RJMCMC) algorithm (Green, 1995) is very well suited to deal with Bayesian model determination and estimation.

In the RJMCMC context, the number of diffusion profiles is considered as a random variable along with the model parameters and both are obtained in the same estimation process. The estimation is based on the joint posterior probability of the parameters and the number of diffusion profiles $p(\boldsymbol{\varphi}_k, \boldsymbol{\theta}_k, \mathbf{f}_k, \lambda, S_0, k, 1/\sigma^2|\mathbf{S})$ given by Eq. (7). Hosey et al. (2005) proposes the solution of running $k_{\max}$ independent MCMC samplers, each associated with a fixed number of diffusion profiles $k=1,\ldots, k_{\max}$ where $k_{\max}=2$. This approach has major limitations. First it is computationally expensive since $k_{\max}$ can be large and the number of voxels in a regular DWI analysis is of order of tens of thousands. Second, the same computational effort is needed for each model k even though some values of k are not significant in practice because they present low posterior probabilities $p(k|S)$. We therefore used the RJMCMC's capability to jump between models of different dimensionality to develop an efficient stochastic algorithm.

The general methodology introduced here not only accounts for approximate posterior estimates of the fiber parameters (orientation, diffusivities etc), but also gives an empirical posterior distribution of the number of fiber orientations given the DWI data. One of the uses of RJMCMC is in estimating the probability of finding a fiber in a specific orientation given by (φ, θ) independent of the inferred number of fibers (see Eq. (14)). These fiber orientation probability maps (examples shown in Figs. 5, 6 and 7) can be used by fiber tracking algorithms and to develop new measures to characterize the anisotropy of cerebral tissue in normal and abnormal states. The RJMCMC method also allows us to calculate: 1) a three-dimensional map that gives the probability of finding a

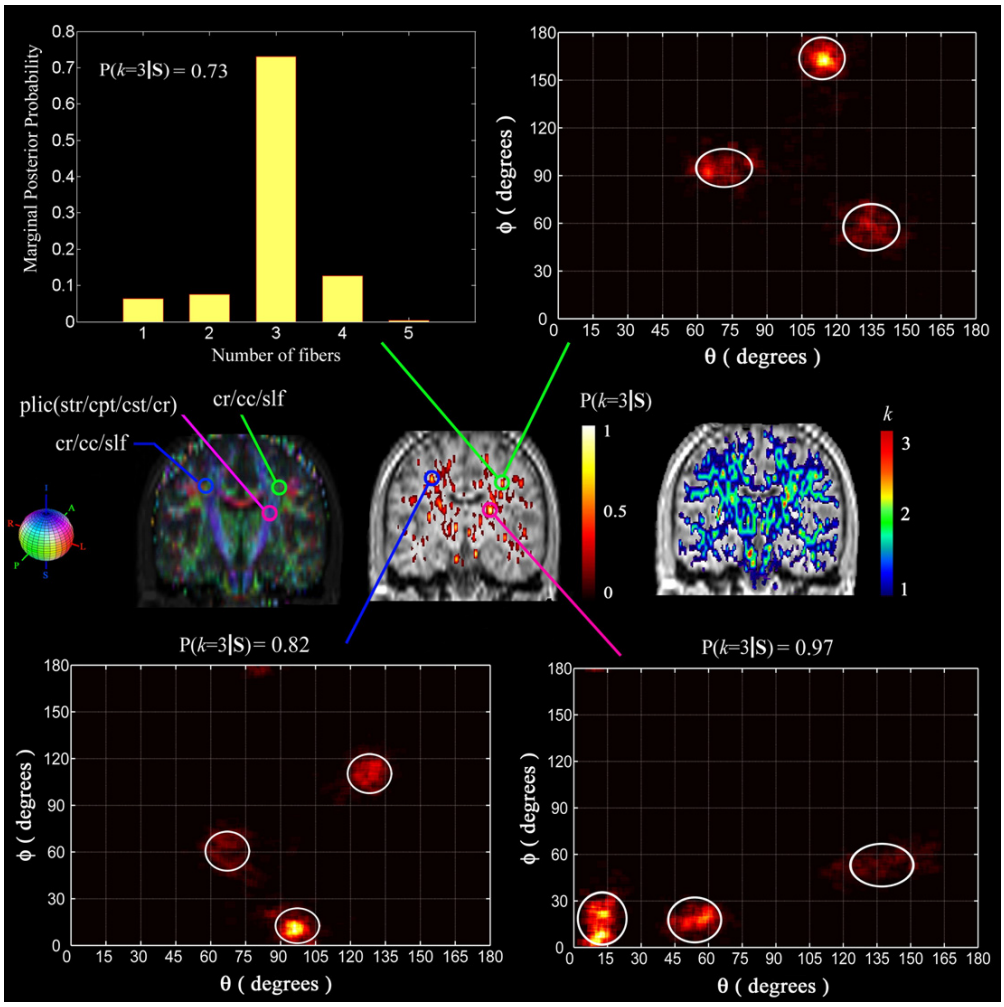

Fig. 13. Coronal slice showing white matter regions with three fiber crossings. Middle: FA map co-registered with a T1 high resolution anatomical image and the probability map of finding 3 fibers $p(k=3|\mathbf{S})$. Two symmetrical voxels, represented in green and blue, belonging to the crossing area of the corona radiata (cr), corpus callosum (cc) and the superior longitudinal fasciculus (slf) are shown. Top left: histogram of the number of fibers for the voxel represented in green. Abbreviations: posterior limb (plic) of the internal capsule, superior thalamic radiation (str), corticopontine tract (cpt), corticospinal tract (cst). (A color figure is available in the online issue.)

particular number of fibers in each voxel in the brain; 2) the three-dimensional MaxPro (maximum probability) map giving the most probable number of fibers in each voxel. A normative database of these maps could be the basis of an analysis of the principal fiber bundles in the brain.

Recently Behrens et al. (2007) introduced a methodology to deal with diffusion model selection and estimation. The generative model of diffusion signal is the same (see Eq. (2)) as the one we have used here. It follows that the forward probabilistic generative model and the Bayesian inference are the main factors responsible for differences in the results of the two methods. The principal difference is the algorithm used to tackle the model order selection. In particular, Behrens et al. (2007) used Automatic Relevance Determination (ARD) instead of the RJMCMC algorithm used here.

One advantage of the ARD is that it requires only a simple model to be fit to the data. In contrast, our approach involves fitting every candidate model and comparing between them. The ARD estimation starts with all available variables. This can be computationally demanding when the probable model order (k_{max} — maximum number of diffusion profiles to be estimated) is high. The nonlinear nature of the objective function increases with k_{max}, which could lead to unstable solutions that are starting point dependent. Even in these cases, ARD will still run faster than RJMCMC. The ARD prunes variables that are never re-included. This has the potential to lose informative variables by chance and some candidate models could be prematurely discarded. This problem is more likely when SNR is low and the real number of fibers is high. This premature rejection may make ARD more conservative because it can lead to underestimation of the actual number of fibers. ARD is also inflexible in the sense that it constrains the parameters to have a unique ARD prior probability.

In contrast to ARD, RJMCMC starts from a subset of variables. This aspect is important if the number of candidate models is large. Though RJMCMC can be slower than ARD, it is still an attractive method

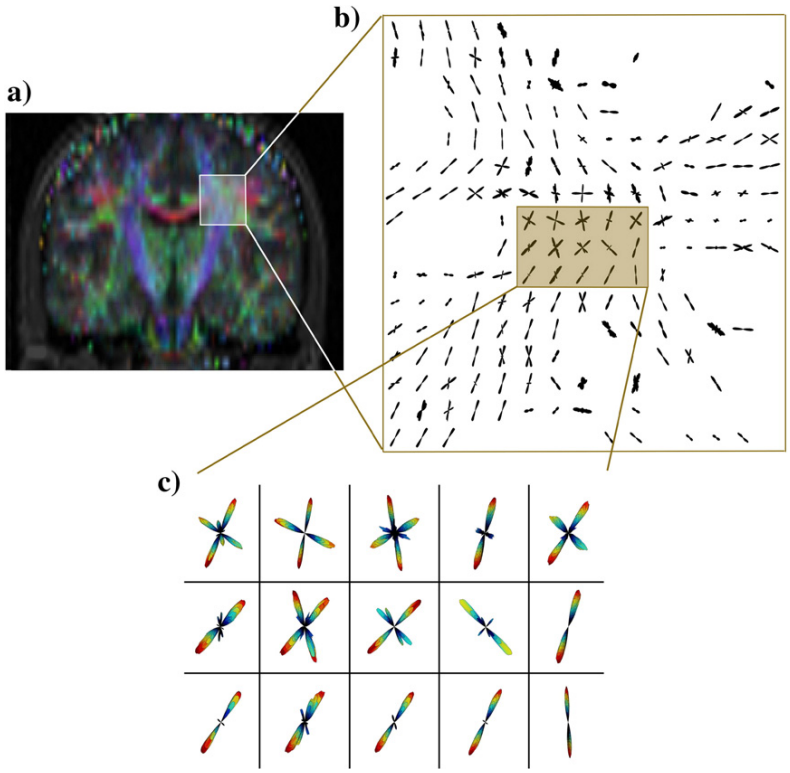

Fig. 14. Panel a): FA map co-registered with a T1 high resolution anatomical image. Panel b): Detail of crossing area of the corona radiata (cr), corpus callosum (cc) and the superior longitudinal fasciculus (slf) highlighted in panel a). Panel c): Detail of the region highlighted in panel b) to show a three-dimensional version of the fiber orientation probability maps (see Eq. (21)) for a set of voxels. (A color figure is available in the online issue.)

because it exhaustively explores the model order space. In this way eliminated variables (models) can be re-included at later stages of the Markov chain. This feature reduces the possibility of model order underestimation. RJMCMC also allows output measures such as the probability of each model given the data (and model evidence) that are not possible using ARD. These measures can offer new and relevant information to characterize the intravoxel anisotropy. Nevertheless, it should be pointed out that RJMCMC can be inefficient if the proposed distribution is not carefully designed.

As mentioned above, there are difference in the forward probabilistic generative model between the approach of Behrens et al. (2007) and ours. The differences arise from prior probabilities: Behrens et al. used an ARD-type prior on fiber volume fraction parameters, while we have used a Dirichlet prior. Unlike Behrens et al, we have included the number of fibers as a parameter in our model, by specifying a prior using information derived from published diffusion data.

We suggest that the differences in forward probabilistic generative model and model inference are the reason that Behrens et al. (2007) required simulated data with b-values upwards of 4000 s/mm^2, 60 gradient encoding directions, and high SNRs in order to estimate 3 orthogonal fibers. Under the same experimental conditions, RJMCMC can reconstruct more complex fiber configurations (5 fibers, see Fig. 6) with lower SNRs.

To test our methodology, we generated a set of synthetic data for different SNRs, gradient encoding schemes and b-values. We evaluated performance in terms of fiber spatial localization error, blurring around the mean localization and the probability of detecting the correct number of fibers. As expected, algorithm performance decreases with SNR. We have also shown that our method gives sensible results for fiber crossing in the analysis of DWI data from an MRI phantom of capillaries intersecting at 90°.

The scope of our method can be extended to other diffusion signal generative models similar to that introduced by Assaf et al. (2004). It can also be used for DSI and QBI gradient encoding experiments. It is flexible enough to use a mixture of models to capture different types of diffusion profiles. For example, we can use a mixture of cylindrical and degenerate models in our estimation. In principle, this could improve the estimation of spatial microstructure. Fiber tracking methods can benefit from our method, in particular by the introduction of the probability of finding a number of fibers in a voxel given by $p(k|\mathbf{S})$. This probability has not previously been used. We will address this issue in future work.

Our methodology has limitations. The primary drawback is a high computational load compared to classical methods such as the diffusion tensor model. This limitation can be reduced by precomputing parameters such as the signal model for different fiber orientations — which have a considerable impact on the speed of the estimation process. Voxels are processed independently, so the computation is easy to run in parallel. Another inconvenience of our method is that it is necessary to design a suitable RJMCMC algorithm, in particular, one has to specify move types so that they guarantee reversibility and thus fulfill the invariance condition of the Markov chain with respect to the posterior distribution.

The convergence of the algorithm could be improved by introducing the simulated annealing technique into the RJMCMC algorithm. This technique has been applied by other authors (Andrieu et al., 2001) in signal processing applications. This is another direction for future investigation.

We suggest that our methodology is a useful and powerful alternative approach to the analysis of diffusion data collected in standard MRI scanners. It can be applied to clinical populations, and improve the characterization of normal and abnormal cerebral tissue.

Acknowledgments

The human DWI data used in this paper were acquired during a scientific visit by Lester Melie-Garcia to the University Hospital of Bern, Switzerland, funded by the Swiss National Foundation (SNF). We thank Claus Kiefer PhD, Andrea Federspiel PhD and Dr. Thomas Koenig (University Hospital Bern, Switzerland) for their help in acquiring the human DWI data used in this paper. We are also grateful to Dr. Pedro Valdés-Sosa, Dr. Eduardo Martínez-Montes (Cuban Neuroscience Center) and specially to Dr. Matthew Brett (MRC Cognition and Brain Sciences Unit, Cambridge, United Kingdom) for their help with the final revisions of the manuscript. Finally, our thanks to 3T MRI research center at National Yang-Ming University (Taipei, Taiwan) where phantom data was acquired, and to our anonymous reviewers for their comments and suggestions that have considerably improved the manuscript.

Appendix A. Probability distribution functions

Dirichlet: $\mathrm{Di}_k(\mathbf{x}|\boldsymbol{\alpha})$

$$\mathbf{x}=(x_1,\ldots,x_k),0<x_i<1,\sum_{l=1}^{k}x_l\leq 1;\boldsymbol{\alpha}=(\alpha_1,\ldots,\alpha_{k+1}),\alpha_i>0;$$

$$p(\boldsymbol{x})=c_k\left(1-\sum_{l=1}^{k}x_l\right)^{\alpha_{k+1}-1}\prod_{l=1}^{k}x_l^{\alpha_l-1},\ c_k=\Gamma\left(\sum_{l=1}^{k+1}\alpha_l\right)\Big/\prod_{l=1}^{k+1}\Gamma(\alpha_l)$$

Gamma: $\mathrm{Ga}(x|\alpha,\beta)$

$$p(x)=cx^{\alpha-1}e^{-\beta x},c=\beta^{\alpha}/\Gamma(\alpha),\alpha>0,\beta>0$$
$$E[x]=\alpha\beta^{-1},V[x]=\alpha\beta^{-2}$$

Appendix B. Description of RJMCMC moves

In this Appendix we develop the RJMCMC moves in order to obtain their particular acceptance ratios. In general, the acceptance ratio for each move type is defined as (Green, 1995):

$$r_{\text{move}}\triangleq(\text{likelihood ratio})\times(\text{prior ratio})\times(\text{proposal ratio})\times(\text{Jacobian}) \tag{21}$$

Thus, the acceptance probability of a particular move for the standard RJMCMC algorithm is obtained as:

$$\alpha_{\text{move}}=\min\left(1,r_{\text{move}}\right) \tag{22}$$

where 'move' is defined as: *birth*, *death*, *split*, *merge* or *update*.

If a move is proposed from model M_k of k fibers with parameters $\Omega_k=[\boldsymbol{\varphi}_k,\boldsymbol{\theta}_k,\mathbf{f}_k,\lambda,k]$ to a new one $M_{k'}$ of k' fibers ($k'\in\{k-1,k,k+1\}$) with $\Omega_{k'}=[\boldsymbol{\varphi}_{k'},\boldsymbol{\theta}_{k'},\mathbf{f}_{k'},\lambda,k']$, the previous terms can be defined as follows:

- likelihood ratio $=\dfrac{p(\mathbf{S}|\boldsymbol{\varphi}_{k'},\boldsymbol{\theta}_{k'},\mathbf{f}_{k'},\lambda,S_0,k',1/\sigma^2)}{p(\mathbf{S}|\boldsymbol{\varphi}_k,\boldsymbol{\theta}_k,\mathbf{f}_k,\lambda,S_0,k,1/\sigma^2)}$

$$=\frac{\sigma_k^{N_g}}{\sigma_{k'}^{N_g}}L_r,\text{ where}$$

$$L_r=\exp\left(\frac{1}{2\sigma_k^2}(\mathbf{S}-\mathbf{S}_k)^{\mathrm{T}}(\mathbf{S}-\mathbf{S}_k)-\frac{1}{2\sigma_{k'}^2}(\mathbf{S}-\mathbf{S}_{k'})^{\mathrm{T}}(\mathbf{S}-\mathbf{S}_{k'})\right) \tag{23}$$

- prior ratio $=\dfrac{p(\boldsymbol{\varphi}_{k'},\boldsymbol{\theta}_{k'},\mathbf{f}_{k'},\lambda,S_0,k',1/\sigma^2)}{p(\boldsymbol{\varphi}_k,\boldsymbol{\theta}_k,\mathbf{f}_k,\lambda,S_0,k,1/\sigma^2)}$ (24)

- proposal ratio $=\begin{cases}q(\boldsymbol{\Omega}_{k'}|\boldsymbol{\Omega}_k)/p(u_p)q(\boldsymbol{\Omega}_k|\boldsymbol{\Omega}_{k'}),&\text{if } k'>k\\ p(u_p)q(\boldsymbol{\Omega}_{k'}|\boldsymbol{\Omega}_k)/q(\boldsymbol{\Omega}_k|\boldsymbol{\Omega}_{k'}),&\text{if } k>k'\end{cases}$

The algorithm draws a p-dimensional vector of continuous variable u_p that is independent of the current state $\boldsymbol{\Omega}_k$, so the dimension matching condition is satisfied:

$$\begin{cases}\dim(\boldsymbol{\Omega}_k)+\dim(u_p)=\dim(\boldsymbol{\Omega}_{k'}),&\text{if } k'>k\\ \dim(\boldsymbol{\Omega}_{k'})+\dim(u_p)=\dim(\boldsymbol{\Omega}_k),&\text{if } k>k'\end{cases}$$

- Jacobian (J): $J=\begin{cases}\left|\dfrac{\partial\boldsymbol{\Omega}_{k'}}{\partial(\boldsymbol{\Omega}_k,u_p)}\right|,&\text{if } k'>k\\ \left|\dfrac{\partial(\boldsymbol{\Omega}_{k'},u_p)}{\partial\boldsymbol{\Omega}_k}\right|,&\text{if } k>k'\end{cases}$

Clearly the Jacobian is equal to 1 when $k=k'$.

Here it is assumed that parameters S_0, λ, and the nuisances parameters $1/\sigma^2$ and Λ will only change in the update move.

B.1. Birth/death moves

Birth move

In the birth move there is a transition from model M_k to M_{k+1} (i.e., $k'=k+1$). Here $\sigma_k=\sigma_{k+1}$, thus the likelihood ratio $=L_r$ (see Eq. (23)). The prior ratio for Λ, S_0, $1/\sigma^2$ and λ parameters are equal to one. Thus, the prior ratio for the birth move, substituting priors for each parameter in Eq. (24), is expressed by:

$$\text{prior ratio}=\frac{c_{k+1}}{4\pi c_k}\frac{\Lambda}{(k+1)}\sin\theta_{k+1} \tag{25}$$

Terms c_k, c_{k+1} are the Dirichlet normalization constants (see Appendix A).

The proposal ratio is given by the following expression:

$$\begin{aligned}\text{proposal ratio}&=\frac{q(\boldsymbol{\Omega}_{k+1}|\boldsymbol{\Omega}_k)}{q(\boldsymbol{\Omega}_k|\boldsymbol{\Omega}_{k+1})p(u_p)}\\&=\frac{d_{k+1}/(k+1)}{b_k(1/4\pi)\sin\theta_{k+1}\left|\left(1-\sum_{p=1}^{k}f_p-f_{\text{thres}}\right)\right|}\\&=4\pi\left(1-\sum_{p=1}^{k}f_p-f_{\text{thres}}\right)\Big/\Lambda\sin\theta_{k+1}\end{aligned} \tag{26}$$

Terms b_k and d_k are given by Eq. (9) and we defined $f_{\text{thres}}=0.05$.

In the birth and death moves the Jacobian of the transformation is $J=1$.

The expression for r_{birth} after substituting Eqs. (23), (25) and (26) in (21) is given by:

$$r_{\text{birth}} = \frac{c_{k+1}}{c_k(k+1)} \cdot \left(1 - \sum_{p=1}^{k} f_p - f_{\text{thres}}\right) L_{\text{r}} \tag{27}$$

The acceptance probability for the birth move is $\alpha_{\text{birth}}=\min(1, r_{\text{birth}})$.

The birth move algorithm is summarized as:

- If $1 - \sum_{j=1}^{k} f_j > f_{\text{thres}}$ the birth move is accepted otherwise it is automatically rejected and the next steps are not valid.
- Propose a new fiber at a uniform random direction on a sphere. One direction (φ, θ) is drawn in spherical coordinates.
- Evaluate α_{birth}.
- Sample $u \sim \text{U}(0,1)$.
- If $u \le \alpha_{\text{birth}}$ the Markov chain state becomes $(\boldsymbol{\varphi}_{k+1}, \boldsymbol{\theta}_{k+1}, \mathbf{f}_{k+1}, k+1)$ else stay at $(\boldsymbol{\varphi}_k, \boldsymbol{\theta}_k, \mathbf{f}_k, k)$.

Death move

In the death move there is a transition from model M_{k+1} to M_k. Since the reversibility of the estimation process is guaranteed, the death move acceptance ratio is $r_{\text{death}}=r_{\text{birth}}^{-1}$ and the acceptance probability of this move will be: $\alpha_{\text{death}}=\min(1, r_{\text{death}})$.

The death move algorithm is summarized as:

- Choose one fiber w at random among $k+1$ existing fibers, using a discrete uniform probability distribution $w \sim \text{U}(1, k+1)$.
- Evaluate α_{death}.
- Sample $u \sim \text{U}(0,1)$.
- If $u \le \alpha_{\text{death}}$ the Markov chain state becomes $(\boldsymbol{\varphi}_k, \boldsymbol{\theta}_k, \mathbf{f}_k, k)$ else stay at $(\boldsymbol{\varphi}_{k+1}, \boldsymbol{\theta}_{k+1}, \mathbf{f}_{k+1}, k+1)$.

B.2. Merge/split moves

Split move

In this move there is a transition from model M_k to M_{k+1}. If we consider that one fiber m of the k existing fibers is split into two, m_1 and m_2, then we need to introduce the following new equations:

$$f_m = f_{m_1} + f_{m_2};\ \varphi_m = c_1\varphi_{m_1} + c_2\varphi_{m_2};\ \theta_m = c_1\theta_{m_1} + c_2\theta_{m_2} \tag{28}$$

where $c_1+c_2=1$.

In our case we selected $c_1=c_2=0.5$, that means no preference for either of the two fibers. The values for the new azimuthal angles will be:

$$\begin{aligned} \varphi_{m_1} &= \varphi_m + \varphi_{\text{thres}} + u_\varphi \cdot \Delta\varphi \\ \varphi_{m_2} &= \varphi_m - c_1/c_2 \cdot \left(\varphi_{thres} + u_\varphi \Delta\varphi\right) \end{aligned} \tag{29}$$

The same expressions can be derived for the new elevation angles:

$$\begin{aligned} \theta_{m_1} &= \theta_m + \theta_{\text{thres}} + u_\theta \cdot \Delta\theta \\ \theta_{m_2} &= \theta_m - c_1/c_2 \cdot (\theta_{thres} + u_\theta \Delta\theta)\,. \end{aligned} \tag{30}$$

The parameters u_φ, and u_θ are drawn from the uniform distribution functions $u_\varphi \sim \text{U}[0,1]$; $u_\theta \sim \text{U}[0,1]$ respectively. Terms $\Delta\varphi$, $\Delta\theta$ with φ_{thres} and θ_{thres} define the minimum and the maximum azimuthal and elevation angle separation between new fibers. We selected $\Delta\varphi=\Delta\theta=\pi/6$ and $\varphi_{\text{thres}}=\theta_{\text{thres}}=\pi/12$. Terms φ_{thres}, θ_{thres} are introduced to overcome the problem of $u_\varphi=0$, $u_\theta=0$.

By definition in our algorithm $f_{m_1} \ge f_{\text{thres}}, f_{m_2} \ge f_{\text{thres}}$. For the acceptance of the split move the current value of f obeys the relationship: $1 \ge f_m \ge 2f_{\text{thres}}$, then $f_{m_1} = f_{\text{thres}} + u_f \Delta f$ where $\Delta f = f_m - 2f_{\text{thres}}$ and u_f is drawn from the uniform distribution function $u_f \sim \text{U}[0,1]$. The values for the new volume fractions are:

$$\begin{aligned} f_{m_1} &= f_{\text{thres}} + (f_m - 2f_{\text{thres}})u_f \\ f_{m_2} &= f_m - f_{m_1} = f_{\text{thres}} + (f_m - 2f_{\text{thres}})(1 - u_f) \end{aligned} \tag{31}$$

Thus, from the previous definitions, we can develop the computation of the split move acceptance ratio. The *likelihood ratio* has the same expression as the birth move likelihood ratio. The prior ratio is expressed by:

$$\text{prior ratio} = \frac{\Lambda c_{k+1}\ \sin\ \theta_{m_1}\ \sin\ \theta_{m_2}}{4\pi c_k(k+1)\ \sin\ \theta_m} \tag{32}$$

The proposal ratio has the following form:

$$\text{proposal ratio} = \frac{q(\boldsymbol{\Omega}_{k+1}|\boldsymbol{\Omega}_k)}{q(\boldsymbol{\Omega}_k|\boldsymbol{\Omega}_{k+1})p(u_p)} = \frac{m_{k+1}/(k+1)}{p(u_\varphi)p(u_\theta)p(u_f)s_k/k} = \frac{k}{\Lambda} \tag{33}$$

where $p(u_p)=p(u_\varphi)\ p(u_\theta)\ p(u_f)$, $u_\varphi = \text{U}[0,1]$; $u_\theta = \text{U}[0,1]$; $u_f = \text{U}[0,1]$.

In our case $s_k=b_k$ and $m_{k+1}=d_{k+1}$ — see Eq. (9).

The Jacobian for the merge move has the following expression:

$$J_{\text{merge}} = \left| \frac{\partial(\varphi_m, \theta_m, f_m, u_\varphi, u_\theta, u_f)}{\partial(\varphi_{m_1}, \varphi_{m_2}, \theta_{m_1}, \theta_{m_2}, f_{m_1}, f_{m_2})} \right| = \frac{c_2}{\Delta\varphi\Delta\theta(f_m - 2f_{\text{thres}})}$$

The Jacobian for the split move is: $J_{\text{split}}=1/J_{\text{merge}}$. You can find the derivation of this expression in Appendix C. Thus, the acceptance ratio for the split move is:

$$r_{\text{split}} = L_{\text{r}} \cdot \frac{c_{k+1} k \sin\ \theta_{m_1}\ \sin\theta_{m_2} \Delta\varphi\Delta\theta(f_m - 2f_{\text{thres}})}{4\pi c_k c_2 (k+1)\ \sin\theta_m} \tag{34}$$

We defined $f_{\text{thres}}=0.05$. The acceptance probability for the split move will be:

$$\alpha_{\text{split}} = \min\ (1, r_{\text{split}})$$

The split move algorithm is summarized with:

- Choose uniformly at random one fiber m among k existing fibers using a discrete uniform distribution $m \sim \text{U}(1,k)$.
- If $1 - \sum_{j=1}^{k} f_j > 2 \cdot f_{\text{thres}}$ the split move is accepted otherwise it is automatically rejected and the next steps are not valid.
- Compute the parameters of the new candidate fibers $(\varphi_{m_1}, \theta_{m_1}, f_{m_1})$ and $(\varphi_{m_2}, \theta_{m_2}, f_{m_2})$ from $(\varphi_m, \theta_m, f_m)$ using equation set (29), (30) and (31).
- Evaluate α_{split} acceptance ratio.
- Sample $u \sim \text{U}(0,1)$.
- If $u \le \alpha_{\text{split}}$ the Markov chain state becomes $(\boldsymbol{\varphi}_{k+1}, \boldsymbol{\theta}_{k+1}, \mathbf{f}_{k+1}, k+1)$ else stay at $(\boldsymbol{\varphi}_k, \boldsymbol{\theta}_k, \mathbf{f}_k, k)$.

Merge move

In this move there is a transition from model M_{k+1} to M_k. Since the reversibility of the estimation process is guaranteed the merge move acceptance ratio is the inverse of the split acceptance ratio $r_{\text{merge}}=r_{\text{split}}^{-1}$, thus $\alpha_{\text{merge}}=\min(1, r_{\text{merge}})$.

The merge move algorithm is summarized with:

- Choose uniformly at random one fiber m_1 $\left(\varphi_{m_1}, \theta_{m_1}, f_{m_1}\right)$ among $k+1$ existing fibers $m_1 \sim \mathrm{U}(1, k+1)$. Select the most adjacent fiber to m_1 denoted as m_2 characterized by $\left(\varphi_{m_2}, \theta_{m_2}, f_{m_2}\right)$.
- Compute parameters (φ_m, θ_m, f_m) of the new candidate fiber from $\left(\varphi_{m_1}, \theta_{m_1}, f_{m_1}\right)$ and $\left(\varphi_{m_2}, \theta_{m_2}, f_{m_2}\right)$ using the equation set defined by Eq. (28).
- Evaluate acceptance ratio α_{merge}.
- Sample $u \sim \mathrm{U}(0,1)$.
- If $u \leq \alpha_{\text{merge}}$ the Markov chain state becomes (k, $\boldsymbol{\varphi}_k$, $\boldsymbol{\theta}_k$, $\mathbf{f}_k$) else stay at ($k+1$, $\boldsymbol{\varphi}_{k+1}$, $\boldsymbol{\theta}_{k+1}$, $\mathbf{f}_{k+1}$).

B.3. Update move

In this case the model order k is fixed (i.e., $k'=k$). We use a hybrid MCMC algorithm to draw samples from the conditional joint distribution of the model parameters. The hybrid MCMC combines Gibbs steps with Metropolis Hastings (MH) steps. In particular, we used a MH for the $\boldsymbol{\varphi}_k$, $\boldsymbol{\theta}_k$, $\mathbf{f}_k$, λ, S_0 parameters and a Gibbs sampler for the full conditional posteriors of nuisance parameters $1/\sigma^2$ and Λ:

$$p(1/\sigma^2|\mathbf{S}, \boldsymbol{\varphi}_k, \boldsymbol{\theta}_k, \mathbf{f}_k, \lambda, S_0, k) \propto p(\mathbf{S}|\boldsymbol{\varphi}_k, \boldsymbol{\theta}_k, \mathbf{f}_k, \lambda, S_0, k, 1/\sigma^2) p(1/\sigma^2|a_\sigma, b_\sigma) \propto Ga(N_g/2 + a_\sigma, \tfrac{1}{2}(\mathbf{S}-\mathbf{S}_k)^{\mathrm{T}}(\mathbf{S}-\mathbf{S}_k) + b_\sigma) \tag{35}$$

$$p(\Lambda|k) \propto p(k|\Lambda) p(\Lambda|a_\Lambda, b_\Lambda) = C \cdot \Lambda^{\frac{1}{2}+a_\Lambda+k-1} \exp(-(1+b_\Lambda)\Lambda) \propto \mathrm{Ga}(1/2 + a_\Lambda + k, 1 + b_\Lambda) \tag{36}$$

where c is the normalization constant of the truncated Poisson distribution (see Appendix A). All samples in these cases are automatically accepted.

$$\text{likelihood ratio} = L_{\text{update}} = \exp\left[\frac{1}{2\sigma^2}\left((\mathbf{S}-\mathbf{S}_k)^{\mathrm{T}}(\mathbf{S}-\mathbf{S}_k) - (\mathbf{S}-\mathbf{S}'_k)^{\mathrm{T}}(\mathbf{S}-\mathbf{S}'_k)\right)\right]$$

$$\text{prior ratio} = \frac{p(\boldsymbol{\varphi}'_k, \boldsymbol{\theta}'_k|k)}{p(\boldsymbol{\varphi}_k, \boldsymbol{\theta}_k|k)} \frac{p(\mathbf{f}'_k|k)}{p(\mathbf{f}_k|k)} \frac{p(S'_0)}{p(S_0)} \frac{p(\lambda'|a_\lambda, b_\lambda)}{p(\lambda|a_\lambda, b_\lambda)}.$$

The prior ratio simplifies to:

$$\text{prior ratio} = \prod_{j=1}^{k} \sin\theta'_j \Big/ \prod_{i=1}^{k} \sin\theta_i \tag{37}$$

The proposal of the joint distribution of the parameters is obtained as follows:

$$q(\boldsymbol{\Omega}'_k|\boldsymbol{\Omega}_k) = q(\boldsymbol{\varphi}'_k|\boldsymbol{\varphi}_k) q(\boldsymbol{\theta}'_k|\boldsymbol{\theta}_k) q(\mathbf{f}'_k|\mathbf{f}_k) q(\lambda'|\lambda) q(S'_0|S_0)$$

where:

$$q(\boldsymbol{\varphi}'_k|\boldsymbol{\theta}_k) = \prod_{i=1}^{k} N(\varphi_i, \sigma_\varphi), q(\boldsymbol{\theta}'_k|\boldsymbol{\theta}_k) = \prod_{i=1}^{k} N(\theta_i, \sigma_\theta),$$

$$q(\mathbf{f}'_k|\mathbf{f}_k) = \prod_{i=1}^{k} N(f_i, \sigma_f), q(\lambda'|\lambda) = N(\lambda, \sigma_\lambda), q(S'_0|S_0) = N(S_0, \sigma_{S_0}). \tag{38}$$

We selected all proposals as normal distributions thus the proposal ratio = 1. Heuristically we chose the following values for the standard deviation of the previous normal distribution functions: $\sigma_\varphi = \sigma_\theta = \pi/36$, $\sigma_f = 0.01$ and $\sigma_\lambda = 0.03 \times 10^{-3}$ mm^2 s^{-1}. These values guarantee a gradual Markov chain convergence.

$$r_{\text{update}} = L_{\text{update}} \cdot \prod_{j=1}^{k} \sin\theta'_j \Big/ \prod_{i=1}^{k} \sin\theta_i. \tag{39}$$

The acceptance probability is: $\alpha_{\text{update}} = \min(1, r_{\text{update}})$.

The update move algorithm can be summarized as:

- Propose a new set parameter values $\boldsymbol{\varphi}_k'$, $\boldsymbol{\theta}_k'$, $\mathbf{f}_k'$, λ', S_0' from the proposal distribution for each parameter (see Eq. (38)).
- Sample $u \sim \mathrm{U}(0,1)$.
- Evaluate α_{update}.
- If $u \leq \alpha_{\text{update}}$ the Markov chain state becomes ($\boldsymbol{\varphi}_k'$, $\boldsymbol{\theta}_k'$, $\mathbf{f}_k'$, λ', S_0') else stay at ($\boldsymbol{\varphi}_k$, $\boldsymbol{\theta}_k$, $\mathbf{f}_k$, λ, S_0).
- Update of $1/\sigma^2$ sampled from the full conditional $p(1/\sigma^2|\mathbf{S}, \boldsymbol{\varphi}_k, \boldsymbol{\theta}_k, \mathbf{f}_k, k, S_0, \lambda)$, (see Eq. (38)).
- Update of Λ sampled from the full conditional $p(\Lambda|k)$.

Appendix C. Jacobian evaluation for merge/split moves

$$J_{\text{merge}} = \left|\frac{\partial\left(\varphi_m, \theta_m, f_m, u_\varphi, u_\theta, u_f\right)}{\partial\left(\varphi_{m_1}, \varphi_{m_2}, \theta_{m_1}, \theta_{m_2}, f_{m_1}, f_{m_2}\right)}\right|$$

$$J_{\text{merge}} = \begin{vmatrix} \frac{\partial\varphi_m}{\partial\varphi_{m_1}} & \frac{\partial\theta_m}{\partial\varphi_{m_1}} & \frac{\partial f_m}{\partial\varphi_{m_1}} & \frac{\partial u_\varphi}{\partial\varphi_{m_1}} & \frac{\partial u_\theta}{\partial\varphi_{m_1}} & \frac{\partial u_f}{\partial\varphi_{m_1}} \\ \frac{\partial\varphi_m}{\partial\varphi_{m_2}} & \frac{\partial\theta_m}{\partial\varphi_{m_2}} & \frac{\partial f_m}{\partial\varphi_{m_2}} & \frac{\partial u_\varphi}{\partial\varphi_{m_2}} & \frac{\partial u_\theta}{\partial\varphi_{m_2}} & \frac{\partial u_f}{\partial\varphi_{m_2}} \\ \frac{\partial\varphi_m}{\partial\theta_{m_1}} & \frac{\partial\theta_m}{\partial\theta_{m_1}} & \frac{\partial f_m}{\partial\theta_{m_1}} & \frac{\partial u_\varphi}{\partial\theta_{m_1}} & \frac{\partial u_\theta}{\partial\theta_{m_1}} & \frac{\partial u_f}{\partial\theta_{m_1}} \\ \frac{\partial\varphi_m}{\partial\theta_{m_2}} & \frac{\partial\theta_m}{\partial\theta_{m_2}} & \frac{\partial f_m}{\partial\theta_{m_2}} & \frac{\partial u_\varphi}{\partial\theta_{m_2}} & \frac{\partial u_\theta}{\partial\theta_{m_2}} & \frac{\partial u_f}{\partial\theta_{m_2}} \\ \frac{\partial\varphi_m}{\partial f_{m_1}} & \frac{\partial\theta_m}{\partial f_{m_1}} & \frac{\partial f_m}{\partial f_{m_1}} & \frac{\partial u_\varphi}{\partial f_{m_1}} & \frac{\partial u_\theta}{\partial f_{m_1}} & \frac{\partial u_f}{\partial f_{m_1}} \\ \frac{\partial\varphi_m}{\partial f_{m_2}} & \frac{\partial\theta_m}{\partial f_{m_2}} & \frac{\partial f_m}{\partial f_{m_2}} & \frac{\partial u_\varphi}{\partial f_{m_2}} & \frac{\partial u_\theta}{\partial f_{m_2}} & \frac{\partial u_f}{\partial f_{m_2}} \end{vmatrix}$$

$$= \begin{vmatrix} c_1 & 0 & 0 & \frac{c_2}{\Delta\varphi} & 0 & 0 \\ c_2 & 0 & 0 & -\frac{c_2}{\Delta\varphi} & 0 & 0 \\ 0 & c_1 & 0 & 0 & \frac{c_2}{\Delta\theta} & 0 \\ 0 & c_2 & 0 & 0 & -\frac{c_2}{\Delta\theta} & 0 \\ 0 & 0 & 1 & 0 & 0 & \frac{f_{m_2} - f_{\text{thres}}}{(f_m - 2f_{\text{thres}})^2} \\ 0 & 0 & 1 & 0 & 0 & -\frac{f_{m_1} - f_{\text{thres}}}{(f_m - 2f_{\text{thres}})^2} \end{vmatrix}$$

Below we present the development of the differential terms in the Jacobian.

Separating out u_φ by means of Eq. (29), we obtain the following differential terms:

$$\frac{\partial u_\varphi}{\partial\varphi_1} = \frac{1-c_1}{\Delta\varphi} = \frac{c_2}{\Delta\varphi}; \frac{\partial u_\varphi}{\partial\varphi_2} = -\frac{1-c_1}{\Delta\varphi} = -\frac{c_2}{\Delta\varphi}.$$

Separating out u_θ by means of Eq. (30), we obtained the following differential terms:

$$\frac{\partial u_\theta}{\partial \theta_1} = \frac{1-c_1}{\Delta\theta} = \frac{c_2}{\Delta\theta}; \frac{\partial u_\theta}{\partial \theta_2} = -\frac{1-c_1}{\Delta\theta} = -\frac{c_2}{\Delta\theta}$$

Separating out u_f for the case of the volume fraction f, we obtain the following differential terms: $\frac{\partial u_f}{\partial f_{m_1}} = \frac{f_{m_2} - f_{\text{thres}}}{(f_m - 2f_{\text{thres}})^2}; \frac{\partial u_f}{\partial f_{m_2}} = -\frac{f_{m_1} - f_{\text{thres}}}{(f_m - 2f_{\text{thres}})^2}$. In order to compute the Jacobian previously defined, the standard column/row development techniques are used to obtain the following final expression:

$$J_{\text{merge}} = \frac{c_2}{\Delta\varphi\Delta\theta(f_m - 2f_{\text{thres}})}. \quad (40)$$

The expression of the Jacobian for the split move is calculated by: $J_{\text{split}} = 1/J_{\text{merge}}$.

References

Alexander, D.C., Barker, G.J., Arridge, S.R., 2002. Detection and modeling of non-Gaussian apparent diffusion coefficient profiles in human brain data. Magn. Reson. Med. 48, 331–340.

Andrieu, C., Doucet, A., 1999. Joint Bayesian model selection and estimation of noisy sinusoids via reversible jump MCMC. IEEE Trans. Signal Process. 47, 2667–2676.

Andrieu, C., de Freitas, N., Doucet, A., 2001. Robust full Bayesian learning for radial basis networks. Neural Comput. 13, 2359–2407.

Assaf, Y., Freidlin, R.Z., Rohde, G.K., Basser, P.J., 2004. New modeling and experimental framework to characterize hindered and restricted water diffusion in brain white matter. Magn. Reson. Med. 52, 965–978.

Bandyopadhyay, S., 2005. Simulated annealing using a reversible jump Markov chain Monte Carlo algorithm for fuzzy clustering. IEEE Trans. Knowl. Data Eng. 17, 479–490.

Basser, P.J., Pierpaoli, C., 1996. Microstructural and physiological features of tissues elucidated by quantitative-diffusion-tensor MRI. J. Magn. Reson., Ser. B 111, 209–219.

Basser, P.J., Mattiello, J., LeBihan, D., 1994a. Estimation of the effective self-diffusion tensor from the NMR spin echo. J. Magn. Reson., Ser. B 103, 247–254.

Basser, P.J., Mattiello, J., LeBihan, D., 1994b. MR diffusion tensor spectroscopy and imaging. Biophys. J, 66, 259–267.

Behrens, T.E., Woolrich, M.W., Jenkinson, M., Johansen-Berg, H., Nunes, R.G., Clare, S., Matthews, P.M., Brady, J.M., Smith, S.M., 2003. Characterization and propagation of uncertainty in diffusion-weighted MR imaging. Magn. Reson. Med. 50, 1077–1088.

Behrens, T.E., Berg, H.J., Jbabdi, S., Rushworth, M.F., Woolrich, M.W., 2007. Probabilistic diffusion tractography with multiple fibre orientations: what can we gain? NeuroImage 34, 144–155.

Bertrand, C., Ohmi, M., Suzuki, R., Kado, H., 2001. A probabilistic solution to the MEG inverse problem via MCMC methods: the reversible jump and parallel tempering algorithms. IEEE Trans. Biomed. Eng. 48, 533–542.

Brooks, S.P., 2001. On Bayesian analyses and finite mixtures for proportions. Stat. Comput. 11, 179–190.

Frank, L.R., 2001. Anisotropy in high angular resolution diffusion-weighted MRI. Magn. Reson. Med. 45, 935–939.

Frank, L.R., 2002. Characterization of anisotropy in high angular resolution diffusion-weighted MRI. Magn. Reson. Med. 47, 1083–1099.

Gilks, W.R., R.S.S., 1995. Markov Chain Monte Carlo in Practice.

Green, P.J., 1995. Reversible jump Markov chain Monte Carlo computation and Bayesian model determination. Biometrika 82, 711–732.

Hoeting, J.A., Madigan, D., Raftery, A.E., Volinsky, C.T., 1999. Bayesian model averaging: a tutorial. Stat. Sci. 14, 382–401.

Hosey, T., Williams, G., Ansorge, R., 2005. Inference of multiple fiber orientations in high angular resolution diffusion imaging. Magn. Reson. Med. 54, 1480–1489.

Larocque, J.R., Reilly, J.P., Ng, W., 2002. Particle filters for tracking an unknown number of sources. IEEE Trans. Signal Process. 50, 2926–2937.

Le Bihan, D., 2003. Looking into the functional architecture of the brain with diffusion MRI. Nat. Rev., Neurosci. 4, 469–480.

Lin, C.P., Wedeen, V.J., Chen, J.H., Yao, C., Tseng, W.Y., 2003. Validation of diffusion spectrum magnetic resonance imaging with manganese-enhanced rat optic tracts and ex vivo phantoms. NeuroImage 19, 482–495.

Melie-García, L., Canales-Rodríguez, E., Valdés-Hernández, P.A., 2004. Anisotropy characterization in diffusion weighted MRI via reversible jump MCMC. Available on CD-Rom in NeuroImage, WE 242, Vol. 22, Supplement 1, Presented at the 10th International Conference on Functional Mapping of the Human Brain, June 14–17, 2004, Budapest, Hungary.

Mori, S., Wakana, S., van Zijl, P.C.M., Nagae-Poetscher, L.M., 2005. MRI Atlas of Human White Matter. Elsevier.

Parker, G.J.M., Luzzi, S., Alexander, D.C., Wheeler-Kingshott, C.A.M., Clecarelli, O., Ralph, M.A.L., 2005. Lateralization of ventral and dorsal auditory-language pathways in the human brain. NeuroImage 24, 656–666.

Richardson, S., Green, P.J., 1997. On Bayesian analysis of mixtures with an unknown number of components. J. R. Stat. Soc., B 59, 731–758.

Rue, H., Hurn, M.A., 1999. Bayesian object identification. Biometrika 86, 649–660.

Salvador, R., Pena, A., Menon, D.K., Carpenter, T.A., Pickard, J.D., Bullmore, E.T., 2005. Formal characterization and extension of the linearized diffusion tensor model. Hum. Brain Mapp. 24, 144–155.

Stephens, D.A., 1998. Bayesian analysis of quantitative trait locus data using reversible jump Markov chain Monte Carlo. Biometrics 54, 1334–1347.

Tuch, D.S., Reese, T.G., Wiegell, M.R., Makris, N., Belliveau, J.W., Wedeen, V.J., 2002. High angular resolution diffusion imaging reveals intravoxel white matter fiber heterogeneity. Magn. Reson. Med. 48, 577–582.

Westin, C.F., Peled, S., Gudbjartsson, H., Kikinis, R., Jolesz, F.A., 1997. Geometrical Diffusion Measures for MRI from Tensor Basis Analysis. Vancouver, p. 1742.

5.5 Robust and unbiased model-based spherical deconvolution of multichannel diffusion MRI data

Autores: Erick J. Canales-Rodríguez, Alessandro Daducci, Stamatios N. Sotiropoulos, Emmanuel Caruyer, Santiago Aja-Fernández, Joaquim Radua, Jesús M. Yurramendi Mendizabal, Yasser Iturria-Medina, Lester Melie-García, Yasser Alemán-Gómez, Jean-Philippe Thiran, Salvador Sarró, Edith Pomarol-Clotet, Raymond Salvador.

Título: *Spherical deconvolution of multichannel diffusion MRI data with non-Gaussian noise models and spatial regularization*

Revista: *PLoS ONE*

Año y volumen: Artículo aceptado en 2015 (actualmente en la imprenta de la casa editorial).

Factor de impacto (actual): 3.23

La técnica propuesta también se presentó en el siguiente congreso internacional:

Autores: Erick J Canales-Rodríguez

Título: *Richardson-Lucy Spherical Deconvolution under Rician noise with Total Variation Spatial Regularization*

Conferencia (abstract): IEEE International Symposium on Biomedical Imaging (ISBI 2013), High Angular Resolution Diffusion MRI Reconstruction Challenge, 7-11 April 2013, San Francisco (USA).

Spherical deconvolution of multichannel diffusion MRI data with non-Gaussian noise models and spatial regularization

Erick J. Canales-Rodríguez[1,2♫], Alessandro Daducci[3,4¶], Stamatios N. Sotiropoulos[5¶], Emmanuel Caruyer[6], Santiago Aja-Fernández[7], Joaquim Radua[1,2,8,9], Jesús M. Yurramendi Mendizabal[10], Yasser Iturria-Medina[11], Lester Melie-García[12], Yasser Alemán-Gómez[2,13,14], Jean-Philippe Thiran[3,4], Salvador Sarró[1,2], Edith Pomarol-Clotet[1,2], Raymond Salvador[1,2].

[1] FIDMAG Germanes Hospitalàries, C/ Dr. Antoni Pujadas, 38, 08830, Sant Boi de Llobregat, Barcelona, Spain. Tel: +34 93 6529999, Fax: +34 936400268.

[2] Centro de Investigación Biomédica en Red de Salud Mental, CIBERSAM, C/Dr Esquerdo, 46, 28007, Madrid, Spain.

[3] Signal Processing Lab (LTS5), École polytechnique fédérale de Lausanne (EPFL), Lausanne, Switzerland.

[4] University Hospital Center (CHUV) and University of Lausanne (UNIL), Lausanne, Switzerland.

[5] Centre for Functional Magnetic Resonance Imaging of the Brain (FMRIB), University of Oxford, John Radcliffe Hospital, Oxford OX39DU, United Kingdom.

[6] CNRS - IRISA (UMR 6074), Inria - VisAGeS Project-Team, INSERM - VisAGeS U746, Université de Rennes 1, Campus de Beaulieu, 35042 Rennes Cedex, France.

[7] Laboratorio de Procesado de Imagen (LPI), ETSI Telecomunicación, Universidad de Valladolid, Valladolid, Spain.

[8] Department of Psychosis Studies, Institute of Psychiatry, Psychology & Neuroscience, King's College London, United Kingdom.

[9] Department of Clinical Neuroscience, Karolinska Institutet, Stockholm, Sweden.

[10] Departamento de Ciencia de la Computación e Inteligencial Artificial, Universidad del País Vasco - Euskal Herriko Unibertsitatea, Spain.

[11] McConnell Brain Imaging Center, Montreal Neurological Institute, McGill University, Montreal, Quebec, Canada.

[12] The Neuroimaging Research Laboratory (Laboratoire de Recherche en Neuroimagerie: LREN), Department of Clinical Neurosciences, University Hospital Center (CHUV), Lausanne, Switzerland.

[13] Departamento de Bioingeniería e Ingeniería Aeroespacial. Universidad Carlos III de Madrid, Madrid, Spain.

[14] Instituto de Investigación Sanitaria Gregorio Marañón, Madrid, Spain.

♫ **Corresponding author**

Erick Jorge Canales-Rodríguez

E-mail: ejcanalesr@gmail.com

¶ These authors contributed equally to this work

Abstract

Spherical deconvolution (SD) methods are widely used to estimate the intra-voxel white-matter fiber orientations from diffusion MRI data. However, while some of these methods assume a zero-mean Gaussian distribution for the underlying noise, its real distribution is known to be non-Gaussian and to depend on many factors such as the number of coils and the methodology used to combine multichannel MRI signals. Indeed, the two prevailing methods for multichannel signal combination lead to noise patterns better described by Rician and noncentral Chi distributions. Here we develop a Robust and Unbiased Model-BAsed Spherical Deconvolution (RUMBA-SD) technique, intended to deal with realistic MRI noise, based on a Richardson-Lucy (RL) algorithm adapted to Rician and noncentral Chi likelihood models. To quantify the benefits of using proper noise models, RUMBA-SD was compared with dRL-SD, a well-established method based on the RL algorithm for Gaussian noise. Another aim of the study was to quantify the impact of including a total variation (TV) spatial regularization term in the estimation framework. To do this, we developed TV spatially-regularized versions of both RUMBA-SD and dRL-SD algorithms. The evaluation was performed by comparing various quality metrics on 132 three-dimensional synthetic phantoms involving different inter-fiber angles and volume fractions, which were contaminated with noise mimicking patterns generated by data processing in multichannel scanners. The results demonstrate that the inclusion of proper likelihood models leads to an increased ability to resolve fiber crossings with smaller inter-fiber angles and to better detect non-dominant fibers. The inclusion of TV regularization dramatically improved the resolution power of both techniques. The above findings were also verified in human brain data.

Keywords: diffusion weighted imaging; spherical deconvolution; Rician noise; noncentral Chi noise; total variation.

Introduction

After decades of developments in diffusion Magnetic Resonance Imaging (MRI), the successful implementation of a variety of advanced methods has shed light on the complex patterns of brain organization present at micro [1] and macroscopic scales [2-4]. Among these methods, Diffusion Tensor Imaging (DTI) [5] has become a classic in both clinical and research studies. DTI can deliver quantitative results, it may be easily implemented in any clinical MRI system and, thanks to its short acquisition time, it may be suitable for studying a wide range of brain diseases. Unfortunately, it is now well recognized that due to its simplistic assumptions, the DTI model does not adequately describe diffusion processes in areas of complex tissue organization, like in areas with kissing, branching or crossing fibers [6].

Such limitations in the DTI approach have prompted the recent development of numerous sampling protocols, diffusion models and reconstruction techniques (e.g., see [7-9] and references therein). While some of these techniques have been based on model-free methods, including q-ball imaging [10] and its extensions [11-17], diffusion orientation transforms [18, 19], diffusion spectrum imaging [20] and related q-space techniques [21-26], other approaches have relied on parametric diffusion models using higher-order tensors [27-29] and multiple second-order diffusion tensors [6]. In the later group, different numerical techniques involving gradient descent [6], Bayesian inference [30-32] and algorithms inspired from compressed sensing theory [33-35] have been applied to solve the resulting inverse problems.

Spherical Deconvolution (SD) is a class of multi-compartment reconstruction technique that can be implemented using both parametric and nonparametric signal models [36-49]. SD methods have become very popular owing to their ability to resolve fiber crossings with small inter-fiber angles in datasets acquired within a clinically feasible scan time. This resolving power is driven by the fact that, as opposed to model-free techniques that estimate the diffusion Orientational Distribution Function (ODF), the output from SD is directly the fiber ODF itself.

Among the different SD algorithms, Constrained Spherical Deconvolution (CSD) [39, 40] has been received with special interest due to its good performance and short computational time. In CSD, the average signal profile from white-matter regions of parallel fibers is first estimated, and

afterwards, the fiber ODF is estimated by deconvolving the measured diffusion data in each voxel with this signal profile, which is also known as the single-fiber 'response function'.

More recently and as an alternative to CSD, a new SD method based on a damped Richardson-Lucy algorithm adapted to Gaussian noise (dRL-SD) has been proposed [37, 42]. An extensive evaluation of both CSD and dRL-SD algorithms has revealed a superior ability to resolve low anisotropy crossing-fibers by CSD but a lower percentage of spurious fiber orientations and a lower over-all sensitivity to the selection of the response function by the dRL-SD approach [50]. This later feature is of great relevance since the assumption of a common response function for all brain tracts is a clear over-simplification of both methods, with the consequences of it minimized by the dRL-SD.

From an algorithmic perspective dRL-SD inherits the benefits of the standard RL deconvolution method applied with great success in diverse fields ranging from microscopy [51] to astronomy [52]. Remarkably, RL deconvolution is robust to the experimental noise and the obtained solution can be constrained to be non-negative without the need for including additional penalization functions in the estimation process. Moreover, from a modeling point of view, dRL-SD is implemented using an extended multi-compartment model that allows considering the partial volume effect in brain voxels with mixture of white matter (WM), gray matter (GM) and cerebrospinal fluid (CSF), a strategy that has been shown to be effective in reducing the occurrence of spurious fiber orientations [37].

However, in spite of the good properties of dRL-SD and other SD methods some methodological issues remain. These methods, to some extent, assume additivity and zero mean Gaussianity for the underlying noise and are potentially vulnerable to significant departures from such an assumption. Indeed, it is well known that the MRI noise is non-Gaussian and depends on many factors, including the number of coils in the scanner and the multichannel image combination method. Real experiments have shown that noise follows Rician [53] and noncentral Chi (nc-χ) distributions [54] evidencing the inappropriateness of the Gaussian model. This issue is especially relevant in diffusion MRI data where the high b-values required to enhance the angular contrast lead to extremely low signal-to-noise (SNR) ratios. A recent study [55] has

shown that different multichannel image combination methods can changes the properties of the signal and can have an effect on fiber orientation estimation.

On the other hand, the standard reconstruction in SD, based on a voxel-by-voxel fiber ODF estimation, although reasonable it may not be optimal in a global sense as it does not take into account the underlying spatial continuity of the image. Recent research on the inclusion of spatial continuity into SD methods via regularization has yielded promising results [9, 56, 57]**.** Among these, spatially regularized SD methods based on Total Variation (TV) [9] are very appealing due to their outstanding ability to simultaneously smooth away noise in flat regions whilst preserving edges, and due to their robustness to high levels of noise [58].

This work has two main aims: (1) the study and quantification of the benefits of the adequate modelling of the noise distribution in the context of spherical deconvolution, and (2) the study and quantification of the effects of including a TV spatial regularization term in the proposed estimation framework.

To address the first objective we developed a new SD methodology which, following a more realistic view, deals with non-Gaussian noise models. Specifically, the estimation framework is based on a natural extension to the RL algorithm for Rician and nc-χ likelihood distributions. We had chosen the RL algorithm as a starting point for our work because this algorithm has proven to be highly efficient in diverse applications, and because the performance of the resulting method can be directly compared to the state-of-the-art dRL-SD method, which employs a nearly-equivalent SD estimation algorithm but based on a Gaussian noise model. The second aim was addressed by including TV regularization to the developed formulation. Moreover, for completeness we have extended also the dRL-SD method via the spatially-regularized proposed estimation.

To compare the relative performance between the SD methods based on Gaussian and non-Gaussian noise models, and their respective implementations including the TV regularization, the different algorithms were applied to several synthetic phantom datasets which had been contaminated with noise patterns mimicking the Rician and nc-χ noise distributions produced in multichannel scanners. To the best of our knowledge, this is the first evaluation of such methods

in a scenario where Rician and nc-χ noise are explicitly created as a function of the number of coils, their spatial sensitivity maps, the correlation between coils, and the reconstruction methodology used to combine the multichannel signals. As a final analysis, the new method is also applied to real multichannel diffusion MRI data from a healthy subject.

Following this introduction there is a 'Theory' section providing an overview of the different topics relevant to the study and the derivation of the new SD reconstruction algorithm. Description about computer simulations, image acquisition strategies and metrics designed to evaluate the performance of the reconstructions is provided in the Materials and Methods section. Relevant findings are succinctly described in the Results section. Finally, main results, contributions and limitations of this work are addressed in the Discussion and Conclusions section.

Theory

This section contains a description of the forward/generative model used to relate the local diffusion process with the measured diffusion MRI data. It also provides a brief review of MRI noise models. Finally, the diffusion and MRI noise models are used to derive the new SD reconstruction algorithms.

1 Generative signal and fiber ODF model

The diffusion MRI signal measured for a given voxel can be expressed as the sum of the signals from each intra-voxel compartment. The term 'compartment' is defined as a homogeneous region in which the diffusion process possesses identical properties in magnitude and orientation throughout, and which is different to the diffusion processes occurring in other compartments. One example of this approach is the multi-tensor model that allows considering multiple WM parallel-fiber populations within the voxel. In this model the diffusion process taking place inside each compartment of parallel fibers is described by a second-order self-diffusion tensor [6].

In real brain data, in addition to the different WM compartments, voxels might also contain GM and CSF components. This issue was considered by [37], who extended the multi-tensor model by incorporating the possible contribution from these compartments. This is the generative multi-tissue signal model that will be used in the present study. In the absence of any source of noise, the resulting expression for the signal is:

$$S_i = S_0 \left(\sum_{j=1}^{M} \mathrm{f}_j \exp\left(-b_i \mathbf{v}_i^T \mathbf{D}_j \mathbf{v}_i\right) + \mathrm{f}_{GM} \exp\left(-b_i D_{GM}\right) + \mathrm{f}_{CSF} \exp\left(-b_i D_{CSF}\right) \right), \qquad \textbf{(1)}$$

where M is the total number of WM parallel fiber bundles; f_j denotes the volume fraction of the jth fiber-bundle compartment; f_{GM} and f_{CSF} are the volume fractions of the GM and CSF

compartments respectively, so that $\sum_{j=1}^{M} \mathrm{f}_j + \mathrm{f}_{GM} + \mathrm{f}_{CSF} = 1$; b_i is the diffusion-sensitization factor (i.e., *b*-value) used in the acquisition scheme to measure the diffusion signal S_i along the diffusion-sensitizing gradient unit vector $\mathbf{v}_i$, $i = 1,...,N$; D_{GM} and D_{CSF} are respectively the mean diffusivity coefficients in GM and CSF; S_0 is the signal amplitude in the absence of diffusion-sensitization gradients ($b_i = 0$); $\mathbf{D}_j = \mathbf{R}_j^T \mathbf{A} \mathbf{R}_j$ denotes the anisotropic diffusion tensor of the jth fiber-bundle, where $\mathbf{R}_j$ is the rotation matrix that rotates a unit vector initially oriented along the x-axis toward the jth fiber orientation (θ_j, ϕ_j) and $\mathbf{A}$ is a diagonal matrix containing information about the magnitude and anisotropy of the diffusion process inside that compartment:

$$\mathbf{A} = \begin{pmatrix} \lambda_1 & 0 & 0 \\ 0 & \lambda_2 & 0 \\ 0 & 0 & \lambda_3 \end{pmatrix}, \qquad \textbf{(2)}$$

where λ_1 is the diffusivity along the jth fiber orientation, λ_2 and λ_3 are the diffusivities in the plane perpendicular to it. It is assumed that $\lambda_1 > \lambda_2 \approx \lambda_3$.

At each voxel, the measured diffusion signals S_i for N different sampling parameters (i.e., $\mathbf{v}_i$ and b_i, $i \in [1,...,N]$) can be recast in matrix form as:

$$\mathbf{S} = \mathbf{H}\mathbf{f}, \qquad \textbf{(3)}$$

where $\mathbf{S} = [S_1 \quad \dots \quad S_i \quad \dots \quad S_N]^T$ and $\mathbf{H} = [\mathbf{H}^{WM} \mid \mathbf{H}^{ISO}]$ comprises two sub-matrices. $\mathbf{H}^{WM}$ is an *N* x *M* matrix where every column of length *N* contains the values of the signal generated by the model given in Eq. (1) for a single fiber-bundle compartment oriented along one of the *M*-

directions, i.e., the (i, j)th element of $\mathbf{H}^{WM}$ is equal to $\mathbf{H}_{ij}^{WM} = S_0 \exp\left(-b_i \mathbf{v}_i^T \mathbf{D}_j \mathbf{v}_i\right)$. Likewise, $\mathbf{H}^{ISO}$ is an *N* x *2* matrix where each of the two columns of length *N* contains the values of the signal for each isotropic compartment, i.e., $\mathbf{H}_{i1}^{ISO} = S_0 \exp\left(-b_i D_{GM}\right)$ and $\mathbf{H}_{i2}^{ISO} = S_0 \exp\left(-b_i D_{CSF}\right)$. Finally, the column-vector $\mathbf{f}$ of length *M+2* includes the volume fractions of each compartment within the voxel.

In the framework of model-based spherical deconvolution, $\mathbf{H}$ is created by specifying the diffusivities, which are chosen according to prior information, and by providing a dense discrete set of equidistant *M*-orientations $\Omega = \left\{\left(\theta_j, \phi_j\right),\ j \in [1, ..., M]\right\}$ uniformly distributed on the unit sphere. Previous studies have used different sets of orientations, ranging from *M*=129 [43] to *M*=752 [42]. Then, the goal is to infer the volume fraction of all predefined oriented fibers, $\mathbf{f}$, from the vector of measurements $\mathbf{S}$ and the 'dictionary' $\mathbf{H}$ of oriented basis signals. Under this reconstruction model, $\mathbf{f}$ can be interpreted to as the fiber ODF evaluated on the set Ω. Matrix $\mathbf{H}$ is also known as the 'diffusion basis functions' [43], or the 'point spread function' [37-39] that blurs the fiber ODF to produce the observed measurements.

It should be noticed that solving the deconvolution problem given by Eq. (3) is not simple because the resulting system of linear equations is ill-conditioned and ill-posed (i.e., there are more unknowns than measurements and some of the columns of $\mathbf{H}$ are highly correlated), which can lead to numerical instabilities and physically meaningless results (e.g., volume fractions with negative values). A common strategy to avoid such instabilities is to use robust algorithms that search for solutions compatible with the observed data but which also satisfy some additional constraints. Thus, in SD it is typical to estimate the fiber ODF by constraining it to be non-negative and symmetric around the origin (i.e., antipodal symmetry). As mentioned in the introduction, though, all these reconstruction algorithms may not be necessarily optimal when dealing with non-Gaussian noise, as it is the case for MRI noise.

2 MRI noise models

In conventional MRI systems, the data are measured using a single quadrature detector (i.e., coil with two orthogonal elements) that gives two signals which, for convenience, are treated as the real and imaginary parts of a complex number. The magnitude of this complex number (i.e. the square root of the sum of their squares) is commonly used because it avoids different kinds of MRI artifacts [53]. Given that the noise in the real and imaginary components follows a Gaussian distribution, the magnitude signal S_i will follow a Rician distribution [53] with a probability function given by

$$P(S_i \left| \overline{S}_i, \sigma^2 \right.) = \frac{S_i}{\sigma^2} \exp\left\{ -\frac{1}{2\sigma^2}\left[{S_i}^2 + \overline{S}_i^2 \right] \right\} I_0\left(\frac{S_i \overline{S}_i}{\sigma^2} \right) u\left(S_i \right), \quad \textbf{(4)}$$

where $\overline{S}_i$ denotes the true magnitude signal intensity in the absence of noise, σ^2 is the variance of the Gaussian noise in the real and imaginary components, I_0 is the modified Bessel function of first kind of order zero and u is the Heaviside step function that is equal to 0 for negative arguments and to 1 for non-negative arguments.

Modern clinical scanners are usually equipped with a set of 4 to 32 multiple phased-array coils, the signals of which can be combined following different strategies that, in turn, will give rise to different statistical properties for the noise [54]. One frequent strategy uses the spatial matched filter (SMF) approach linearly combining the complex signals of each coil and producing voxelwise complex signals [59]. Since the noise in the resulting real and imaginary components remains Gaussian a Rician distribution is expected in the final combined magnitude image. An alternative to the SMF is to create the composite magnitude image as the root of the sum-of-squares (SoS) of the complex signals of each coil. Under this approach the combined image follows a nc-χ distribution [60] given by,

$$P(S_i \left| \overline{S}_i, \sigma^2, n \right.) = \frac{\overline{S}_i}{\sigma^2} \left(\frac{S_i}{\overline{S}_i} \right)^n \exp\left\{ -\frac{1}{2\sigma^2} \left[S_i^{\,2} + \overline{S}_i^{\,2} \right] \right\} I_{n-1}\left(\frac{S_i \overline{S}_i}{\sigma^2} \right) u(S_i), \quad \textbf{(5)}$$

where n is the number of coils and I_{n-1} is the modified Bessel function of first kind of order $n-1$. This expression is strictly valid when the different coils produce uncorrelated noise with equal variance, and when noise correlation cannot be neglected it provides a good approximation if effective n_{eff} and σ^2_{eff} values are considered [61], with n_{eff} being a non-integer number lower than the real number of coils and σ^2_{eff} is higher than the real noise variance in each coil.

A related SoS image combination method that increases the validity of Eq. (5) is the covariance-weighted SoS. This method is equivalent to pre-whitening (i.e., decorrelate) the measured signals before applying the standard SoS image combination. The covariance-weighted SoS approach requires the estimation of the noise covariance matrix of the system which, in practice, may be carried out by digitizing noise from the coils in the absence of excitations [62].

It is important to note that there are additional factors that can change the noise characteristics described above, including the use of accelerated techniques based on under-sampling approaches such as those used in parallel MRI (pMRI) and partial Fourier, certain reconstruction filters in k-space, and some of the preprocessing steps conducted after image reconstruction.

Empirical data suggest that some of these factors do not substantially change the type of distribution of the noise. On the one hand, [54] investigated the effects of the type of filter in k-space, the number of receiving channels and the use of pMRI reconstruction techniques, and found that noise distributions always followed Rician and nc-χ distributions with a reasonable accuracy - although their standard deviations and effective number of receiver channels were altered when fast pMRI and subsequent SoS reconstructions were used. On the other hand, [55] showed real diffusion MRI data noise to also follow Rician and nc-χ noise distributions after a preprocessing that included motion and eddy currents corrections. Unfortunately, the combined effect of all factors has not, to the best of our knowledge, being studied. In this regard, a complete evaluation should include the study of the effects of additional data manipulation

processes routinely applied in many clinical research studies, such as B0-unwarping due to magnetic field inhomogeneity and partial Fourier reconstructions. Although the latter has been investigated in terms of signal-to-noise ratio, its influence on the shape of the noise distribution remains unknown.

However, while it is impossible to ensure that Rician and nc-χ distributions are the optimal noise models for all possible strategies used for sampling, reconstructing and preprocessing diffusion MRI data, such models are flexible enough to adapt to deviations from the initial theoretical assumptions. Their parameterization in terms of spatial-dependent effective parameters (i.e., $n_{eff}(x,y,z)$, $\sigma^2_{eff}(x,y,z)$, as in [61, 63, 64]) allows characterizing the spatially varying nature of the noise observed in accelerated MRI reconstructed data, as well as the spatial correlation introduced by reconstruction algorithms, whilst preserving the good theoretical properties of the models with standard parameters, i.e. the null probability to obtain negative signals and the ability to characterize the signal-dependent non-linear bias of the data.

3 Spherical deconvolution of diffusion MRI data

Equation (5) based on either conventional (i.e., n, σ^2) or effective (i.e., n_{eff}, σ^2_{eff}) parameters provides a very general MRI noise model, which includes the Rician distribution (given in Eq. (4)) as a special case with $n=1$. Consequently, if we derive the spherical deconvolution reconstruction corresponding to Equation (6) any particular solution of interest will become available.

Specifically, if we assume the linear model given by Eqs. (1)-(3) the likelihood model for the vector of measurements $\mathbf{S}$ under a nc-χ distribution is

$$P(\mathbf{S}\left|\mathbf{H},\mathbf{f},\sigma^2,n\right.)=\prod_{i=1}^{N}\frac{\bar{S}_i}{\sigma^2}\left(\frac{S_i}{\bar{S}_i}\right)^n\exp\left\{-\frac{1}{2\sigma^2}\left[S_i^2+\bar{S}_i^2\right]\right\}I_{n-1}\left(\frac{S_i\bar{S}_i}{\sigma^2}\right)u(S_i), \qquad \textbf{(6)}$$

where S_i and $\bar{S}_i = (\mathbf{Hf})_i$ are the measured and expected signal intensities for *i*th sampling parameters, respectively.

3.1 Unbiased and positive recovery: the multiplicative Richardson-Lucy algorithm for nc-χ noise

The maximum likelihood (ML) estimate in Eq. (6) is obtained by differentiating its negative log-likelihood $J(\mathbf{f}) = -\log P(\mathbf{S}|\mathbf{H},\mathbf{f},\sigma^2,n)$ with respect to $\mathbf{f}$ and equating the derivative to zero, which after some algebraic manipulations becomes

$$\mathbf{f} = \mathbf{f} \circ \frac{\mathbf{H}^T\left[\mathbf{S} \circ \dfrac{I_n\left(\mathbf{S} \circ \mathbf{Hf}/\sigma^2\right)}{I_{n-1}\left(\mathbf{S} \circ \mathbf{Hf}/\sigma^2\right)}\right]}{\mathbf{H}^T\mathbf{Hf}}, \tag{7}$$

where '∘' stands for the Hadamard component-wise product, and the division operators are applied component-wise to the vector's elements.

Equation (7) is nonlinear in $\mathbf{f}$ and its solution can be obtained through a modified version of the expectation maximization technique, originally developed by Richardson and Lucy for a Poisson noise model [65, 66] and known as the RL algorithm. When we applied this technique to nc-χ and Rician distributed noise it naturally led to the following iterative estimation formula:

$$\mathbf{f}^{k+1} = \mathbf{f}^k \circ \frac{\mathbf{H}^T\left[\mathbf{S} \circ \dfrac{I_n\left(\mathbf{S} \circ \mathbf{Hf}^k/\sigma^2\right)}{I_{n-1}\left(\mathbf{S} \circ \mathbf{Hf}^k/\sigma^2\right)}\right]}{\mathbf{H}^T\mathbf{Hf}^k}, \tag{8}$$

in which the solution calculated at the kth iteration step ($\mathbf{f}^k$) gradually improves (i.e. its likelihood increases after each step) until a final, stationary solution $\frac{\mathbf{f}^{k+1}}{\mathbf{f}^k}=1$, is reached. As shown Appendix A in S1 File, this formula can also be related to the RL algorithm for Gaussian noise, employed in the undamped RL-SD technique [42].

Under the absence of any prior knowledge about $\mathbf{f}$, the initial estimate ($\mathbf{f}^0$) can be fixed to a non-negative constant density distribution [42]. In that case, the algorithm transforms a perfectly smooth initial estimate into sharper estimates, with sharpness increasing with the number of iterations. So, roughly speaking, the number of iterations can be considered as a regularization parameter controlling the angular smoothness of the final estimate. Notably, if $\mathbf{f}^0$ is non-negative, the successive estimates remain non-negative as well, and the algorithm always produces reconstructions with positive elements. Moreover, as in [37, 42] the estimation does not involve any matrix inversion, thus avoiding related numerical instabilities.

In order to evaluate Eq. (8) an estimate $\tilde{\sigma}^2$ of σ^2 is required. Although obtaining it from a region-of-interest (ROI) is feasible [67] its accuracy may be compromised by systematic experimental issues such as ghosting artifacts, signal suppression by the scanner outside the brain, zero-padding and by filters applied in the *k*-space. Moreover, with the use of fast parallel MRI sequences, where each coil records signals with partial coverage in the k-space, properties of the noise become spatially heterogeneous (i.e. they change from voxel to voxel across the image). While some authors have proposed alternatives to overcome these limitations [68] here we have estimated the noise variance at each voxel from the same data used to infer the fiber ODF.

Specifically, by minimizing the negative log-likelihood with respect to σ^2 we have obtained an iterative scheme analogous to Eq. (8):

$$\alpha^{k+1}=\frac{1}{nN}\left\{\frac{\mathbf{S}^T\mathbf{S}+\mathbf{f}^T\mathbf{H}^T\mathbf{H}\mathbf{f}}{2}-\mathbf{1}_N^T\left[\left(\mathbf{S}\circ\mathbf{H}\mathbf{f}\right)\circ\frac{I_n\left(\mathbf{S}\circ\mathbf{H}\mathbf{f}/\alpha^k\right)}{I_{n-1}\left(\mathbf{S}\circ\mathbf{H}\mathbf{f}/\alpha^k\right)}\right]\right\}, \qquad \textbf{(9)}$$

where α^k is the estimate of σ^2 at the k th iteration (starting with an arbitrarily initial estimate α^0) and $\mathbf{1}_N$ is a $N\times 1$ vector of ones. The resulting algorithm based on equations (8) and (9) is termed RUMBA-SD, which is the abbreviation of '**R**obust and **U**nbiased **M**odel-**Ba**sed **S**pherical **D**econvolution'. The spatially-regularized extension to this algorithm is described in the following section.

3.2 Towards a robust recovery: Total variation regularization

When considering the TV model [58] the maximum a posteriori (MAP) solution at voxel (x, y, z) is obtained by minimizing the augmented functional:

$$J(\mathbf{f}) = -\log P(\mathbf{S}\left|\mathbf{H},\mathbf{f},\sigma^2,n\right.) + \alpha_{TV} TV(\mathbf{f}), \qquad \textbf{(10)}$$

where the first term is the negative log-likelihood defined in previous sections and the second term is the TV energy, defined as the sum of the absolute values of the first-order spatial derivative (i.e., gradient "∇") of the fiber ODF components over the entire brain image, $TV(\mathbf{f}) = \sum_j \left|\nabla\left[\mathbf{f}_{3D}\right]_j\right|$, evaluated at voxel (x, y, z); $\left[\mathbf{f}_{3D}\right]_j$ is a 3D image created in a way that each voxel contains the element at position j of their corresponding estimate vector $\mathbf{f}$, and α_{TV} is a parameter controlling the level of spatial regularization. Importantly, and in contrast to the previous ML estimate, now the solution at a given voxel is not independent from the solutions in other voxels. The spatial dependence introduced by the TV functional promotes smooth solutions in homogeneous regions (discourages the solution from having oscillations), yet it does allow the solution to have sharp discontinuities [58]. This property is highly relevant for SD because, while it promotes continuity and smoothness along individual tracts, it prevents partial volume contamination from adjacent tracts.

In this work, the MAP estimate from Eq.(10) is obtained using an iterative scheme similar to that proposed in [51], where the estimate at each iteration is calculated by the multiplication of two terms: the standard ML estimate, and the regularization term derived from the TV functional

$$\mathbf{f}^{k+1} = \mathbf{f}^{k} \circ \frac{\mathbf{H}^{T}\left[\mathbf{S} \circ \frac{I_{n}\left(\mathbf{S} \circ \mathbf{H}\mathbf{f}^{k}/\sigma^{2}\right)}{I_{n-1}\left(\mathbf{S} \circ \mathbf{H}\mathbf{f}^{k}/\sigma^{2}\right)}\right]}{\mathbf{H}^{T}\mathbf{H}\mathbf{f}^{k}} \circ \mathbf{R}^{k}, \tag{11}$$

with the TV regularization vector $\mathbf{R}^{k}$ at voxel (x, y, z), and at the kth iteration, computed element-by-element as

$$\left(\mathbf{R}^{k}\right)_{j} = \frac{1}{1 - \alpha_{TV}\, div\left(\left.\frac{\nabla\left[\mathbf{f}_{3D}^{k}\right]_{j}}{\left|\nabla\left[\mathbf{f}_{3D}^{k}\right]_{j}\right|}\right)\right|_{(x,y,z)}}, \tag{12}$$

where $\left(\mathbf{R}^{k}\right)_{j}$ is the element j of vector $\mathbf{R}^{k}$ and div is the divergence operator. In practice, to correct for potential singularities at $\left|\nabla\left[\mathbf{f}_{3D}^{k}\right]_{j}\right| = 0$, the term $\left|\nabla\left[\mathbf{f}_{3D}^{k}\right]_{j}\right|$ is replaced by its approximated value $\sqrt{\left|\nabla\left[\mathbf{f}_{3D}^{k}\right]_{j}\right|^{2} + \varepsilon}$, where ε is a small positive constant. Moreover, any negative value in $\mathbf{R}^{k}$ is replaced by its absolute value to preserve the non-negativity of the estimated fiber ODF. Notice that by setting $\alpha_{TV} = 0$ the estimator in Eq. (11) becomes equal to the unregularized version in Eq. (8).

In the current implementation the simultaneous estimation of all the parameters is carried out via an alternating iterative scheme summarized in Table 1. Briefly, it minimizes the functional in Eq.

(10) with respect to the fiber ODF while assuming that σ^2 is known and fixed, and then it updates the noise variance using the new fiber ODF estimate. While for SMF-based data all the equations are evaluated using $n=1$, for SoS-based data n is fixed to the real number of coils, or to the effective value n_{eff} if provided. (But see Appendix B in S1 File)

Table 1. General pseudocode MAP algorithm.

Initialize $\mathbf{f}^0$ and α^0
if SMF, then
$n = 1$
else if SOS, then
n = number of coils (or n_{eff})
end
for k = 1,2,…, repeat the following steps, until a termination criterion is satisfied
compute $\mathbf{f}^{k+1}$ via Eqs. (11) and (12), assuming $\sigma^2 = \alpha^k$
$\mathbf{f}^{k+1} = \mathbf{f}^{k+1}$ /sum($\mathbf{f}^{k+1}$) (*)
compute α^{k+1} via Eq. (9) assuming $\mathbf{f} = \mathbf{f}^{k+1}$
update α_{TV}
end

(*) Optionally, the ODF vector may be scaled to unity, thus preserving the physical definition of the j th element in $\mathbf{f}$ as the volume fraction of the j th compartment of the voxel (see Eqs. (1)-(3)). This step would make sense when the fiber response signal used to create the dictionary matches the real signal from the compartments, whereas it may be omitted when the latter cannot be guaranteed. Notice that the original implementation of dRL-SD did not include this step.

The regularization parameter α_{TV} is adaptively adjusted at each iteration following the discrepancy principle. Specifically, it is selected to match the estimated variance [69] using two

alternative strategies: (i) assuming a constant mean parameter over the entire brain image, $\alpha_{TV} = E\{\alpha^{k+1}\}$ (see Table 1), potentially increasing the precision and robustness of the estimator; or (ii) assuming a spatial dependent parameter, $\alpha_{TV}(x, y, z) = \alpha^{k+1}(x, y, z)$, which may be more appropriate in situations where a differential variance across the image is expected, like in accelerated pMRI based-data.

It should be remembered that the accuracy of the reconstruction for the SoS case depends on the variant used to combine the images. In this work it is assumed that the data is combined using the covariance-weighted SoS method. However, even if the available data were combined using the conventional SoS approach (i.e., without taking into account the noise correlation matrix among coil elements), the method could still provide a reasonable approximation (for more details see Appendix B in S1 File).

The evaluation of the ratio of modified Bessel functions of first kind involved in the updates of Eqs. (11) and (9) is best computed by considering the ratio as a new composite function, and not by means of the simple evaluation of the ratio of the individual functions. Specifically, this ratio is computed here in terms of Perron continued fraction [70]. All the details are provided in Appendix C in S1 File.

Following a similar estimation framework, the TV regularization was also included into the dRL-SD method. All the relevant equations are provided in Appendix D in S1 File.

Materials and Methods

1 Synthetic fiber bundles with different inter-fiber angles

In order to test the resolving power of the methods as a function of the underlying inter-fiber angle, various synthetic phantoms including two fiber bundles were generated. The inter-fiber angles were gradually modified from 1 to 90 degrees applying one degree increases, eventually yielding 90 different phantoms with 50 x 50 x 50 voxels. The volume fractions of the two fiber bundles were assumed to be equal ($f_1 = f_2 = 0.5$) in the fiber crossing region.

The intra-voxel diffusion MRI signal was generated via the multi-tensor model [6] using $N = 70$ sampling orientations with constant b=3000 s/mm^2 plus one additional image with b=0 (i.e., $S_0 = 1$ was assumed in all voxels). The diffusion tensor diffusivities of both fiber groups were assumed to be identical and equal to $\lambda_1 = 1.7\ 10^{-3}$ mm^2/s and $\lambda_2 = \lambda_3 = 0.3\ 10^{-3}$ mm^2/s respectively.

2 Synthetic fiber bundles with different volume fractions

To test the ability of the different methods to detect non-dominant fibers, various synthetic phantoms containing two fiber bundles were generated. In these phantoms the inter-fiber angle was fixed to 70 degrees (an angle presumably detectable by all the methods) and the volume fraction of the non-dominant fiber bundle was gradually changed from 0.1 to 0.5 in 0.01steps, generating 41 different phantoms with 50 x 50 x 50 voxels each. The intra-voxel diffusion MRI signal was created using the same generative multi-tensor model, b-value and sampling orientations as in the previous section.

3 Synthetic "HARDI Reconstruction Challenge 2013" phantom

The reconstruction algorithms were also tested on the synthetic diffusion MRI phantom developed for the "HARDI Reconstruction Challenge 2013" Workshop, within the IEEE International Symposium on Biomedical Imaging (ISBI 2013). This phantom comprises a set of 27 fiber bundles with fibers of varying radii and geometry which connect different areas of a 3D image with 50 x 50 x 50 voxels. It contains a wide range of configurations including branching, crossing and kissing fibers, together with the presence of isotropic compartments mimicking the CSF contamination effects occurring near ventricles in real brain images.

The intra-voxel diffusion MRI signal was generated using N = 64 sampling points on a sphere in q-space with constant b=3000 s/mm^2, plus one additional image with b=0. For pure GM and CSF voxels, signals were generated using two mono-exponential models: $\exp(-D_{GM}b)$ and $\exp(-D_{CSF}b)$ with D_{GM} = 0.2 10^{-3} mm^2/s and D_{CSF} = 1.7 10^{-3} mm^2/s. In voxels belonging to single-fiber WM bundles, the signal measured along the q-space unit direction $\hat{\mathbf{q}} = \mathbf{q}/|\mathbf{q}|$ was generated by a mixture of signals from intra- and extra-axonal compartments: $f_{int}s_{int}(\mathbf{q},\mathbf{v},\tau,L,R) + f_{ext}s_{ext}(\hat{\mathbf{q}},\mathbf{v},b,\lambda_1,\lambda_2)$, where $\mathbf{v}$ denotes the local fiber orientation. Signal from the intra-axonal compartment s_{int} was created following the theoretical model of a restricted diffusion process inside a cylinder of length $L = 5\ mm$ and radius $R = 5\ \mu m$ at the diffusion time τ =20.8 s [19, 71]. The extra-axonal signal s_{ext} was generated using a diffusion tensor model with cylindrical symmetry (i.e., $\lambda_1 = 1.7\ 10^{-3}$ mm^2/s, $\lambda_2 = \lambda_3 = 0.2\ 10^{-3}$ mm^2/s). Mixture fractions were fixed to f_{int} = 0.6 and f_{ext} = 0.4. The noiseless dataset can be freely downloaded from the Webpage of the site: http://hardi.epfl.ch/static/events/2013_ISBI/.

4 Multichannel noise generation

The synthetic diffusion images from the above phantoms were contaminated with noise mimicking the SoS and SMF strategies used in scanners in order to combine multiple-coils

signals. To that aim, the noisy complex-valued image measured from the k th coil was assumed to be equal to

$$S_k = SC_k + e_k^R + ie_k^I, \tag{13}$$

where C_k is the relative sensitivity map [72] of k th coil, $e_k^R \sim N(0,\Sigma)$ and $e_k^I \sim N(0,\Sigma)$ are two different Gaussian noise realizations simulating the noise in the real and imaginary components with zero-mean value and covariance matrix Σ. For simplicity Σ was assumed to be given by

$$\Sigma = \sigma^2 \begin{pmatrix} 1 & \rho & \cdots & \rho \\ \rho & 1 & \cdots & \rho \\ \vdots & \vdots & \ddots & \vdots \\ \rho & \rho & \cdots & 1 \end{pmatrix}, \tag{14}$$

where σ^2 is the noise variance of each coil and ρ indicates the correlation coefficient between any two coils.

For the SoS reconstruction, magnitude images were generated as:

$$S_{SoS} = \sqrt{\sum_{k=1}^{n} |S_k|^2}, \tag{15}$$

where $|S_k|$ stands for the magnitude of S_k. Notice that Eq. (15) is the conventional SoS image combination and not the covariance-weighted variant. We have followed this approach in order to simulate the effect of any remaining residual correlation ρ present in real systems (we have assumed a $\rho = 0.05$) [63].

In the SMF reconstruction, magnitude images were generated as:

$$S_{SMF} = \left| \sum_{k=1}^{n} S_k C_k \right|, \quad \textbf{(16)}$$

with simulated sensitivity maps depicted in Fig A in S2 File satisfying the relationship $\sum_{k=1}^{n} C_k^2 = 1$, which holds in practice when the relative sensitivity maps are calculated as $C_k = |S_k| / S_{SoS}$ [72]. These sensitivity maps have been previously used in [73].

It should be noted that different scanner vendors can implement different SMF and SoS variants. In this work we have used the variants given in [55] for datasets acquired without undersampling in the k-space, i.e., R=1, where R is the acceleration factor of the acquisition defined as the ratio of the total k-space phase-encoding lines over the number of k-space lines actually acquired. Notice that in the absence of noise $S_{SoS} = S_{SMF}$. Besides, for the particular case of a single coil with uniform sensitivity, i.e., $n = 1$ and $C = 1$, Eq. (15) and Eq. (16) become identical.

The 132 3D phantoms resulting from the procedures described in the three previous sections were contaminated with noise using a range of clinical signal-to-noise ratios (SNR) of 10, 15, 20 and 30, where $SNR = S_0 / \sigma$. In order to generate signals under equivalent conditions, for each value of σ the same noise realizations $\{e_k^R\}$ and $\{e_k^I\}$ were used to generate the final images S_{SoS} and S_{SMF}. All datasets were created simulating a scanner with 8 coils (see Figs A and B in S2 File).

5 Evaluation metrics

The performance of the algorithms was quantified by comparing the obtained reconstructions against the ground-truth via three main criteria: (i) the angular error in the orientation of fiber populations, (ii) the proper estimation of the number of fiber populations present in every voxel and (iii) the volume fraction error.

For the analyses, local peaks from the reconstructed fiber ODFs were identified as those vertices in the grid with higher values than their adjacent neighbors, considering only cases where magnitudes exceeded at least one tenth of the amplitude of the highest peak (i.e., $0.1 \cdot \mathrm{f}_{\max}$) [50]. From all identified peaks, the highest four where finally retained.

Next, we adopted some of the evaluation metrics widely used in the literature [9]. Specifically, we used the angular error, defined as the average minimum angle between the extracted peaks and the true fiber directions [74]:

$$\theta = \frac{1}{\mathrm{M}_{\mathrm{true}}} \sum_{k=1}^{\mathrm{M}_{\mathrm{true}}} \min_m \left\{ \arccos\left(\left| \mathbf{e}_m^T \mathbf{v}_k \right| \right) \right\}, \tag{17}$$

where $\mathrm{M}_{\mathrm{true}}$ is the true number of fiber populations, $\mathbf{e}_m$ is the unitary vector along with the m th detected fiber peak and $\mathbf{v}_k$ is the unitary vector along the k th true fiber direction. The volume fraction error of the estimated fiber compartments was assessed by means of the average absolute error between the estimated and the actual peak amplitudes:

$$\Delta f = \frac{1}{\mathrm{M}_{\mathrm{true}}} \sum_{k=1}^{\mathrm{M}_{\mathrm{true}}} \left| \mathrm{f}_m - \mathrm{f}_k \right|, \tag{18}$$

where f_m is the normalized height of the m th detected fiber peak and f_k is the volume fraction of the k th true fiber. As usual, the angular and volume fraction errors between each pair of fibers were measured by comparing the true fiber with the closest estimated fiber.

Finally, the success rate (SR) was employed to quantify the estimation of the number of fiber compartments. The SR is defined as the proportion of voxels in which the algorithms estimate the right number of fiber compartments. To discriminate the different factors leading to an

erroneous estimation, the mean number of over-estimated n^+ and under-estimated n^- fiber populations were computed over the whole image [9].

6 Settings for the evaluation algorithms

Both RUMBA-SD and dRL-SD methods were implemented using in-house developed *Matlab* code, applying the same dictionaries **H** created from the signal generative model given in Eqs.(1)-(3). These used M = 724 fiber orientations distributed on the unit sphere, with a mean angular separation between adjacent neighbor vertices of 8.36 degrees, and a standard deviation of 1.18 degrees.

To assess the effect of using dictionaries with optimal and non-optimal diffusivities, two different dictionaries were created and applied to the datasets described in subsections 1 (i.e., fiber bundles with different inter-fiber angles) and 2 (i.e., fiber bundles with different volume fractions). The first dictionary was generated by using the same diffusivities employed in the synthetic data, whereas the second dictionary was created from diffusivities estimated in regions of parallel fibers (outside the fiber crossing area) by means of a standard diffusion tensor fitting on the noisy data (i.e., *dtifit* tool in FSL package).

Similarly, two dictionaries were created to test the reconstructions on the data described in subsection 3 (i.e., "HARDI Reconstruction Challenge 2013" phantom data). In this case the model diffusivities and the 'true' diffusivities were deliberately set to different values in order to consider the possibility of model misspecification. The first dictionary was created with tensor diffusivities equal to $\lambda_1 = 1.4\ 10^{-3}$ mm^2/s and $\lambda_2 = \lambda_3 = 0.4\ 10^{-3}$ mm^2/s. Two isotropic compartments with diffusivities equal to $0.2\ 10^{-3}$ mm^2/s and $1.4\ 10^{-3}$ mm^2/s were also included. In the second dictionary the diffusivities were assumed to be equal to $\lambda_1 = 1.6\ 10^{-3}$ mm^2/s and $\lambda_2 = \lambda_3 = 0.3\ 10^{-3}$ mm^2/s, and the isotropic diffusivities were equal to $0.2\ 10^{-3}$ mm^2/s and $1.6\ 10^{-3}$ mm^2/s respectively.

The starting condition $\mathbf{f}^0$ in all cases was set as a non-negative iso-probable spherical function [37]. The accuracy and convergence of both methods as a function of the number of iterations

was investigated by repeating the calculations using 200 and 400 iterations, which is within the optimal range as suggested in [37] and [50]. The extended algorithms with TV regularization were also tested using 600 and 1000 iterations. The geometric damping and threshold parameters for dRL-SD were set to ν=8 and η=0.06 respectively [37], see Appendix D in S1 File. For SoS-based data, n was fixed to the real number of coils in RUMBA-SD.

To differentiate the standard RUMBA-SD and dRL-SD algorithms from their regularized versions, we have added the term '+TV' to their names, i.e., RUMBA-SD+TV and dRL-SD+TV.

7 Real brain data

Diffusion MRI data were acquired from a healthy subject on a 3T Siemens scanner (Erlangen) located at the University of Oxford (UK). The subject provided informed written consent before participating in the study, which was approved by the Institutional Review Board of the University of Oxford. Whole brain diffusion images were acquired with a 32-channel head coil along 256 different gradient directions on the sphere in q-space with constant b = 2500 s/mm^2. Additionally, 36 b = 0 volumes were acquired with in-plane resolution = 2.0 x 2.0 mm^2 and slice thickness = 2 mm. The acquisition was carried out without undersampling in the k-space (i.e., R=1). Raw multichannel signals were combined using either the standard GRAPPA approach or the GRAPPA approach with the adaptive combination of the SMF available in the scanner, giving SoS and SMF-based datasets respectively. Then, the two resulting datasets were separately corrected for eddy current distortions and head motion as implemented in FSL [75].

A subset of 64 directions with nearly uniform coverage on the sphere was selected from the full set of 256 gradients directions, and measurements for this subset were used to 'create' an under-sampled version of the data, which also included 3 b=0 volumes. The resulting HARDI sequence based on 64 directions is similar to those widely employed in clinical studies, thus results from this dataset are useful to evaluate the impact of the new technique on standard clinical data.

Results

1 Gaussian versus non-Gaussian noise models

The angular and volume fraction errors from the dRL-SD and RUMBA-SD reconstructions in the 90 synthetic phantoms with different inter-fiber angles are depicted in Fig 1, as well as in Fig C in S2 File. Fig 1 shows results using a dictionary created with the same diffusivities applied to generate the data (i.e., $\lambda_1 = 1.7\ 10^{-3}$ mm^2/s and $\lambda_2 = \lambda_3 = 0.3\ 10^{-3}$ mm^2/s), whereas Fig C in S2 File displays results using tensor diffusivities estimated from the noisy data ($\lambda_1 = 1.1\ 10^{-3}$ mm^2/s and $\lambda_2 = \lambda_3 = 0.35\ 10^{-3}$ mm^2/s). In both dictionaries two isotropic compartments with diffusivities equal to $0.1\ 10^{-3}$ mm^2/s and $2.5\ 10^{-3}$ mm^2/s were included. Average values of SR, n^+ and n^- are also reported in Figs D and E in S2 File. Results shown come from the reconstructions employing 200 iterations and the datasets with a SNR=15.

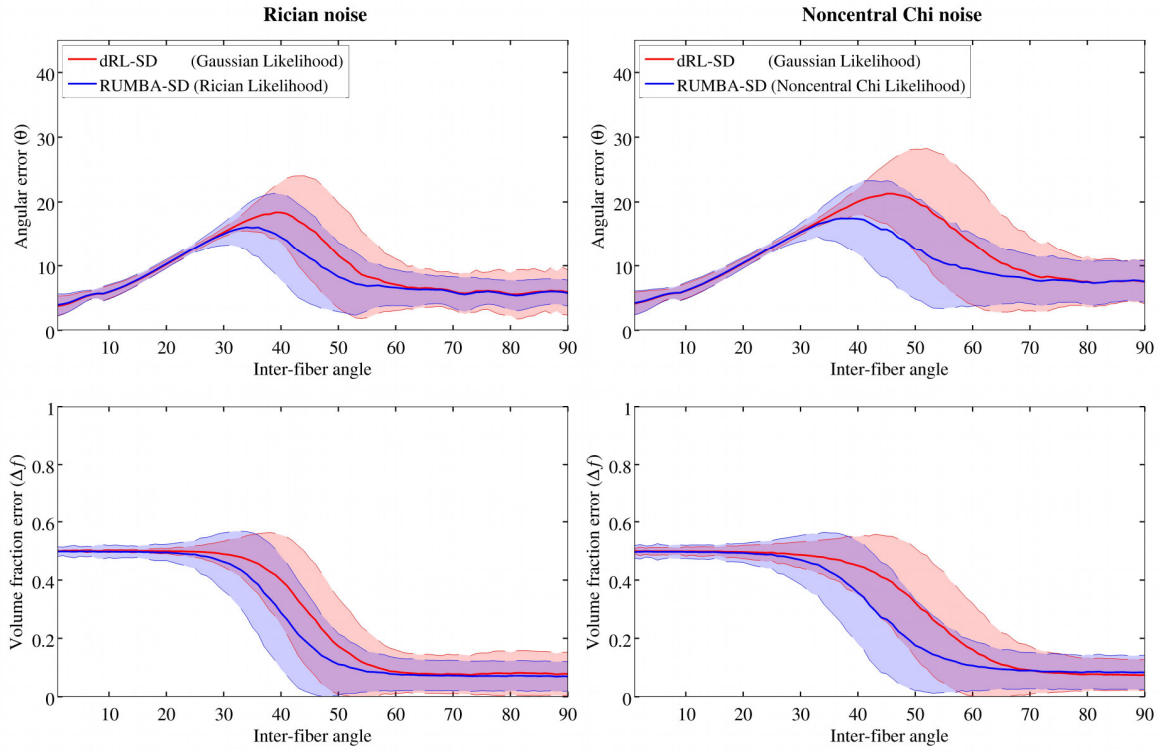

Fig 1. Reconstruction accuracy for RUMBA-SD and dRL-SD using a dictionary based on original diffusivities. Reconstruction accuracy of RUMBA-SD (blue color) and dRL-SD (red color) are shown in terms of the angular error (θ) (see Eq.(17)) and the volume fraction error (Δf) (see Eq. (18)), as a function of the inter-fiber angle in the 90 synthetic phantoms. Continuous lines in each plot represent the mean values for each method. The semi-transparent coloured bands symbolize values within one standard deviation from both sides of the mean. Analyses are based on a dictionary created with the same diffusivities used to generate the data and with a SNR = 15.

A set of patterns can be drawn from these results. First, RUMBA-SD was able to resolve fiber crossings with smaller inter-fiber angles (around 5 degrees and 10 degrees for datasets corrupted with Rician and nc-χ noise respectively). Second, RUMBA-SD produced volume fraction estimates with a higher precision (lower variance), even in phantoms where the fiber configuration was well-resolved by both methods. Third, although dRL-SD produced a relatively lower proportion of spurious fibers (n^+), RUMBA-SD produced a lower proportion of undetected fibers (n^-) leading to a higher success rate (SR). Finally, the performance of both methods was inferior when the dictionary was created using diffusivities estimated from a 'standard' DTI fitting in WM regions of parallel fibers. In line with previous findings on dRL-SD [50], optimal results were obtained from the sharper fiber response model.

All these points also hold for results obtained with other SNRs and with a differing number of algorithm iterations. Specifically, when a higher number of iterations was employed (i.e., 400), a lower proportion of n^- and a higher proportion of n^+ was obtained with both methods.

Fig 2 shows the performance of dRL-SD and RUMBA-SD in the 41 phantoms with inter-fiber angle equal to 70 degrees and using different volume fractions. Specifically, average values and standard deviations for the estimated volume fractions of the smaller fiber group are reported for the SNR=15 datasets. Results are based on 200 iterations, using the dictionary created with the sharper fiber response model. Additional results on n^+ and n^- are show in Fig F in S2 File.

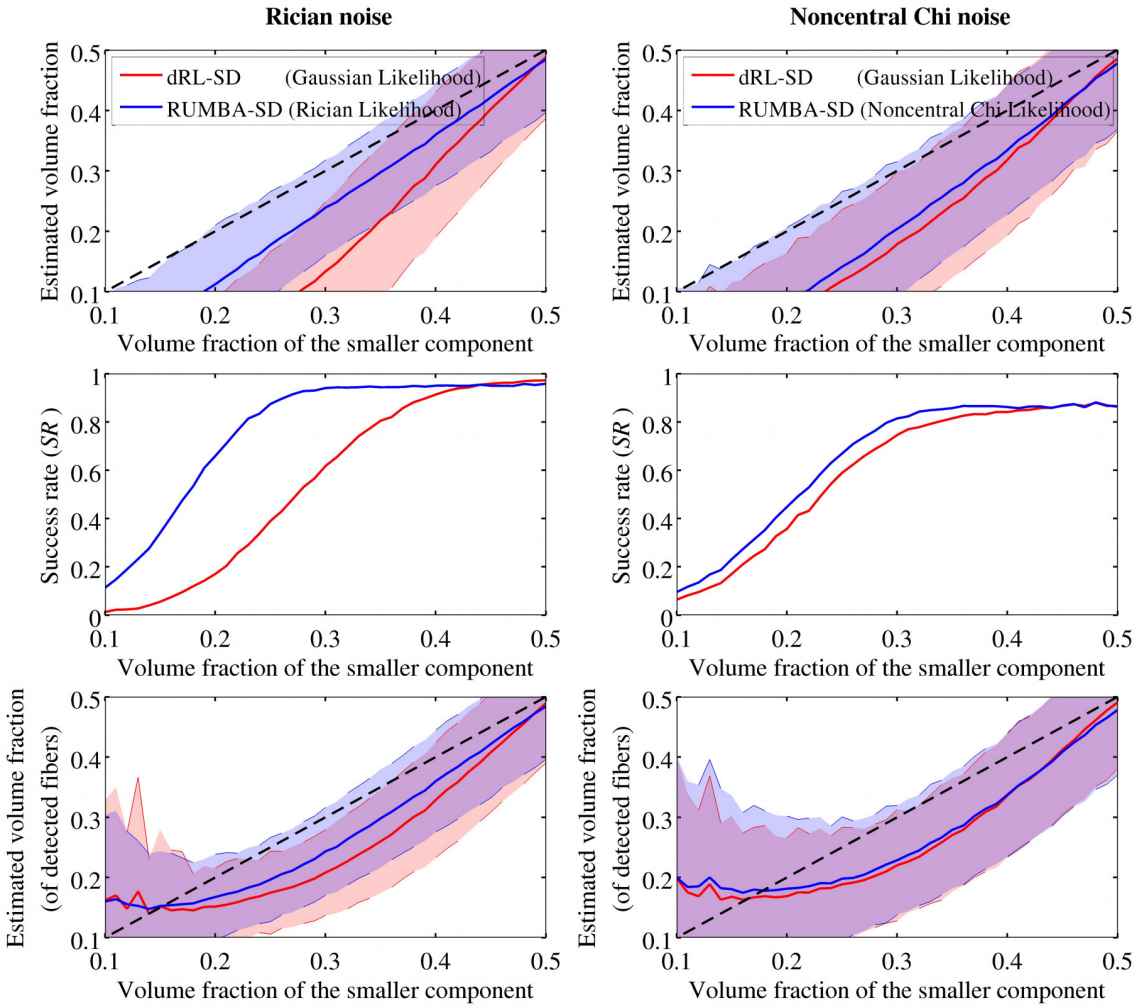

Fig 2. Reconstruction accuracy of RUMBA-SD and dRL-SD measured in phantoms with different volume fractions. Reconstruction accuracy of RUMBA-SD (blue color) and dRL-SD (red color) is shown in terms of the volume fraction of the smaller fiber bundle (upper panel) and the success rate (middle panel) in the 41 synthetic phantoms with inter-fiber angle equal to 70 degrees, using different volume fractions. The lower panel shows results similar to those depicted in the upper panel but considering only voxels where the two fiber bundles were detected. The discontinuous diagonal black line in the upper and lower panels represents the ideal result as a reference. The continuous coloured lines in each plot denote the mean values for each method. The semi-transparent coloured bands represent the values within one standard deviation to both sides of the mean. Results refer to the datasets with SNR=15 and dictionary created with the true diffusivities.

The performance of RUMBA-SD was better in terms of the estimated volume fractions and the success rate, especially in the Rician noise case. In order to verify if the lower bias in the volume fractions estimated by RUMBA-SD could be explained only by its higher success rate, the calculation was repeated by considering only those voxels in each phantom where the two fiber populations were identified. After correcting for this factor, a noticeable advantage was still observed for RUMBA-SD (see left lower panel of Fig 2).

2 Original versus TV-regularized algorithms

Fig 3 reports angular and volume fraction errors corresponding to the TV spatially-regularized versions of both methods applied to the 90 phantoms characterizing the different inter-fiber angles. Results are based on the same parameters and options used in Fig 1: dictionary created using the sharper fiber response model; noisy datasets with a SNR=15 and reconstructions using 200 iterations. Average values of SR, n^+ and n^- are reported in Fig G in S2 File.

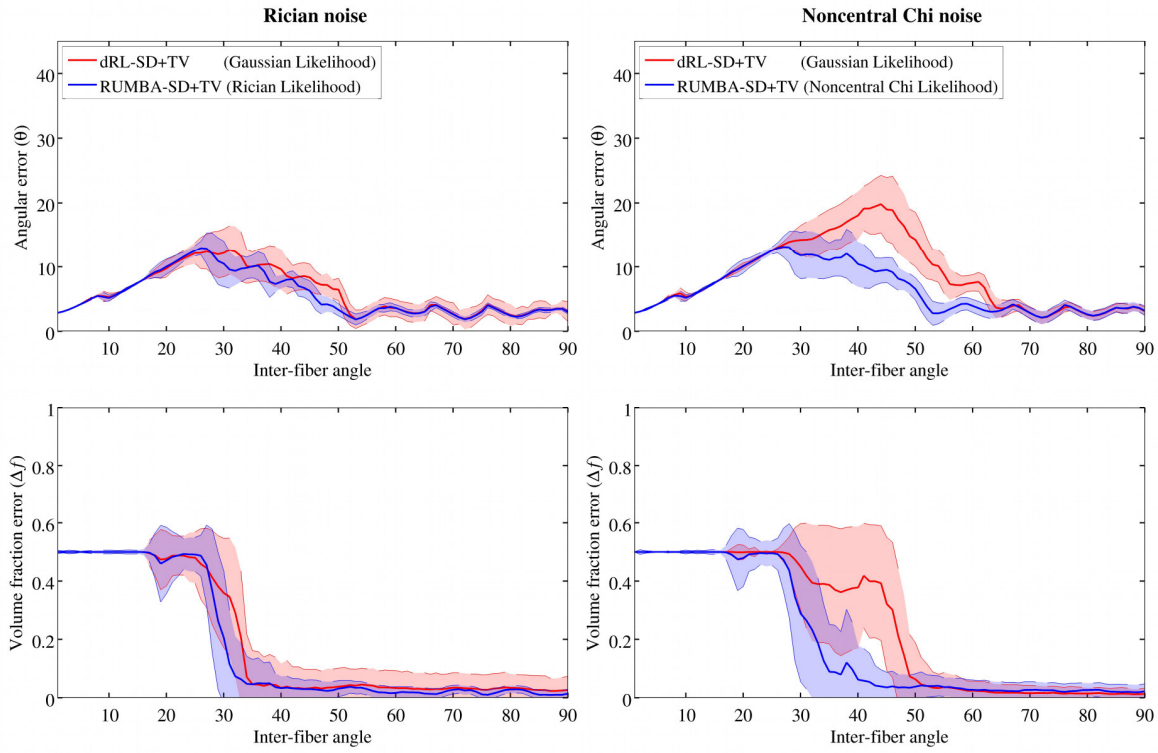

Fig 3. Reconstruction accuracy levels of RUMBA-SD+TV and dRL-SD+TV. Reconstruction accuracy of RUMBA-SD+TV (blue color) and dRL-SD+TV (red color) is shown in terms of the angular error (θ) (see Eq. (17)) and the volume fraction error (Δf) (see Eq. (18)) as a function of the inter-fiber angle in the 90 synthetic phantoms. Continuous lines are the mean values for each method, and semi-transparent coloured bands contain values within one standard deviation on both sides of the mean. This analysis is based on a dictionary created with the same diffusivities used to generate the data with a SNR = 15.

When comparing these results with those from Fig 1 (and Fig D in S2 File), it is clear that TV regularization provides multiple benefits in both algorithms, including a superior ability to detect fiber crossings with smaller inter-fiber angles and a higher success rate. The later is due to a lower proportion of undetected fibers (n^-) and of spurious fibers (n^+). This pattern is evident in Fig 4, which depicts the peaks extracted from the fiber ODFs estimated from the SMF-based phantom with inter-fiber angle equal to 45 degrees and SNR=15. Peaks are plotted as thin cylinders.

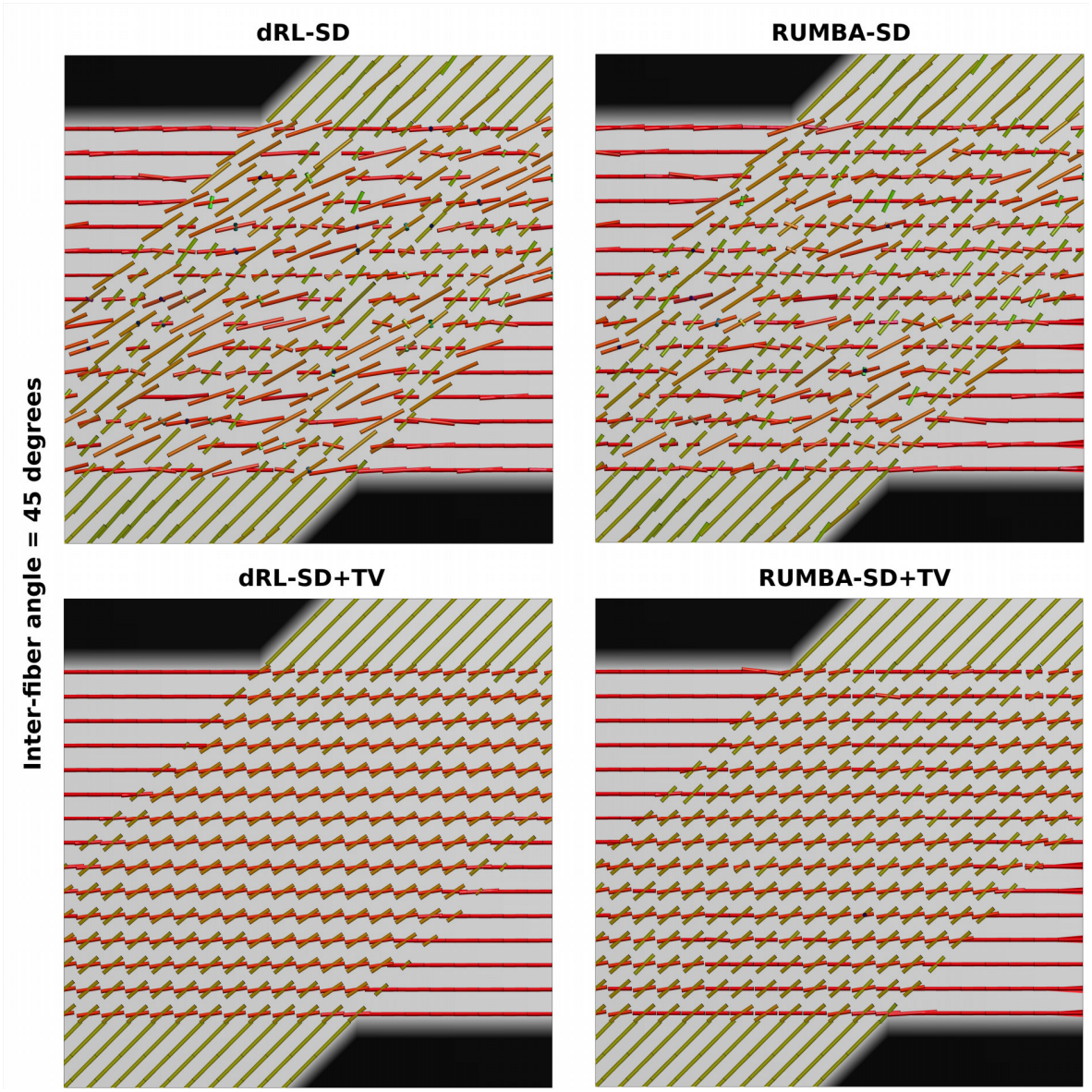

Fig 4. Main peaks in the 45-degrees phantom data. Main peaks extracted from the fiber ODFs estimated in the phantom data with inter-fiber angle equal to 45 degrees and Rician noise with a SNR=15 are shown. Results are based on reconstructions using 200 iterations. Peaks are visualized as thin cylinders.

As before, the above patterns were also observed in the analyses obtained with datasets based on other SNRs and with different number of iterations. In all cases RUMBA-SD+TV detected fiber crossings at lower inter-fiber angles. Fig 5 shows an example of this in the phantom with inter-fiber angle equal to 33 degrees corrupted with Rician noise and SNR=15.

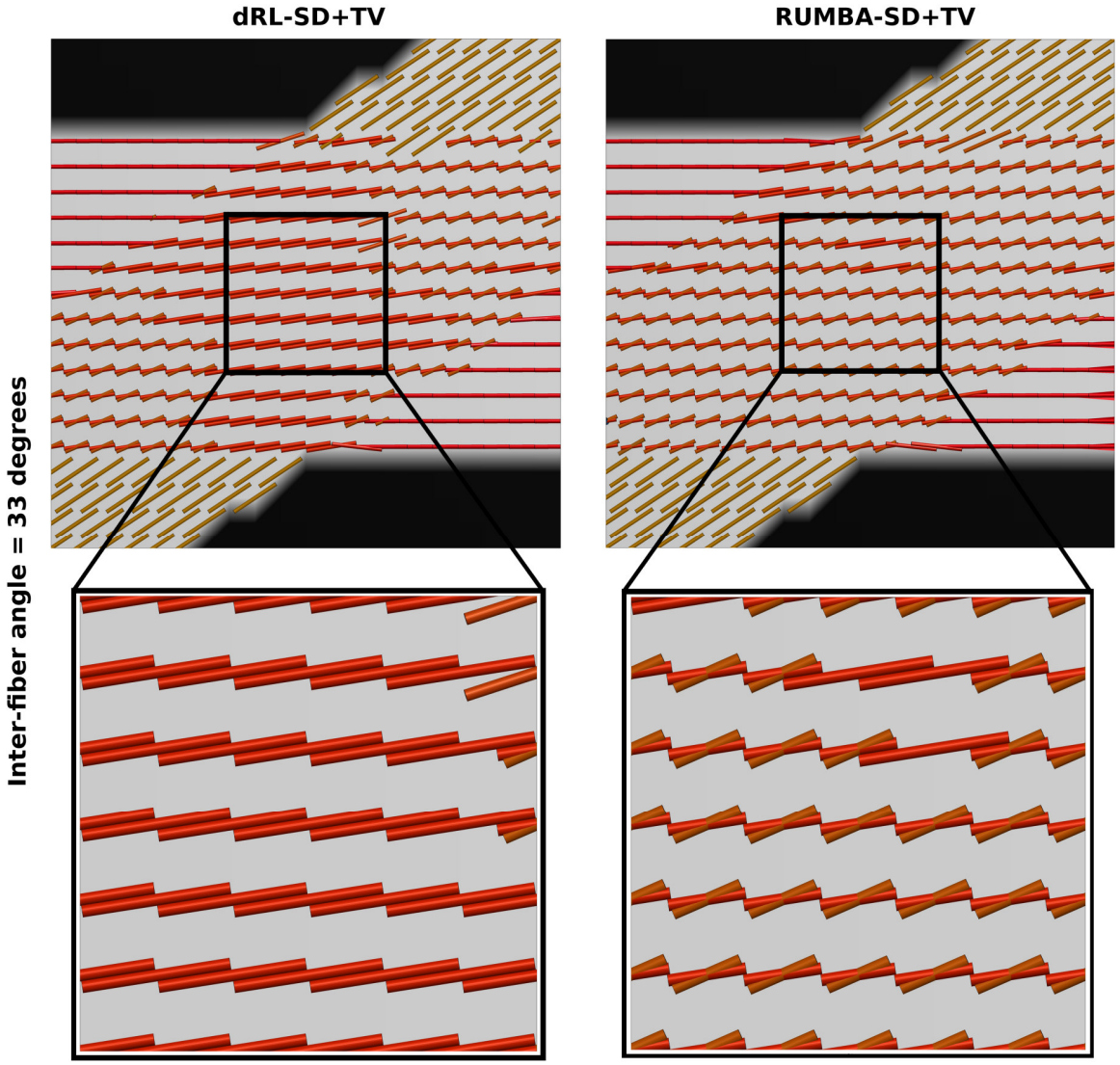

Fig 5. **Main peaks in the 33-degrees phantom data**. Main peaks extracted from the fiber ODFs estimated in the phantom data with inter-fiber angle equal to 33 degrees and Rician noise with a SNR=15 are shown. Results are based on reconstructions using 200 iterations. Peaks are visualized as thin cylinders.

3 "HARDI Reconstruction Challenge 2013" phantom data

Fig 6 depicts the peaks extracted from the fiber ODFs estimated in a complex region containing various tracts from the SMF-based data generated with a SNR = 20. Results come from reconstructions using 400 iterations and a dictionary with diffusivities equal to $\lambda_1 = 1.6\ 10^{-3}$ mm^2/s and $\lambda_2 = \lambda_3 = 0.3\ 10^{-3}$ mm^2/s. Figs H, I, J and K in S2 File show the results from both methods and their regularized versions in the whole slice. Additionally, Fig L in S2 File shows the results corresponding to the reconstructions using 1000 iterations on the same region of interest depicted in Fig 6.

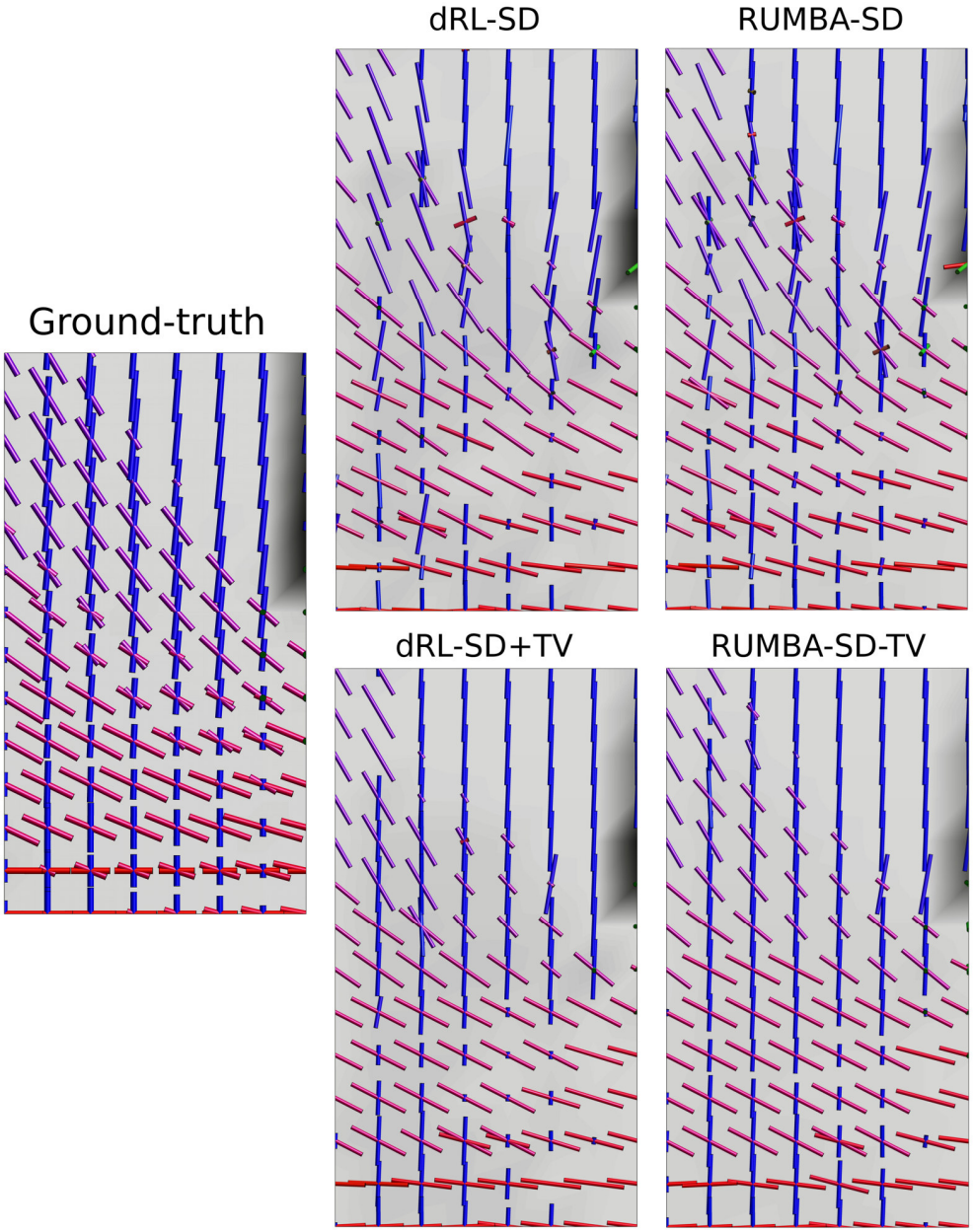

Fig 6. **Main peaks from the fiber ODFs estimated in the "HARDI Reconstruction Challenge 2013" phantom**. Visualization of the main peaks extracted from the fiber ODFs reconstructed from the SMF-based data generated with SNR = 20 in a complex region of the "HARDI Reconstruction Challenge 2013" phantom. Results are based on reconstructions using 400 iterations. Peaks are visualized as thin cylinders.

On the one hand, RUMBA-SD was able to resolve some fiber configurations that were not detected by dRL-SD, especially in voxels involving small inter-fiber angles or fiber crossings with a non-dominant tract. On the other hand, the spatially-regularized algorithms have substantially improved the performance of the original methods. Moreover, RUMBA-SD+TV was the method providing better reconstructions. These findings are in line with results from previous sections and remained valid also when different dictionaries, number of iterations and noise levels were employed.

Additional complementary results about the performance of RUMBA-SD in relation to several other reconstruction methods can be found in the website of the 'HARDI Reconstruction Challenge 2013': http://hardi.epfl.ch/static/events/2013_ISBI/workshop.html#results. An earlier version of RUMBA-SD took part in that Challenge, ranking number one in the 'HARDI-like' category (team name: 'Capablanca'). In the discussion section we provide additional information.

4 Real brain data

Fiber ODFs were estimated separately for each different SMF- and SoS-based dataset, including the original measured data with the full set of 256 gradient directions and its reduced form including a subset of 64 directions. In all cases, both RUMBA-SD and dRL-SD methods were implemented using the same dictionary, which was created assuming a sharp fiber response model with diffusivities equal to $\lambda_1 = 1.7\ 10^{-3}$ mm^2/s and $\lambda_2 = \lambda_3 = 0.3\ 10^{-3}$ mm^2/s, and two isotropic terms with diffusivities equal to $0.7\ 10^{-3}$ mm^2/s and $2.5\ 10^{-3}$ mm^2/s.

Fig 7 shows the fiber ODFs estimated from the reduced SMF- and SoS-based datasets (i.e., data containing the reduced set of 64 gradient directions) in a coronal ROI on the right brain hemisphere. These results correspond to the reconstructions employing 200 iterations. Visual inspection of Fig 7 reveals that RUMBA-SD has produced sharper fiber ODFs than dRL-SD in

both data. It has detected more clearly the fiber crossings. Interestingly, the fiber ODF profiles estimated by dRL-SD from the SoS-based data are smoother than those estimated from the SMF-based data. This behavior is less perceptible in the case of RUMBA-SD, suggesting that it could be more robust to different multichannel combination methods.

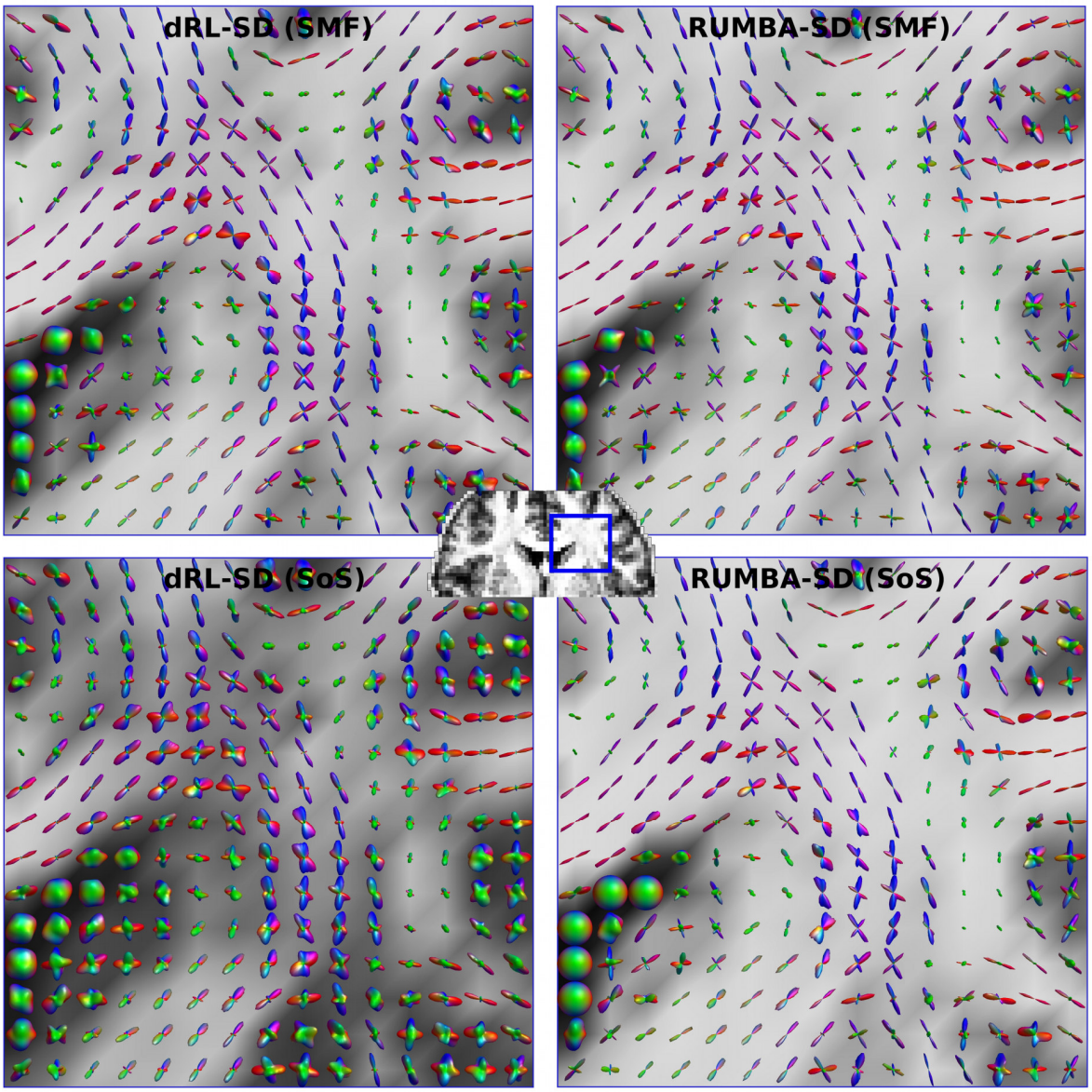

Fig 7. Fiber ODF profiles estimated from real data. Visualization of the fiber ODFs estimated in a region of interest on the right brain hemisphere. Results from both SMF- and SoS-based multichannel diffusion datasets (i.e., with Rician and Noncentral Chi noise, respectively) are depicted. The background images are the generalized fractional anisotropy images computed from each reconstruction.

Fig 8 depicts the fiber ODFs estimated with RUMBA-SD and RUMBA-SD+TV in a ROI of both the full and reduced SMF-based datasets. This region contains complex fiber geometries, including the mixture of the anterior limb of internal capsule (alic), the external capsule (ec) and part of the superior longitudinal fasciculus (slf) on the left brain hemisphere. Although in both cases multiple fibers were detected in the area of intersection, RUMBA-SD+TV has provided multi-directional fiber ODFs with a higher number of lobes, which may represent fiber crossings as well as intra-voxel fiber dispersion. The similarity of the reconstructions from the full and reduced datasets suggests that the method is robust with respect to the number of measurements, with the regularized version being the most robust.

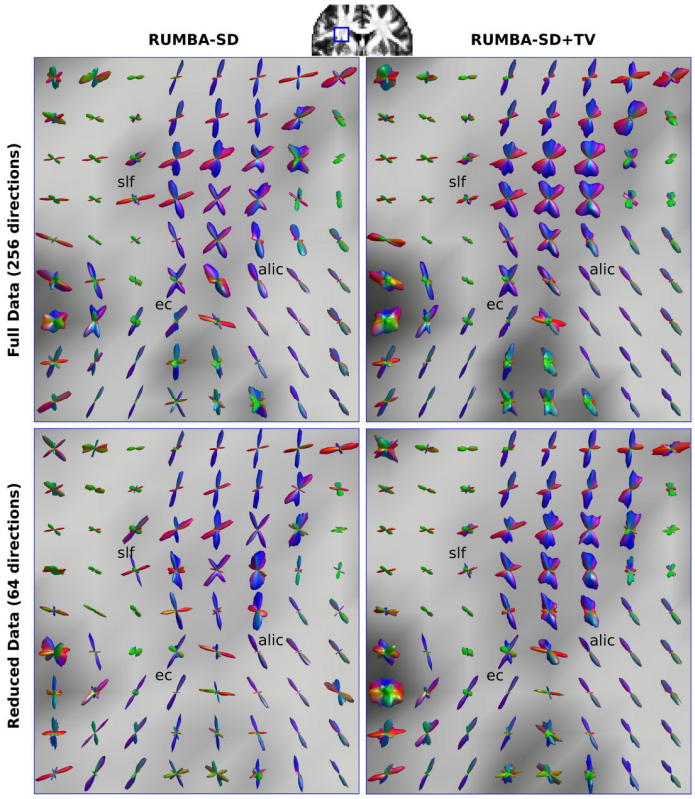

Fig 8. Fiber ODF profiles estimated from real data. Visualization of the fiber ODFs estimated from RUMBA-SD and RUMBA-SD+TV in a region of interest on the left brain hemisphere. Results are based on estimates employing 300 iterations. The upper and lower panels correspond to results from the full and reduced SMF-based datasets, respectively. The following tracts are highlighted: alic (anterior limb of internal capsule), ec (external capsule), and part of the slf (superior longitudinal fasciculus).

In a subsequent analysis we examined the statistical properties of inter-fiber angles as estimated by all methods. Fig 9 depicts scatter plots of inter-fiber angles estimated by dRL-SD and RUMBA-SD (panel A) and by dRL-SD+TV and RUMBA-SD+TV (panel B). These results are based on reconstructions employing 300 iterations in the 64-direction SMF-based dataset. Only white matter voxels where both methods detected one or two fibers are included in each plot, with inter-fiber angles in single fiber voxels assumed to be zero. Points on the main diagonal line characterize voxels where both methods gave identical inter-fiber angle estimates, whereas points above and below the main diagonal correspond to voxels where the two methods detected

two fibers with different inter-fiber angle. The high density of points forming two secondary lines near the main diagonal indicates nearly similar reconstructions by both methods, with the angular differences being similar to the angular resolution of the reconstruction grid (i.e., about 8 degrees). The higher number of points above the main diagonal in both panels, especially for inter-fiber angles lower than 50 degrees, suggests that RUMBA-SD and RUMBA-SD+TV provide higher inter-fiber angles than dRL-SD and dRL-SD+TV, respectively. Finally, points located on the X and Y axes are voxels where one method detected two fibers while the other detected one. The very low density of points on the X axis of panel A for inter-fiber angles lower than 50 degrees (see the blue bracket) indicates that in nearly all voxels where dRL-SD detected two fibers, RUMBA-SD was also able to detect two fibers. In contrast, the high density of points on the Y axis in the same range of inter-fiber angles indicates that in many voxels RUMBA-SD detected two fibers whereas dRL-SD detected a single one. A similar but attenuated effect can be noticed in panel B, suggesting that TV regularization contributes to reduce the differences between both methods.

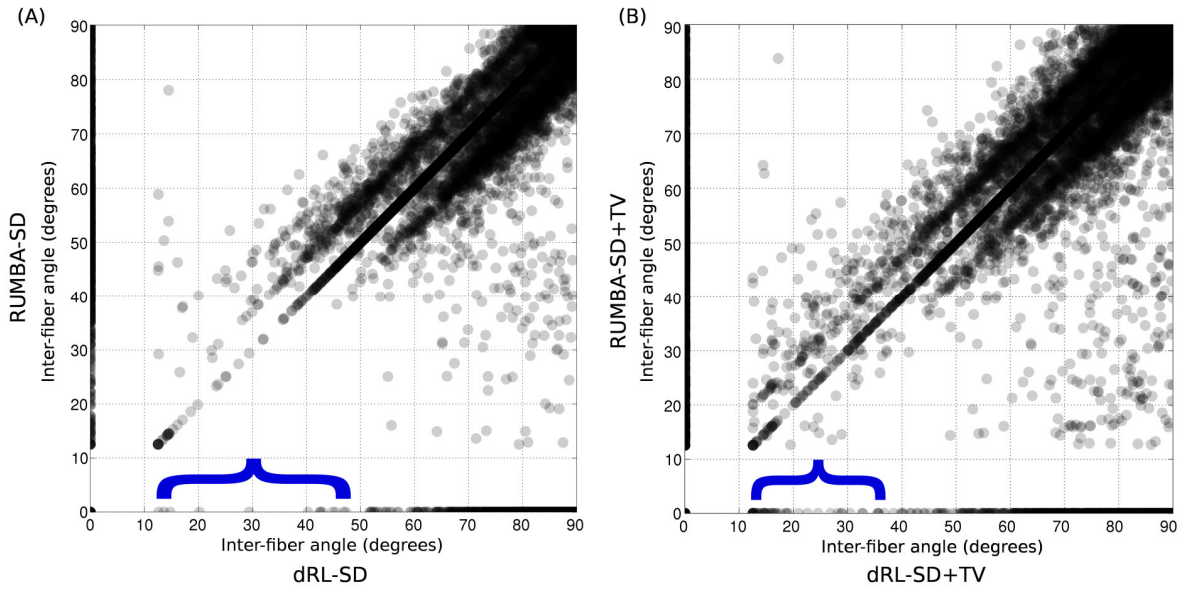

Fig 9. **Scatter plots of inter-fiber angles estimated in real data**. Scatter plots of the inter-fiber angles estimated by dRL-SD and RUMBA-SD (panel A) and by dRL-SD+TV and RUMBA-SD+TV (panel B)

in the same voxels. Results are based on reconstructions in the 64-direction SMF dataset. Only voxels in white matter where both methods detected one or two fibers are included. The inter-fiber angle in voxels with a single fiber was assumed to be equal to zero. Points on the main diagonal line are those voxels where the inter-fiber angle estimated from both methods was identical, whereas points above and below the main diagonal correspond to voxels where the two methods detected two fibers but with different inter-fiber angle. Points located on the X and Y axes are voxels where one method detected two fibers whereas the other detected a single fiber.

Discussion and Conclusions

In this study we propose a new model-based spherical deconvolution method, RUMBA-SD. In contrast to previous methods, usually based on Gaussian noise with zero mean, RUMBA-SD considers Rician and noncentral Chi noise models, which are more adequate for characterizing the non-linear bias introduced in the diffusion images measured in current 1.5T and 3T multichannel MRI scanners. Although recent progress has been made in new SD methods adapted to corrupted Rician data, e.g., see [41, 76] to the best of our knowledge, our study provides the first SD extension to noncentral Chi noise. Furthermore, RUMBA-SD offers a very general estimation framework applicable to different datasets, with its flexibility emanating from two features: i) the explicit dependence between the likelihood model and the number of coils in the scanner and ii) the specific methodology employed to combine multichannel signals. In addition, the voxel-wise estimation of the noise variance adequately deals with potential deviations in the noise distribution, due, for instance, to accelerated MRI techniques or to preprocessing effects. We hope that the proposed technique will help extend SD methods to a wide range of datasets taken from different scanners and using different protocols.

This study adds to previous diffusion MRI studies trying to overcome the signal-dependent bias introduced by Rician and noncentral Chi noise. Apart from the robust DTI estimation methods in [77] and the earlier DTI study conducted by [78], the noise filtering techniques recently described in [79, 80] are specially relevant. These techniques can be applied in the pre-processing steps prior to HARDI data estimation.

The performance of RUMBA-SD has been evaluated exhaustively against the state-of-the-art dRL-SD technique. For that, we have used 132 different 3D synthetic phantoms, including 90 phantoms simulating fiber crossings with different inter-fiber angle, 41 phantoms simulating fiber crossings with different volume fraction, and the complex phantom designed for the "HARDI Reconstruction Challenge 2013" Workshop organized within the IEEE International Symposium on Biomedical Imaging. The comparison of these two methods has allowed us to weight the impact on the results of the Rician and noncentral Chi likelihood models included in RUMBA-SD, in relation to the Gaussian model assumed in dRL-SD. Since both approaches

were implemented using the same dictionary of basis signals and similar reconstruction methods based on Richardson-Lucy algorithms adapted to Gaussian, Rician and noncentral Chi noise models, results should be considered comparable.

Taken together, findings from all synthetic datasets demonstrate the benefits of an adequate modelling of the noise distribution in the context of spherical deconvolution, and of the inclusion of TV regularization. Interestingly, RUMBA-SD resolved fiber crossings with smaller inter-fiber angles and smaller non-dominant fibers. Likewise, RUMBA-SD produced volume fraction estimates with higher accuracies and precision and produced, as well, a lower proportion of undetected fibers, resulting in a higher success rate (see Figs 1 and 2 and supplementary figures in S2 File). On the other hand, the TV spatially-regularized versions of both dRL-SD and RUMBA-SD have substantially improved the performance of the original methods in all studied metrics (see Figs 3-6 and supplementary figures in S2 File).

As previously mentioned, an earlier version of RUMBA-SD took part in the HARDI Reconstruction Challenge 2013, ranking number one in the 'HARDI-like' category. Notably, this position was shared with a reconstruction based on the CSD method included in *Dipy* software [81] (http://nipy.org/dipy/), which had applied a Rician denoising algorithm [82] to the raw diffusion MRI data prior to the actual CSD reconstruction. The superior performance of these two approaches strengthens the importance of taking into account the non-Gaussian nature of the noise. Moreover, it opens new questions on the optimal strategy to be followed. Should we divide the deconvolution process into to two disjoint steps (first denoising and then estimation) or it is more adequate to follow the unified approach proposed here?. The main advantage of the former is that it may benefit from including state-of-art denoising algorithms like the adaptative non-local means denoising method proposed in [82]. Conversely, the main advantage of the unified approach is that it provides a precise model to distinguish real signals from noise throughout all the 4D diffusion MRI data. Many of the advanced denoising algorithms that are currently applied in isolation were developed to filter volumetric (3D) data. Since each 3D image is processed individually, their mutual dependence in terms of orientation is ignored. In contrast, the unified approach described here provides a more general estimation framework that may be extended to include advanced similarity measures like those employed in [82], merging the

benefits of both strategies. A new manuscript on the 'Challenge' phantom (currently under preparation) will provide additional information on the performance of RUMBA-SD in relation to several reconstruction methods and in terms of connectivity metrics derived from fiber tracking analyses.

When applied to human brain data, RUMBA-SD has also achieved the best results, with its reconstructions showing the highest ability to detect fiber crossings (see Figs 7-9). And although any conclusion derived from real data is hampered by the unknown anatomy at the voxel level, all previous results on synthetic data seem to support the validity of RUMBA-SD for real data.

Our findings can also be contrasted with those reported in [55]. In that study, the authors show that the SoS approach produces a signal-dependent bias that reduces the signal dynamic range and may subsequently lead to decreased precision and accuracy in fiber orientation estimates. Our study, however, suggests that the noncentral Chi noise in SoS-based data is not a major concern for the SD methods considered. Thus, heavier squashing of fiber ODFs when SoS reconstruction is used [55] is not that prominent with the SD if compared to diffusion ODF estimation methods [11]. This result may have different explanations for each technique. The robustness of dRL-SD may be explained, in part, by its lower over-all sensitivity to selection of the response function [50], which make it robust to the use of dictionaries estimated from either biased or unbiased signals. This behaviour may be additionally boosted by the inclusion of the damping factor in the RL algorithm. In contrast, the robustness of RUMBA-SD can be explained by the use of proper likelihood models that explicitly consider the bias as a function of the noise corrupting the data.

To finish, some limitations and future extensions of the study should be acknowledged. First, we have not evaluated the proposed method in synthetic data simulating partial Fourier *k*-space acquisitions and with parallel imaging using various acceleration factors (i.e., R>1), yet it may be interesting to consider it. Second, the RUMBA-SD estimation framework is based on a discrete approximation of the fiber ODF, which may be potentially extended to continuous functions on the sphere, like the spherical harmonics and the wavelets. Third, the TV regularization implemented in this study is based on a channel-by-channel first order scheme. New studies may

be designed to compare different regularization techniques such as higher order TV, vectorial TV and the fiber continuity approach introduced in [56], to mention only a few examples. Fourth, different strategies for creating the signal dictionary could be explored, like using mixtures of intra-compartment models to capture different diffusion profiles, or applying more appropriate models to fit multi-shell data [31, 83]. Fifth, the recursive calibration of the single-fiber response function proposed by [84] may be another possible add-on. Finally, it is worth mentioning that the inversion algorithm behind RUMBA-SD is not limited to fiber ODF reconstructions, but it can be also applied to solve other linear mixture models from diffusion MRI data. It was recently showed that some microstructure imaging methods such as ActiveAx and NODDI can be reformulated as convenient linear systems, however, the deconvolution methods proposed for them assume Gaussian noise and are performed on a voxel-by-voxel basis [85]. Here the iterative scheme proposed in RUMBA-SD could be used to address both limitations, potentially leading to improved reconstructions in microstructure imaging.

Acknowledgments

We would like to thank Dr Karla Miller for assisting us with data collection. The presented study is a tribute to composers who popularized Rumba music in the 1940s and 50s, including Dámaso Pérez Prado, Mongo Santamaría, Xavier Cugat, and Chano Pozo.

References

1. Salat DH, Tuch DS, Greve DN, van der Kouwe AJ, Hevelone ND, Zaleta AK, et al. Age-related alterations in white matter microstructure measured by diffusion tensor imaging. Neurobiol Aging. 2005;26(8):1215-27.
2. Iturria-Medina Y, Perez Fernandez A, Morris DM, Canales-Rodriguez EJ, Haroon HA, Garcia Penton L, et al. Brain hemispheric structural efficiency and interconnectivity rightward asymmetry in human and nonhuman primates. Cereb Cortex. 2011;21(1):56-67.
3. Iturria-Medina Y, Sotero RC, Canales-Rodriguez EJ, Aleman-Gomez Y, Melie-Garcia L. Studying the human brain anatomical network via diffusion-weighted MRI and Graph Theory. Neuroimage. 2008;40(3):1064-76.
4. Hagmann P, Cammoun L, Gigandet X, Meuli R, Honey CJ, Wedeen VJ, et al. Mapping the structural core of human cerebral cortex. PLoS Biol. 2008;6(7):e159.
5. Basser PJ, Mattiello J, LeBihan D. Estimation of the effective self-diffusion tensor from the NMR spin echo. J Magn Reson B. 1994;103(3):247-54.
6. Tuch DS, Reese TG, Wiegell MR, Makris N, Belliveau JW, Wedeen VJ. High angular resolution diffusion imaging reveals intravoxel white matter fiber heterogeneity. Magn Reson Med. 2002;48(4):577-82.
7. Fillard P, Descoteaux M, Goh A, Gouttard S, Jeurissen B, Malcolm J, et al. Quantitative evaluation of 10 tractography algorithms on a realistic diffusion MR phantom. Neuroimage. 2011;56(1):220-34.
8. Assemlal HE, Tschumperle D, Brun L, Siddiqi K. Recent advances in diffusion MRI modeling: Angular and radial reconstruction. Med Image Anal. 2011;15(4):369-96.
9. Daducci A, Canales-Rodriguez EJ, Descoteaux M, Garyfallidis E, Gur Y, Ying-Chia L, et al. Quantitative Comparison of Reconstruction Methods for Intra-Voxel Fiber Recovery From Diffusion MRI. Medical Imaging, IEEE Transactions on. 2014;33(2):384-99.
10. Tuch DS. Q-ball imaging. Magn Reson Med. 2004;52(6):1358-72.
11. Aganj I, Lenglet C, Sapiro G, Yacoub E, Ugurbil K, Harel N. Reconstruction of the orientation distribution function in single- and multiple-shell q-ball imaging within constant solid angle. Magn Reson Med. 2010;64(2):554-66.
12. Canales-Rodriguez EJ, Melie-Garcia L, Iturria-Medina Y. Mathematical description of q-space in spherical coordinates: exact q-ball imaging. Magn Reson Med. 2009;61(6):1350-67.
13. Descoteaux M, Angelino E, Fitzgibbons S, Deriche R. Regularized, fast, and robust analytical Q-ball imaging. Magn Reson Med. 2007;58(3):497-510.
14. Anderson AW. Measurement of fiber orientation distributions using high angular resolution diffusion imaging. Magn Reson Med. 2005;54(5):1194-206.
15. Hess CP, Mukherjee P, Han ET, Xu D, Vigneron DB. Q-ball reconstruction of multimodal fiber orientations using the spherical harmonic basis. Magn Reson Med. 2006;56(1):104-17.
16. Tristan-Vega A, Westin CF, Aja-Fernandez S. A new methodology for the estimation of fiber populations in the white matter of the brain with the Funk-Radon transform. Neuroimage. 2010;49(2):1301-15.
17. Tristan-Vega A, Westin CF, Aja-Fernandez S. Estimation of fiber orientation probability density functions in high angular resolution diffusion imaging. Neuroimage. 2009;47(2):638-50.

18. Canales-Rodriguez EJ, Lin CP, Iturria-Medina Y, Yeh CH, Cho KH, Melie-Garcia L. Diffusion orientation transform revisited. Neuroimage. 2010;49(2):1326-39.
19. Ozarslan E, Shepherd TM, Vemuri BC, Blackband SJ, Mareci TH. Resolution of complex tissue microarchitecture using the diffusion orientation transform (DOT). Neuroimage. 2006;31(3):1086-103.
20. Wedeen VJ, Hagmann P, Tseng WY, Reese TG, Weisskoff RM. Mapping complex tissue architecture with diffusion spectrum magnetic resonance imaging. Magn Reson Med. 2005;54(6):1377-86.
21. Canales-Rodriguez EJ, Iturria-Medina Y, Aleman-Gomez Y, Melie-Garcia L. Deconvolution in diffusion spectrum imaging. Neuroimage. 2010;50(1):136-49.
22. Hosseinbor AP, Chung MK, Wu YC, Alexander AL. Bessel Fourier Orientation Reconstruction (BFOR): an analytical diffusion propagator reconstruction for hybrid diffusion imaging and computation of q-space indices. Neuroimage. 2013;64:650-70.
23. Descoteaux M, Deriche R, Le Bihan D, Mangin JF, Poupon C. Multiple q-shell diffusion propagator imaging. Med Image Anal. 2011;15(4):603-21.
24. Wu YC, Alexander AL. Hybrid diffusion imaging. Neuroimage. 2007;36(3):617-29.
25. Yeh FC, Wedeen VJ, Tseng WY. Generalized q-sampling imaging. IEEE Trans Med Imaging. 2010;29(9):1626-35.
26. Ozarslan E, Koay CG, Shepherd TM, Komlosh ME, Irfanoglu MO, Pierpaoli C, et al. Mean apparent propagator (MAP) MRI: a novel diffusion imaging method for mapping tissue microstructure. Neuroimage. 2013;78:16-32.
27. Ozarslan E, Mareci TH. Generalized diffusion tensor imaging and analytical relationships between diffusion tensor imaging and high angular resolution diffusion imaging. Magn Reson Med. 2003;50(5):955-65.
28. Liu C, Bammer R, Acar B, Moseley ME. Characterizing non-Gaussian diffusion by using generalized diffusion tensors. Magn Reson Med. 2004;51(5):924-37.
29. Jensen JH, Helpern JA, Ramani A, Lu H, Kaczynski K. Diffusional kurtosis imaging: the quantification of non-gaussian water diffusion by means of magnetic resonance imaging. Magn Reson Med. 2005;53(6):1432-40.
30. Behrens TE, Berg HJ, Jbabdi S, Rushworth MF, Woolrich MW. Probabilistic diffusion tractography with multiple fibre orientations: What can we gain? Neuroimage. 2007;34(1):144-55.
31. Jbabdi S, Sotiropoulos SN, Savio AM, Grana M, Behrens TE. Model-based analysis of multishell diffusion MR data for tractography: how to get over fitting problems. Magn Reson Med. 2012;68(6):1846-55.
32. Melie-Garcia L, Canales-Rodriguez EJ, Aleman-Gomez Y, Lin CP, Iturria-Medina Y, Valdes-Hernandez PA. A Bayesian framework to identify principal intravoxel diffusion profiles based on diffusion-weighted MR imaging. Neuroimage. 2008;42(2):750-70.
33. Michailovich O, Rathi Y, Dolui S. Spatially regularized compressed sensing for high angular resolution diffusion imaging. IEEE Trans Med Imaging. 2011;30(5):1100-15.
34. Landman BA, Bogovic JA, Wan H, El Zahraa ElShahaby F, Bazin PL, Prince JL. Resolution of crossing fibers with constrained compressed sensing using diffusion tensor MRI. Neuroimage. 2012;59(3):2175-86.

35. Daducci A, Van De Ville D, Thiran JP, Wiaux Y. Sparse regularization for fiber ODF reconstruction: from the suboptimality of l2 and l1 priors to l0. Med Image Anal. 2014;18(6):820-33.
36. Patel V, Shi Y, Thompson PM, Toga AW. Mesh-based spherical deconvolution: a flexible approach to reconstruction of non-negative fiber orientation distributions. Neuroimage. 2010;51(3):1071-81.
37. Dell'acqua F, Scifo P, Rizzo G, Catani M, Simmons A, Scotti G, et al. A modified damped Richardson-Lucy algorithm to reduce isotropic background effects in spherical deconvolution. Neuroimage. 2010;49(2):1446-58.
38. Kaden E, Knosche TR, Anwander A. Parametric spherical deconvolution: inferring anatomical connectivity using diffusion MR imaging. Neuroimage. 2007;37(2):474-88.
39. Tournier JD, Calamante F, Connelly A. Robust determination of the fibre orientation distribution in diffusion MRI: non-negativity constrained super-resolved spherical deconvolution. Neuroimage. 2007;35(4):1459-72.
40. Tournier JD, Calamante F, Gadian DG, Connelly A. Direct estimation of the fiber orientation density function from diffusion-weighted MRI data using spherical deconvolution. Neuroimage. 2004;23(3):1176-85.
41. Kaden E, Kruggel F. Nonparametric Bayesian inference of the fiber orientation distribution from diffusion-weighted MR images. Med Image Anal. 2012;16(4):876-88.
42. Dell'Acqua F, Rizzo G, Scifo P, Clarke RA, Scotti G, Fazio F. A model-based deconvolution approach to solve fiber crossing in diffusion-weighted MR imaging. IEEE Trans Biomed Eng. 2007;54(3):462-72.
43. Ramirez-Manzanares A, Rivera M, Vemuri BC, Carney P, Mareci T. Diffusion basis functions decomposition for estimating white matter intravoxel fiber geometry. IEEE Trans Med Imaging. 2007;26(8):1091-102.
44. Jian B, Vemuri BC. A unified computational framework for deconvolution to reconstruct multiple fibers from diffusion weighted MRI. IEEE Trans Med Imaging. 2007;26(11):1464-71.
45. Alexander DC. Maximum entropy spherical deconvolution for diffusion MRI. Inf Process Med Imaging. 2005;19:76-87.
46. Sotiropoulos SN, Behrens TE, Jbabdi S. Ball and rackets: Inferring fiber fanning from diffusion-weighted MRI. Neuroimage. 2012;60(2):1412-25.
47. Behrens TE, Woolrich MW, Jenkinson M, Johansen-Berg H, Nunes RG, Clare S, et al. Characterization and propagation of uncertainty in diffusion-weighted MR imaging. Magn Reson Med. 2003;50(5):1077-88.
48. Descoteaux M, Deriche R, Knosche TR, Anwander A. Deterministic and probabilistic tractography based on complex fibre orientation distributions. IEEE Trans Med Imaging. 2009;28(2):269-86.
49. Yeh FC, Tseng WY. Sparse solution of fiber orientation distribution function by diffusion decomposition. PLoS One. 2013;8(10):e75747.
50. Parker GD, Marshall D, Rosin PL, Drage N, Richmond S, Jones DK. A pitfall in the reconstruction of fibre ODFs using spherical deconvolution of diffusion MRI data. Neuroimage. 2013;65:433-48.

51. Dey N, Blanc-Feraud L, Zimmer C, Roux P, Kam Z, Olivo-Marin JC, et al. Richardson-Lucy algorithm with total variation regularization for 3D confocal microscope deconvolution. Microsc Res Tech. 2006;69(4):260-6.
52. Starck JL, Pantin E, Murtagh F. Deconvolution in Astronomy: A Review. Publications of the Astronomical Society of the Pacific. 2002;114:1051–69.
53. Gudbjartsson H, Patz S. The Rician distribution of noisy MRI data. Magn Reson Med. 1995;34(6):910-4.
54. Dietrich O, Raya JG, Reeder SB, Ingrisch M, Reiser MF, Schoenberg SO. Influence of multichannel combination, parallel imaging and other reconstruction techniques on MRI noise characteristics. Magn Reson Imaging. 2008;26(6):754-62.
55. Sotiropoulos SN, Moeller S, Jbabdi S, Xu J, Andersson JL, Auerbach EJ, et al. Effects of image reconstruction on fibre orientation mapping from multichannel diffusion MRI: Reducing the noise floor using SENSE. Magn Reson Med. 2013.
56. Reisert M, Kiselev VG. Fiber continuity: an anisotropic prior for ODF estimation. IEEE Trans Med Imaging. 2011;30(6):1274-83.
57. Tournier J-D, Calamante F, Connelly A, editors. A Robust Spherical Deconvolution Method for the Analysis of Low SNR or Low Angular Resolution Diffusion Data. ISMRM 21st Annual Meeting; 2013 20-26 April 2013; Salt Lake City, Utah, USA.
58. Rudin LI, Osher S, Fatemi E. Nonlinear total variation based noise removal algorithms. Physica D. 1992;60:259–68.
59. Blaimer M, Breuer F, Mueller M, Heidemann RM, Griswold MA, Jakob PM. SMASH, SENSE, PILS, GRAPPA: how to choose the optimal method. Top Magn Reson Imaging. 2004;15(4):223-36.
60. Constantinides CD, Atalar E, McVeigh ER. Signal-to-noise measurements in magnitude images from NMR phased arrays. Magn Reson Med. 1997;38(5):852-7.
61. Aja-Fernandez S, Tristan-Vega A, Hoge WS. Statistical noise analysis in GRAPPA using a parametrized noncentral Chi approximation model. Magn Reson Med. 2011;65(4):1195-206.
62. Keil B, Wald LL. Massively parallel MRI detector arrays. J Magn Reson. 2013;229:75-89.
63. Aja-Fernandez S, Tristan-Vega A. Influence of noise correlation in multiple-coil statistical models with sum of squares reconstruction. Magn Reson Med. 2012;67(2):580-5.
64. Aja-Fernandez S, Vegas-Sanchez-Ferrero G, Tristan-Vega A. Noise estimation in parallel MRI: GRAPPA and SENSE. Magn Reson Imaging. 2014;32(3):281-90.
65. Lucy LB. An iterative technique for the rectification of observed distributions. Astron J. 1974;79:745–54.
66. Richardson WH. Bayesian-based iterative method of image restoration. J Opt Soc Am. 1972;62:55–9.
67. Henkelman RM. Measurement of signal intensities in the presence of noise in MR images. Med Phys. 1985;12(2):232-3.
68. Aja-Fernandez S, Tristan-Vega A, Alberola-Lopez C. Noise estimation in single- and multiple-coil magnetic resonance data based on statistical models. Magn Reson Imaging. 2009;27(10):1397-409.
69. Chambolle A. An algorithm for total variation minimization and applications. Journal of Mathematical Imaging and Vision. 2004;20:89–97.

70. Gautschi W, Slavik J. On the Computation of Modified Bessel Function Ratios. MATHEMATICS OF COMPUTATION. 1978;32(143):865-75.
71. Söderman O, Jönsson B. Restricted diffusion in cylindrical geometry. Journal of Magnetic Resonance. 1995;Series A, 117:94-7.
72. Pruessmann KP, Weiger M, Scheidegger MB, Boesiger P. SENSE: sensitivity encoding for fast MRI. Magn Reson Med. 1999;42(5):952-62.
73. Aja-Fernandez S, Brion V, Tristan-Vega A. Effective noise estimation and filtering from correlated multiple-coil MR data. Magn Reson Imaging. 2013;31(2):272-85.
74. Canales-Rodriguez EJ, Melie-Garcia L, Iturria-Medina Y, Martinez-Montes E, Aleman-Gomez Y, Lin CP. Inferring multiple maxima in intravoxel white matter fiber distribution. Magn Reson Med. 2008;60(3):616-30.
75. Smith SM, Jenkinson M, Woolrich MW, Beckmann CF, Behrens TE, Johansen-Berg H, et al. Advances in functional and structural MR image analysis and implementation as FSL. Neuroimage. 2004;23 Suppl 1:S208-19.
76. Clarke RA, Scifo P, Rizzo G, Dell'Acqua F, Scotti G, Fazio F. Noise correction on Rician distributed data for fibre orientation estimators. IEEE Trans Med Imaging. 2008;27(9):1242-51.
77. Tristan-Vega A, Aja-Fernandez S, Westin CF. Least squares for diffusion tensor estimation revisited: propagation of uncertainty with Rician and non-Rician signals. Neuroimage. 2012;59(4):4032-43.
78. Salvador R, Pena A, Menon DK, Carpenter TA, Pickard JD, Bullmore ET. Formal characterization and extension of the linearized diffusion tensor model. Hum Brain Mapp. 2005;24(2):144-55.
79. Brion V, Poupon C, Riff O, Aja-Fernandez S, Tristan-Vega A, Mangin JF, et al. Noise correction for HARDI and HYDI data obtained with multi-channel coils and Sum of Squares reconstruction: An anisotropic extension of the LMMSE. Magn Reson Imaging. 2013;31(8):1360-71.
80. Koay CG, Ozarslan E, Basser PJ. A signal transformational framework for breaking the noise floor and its applications in MRI. J Magn Reson. 2009;197(2):108-19.
81. Garyfallidis E, Brett M, Amirbekian B, Rokem A, Van Der Walt S, Descoteaux M, et al. Dipy, a library for the analysis of diffusion MRI data. Front Neuroinform. 2014;8:8.
82. Manjon JV, Coupe P, Marti-Bonmati L, Collins DL, Robles M. Adaptive non-local means denoising of MR images with spatially varying noise levels. J Magn Reson Imaging. 2010;31(1):192-203.
83. Jeurissen B, Tournier JD, Dhollander T, Connelly A, Sijbers J. Multi-tissue constrained spherical deconvolution for improved analysis of multi-shell diffusion MRI data. Neuroimage. 2014.
84. Tax CM, Jeurissen B, Vos SB, Viergever MA, Leemans A. Recursive calibration of the fiber response function for spherical deconvolution of diffusion MRI data. Neuroimage. 2014;86:67-80.
85. Daducci A, Canales-Rodriguez EJ, Zhang H, Dyrby TB, Alexander DC, Thiran JP. Accelerated Microstructure Imaging via Convex Optimization (AMICO) from diffusion MRI data. Neuroimage. 2015;105:32-44.

Supporting Information

S1 File. Supplementary appendices

S2 File. Supplementary figures

S1 File. Supplementary appendices

A) Relationship with the RL-SD method

In the limit of very high signal to noise ratio (i.e., $\mathbf{S} \circ \mathbf{H}\mathbf{f}^k / \sigma^2 \gg n$) the modified Bessel functions ratio in Eq. (8) tends to the unity (see Fig M in **S2 File**). In that limit, Eq. (8) becomes:

$$\mathbf{f}^{k+1} = \mathbf{f}^k \circ \frac{\mathbf{H}^T\mathbf{S}}{\mathbf{H}^T\mathbf{H}\mathbf{f}^k}, \qquad \textbf{(A-1)}$$

which is just the undamped RL-SD method originally proposed in [42] under the assumption of zero-mean Gaussian noise .

B) Noncentral Chi noise model for SoS data - effective or standard values?

As previously discussed, for scanners with a high number of coils where the effect of noise correlation cannot be easily decoupled, a best approximation for the noise model in SoS-based images is obtained by using effective n_{eff} and σ^2_{eff} values [63]. This section is devoted to provide an initial insight on the implication of using a noncentral Chi noise model in our estimation with standard parameters, instead of the effective ones.

If considering the limit $n \gg 1$, the ratio provided by Eq. (C-1) in Appendix C can be approximated as:

$$\frac{I_n(x)}{I_{n-1}(x)} \approx \frac{x}{n + \sqrt{x^2 + n^2}}, \qquad \textbf{(B-1)}$$

where we have used the identity relating the expansion of a square root in terms of continued fraction. This expression can be regarded as a lower bound for the true ratio, which is more accurate insofar as n increases.

Notably, based on this result we obtain

$$\frac{I_n\left(\mathbf{S}\circ\mathbf{Hf}/\sigma^2\right)}{I_{n-1}\left(\mathbf{S}\circ\mathbf{Hf}/\sigma^2\right)}\approx\frac{\mathbf{S}\circ\mathbf{Hf}}{n\sigma^2+\sqrt{\left(\mathbf{S}\circ\mathbf{Hf}\right)^2+\left(n\sigma^2\right)^2}}. \qquad \textbf{(B-2)}$$

Similarly,

$$\frac{I_{neff}\left(\mathbf{S}\circ\mathbf{Hf}/\sigma_{eff}^2\right)}{I_{neff-1}\left(\mathbf{S}\circ\mathbf{Hf}/\sigma_{eff}^2\right)}\approx\frac{\mathbf{S}\circ\mathbf{Hf}}{n_{eff}\sigma_{eff}^2+\sqrt{\left(\mathbf{S}\circ\mathbf{Hf}\right)^2+\left(n_{eff}\sigma_{eff}^2\right)^2}}. \qquad \textbf{(B-3)}$$

The relevant feature of these relationships is that they do not depend on the individual parameters of interest but just on their products $n\sigma^2$ and $n_{eff}\sigma_{eff}^2$. This implies that although in general the functions $I_n\left(\mathbf{S}\circ\mathbf{Hf}/\sigma^2\right)$ and $I_{neff}\left(\mathbf{S}\circ\mathbf{Hf}/\sigma_{neff}^2\right)$ are different, if $n_{eff}\sigma_{eff}^2=n\sigma^2$ then their ratios (which are the terms used in the computation) satisfy:

$$\frac{I_n\left(\mathbf{S}\circ\mathbf{Hf}/\sigma^2\right)}{I_{n-1}\left(\mathbf{S}\circ\mathbf{Hf}/\sigma^2\right)}\approx\frac{I_{neff}\left(\mathbf{S}\circ\mathbf{Hf}/\sigma_{eff}^2\right)}{I_{neff-1}\left(\mathbf{S}\circ\mathbf{Hf}/\sigma_{eff}^2\right)}. \qquad \textbf{(B-4)}$$

The accuracy of this approximation is determined by the accuracy of Eq. (B-1) and the assumption $n_{eff}\sigma_{eff}^2=n\sigma^2$. Interestingly, in [54] was reported that for a system with 32 receiver channels of non-accelerated SoS-based data, the mean effective number of channels was n_{eff}=12. Theoretical calculations in [63] predict similar n_{eff} values for 32 and 16 coil systems with correlation coefficients between coil of $\rho\approx0.3$ and $\rho\approx0.2$, respectively. In a complementary analysis we have verified that Eq. (B-1) provides a 'reasonable' approximation for that effective

number of channels. Moreover, in [73] was showed that for SoS reconstructions without using fast pMRI techniques the product $n_{eff}\sigma_{eff}^2$ is constant across the image and equal to $n\sigma^2$. These results, taken together, indicate that for *non-accelerated* SoS-based data acquired in multichannel scanners with a high number of coils and moderate correlation coefficients between coils the SD estimation process may be approximately performed using the standard parameters. That is, by working in terms of the real parameters n and σ^2, we can avoid the complex estimation of the spatial-dependent effective parameters.

C) A note on the evaluation of the term $I_n(x)/I_{n-1}(x)$

The proposed SD algorithm involves the evaluation of the ratio of modified Bessel functions of first kind. Such evaluation is best computed by considering the ratio as a new composite function, and not by means of the simple evaluation of the ratio of the individual functions. The main reason for this is related to the divergence towards infinity of the individual functions. For instance, in *Matlab* software, numerical values for $I_n(x)$ are only available for $x \leq 700$; for higher values an infinity value is returned, and thus the ratio cannot be computed.

Interestingly, this ratio can be expressed in terms of Perron continued fraction [70]:

$$\frac{I_n(x)}{I_{n-1}(x)} = \cfrac{x}{2n+x-\cfrac{2x(n+1/2)}{2n+1+2x-\cfrac{2x(n+3/2)}{2n+2+2x-\cfrac{2x(n+5/2)}{2n+3+2x-\ddots}}}} \qquad \textbf{(C-1)}$$

A study about the convergence of this expansion [70] revealed that it converges faster than other analogous representation based on Gauss continued fraction. For the purpose of this application, the summation in Eq. (C-1) is performed up to the final term $\frac{2x(n+5/2)}{2n+3+2x}$. Fig M in **S2 File** shows the accuracy of this approximation for different values of n and for a wide range of values of x.

D) dRL-SD+TV

The dRL-SD method is based on the following iterative scheme [37]:

$$\mathbf{f}^{k+1} = \mathbf{f}^{k} \circ \mathbf{L}^{k}, \tag{D-1}$$

where

$$\mathbf{L}^{k} = \left[1 + \underbrace{\left(1 - \mu \left(1 - \frac{\left(\mathbf{f}^{k}\right)^{\nu}}{\left(\mathbf{f}^{k}\right)^{\nu} + \eta^{\nu}} \right) \right)}_{\mathbf{u}} \circ \left(\frac{\mathbf{H}^{T}\mathbf{S} - \mathbf{H}^{T}\mathbf{H}\mathbf{f}^{k}}{\mathbf{H}^{T}\mathbf{H}\mathbf{f}^{k}} \right) \right] \tag{D-2}$$

and μ is a parameter that depends on the standard deviation of the vector of measurements, $\mu = \max\left(0, 1 - 4std\left(\mathbf{S}\right)\right)$. Notice that when the term $\mathbf{u}$ highlighted in (D-2) is equal to 1, the resulting damped version becomes equal to the original one described in (C-1).

The TV spatially-regularized extension to this method proposed in this work is based on the following modification:

$$\mathbf{f}^{k+1} = \mathbf{f}^{k} \circ \mathbf{L}^{k} \circ \mathbf{R}^{k}, \tag{D-3}$$

where $\mathbf{R}^{k}$ is computed via Eq. (12) and the regularization parameter α_{TV} is computed following an approach similar to that used in RUMBA-SD+TV. Likewise, the noise variance is obtained by minimizing the negative Gaussian log-likelihood with respect to σ^{2}, which yields an iterative scheme analogous to Eq. (9).

S2 File: Supplementary figures

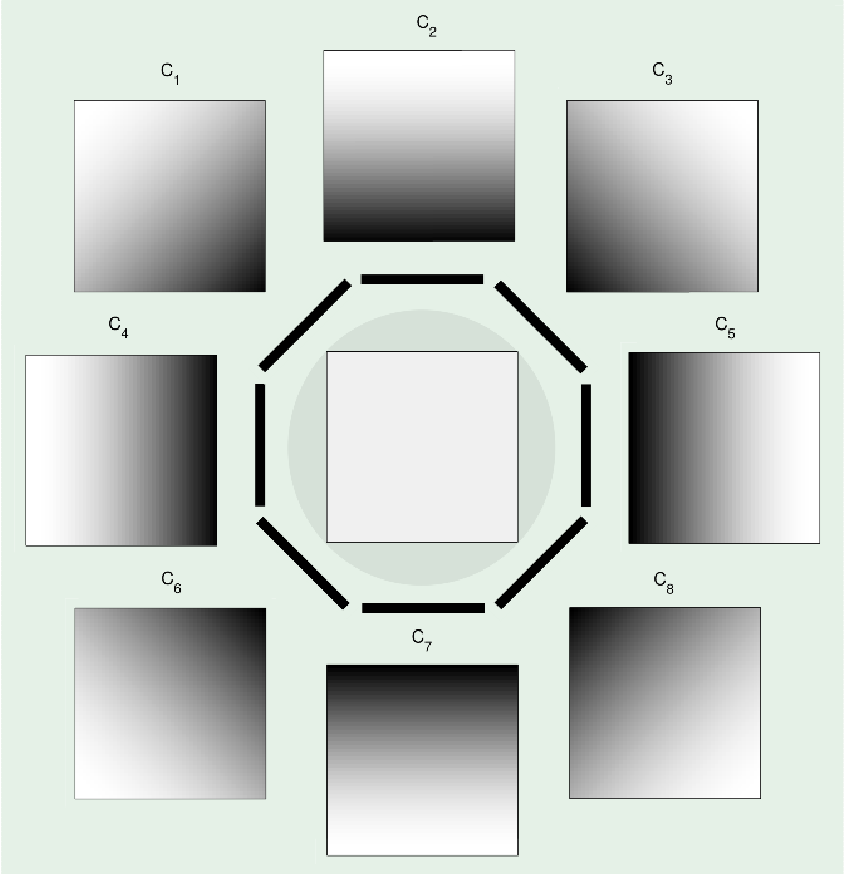

Fig A. Sensitivity maps simulating an eight-coil system. White colors denote higher values. The constant image in the center is the sum-of-squares of the individual sensitivity maps.

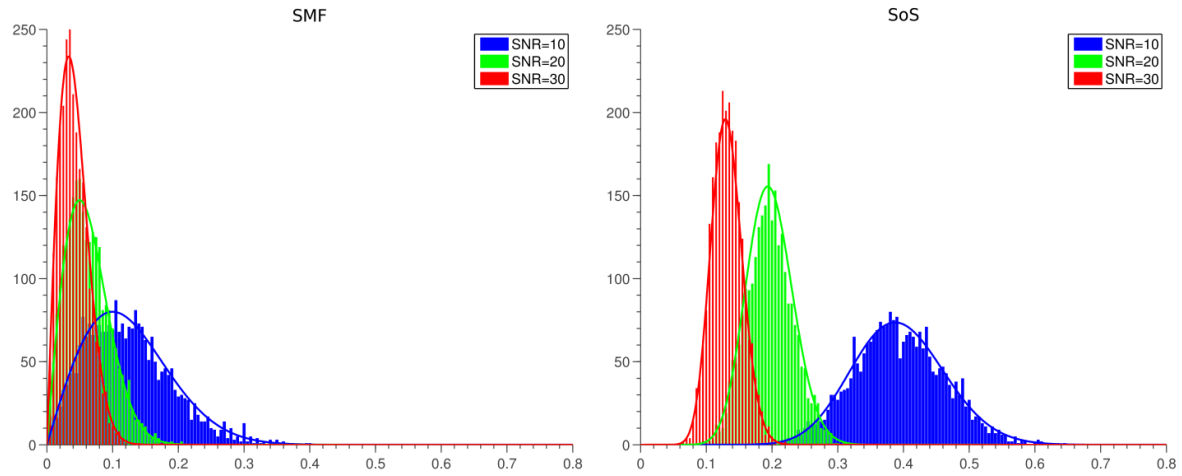

Fig B. Noise distribution profiles resulting from background regions outside the "HARDI Reconstruction Challenge 2013" phantom for the two reconstruction methods and SNR =10, 20 and 30. Rician and noncentral Chi distributions are obtained in SMF- and SoS-based data, respectively. The mean value of the distributions increases as long as the SNR decreases. This bias is higher in the SoS data.

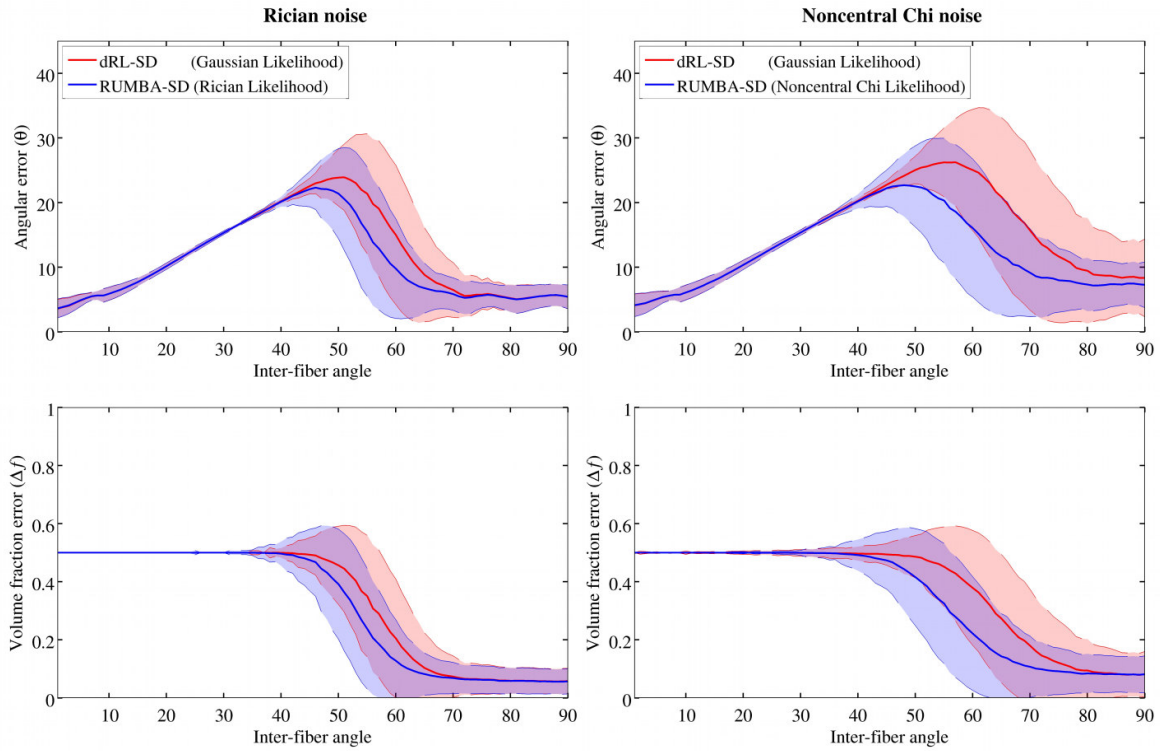

Fig C. Reconstruction accuracy levels for RUMBA-SD and dRL-SD using a dictionary based on estimated diffusivities. Reconstruction accuracy of RUMBA-SD (blue color) and dRL-SD (red color) is shown in terms of the angular error (θ) (see Eq. (17)) and the volume fraction error (Δf) (see Eq.(18)) as a function of the inter-fiber angle in the 90 synthetic phantoms. Continuous lines are mean values and semi-transparent coloured bands contain values within one standard deviation from the mean. Results are based on a dictionary created with empirical diffusivities from a diffusion tensor model applied on the data with a SNR = 15.

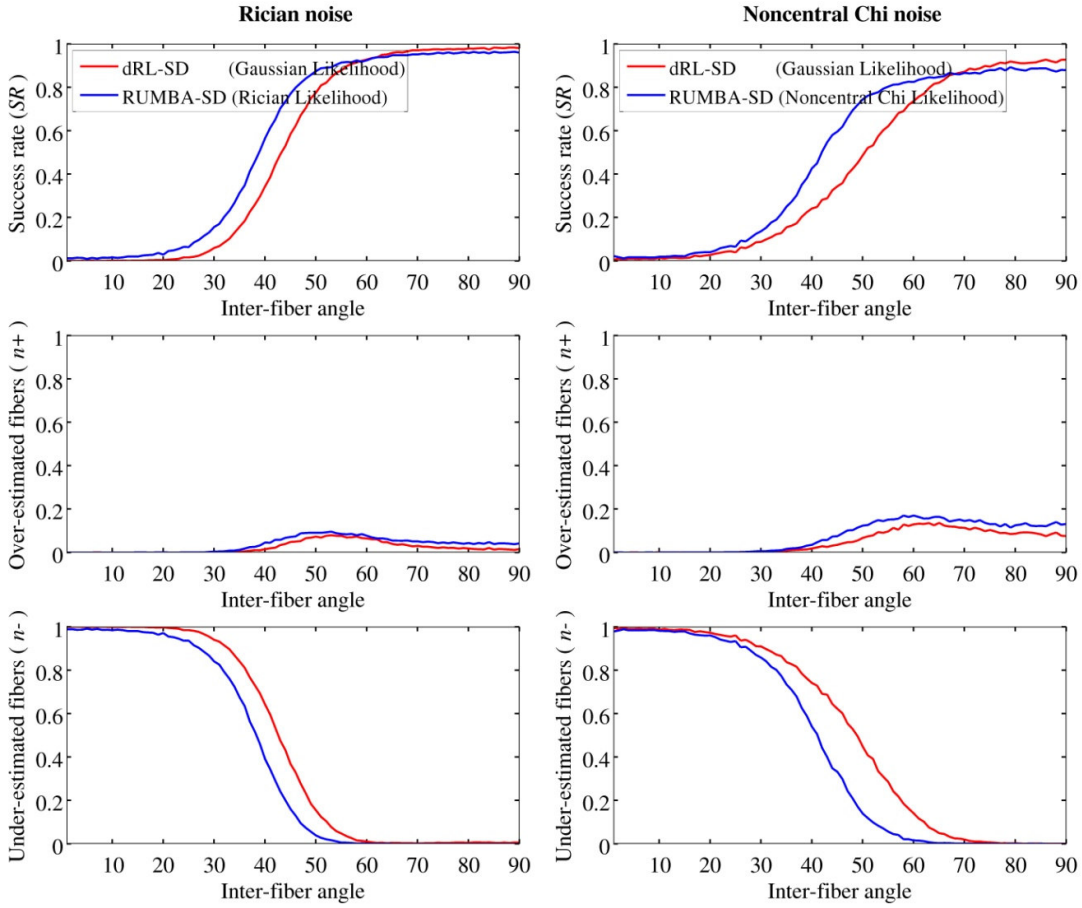

Fig D. Quantification of the reconstruction accuracy of RUMBA-SD (blue color) and dRL-SD (red color) in terms of the success rate (SR) and the mean number of over-estimated (n^+) and under-estimated (n^-) fiber populations, as a function of the inter-fiber angle in the 90 synthetic phantoms. The continuous lines in each plot represent the mean values for each method. This analysis refers to results using a dictionary created with the same diffusivities utilized to generate the data and a level of noise with a SNR = 15.

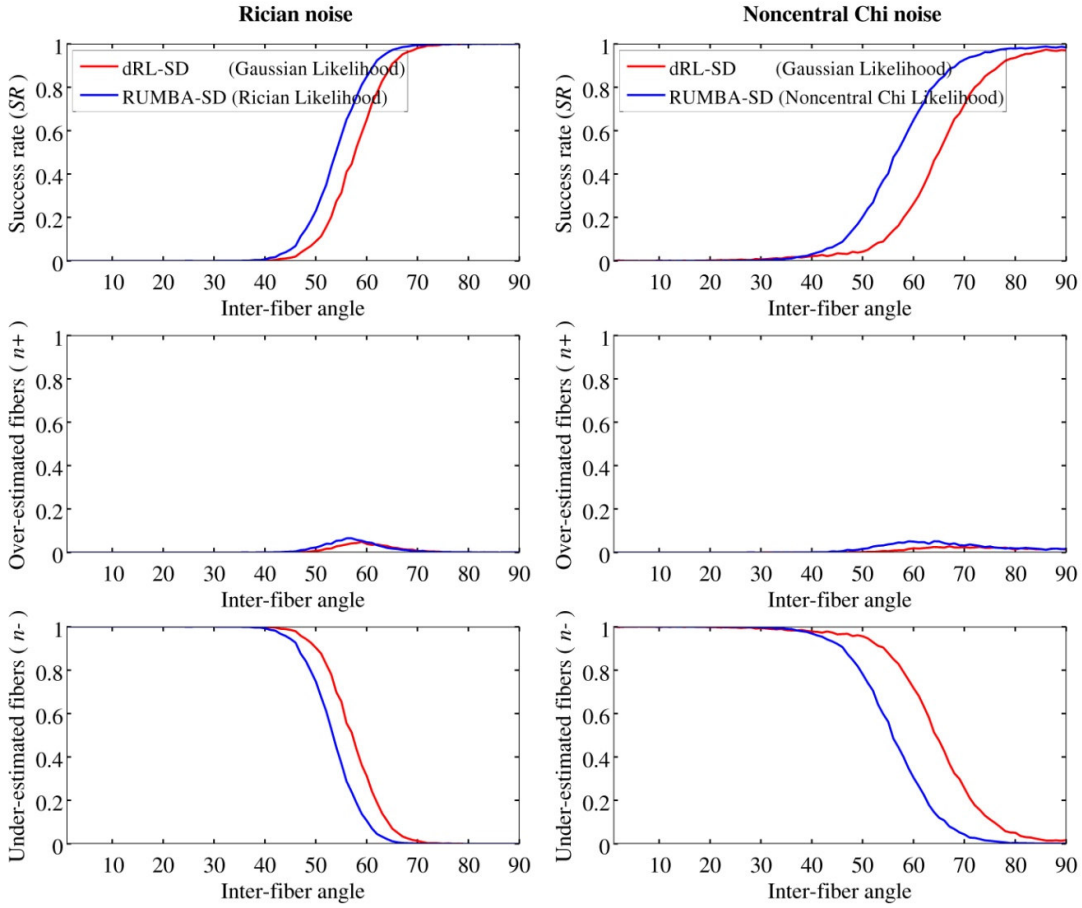

Fig E. Quantification of the reconstruction accuracy of RUMBA-SD (blue color) and dRL-SD (red color) in terms of the success rate (SR) and the mean number of over-estimated (n^+) and under-estimated (n^-) fiber populations, as a function of the inter-fiber angle in the 90 synthetic phantoms. The continuous lines in each plot represent the mean values for each method. This analysis refers to results using a dictionary created with empirical diffusivities estimated by means of the diffusion tensor model from the noisy data with a SNR = 15.

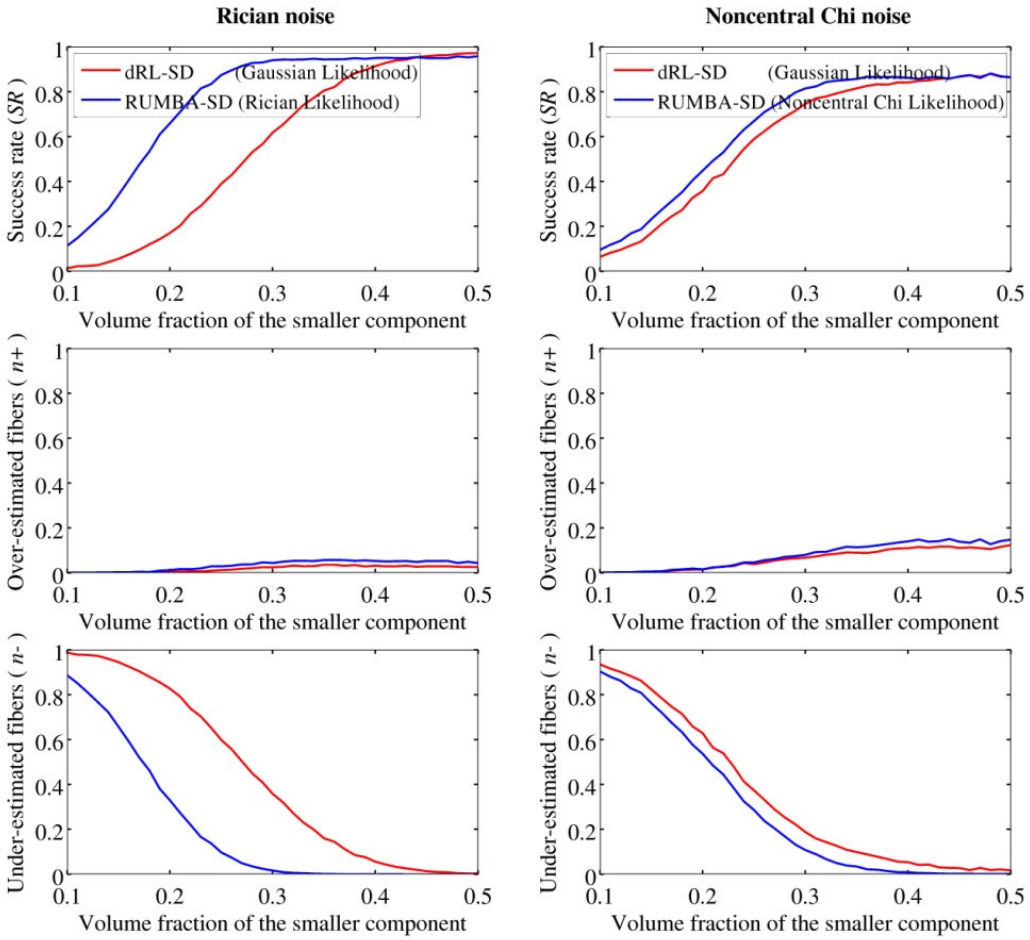

Fig F. Quantification of the reconstruction accuracy of RUMBA-SD (blue color) and dRL-SD (red color) in terms of the success rate (SR) and the mean number of over-estimated (n^+) and under-estimated (n^-) fiber populations, as a function of the volume fraction of the smaller fiber bundle in the 41 synthetic phantoms with inter-fiber angle equal to 70 degrees and different volume fractions. Results refer to the datasets with SNR=15 and dictionary created with the true diffusivities.

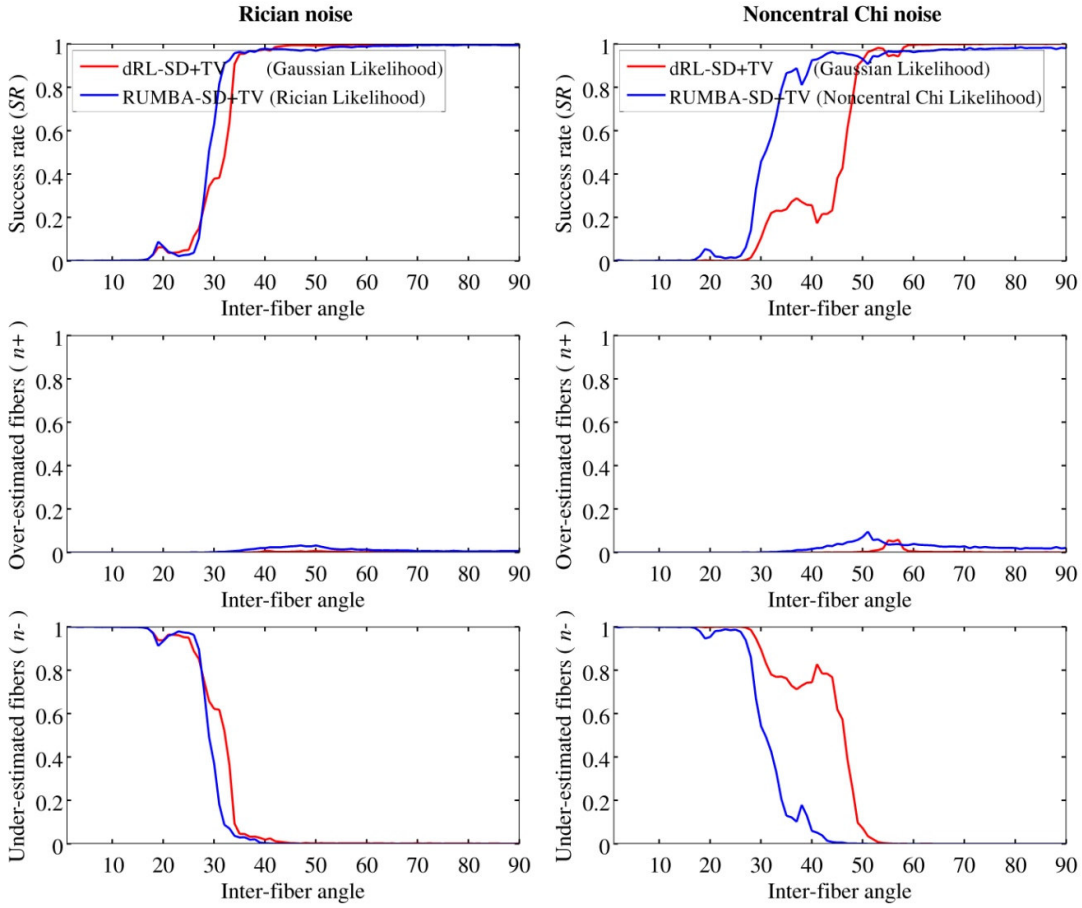

Fig G. Quantification of the reconstruction accuracy of RUMBA-SD+TV (blue color) and dRL-SD+TV (red color) in terms of the success rate (SR) and the mean number of over-estimated (n^+) and under-estimated (n^-) fiber populations, as a function of the inter-fiber angle in the 90 synthetic phantoms. The continuous lines in each plot represent the mean values for each method. This analysis refers to results using a dictionary created with the same diffusivities utilized to generate the data and a level of noise with a SNR = 15.

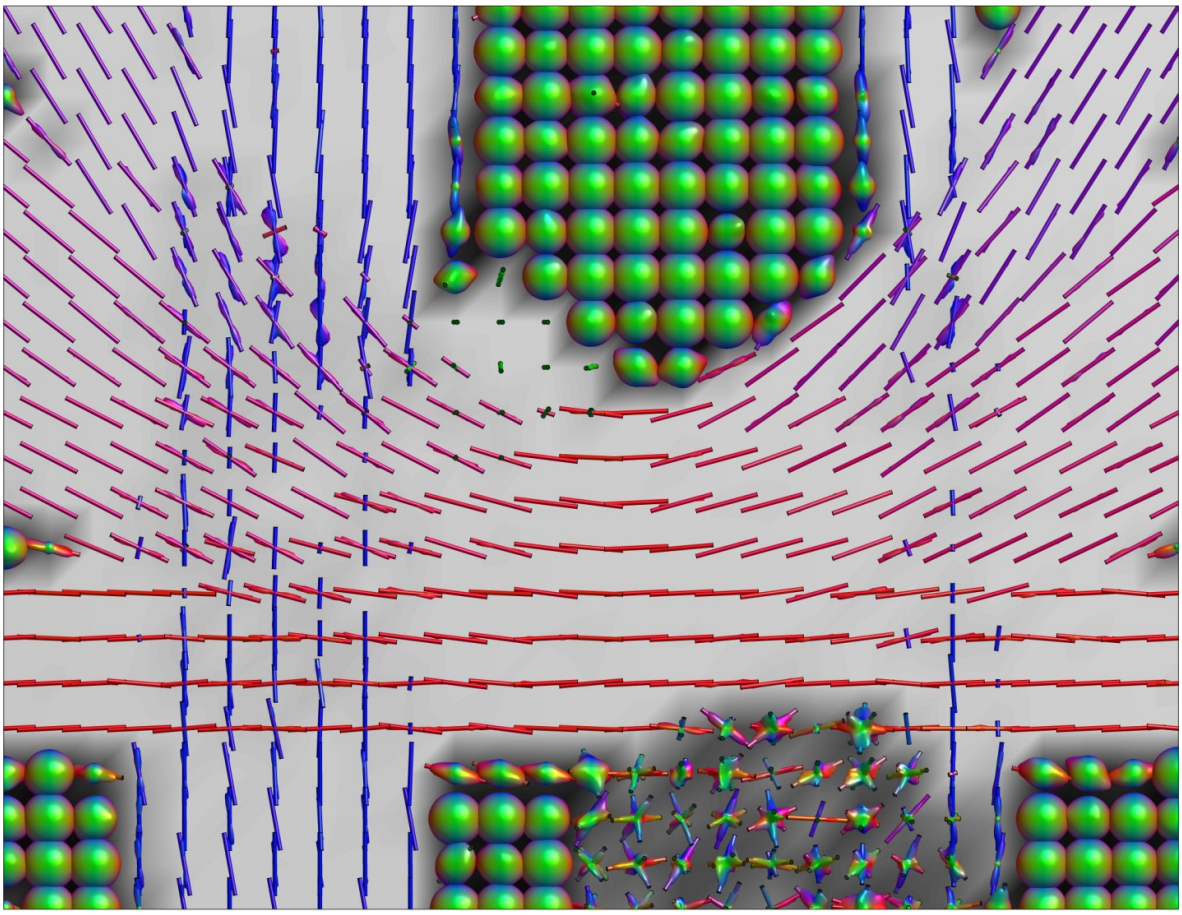

Fig H. Visualization of the fiber ODFs and their peaks (plotted as thin cylinders) reconstructed from the SMF-based data generated with SNR = 20 in a coronal slice of the "HARDI Reconstruction Challenge 2013" phantom. Depicted fiber ODF profiles correspond to the estimates from **dRL-SD** using 400 iterations.

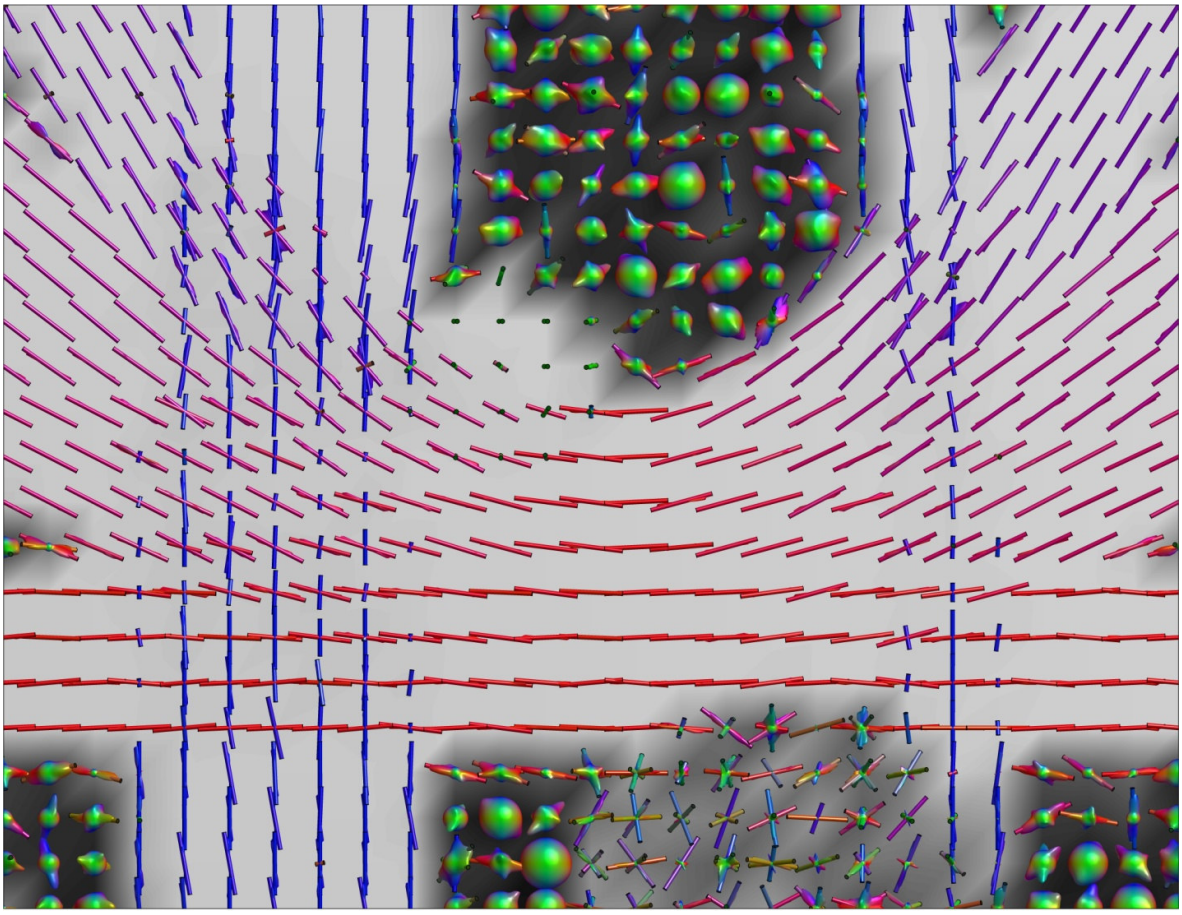

Fig I. Visualization of the fiber ODFs and their peaks (plotted as thin cylinders) reconstructed from the SMF-based data generated with SNR = 20 in a coronal slice of the "HARDI Reconstruction Challenge 2013" phantom. Depicted fiber ODF profiles correspond to the estimates from **RUMBA-SD** using 400 iterations.

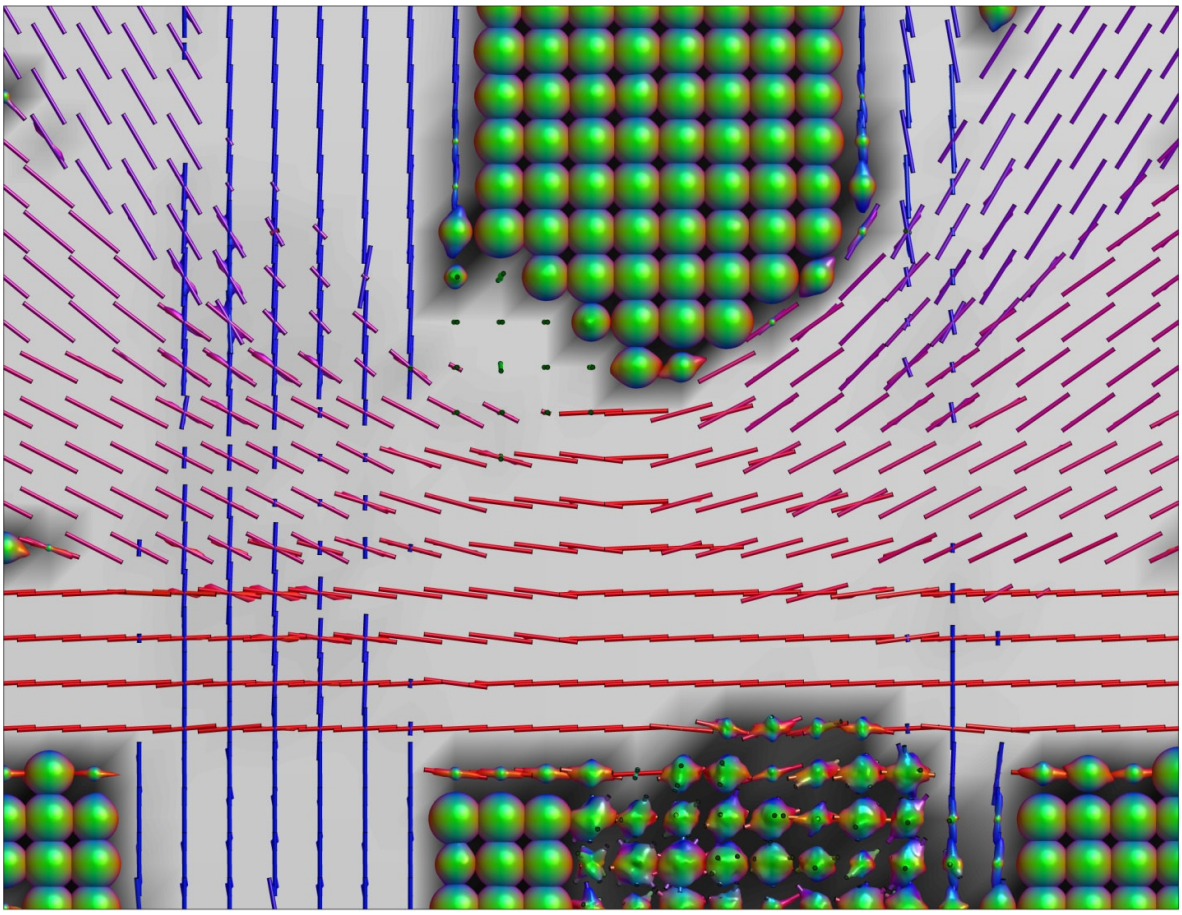

Fig J. Visualization of the fiber ODFs and their peaks (plotted as thin cylinders) reconstructed from the SMF-based data generated with SNR = 20 in a coronal slice of the "HARDI Reconstruction Challenge 2013" phantom. Depicted fiber ODF profiles correspond to the estimates from **dRL-SD+TV** using 400 iterations.

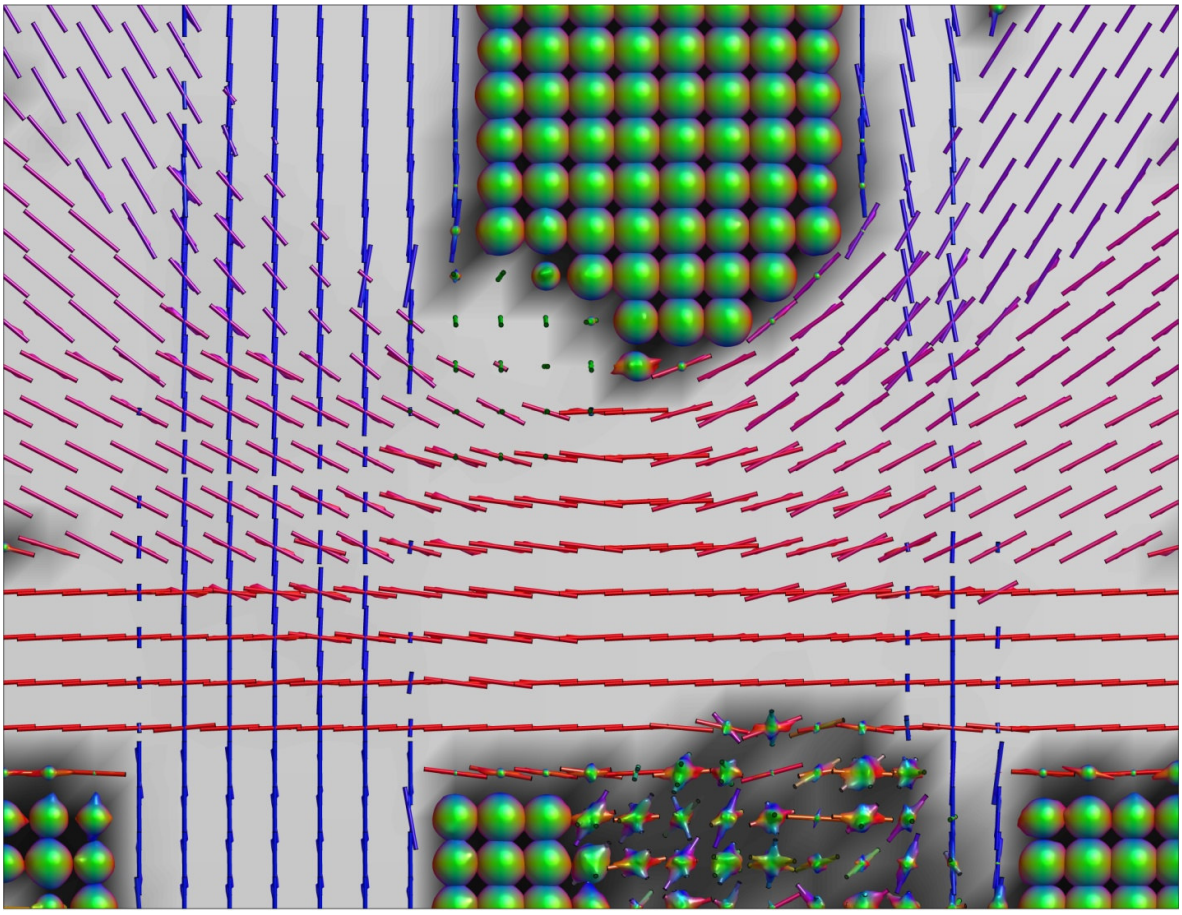

Fig K. Visualization of the fiber ODFs and their peaks (plotted as thin cylinders) reconstructed from the SMF-based data generated with SNR = 20 in a coronal slice of the "HARDI Reconstruction Challenge 2013" phantom. Depicted fiber ODF profiles correspond to the estimates from **RUMBA-SD+TV** using 400 iterations.

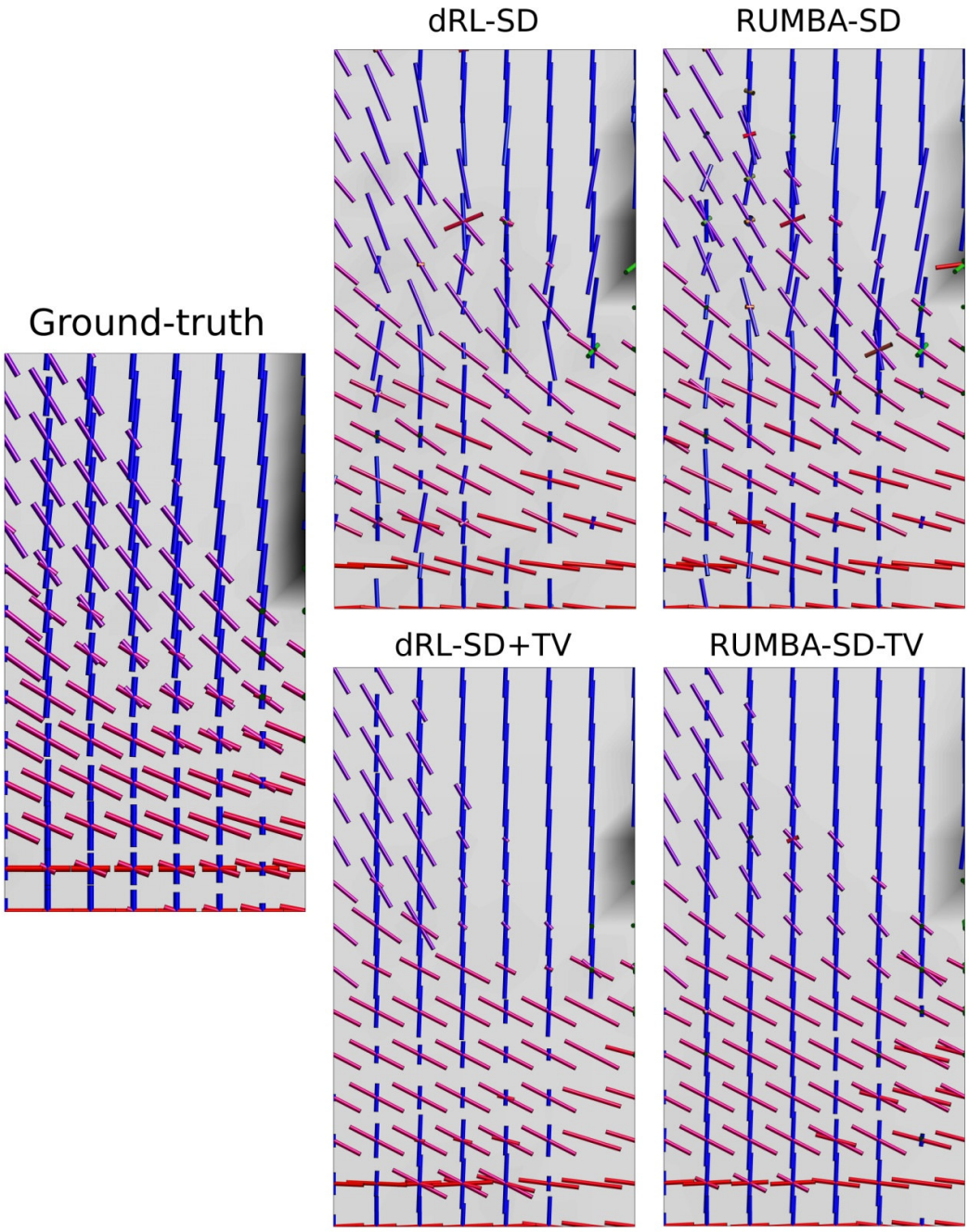

Fig L. Main peaks from the fiber ODFs estimated in the "HARDI Reconstruction Challenge 2013" phantom. Visualization of the main peaks extracted from the fiber ODFs reconstructed

from the SMF-based data generated with SNR = 20 in a complex region of the "HARDI Reconstruction Challenge 2013" phantom. Results are based on reconstructions using 1000 iterations. Peaks are visualized as thin cylinders.

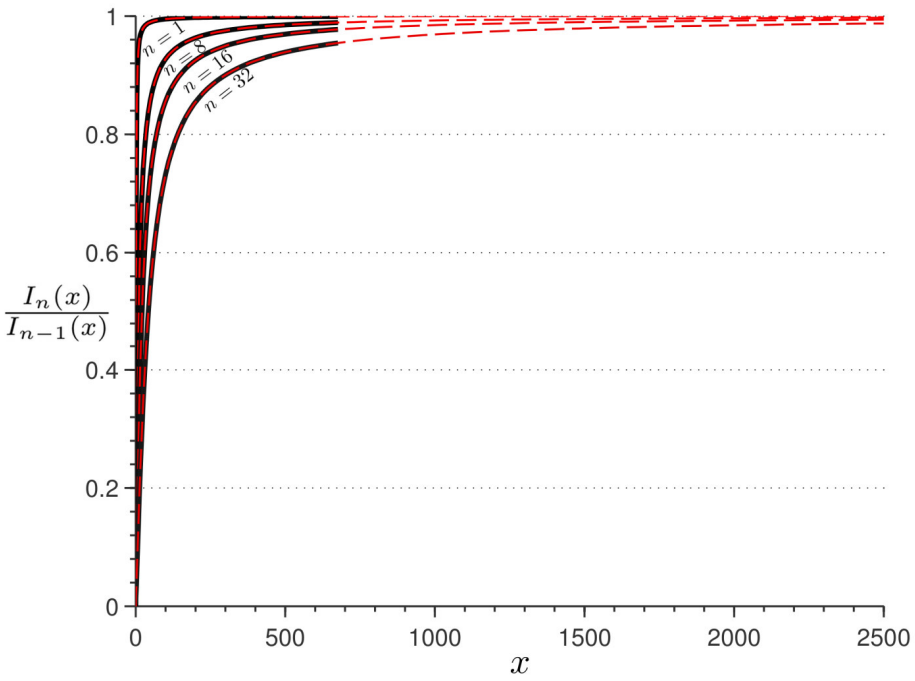

Fig M. Ratio of modified Bessel functions of first kind. Black continuous curves denote the exact values computed by means of the evaluation of the ratio of the individual Bessel functions. The fast divergence towards infinity of the individual functions does not allow evaluating this expression for the whole range of values. Red discontinuous curves denote the values computed by means of the Perron continued fraction approximation in Appendix C in S1 File, in the whole range of values.

PARTE IV: DISCUSIÓN Y CONCLUSIONES GENERALES

CAPÍTULO 6: DISCUSIÓN Y CONCLUSIONES

En este trabajo se han desarrollado varios métodos para la caracterización de la microestructura y la organización compleja de los tejidos cerebrales a través de imágenes de resonancia magnética por difusión. Estos métodos permiten obtener una representación de la forma geométrica en la que ocurre el proceso de difusión del agua y la distribución de la orientación de las fibras nerviosas en cada región de la sustancia blanca. A partir de estas estimaciones es posible obtener información morfológica relevante en aspectos tales como las orientaciones de las fibras, los parámetros físicos que cuantifican los procesos difusivos y las medidas derivadas de anisotropía, así como del volumen relativo de cada grupo de fibras nerviosas.

A modo de resumen, este trabajo aporta las siguientes contribuciones:

(1) Se desarrolló un método de determinación de la magnitud del proceso de difusión del agua a lo largo de cada dirección espacial denominado ‘imagen q-ball exacta’. Este método se basa en una extensión de la popular técnica 'imagen q-ball' y presenta un desarrollo matemático del espacio-q en coordenadas esféricas que permite obtener una expresión analítica y exacta para calcular la función de distribución de orientación del proceso de difusión a partir de los datos medidos.

(2) Se desarrolló un formalismo matemático que extiende el método de la transformada de orientación de la difusión. En particular, se derivaron nuevas ecuaciones analíticas para estimar diferentes variantes de la función de distribución de orientación del proceso de difusión que no existían anteriormente. Los nuevos descriptores son relativamente inmunes a los artefactos producidos por la versión predecesora de la técnica. Además, se realizó un análisis teórico que permite entender los límites de validez de las aproximaciones en las que se sustenta esta metodología.

(3) Se demostró por vez primera que la implementación actual de la técnica de imagen espectral de difusión produce una versión contaminada y borrosa de la verdadera función de distribución de probabilidad de los desplazamientos moleculares, y que el nivel de contaminación depende de la naturaleza finita y discreta de los esquemas experimentales de

medición. Se desarrolló un marco general para rectificar y descontaminar los estimadores que produce soluciones con mayor calidad.

(4) Se desarrolló un enfoque Bayesiano-Estadístico y un algoritmo de estimación basado en cadenas de Markov de Monte Carlo para la identificación de los principales modos de difusión dentro del voxel, así como de algunos de los parámetros físicos que los caracterizan. Se obtuvieron mapas probabilísticos de los cruces de fibras en el cerebro.

(5) Se desarrolló un nuevo algoritmo robusto y sin sesgo para la estimación de la función de distribución de orientación de las fibras nerviosas mediante deconvolución esférica, que toma en cuenta la verdadera distribución del ruido generado en los escáneres de resonancia magnética. Además, este método incorporó un término de corrección espacial que considera la continuidad espacial de las imágenes, el cual resultó muy efectivo para minimizar el efecto negativo del alto nivel de ruido presente en las imágenes de difusión.

(6) La implementación y funcionamiento de los métodos propuestos fueron extensivamente validados en conjuntos de datos simulados, así como en datos reales obtenidos a partir de un arreglo de capilares cilíndricos inmersos en agua (que imitan la geometría de las fibras de sustancia blanca del cerebro) y en datos reales de cerebros humanos. Los resultados obtenidos demuestran que los métodos identifican de forma adecuada las orientaciones de las fibras nerviosas y proveen información relevante de los procesos difusivos que ocurren en los tejidos del cerebro.

6.1 Aplicaciones y colaboraciones

Este trabajo fue realizado parcialmente en colaboración con investigadores de las siguientes instituciones:

- Fundación FIDMAG Germanes Hospitalàries y el Hospital Benito Menni CASM, Barcelona, España.
- Departamento de Ciencias de la Computacion e Inteligencial Artificial, Universidad del País Vasco - Euskal Herriko Unibertsitatea, España.
- Centro de Investigación Biomédica en Red de Salud Mental, CIBERSAM, Madrid, España.
- Centro de Neurociencias de Cuba, La Habana, Cuba.

- Laboratorio de Imagen Médica, Unidad de Medicina y Cirugía Experimental, Hospital Gregorio Marañón, Madrid, España.
- Departamento de Bioingeniería e Ingeniería Aeroespacial. Universidad Carlos III de Madrid, España.
- Laboratorio de Procesado de Imagen (LPI), ETSI Telecomunicación, Universidad de Valladolid, Valladolid, España.
- Department of Biomedical Imaging and Radiological Sciences and the Laboratory for Brain Connectivity, Institute of Neuroscience, National Yang-Ming University, Taipei, Taiwan.
- Signal Processing Lab (LTS5), Ecole polytechnique federale de Lausanne (EPFL), Switzerland.
- The Neuroimaging Research Laboratory (Laboratoire de Recherche en Neuroimagerie: LREN), Department of Clinical Neurosciences, University Hospital Center (CHUV) and the University of Lausanne (UNIL), Switzerland.
- Centre for Functional Magnetic Resonance Imaging of the Brain (FMRIB), University of Oxford, John Radcliffe Hospital, Oxford OX39DU, United Kingdom.
- Institute of Psychiatry, King's College London, London, United Kingdom.
- Section of Biomedical Image Analysis, Department of Radiology, University of Pennsylvania, USA.
- McConnell Brain Imaging Center, Montreal Neurological Institute, McGill University, Montreal, Quebec, Canada.

Además, se ha trabajado de forma conjunta con investigadores de 'Sherbrooke Connectivity Imaging Lab, (SCIL), University of Sherbrooke, Canada' para incorporar el método propuesto en la sección 5.3 (Capítulo 5) al software 'dipy' (84) (web: http://nipy.org/dipy/). Actualmente hay varios proyectos en marcha con el objetivo de extender y aplicar el algoritmo de estimación propuesto en la sección 5.5 a una nueva técnica de reconstrucción de imágenes de la microestructura de los tejidos, surgida de una colaboración previa (85).

6.2 Software

Todos los modelos y técnicas desarrollados en esta tesis han siso implementados en Matlab y se encuentran disponibles de forma gratuita en la web 'HARDI Tools', ubicada en la web de la Sociedad Española de Neuroimagen. Para más detalle véase el APÉNDICE E.

6.3 Reconocimiento e impacto de los métodos propuestos

Varios de los métodos presentados en esta tesis han sido premiados tanto a nivel nacional como internacional.

Los métodos presentados en las secciones 5.1, 5.2, 5.3 y 5.4 del Capítulo 5 forman parte de un compendio de publicaciones para estimar la conectividad anatómica y morfología del cerebro que fue premiado por la Academia de Ciencias de Cuba en 2011.

El método presentado en la sección 5.3 fue premiado por la Sociedad Española de Neuroimagen al trabajo más relevante de 2010. Además, en la primera edición del concurso internacional de reconstrucción de imágenes de difusión de alta resolución angular celebrado en 2012, como parte del congreso 'IEEE International Symposium on Biomedical Imaging', este método fue el que más puntuación global obtuvo en base a diversas métricas para cuantificar la calidad de la reconstrucción.

El método presentado en la sección 5.5 obtuvo el primer premio en la segunda edición del concurso internacional de reconstrucción de imágenes de difusión celebrado en 2013, como parte del congreso 'IEEE International Symposium on Biomedical Imaging', en la categoría de imágenes de alta resolución angular. Al concurso se presentaron un total de 24 equipos de prestigiosas universidades y laboratorios.

En el APÉNDICE D se proporciona más información.

6.4 Recomendaciones

Las contribuciones presentadas en este material no representan el final de esta línea de investigación, puesto que quedan múltiples problemas por solucionar y posibles mejoras a los trabajos propuestos. A continuación se presenta una lista de recomendaciones para trabajos futuros inmediatos:

(1) Las metodologías propuestas en esta tesis pueden ser implementadas en lenguajes de programación que posibiliten un tiempo menor de ejecución y que sean gratuitos (por ejemplo, Lenguaje C, Fortran, etc) de forma que puedan ser usadas por un mayor número de investigadores y de forma más eficiente.

(2) Las técnicas introducidas se deben aplicar en conjuntos de datos de cerebros normales y patológicos para la obtención de mapas cuantitativos que posibiliten testar nuevos biomarcadores. En esta línea, el empleo de máquinas de aprendizaje podría permitir clasificar y predecir el grado de afectación de los pacientes en función de los parámetros microestructurales estimados.

(3) La calidad de la estimación de las técnicas propuestas en la sección 5.5 (Capítulo 5) debe mejorarse con el empleo de otros modelos generativos de la señal de difusión empleada para crear el diccionario. Por ejemplo, mediante modelos recientemente propuestos que aportan una descripción más precisa de los datos en el espacio-q (85–87).

(4) El algoritmo de estimación robusta y sin sesgo propuesto en la sección 5.5, basado en un modelo realista del ruido producido en los escáneres, debe ser extendido para estimar los parámetros del resto de las técnicas propuestas en el marco de esta tesis, así como de otras técnicas similares de reconstrucción de datos de resonancia magnética basadas en modelos lineales.

APÉNDICES

APÉNDICE A: Derivaciones matemáticas del Movimiento Browniano

Supongamos que hay n partículas suspendidas en un medio líquido homogéneo. En un intervalo de tiempo τ las coordenadas (caso unidimensional) de las partículas individuales pueden variar en L, donde L puede ser positivo o negativo y diferente para cada partícula. Para la variable aleatoria L es posible definir una ley de probabilidades ϕ_τ. El número de partículas que experimentan en el intervalo de tiempo τ un desplazamiento que está en el intervalo [L, $L+dL$] puede ser expresado por:

$$dn = \int_{L}^{L+dL} n\phi_\tau(x)dx = n\phi_\tau(L)dL, \qquad \textbf{(A.1)}$$

con la condición de normalización:

$$\int_{-\infty}^{+\infty} \phi_\tau(L)dL = 1. \qquad \textbf{(A.2)}$$

De acuerdo a la definición anterior la magnitud $\phi_\tau(L)dL$ puede ser interpretada como la fracción de moléculas dn/n que en el intervalo de tiempo τ realizan un desplazamiento relativo que está en el intervalo [L, $L+dL$]. Resulta natural asumir que ϕ_τ es diferente de cero solamente para valores muy pequeños de L (debido a los pequeños desplazamientos moleculares que pueden ocurrir en pequeños intervalos de tiempo). Si no hay ninguna dirección preferencial al movimiento, ϕ_τ es simétrica $\phi_\tau(L) = \phi_\tau(-L)$.

Ahora vamos a investigar como el coeficiente de difusión depende de ϕ_τ. Sea $C(x,t)$ la concentración (o densidad de partícula, definida como el número de partículas por unidad de volumen), función del espacio y el tiempo. A partir del valor de esta función en el tiempo t es posible predecir el valor de la concentración en el tiempo $t+\tau$. Si τ es pequeño es posible escribir:

$$C(x,t+\tau) = C(x,t) + \frac{\partial C}{\partial t}\tau. \qquad \textbf{(A.3)}$$

Similarmente, a partir del valor de la concentración en la coordenada espacial x es posible predecir el valor de la concentración en la coordenada $x+L$ para un mismo instante de tiempo. La concentración $C(x+L,t)$ puede ser expandida en potencias de L de acuerdo a:

$$C(x+L,t)=C(x,t)+L\frac{\partial C(x,t)}{\partial x}+\frac{L^2}{2!}\frac{\partial^2 C(x,t)}{\partial x^2}+\ldots \qquad \textbf{(A.4)}$$

De la definición de ϕ_τ se puede obtener la concentración de partículas en la posición espacial x en el tiempo $t+\tau$, a partir de la concentración de partículas en todo el espacio en el tiempo t:

$$C(x,t+\tau)=\int_{L=-\infty}^{L=+\infty} C(x+L,t)\phi_\tau(L)dL. \qquad \textbf{(A.5)}$$

Sustituyendo las ecuaciones (A.3) y (A.4) en (A.5) obtenemos:

$$C(x,t)+\frac{\partial C}{\partial t}\tau=C(x,t)\int_{-\infty}^{+\infty}\phi_\tau(L)dL+\frac{\partial C(x,t)}{\partial x}\int_{-\infty}^{+\infty}L\phi_\tau(L)dL+\frac{1}{2!}\frac{\partial^2 C(x,t)}{\partial x^2}\int_{-\infty}^{+\infty}L^2\phi_\tau(L)dL+\ldots(6)$$

Pudiendo escribirse en virtud de la condición de normalización definida en (A.2):

$$\begin{aligned}&\frac{\partial C}{\partial t}=A\frac{\partial C(x,t)}{\partial x}+D\frac{\partial^2 C(x,t)}{\partial x^2}+\ldots\\&A=\frac{1}{\tau}\int_{-\infty}^{+\infty}L\phi_\tau(L)dL;\quad D=\frac{1}{2\tau}\int_{-\infty}^{+\infty}L^2\phi_\tau(L)dL\end{aligned} \qquad \textbf{(A.6)}$$

Los términos impares en la ecuación anterior son iguales a cero debido a la condición de simetría de ϕ_τ, y los pares de orden mayor que dos pueden ser despreciados al asumirse que ϕ_τ es solamente diferente de cero para valores muy pequeños de L (53). Luego, la ecuación (A.6) puede ser escrita como:

$$\frac{\partial C}{\partial t}=D\frac{\partial^2 C(x,t)}{\partial x^2}. \qquad \textbf{(A.7)}$$

Resulta interesante notar que hemos obtenido la segunda ley de Fick expresada anteriormente por la ecuación (2.4). Esta derivación permite relacionar el coeficiente de difusión molecular D, una magnitud macroscópica, con la función de distribución de probabilidad de los desplazamientos moleculares ϕ_τ, una entidad microscópica [véase la ecuación (A.6)].

La dependencia espacio-temporal de la concentración viene dada por la ecuación diferencial (A.7) y por el conjunto de condiciones iniciales del experimento en particular. El siguiente desarrollo está encaminado a encontrar una expresión analítica para la función ϕ_τ. Sea $R(k,t)$ la transformada de Fourier de la distribución $C(x,t)$

$$R(k,t) = \int_{-\infty}^{\infty} C(x,t)\exp(ikx)\,dx, \qquad \textbf{(A.8)}$$

entonces si multiplicamos la ecuación (A.7) por $\exp(ikx)$ e integramos por todo el espacio, y usamos la relación (A.8), obtenemos:

$$\frac{\partial R(k,t)}{\partial t} = D\int_{-\infty}^{\infty} \frac{\partial^2 C(x,t)}{\partial x^2}\exp(ikx)dx. \qquad \textbf{(A.9)}$$

Suponiendo que

$$\lim_{x\to\pm\infty} C(x,t) = \lim_{x\to\pm\infty} \frac{\partial C(x,t)}{\partial x} = 0, \qquad \textbf{(A.10)}$$

al integrar dos veces por parte la ecuación (A.9), hallamos:

$$\frac{\partial R(k,t)}{\partial t} = -Dk^2 R(k,t). \qquad \textbf{(A.11)}$$

De manera que si $R(k,t)$ es la transformada de la distribución de concentración en el instante t, tenemos como solución en el instante $t+\tau$:

$$R(k,t+\tau) = \exp\left(-Dk^2\tau\right)R(k,t) \qquad \textbf{(A.12)}$$

Si aplicamos la transformada inversa de Fourier a la ecuación anterior, obtenemos:

$$
\begin{aligned}
C(x,t+\tau) &= \int_{-\infty}^{\infty} \exp\left(-Dk^2\tau\right) R(k,t) \exp\left(-ikx\right) dk \\
&= \int_{-\infty}^{\infty} \exp\left(-Dk^2\tau\right) \left(\int_{-\infty}^{\infty} C(x',t) \exp\left(ikx'\right) dx' \right) \exp\left(-ikx\right) dk \\
&= \int_{-\infty}^{\infty} C(x',t) \left(\int_{-\infty}^{\infty} \exp\left(-Dk^2\tau\right) \exp\left[ik(x'-x)\right] dk \right) dx' \\
&= \int_{-\infty}^{\infty} C(x',t) P\left(x'-x,\tau\right) dx',
\end{aligned}
\qquad \textbf{(A.13)}
$$

donde

$$
P\left(x'-x,\tau\right) = \int_{-\infty}^{\infty} \exp\left(-Dk^2\tau\right) \exp\left[ik(x'-x)\right] dk\,. \qquad \textbf{(A.14)}
$$

Haciendo el cambio de variables $x'-x=L$, el resultado final en (A.13) se transforma en:

$$
C(x,t+\tau) = \int_{-\infty}^{\infty} C(x+L,t) P\left(L,\tau\right) dL\,. \qquad \textbf{(A.15)}
$$

De la comparación entre las ecuaciones (A.15) y (A.5) se obtiene que $P\left(L,\tau\right) \equiv \phi_\tau(L)$. Por tanto, la función P es la probabilidad de que una partícula recorra una distancia neta L en un tiempo τ. El desarrollo anterior nos permite obtener una solución analítica para la ley de probabilidad de los desplazamientos moleculares en un medio homogéneo en el que no existen direcciones preferenciales al movimiento; integrando la expresión (A.14), obtenemos:

$$
\begin{aligned}
P\left(L,\tau\right) &= \int_{-\infty}^{\infty} \exp\left(-Dk^2\tau\right) \exp\left(ikL\right) dk \\
&= \frac{1}{\sqrt{4\pi D\tau}} \exp\left(-\frac{L^2}{4D\tau} \right),
\end{aligned}
\qquad \textbf{(A.16)}
$$

que es el caso especial de la distribución de Gauss unidimensional con una dispersión dependiente del tiempo $\sigma = \sqrt{2D\tau}$ y un valor medio igual a cero. Con ayuda de esta ecuación es posible cuantificar los desplazamientos cuadráticos medios que experimentan las partículas (caso unidimensional – eje X):

$$
\overline{x^2} = \int_{-\infty}^{\infty} x^2 P\left(x,\tau\right) dx = \frac{1}{\sqrt{4\pi D\tau}} \int_{-\infty}^{\infty} x^2 \exp\left(-\frac{x^2}{4D\tau} \right) dx = 2D\tau\,, \qquad \textbf{(A.17)}
$$

la extensión al caso tridimensional es directa, denotando a r por el desplazamiento total de la partícula, entonces $r^2 = x^2 + y^2 + z^2$, luego $\overline{r^2} = \overline{x^2} + \overline{y^2} + \overline{z^2}$. Tomando en cuenta la homogeneidad del líquido obtenemos: $\overline{r^2} = 3\overline{x^2} = 6D\tau$.

Resulta interesante advertir que bajo la siguiente condición inicial (todas las partículas en el instante inicial $t = 0$ se encuentran en el origen de coordenadas $x' = 0$):

$$C(x',0) = \delta(x'), \tag{A.18}$$

donde δ es la delta de Dirac, el resultado final obtenido en la ecuación (A.13) se transforma en:

$$\begin{aligned} C(x,\tau) &= \int_{-\infty}^{\infty} C(x',0) P(x'-x,\tau)\, dx' \\ &= \int_{-\infty}^{\infty} \delta(x') P(x'-x,\tau)\, dx' \\ &= P(x,\tau). \end{aligned} \tag{A.19}$$

De este resultado se puede confirmar que, para las condiciones iniciales asumidas, la dependencia espacio-temporal de la concentración viene dada exactamente por la ley de distribución de los desplazamientos moleculares; en este caso la distribución de Gauss.

APÉNDICE B: Expansión de Kramers-Moyal y ley de Fick generalizada

En tres dimensiones, la ecuación (A.15) se escribe como:

$$C(\vec{\mathbf{r}}, t+\tau) = \int C(\vec{\mathbf{r}} - \Delta\vec{\mathbf{r}}, t)\, P(\Delta\vec{\mathbf{r}}, \tau)\, d\Delta\vec{\mathbf{r}}, \tag{B.1}$$

donde $\Delta\vec{\mathbf{r}}$ es el vector de desplazamiento relativo. Expandiendo en Taylor las concentraciones involucradas en (B.1) (véase las ecuaciones (A.3) y (A.4)), obtenemos:

$$C(\vec{\mathbf{r}}, t+\tau) = C(\vec{\mathbf{r}}, t) + \frac{\partial C}{\partial t}\tau + \sum_{n=2}^{\infty} \frac{1}{n!} \frac{\partial^n C}{\partial t^n} \tau^n \tag{B.2}$$

$$C\left(\vec{\mathbf{r}}-\Delta\vec{\mathbf{r}},t\right)=C\left(\vec{\mathbf{r}},t\right)+\sum_{n=1}^{\infty}\frac{(-1)^n}{n!}\left\{\left[\Delta x\frac{\partial}{\partial x'}+\Delta y\frac{\partial}{\partial y'}+\Delta z\frac{\partial}{\partial z'}\right]^n C\left(\vec{\mathbf{r}}',t\right)\right\}_{\substack{x'=x\\y'=y\\z'=z}} \qquad \textbf{(B.3)}$$

donde $\vec{\mathbf{r}}=(x\ y\ z)$, $\vec{\mathbf{r}}'=(x'\ y'\ z')$ y $\Delta\vec{\mathbf{r}}=(\Delta x\ \Delta y\ \Delta z)$. La ecuación (B.3) puede ser escrita como

$$C\left(\vec{\mathbf{r}}-\Delta\vec{\mathbf{r}},t\right)=C\left(\vec{\mathbf{r}},t\right)+\sum_{n=1}^{\infty}\sum_{k=0}^{n}\sum_{q=0}^{k}\frac{(-1)^n}{n!}\binom{n}{k}\binom{k}{q}\Delta x^{n-k}\Delta y^{k-q}\Delta z^{q}\nabla_{n-k,k-q,q}C\left(\vec{\mathbf{r}},t\right), \qquad \textbf{(B.4)}$$

donde

$$\nabla_{n-k,k-q,q}C\left(\vec{\mathbf{r}},t\right)=\left\{\left(\frac{\partial}{\partial x'}\right)^{n-k}\left(\frac{\partial}{\partial y'}\right)^{k-q}\left(\frac{\partial}{\partial z'}\right)^{q}C\left(\vec{\mathbf{r}}',t\right)\right\}_{\substack{x'=x\\y'=y\\z'=z}}. \qquad \textbf{(B.5)}$$

En esta derivación se empleado el teorema del binomio de newton

$$(a+b)^n=\sum_{k=0}^{\infty}\binom{n}{k}a^k b^{n-k}=\sum_{k=0}^{\infty}\frac{n!}{(n-k)!k!}a^k b^{n-k}, \qquad \textbf{(B.6)}$$

donde el factorial del número entero positivo k se calcula como $k!=k\cdot(k-1)\cdots 2\cdot 1$, siendo $0!=1$ por definición. Sustituyendo las expresiones (B.2) y (B.4) en (B.1) obtenemos la expansión de Kramers-Moyal (54):

$$\begin{aligned}\frac{\partial C}{\partial t}\tau+\sum_{n=2}^{\infty}\frac{1}{n!}\frac{\partial^n C}{\partial t^n}\tau^n=&\sum_{n=1}^{\infty}\sum_{k=0}^{n}\sum_{q=0}^{k}\frac{(-1)^n}{n!}\binom{n}{k}\binom{k}{q}\nabla_{n-k,k-q,q}C\left(\vec{\mathbf{r}},t\right)\\&\times\int\Delta x^{n-k}\Delta y^{k-q}\Delta z^{q}P\left(\Delta\vec{\mathbf{r}},\tau\right)d\Delta\vec{\mathbf{r}},\end{aligned} \qquad \textbf{(B.7)}$$

para tiempos pequeños los términos cuadráticos y superiores en la sumatoria del lado izquierdo en (B.7) se pueden despreciar, resultando:

$$\frac{\partial C}{\partial t}=\sum_{n=1}^{\infty}\sum_{k=0}^{n}\sum_{q=0}^{k}\binom{n}{k}\binom{k}{q}\nabla_{n-k,k-q,q}C\left(\vec{\mathbf{r}},t\right)D_{n-k,k-q,q}, \qquad \textbf{(B.8)}$$

donde

$$D_{n-k,k-q,q} = \frac{(-1)^n}{n!\tau} \int \Delta x^{n-k} \Delta y^{k-q} \Delta z^q P(\Delta\vec{\mathbf{r}}, \tau)\, d\Delta\vec{\mathbf{r}}\,. \qquad \textbf{(B.9)}$$

La ecuación (B.8) ofrece una generalización a la segunda ley de Fick (véase la ecuación (2.4)) para el proceso de la difusión (55). El término $D_{n-k,k-q,q}$ es un elemento escalar o componente de un tensor de difusión de orden n. Dichos tensores contienen información sobre la anisotropía del proceso de difusión. Si la función de distribución de probabilidad de los desplazamientos tiene simetría antipodal, $P(\Delta\vec{\mathbf{r}}, \tau) = P(-\Delta\vec{\mathbf{r}}, \tau)$, los tensores de difusión de orden impar son idénticamente iguales a cero.

APÉNDICE C: Listado de publicaciones

A continuación se listan las publicaciones del autor relacionadas con las actividades de investigación durante el periodo de este trabajo. Se muestran en negrita aquellas que han sido incluidas como parte de la memoria de la tesis.

Artículos en revistas internacionales indexadas

1. Erick J Canales-Rodríguez, Alessandro Daducci, Stamatios N Sotiropoulos, Emmanuel Caruyer, Santiago Aja-Fernández, Joaquim Radua, Yasser Iturria-Medina, Lester Melie-García, Yasser Alemán-Gómez, Jean-Philippe Thiran, Salvador Sarró, Edith Pomarol-Clotet, Raymond Salvador. Spherical deconvolution of multichannel diffusion MRI data with non-Gaussian noise models and total variation spatial regularization. PLoS One, 2015 10(10): e0138910. doi:10.1371/journal.pone.0138910.

2. Alessandro Daducci, Erick J Canales-Rodríguez, Hui Zhang, Tim B Dyrby, Daniel C Alexander, Jean-Philippe Thiran. Accelerated Microstructure Imaging via Convex Optimization (AMICO) from diffusion MRI data. Neuroimage, Volume 105, 15 January 2015**.**

3. Victor Vicens, Joaquim Radua, Raymond Salvador, Maria Anguera-Camós, Erick J Canales-Rodríguez, Salvador Sarró, Teresa Maristany, Peter J McKenna, and Edith Pomarol-Clotet. Structural and functional brain changes in delusional disorder**.** *British Journal of Psychiatry*, 2015, Sep 17. pii: bjp.bp.114.159087. [Epub ahead of print].

4. Benedikt L. Amann, Erick J Canales-Rodríguez, Mercé Madre, Joaquim Radua, Gemma Monte, Silvia Alonso-Lana, Ramón Landin-Romero, Ana Moreno-Alcázar, Caterina del Mar Bonnin, Salvador Sarró, Jordi Ortiz-Gil, Jesús J. Gomar, Noemi Moro, Paloma Fernandez-Corcuera, Jose Manuel Goikolea, Josep Blanch, Raymond Salvador, Eduard Vieta, Peter J McKenna, Edith Pomarol-

Clotet. Brain structural changes in schizoaffective disorder compared to schizophrenia and bipolar disorder. *Acta Psychiatrica Scandinavica*, 2015 (In press).

5. Raymond Salvador, Daniel Vega, Juan Carlos Pascual, Josep Marco, Erick J Canales-Rodríguez, Salvatore Aguilar, Maria Anguera, Angel Soto, Joan Ribas, Joaquim Soler, Teresa Maristany, Antoni Rodríguez-Fornells, Edith Pomarol-Clotet. Converging Medial Frontal Resting State and Diffusion Based Abnormalities in Borderline Personality Disorder. Biological Psychiatry, 2014 (In press).

6. Alejandro Pérez Fernández, Lorna García-Pentón, Erick J Canales-Rodríguez, Garikoitz Lerma-Usabiaga, Yasser Iturria-Medina, Francisco J Román, Doug Davidson, Yasser Alemán-Gómez, Joana Acha, Manuel Carreiras. Brain morphometry of Dravet Syndrome. Epilepsy Res. 2014, Oct;108(8):1326-34.

7. Radua J, Rubia K, Erick J Canales-Rodríguez, Pomarol-Clotet E, Fusar-Poli P and Mataix-Cols D (2014). Anisotropic kernels for coordinate-based meta-analyses of neuroimaging studies. Front Psychiatry, 2014 Feb 10;5:13.

8. Joaquim Radua, Mar Grau, Odile A van den Heuvel, Michel Thiebaut de Schotten, Dan J Stein, Erick J Canales-Rodríguez, Marco Catani, David Mataix-Cols. Multimodal Voxel-Based Meta-Analysis of White Matter Abnormalities in Obsessive-Compulsive Disorder.Neuropsychopharmacology, 2014, Jun;39(7):1547-57.

9. Erick J Canales-Rodríguez, Edith Pomarol-Clotet, Joaquim Radua, Salvador Sarró, Silvia Alonso, Caterina Del Mar Bonnín, José M Goikolea, Teresa Maristany, Roberto García-Álvarez, Eduard Vieta, Peter McKenna, Raymond Salvador. Structural abnormalities in bipolareuthymia: a multicontrast molecular diffusion imaging study. Biological Psychiatry, 2014, Aug 1;76(3):239-48.

10. Daducci, Alessandro; Erick J Canales-Rodríguez; Descoteaux, Maxime; Garyfallidis, Eleftherios; Gur, Yaniv; Lin, Ying-Chia; Mani, Merry; Merlet, Sylvain; Paquette, Michael; Ramirez-Manzanares, Alonso; Reisert, Marco; Rodrigues, Paulo Reis; Sepehrband, Farshid; Choupan, Jeiran; Deriche, Rachid; Menegaz, Gloria; Prckovska, Vesna; Rivera, Mariano; Wiaux, Yves; Thiran, Jean-Philippe. Quantitative comparison of reconstruction methods for intra-voxel fiber recovery from diffusion MRI. IEEE Transactions on Medical Imaging, 2014, Feb;33(2):384-99.

11. Joaquim Radua, Erick J Canales-Rodríguez, Edith Pomarol-Clotet, Raymond Salvador. Validity of modulation and optimal settings for advanced voxel-based morphometry. Neuroimage, 2014 Feb 1;86:81-90.

12. Joaquim Radua, Salvador Sarro´, Teresa Vigo, Silvia Alonso-Lana, Mar Bonin, Jordi Ortiz-Gil, Erick J Canales-Rodríguez, Teresa Maristany, Eduard Vieta, Peter J. Mckenna, Raymond Salvador, Edith Pomarol-Clotet. Common and specific brain responses to scenic emotional stimuli. Brain Struct Funct, 2014 Jul;219(4):1463-72.

13. Sans-Sansa B, McKenna PJ, Erick J Canales-Rodríguez, Ortiz-Gil J, López-Araquistain L, Sarró S, Dueñas RM, Blanch J, Salvador R, Pomarol-Clotet E. Association of formal thought disorder in schizophrenia with structural brain abnormalities in language-related cortical regions. Schizophrenia Research, 2013, May;146(1-3):308-13.

14. Erick J Canales-Rodríguez, Joaquim Radua, Edith Pomarol-Clotet, Salvador Sarró, Yasser Alemán-Gómez, Yasser Iturria-Medina and Raymond Salvador. Statistical Analysis of Brain Tissue Images in the Wavelet Domain: Wavelet-Based Morphometry. Neuroimage. 2013 May 15; 72:214-26.

15. Salvador Sarró, Edith Pomarol-Clotet, Erick J Canales-Rodríguez, Raymond Salvador, Jesús J. Gomar, Ramón Landín-Romero, Fidel Vila-Rodríguez, Josep Blanch and Peter J. McKenna. Structural brain changes associated with tardive dyskinesia in schizophrenia. British Journal of Psychiatry, 2013 Jul; 203:51-7.

16. Yasser Iturria-Medina, Alejandro Pérez Fernández, Erick J Canales-Rodríguez, Pedro Valdés Hernández, Lorna García Pentón, Lester Melie García, Agustin Lage Castellanos, Marlis Ontivero Ortega. Automated Discrimination of Brain Pathological State Attending to Complex Structural Brain Network Properties: the Shiverer Mutant Mouse Case. PLoS One. 2011;6(5):e19071. Epub 2011 May 27.

17. Jordi Ortiz-Gil, Edith Pomarol-Clotet, Raymond Salvador, Erick J Canales-Rodríguez, Salvador Sarró, Jesús J. Gomar, Amalia Guerrero, Bibiana Sans-Sansa, Antoni Capdevila, Carme Junqué, Peter J. McKenna. The neural correlates of cognitive impairment in schizophrenia.British Journal of Psychiatry, 2011 Sep;199(3):202-10. Epub 2011 Jul 4.

18. Iturria-Medina Y, Fernández AP, Morris DM, Erick J Canales-Rodríguez, Haroon HA, Pentón LG, Augath M, García LG, Logothetis N, Parker GJ, Melie-García L. Brain Hemispheric Structural Efficiency and Interconnectivity Rightward Asymmetry in Human and Nonhuman Primates. Cerebral Cortex, 2010.

19. Pomarol-Clotet E, Erick J Canales-Rodríguez, Salvador R, Sarró S, Gomar JJ, Vila F, Ortiz-Gil J, Iturria-Medina Y, Capdevila A, McKenna PJ. Medial prefrontal cortex pathology in schizophrenia as revealed by convergent findings from multimodal imaging. Molecular Psychiatry, 2010, 15(8):823-30.

20. Erick J Canales-Rodríguez, Iturria-Medina Y, Alemán-Gómez Y, Melie-García L. Deconvolution in diffusion spectrum imaging. Neuroimage, 2010, Vol 50, 1, 136-149.

21. Erick J Canales-Rodríguez, Lin CP, Iturria-Medina Y, Yeh CH, Cho KH, Melie-García L. Diffusion orientation transform revisited. Neuroimage, 2010, Vol 49, 2, 1326-1339.

22. Erick J Canales-Rodríguez, Lester Melie-García, and Yasser Iturria-Medina. Mathematical Description of q-Space in Spherical Coordinates: Exact q-Ball Imaging. Magnetic Resonance in Medicine, 2009, Vol 61, 3, 1350-1367.

23. Lester Melie-García, Erick J Canales-Rodríguez, Yasser Alemán-Gómez, Ching-Po Lin, Yasser Iturria-Medina, and Pedro Valdés-Hernández. A Bayesian framework to identify principal

intravoxel diffusion profiles based on Diffusion-Weighted MR Imaging. Neuroimage, 2008, Vol 42, 2, 750-770.

24. Erick J Canales-Rodríguez, Lester Melie-García, Yasser Iturria-Medina, Eduardo Martínez-Montes, Yasser Alemán-Gómez and Ching-Po Lin. Inferring Multiple Maxima in Intravoxel White Matter Fiber Distribution. Magnetic Resonance in Medicine, 2008, Vol 60, 3, 616-630.

25. Yasser Iturria-Medina, Roberto C. Sotero, Erick J Canales-Rodríguez, Yasser Alemán-Gómez, Lester Melie-García. Studying the Human Brain Anatomical Network via Diffusion-Weighted MRI and Graph Theory. Neuroimage, 2008, Vol 40, 3, 1064-1076.

26. Y. Iturria-Medina, Erick J Canales-Rodríguez, L. Melie-García, P. A. Valdés-Hernández, E. Martínez-Montes, Y. Alemán-Gómez, and J. M. Sánchez-Bornot. Characterizing brain anatomical connections using diffusion weighted MRI and graph theory. Neuroimage, 2007, Vol 36, 3, 645-660.

27. Pedro A. Valdés-Sosa, Jose M. Sánchez-Bornot, Agustín Lage-Castellanos, Mayrim Vega-Hernández, Jorge Bosch-Bayard, Lester Melie-García and Erick J Canales-Rodríguez. Estimating brain functional connectivity with sparse multivariate autoregression. Philosophical Transactions of the Royal Society B: Biological Sciences, 2005, Vol 360, 1457, 969-981.

Capítulo de libro

1. P. A. Valdés-Sosa, J.M. Bornot-Sánchez, M. Vega-Hernández, L. Melie-García, A. Lage-Castellanos, and Erick J Canales-Rodríguez. Granger Causality on Spatial Manifolds: applications to Neuroimaging. Handbook of Time Series Analysis: Recent Theoretical Developments and Applications. (WILEY), 2006.

Artículos en revistas nacionales

1. Eduardo Martínez Montes, Agustín Lage Castellanos, Erick J Canales-Rodríguez, Yasser Iturria Medina, y Pedro A. Valdés Sosa. El cerebro como sistema complejo: estimación de la conectividad cerebral. Revista Cubana de Física, 2006, 23, 2, 97-106.

2. Yasser Alemán Gómez, Lester Melie García, Erick J Canales-Rodríguez. Modelo de Promediación Bayesiana para la estimación de la distribución de fibras nerviosas en el cerebro. CNIC: Ciencias Biológicas, 2006, Vol 37, 4, 405-413.

3. Erick J Canales-Rodríguez y Lester Melie-García. Caracterización de la anisotropía orientacional intravoxel de las fibras nerviosas en la sustancia blanca del cerebro. CNIC: Ciencias Biológicas, 2006, Vol 37, 4, 336-342.

Conferencias internacionales

1. Anna Auría Rasclosa, Erick J Canales-Rodríguez, Yves Wiaux, Tim Dyrby, Daniel Alexander, Jean-Philippe Thiran, Alessandro Daducci. Accelerated Microstructure Imaging via Convex Optimization (AMICO) in crossing fibers. 23rd annual meeting of the International Society for Magnetic Resonance in Medicine (ISMRM), Toronto, Ontario, Canada, 2015.

2. Erick J Canales-Rodríguez. Robust and unbiased model-based spherical deconvolution of multichannel diffusion MRI data. VERONA DIFFUSION WORKSHOP, 26 May 2014, Verona, Italy.

3. A. Keymer, R. Sauras, S. Roldán, A. Alonso, E. Alvarez, B. Gomez-Anson, F. Nuñez, Erick J Canales-Rodríguez, E. Pomarol-Clotet, S. Duran-Sindreu, I. Corripio. Gray and white matter changes and their relation with prognosis of first episode psychosis. P.3.b. Psychotic disorders and treatment - Psychotic disorders (clinical). European Neuropsychopharmacology, 24, Supplement 2, S509, 2014.

4. Yeh, Ping-Hong; Lee, Namgyun; Morissette, John; Taheri, Arman A.; Kuo, Li-Wei; Yeh, Fang-Cheng; Erick J Canales-Rodríguez; Lui, Wei; Ollinger, John; Oakes, Terrance R.; Ettenhofer, Mark L.; Riedy, Gerard. Evaluation of Diffusion Spectrum Imaging Reconstruction with Trained Dictionaries: Use of 3T MR. Joint Annual Meeting ISMRM-ESMRMB 2014, 10-16 May 2014, Milan, Italy.

5. Yeh, Ping-Hong; Erick J Canales-Rodríguez; Morissette, John; Taheri, Arman A.; Kuo, Li-Wei; Yeh, Fang-Cheng; Lui, Wei; Ollinger, John; Oakes, Terrance R.; Ettenhofer, Mark L.; Riedy, Gerard. Tractography of Richardson-Lucy Spherical Deconvolution Under Rician Noise of Sparse Multiple Q-Shell Diffusion Imaging. Joint Annual Meeting ISMRM-ESMRMB 2014, 10-16 May 2014, Milan, Italy.

6. Erick J Canales-Rodríguez. Richardson-Lucy Spherical Deconvolution under Rician noise with Total Variation Spatial Regularization. IEEE International Symposium on Biomedical Imaging (ISBI 2013), High Angular Resolution Diffusion MRI Reconstruction Challenge, 7-11 April 2013, San Francisco (USA).

7. Erick J Canales-Rodríguez, Lester Melie-García, Yasser Iturria-Medina, Yasser Alemán-Gómez. Evaluation of the Deconvolved Diffusion Spectrum Imaging Technique. IEEE International Symposium on Biomedical Imaging (ISBI 2012), workshop on High Angular Resolution Diffusion MRI Reconstruction Techniques, 2-5 May 2012, (Barcelona, Spain).

8. Erick J Canales-Rodríguez, Lester Melie-García, Yasser Iturria-Medina, Yasser Alemán-Gómez. Multi-Tensor Fitting Guided by ODF Estimation. IEEE International Symposium on Biomedical Imaging (ISBI 2012), workshop on High Angular Resolution Diffusion MRI Reconstruction Techniques, 2-5 May 2012, (Barcelona, Spain).

9. Lorna García-Pentón, Yasser Iturria-Medina, Yasser Aleman-Gómez, Erick J Canales-Rodríguez, Manuel Carreiras. ANATOMICAL CHANGES IN THE BILINGUAL BRAIN: COMBINING VOXEL-BASED MORPHOMETRY (VBM) AND DIFFUSION TENSOR IMAGING (DTI), The 11th International Conference on Cognitive Neuroscience (ICON XI). 25-29 September 2011, (Mallorca, Spain).

10. Iturria Medina Yasser, Ontivero Ortega Marlis, Erick J Canales-Rodríguez, Melie García Lester, Valdés Hernández Pedro, Pérez Fernández Alejandro. Complex mouse brain anatomical network

attributes estimated via diffusion-MRI data and graph theory, Havana 2011, May 16 to 21. V Latin American Congress on Biomedical Engineering (CLAIB2011)

11. Bibiana Sans-Sansa, Edith Pomarol-Clotet, Jordi Ortiz-Gil, Salvador Sarro, Rosa Dueas, Erick J Canales-Rodríguez, Raymond Salvador, Peter McKenna. Neuropsychological, functional MRI and VBM examination of formal thought disorder in schizophrenia. International Clinical Psychopharmacology: September 2011 - Volume 26 - Issue - p e120. The 15th Biennial Winter Workshop in Psychoses, 15-18 November 2009, Barcelona, Spain: IMAGING AND NEUROPATHOLOGY.

12. Peter McKenna, Raymond Salvador, Erick J Canales-Rodríguez, Jesus Gomar, Salvador Sarro, Jordi Ortiz-Gil, Antoni Capdevila; Edith Pomarol-Clotet. Default mode network dysfunction: a potentially important functional brain abnormality in schizophrenia,International Clinical Psychopharmacology: September 2011 - Volume 26 - Issue - p e114. The 15th Biennial Winter Workshop in Psychoses, 15-18 November 2009, Barcelona, Spain: IMAGING AND NEUROPATHOLOGY.

13. Edith Pomarol-Clotet, Erick J Canales-Rodríguez, Raymond Salvador, Salvador Sarró, Jesús J. Gomar, Peter John McKenna. MULTIMODAL IMAGING REVEALS CONVERGENT EVIDENCE OF MEDIAL PREFRONTAL CORTEX PATHOLOGY IN SCHIZOPHRENIA. Schizophrenia Research April 2010 (Vol. 117, Issue 2, Page 460).

14. Peter John McKenna, Jordi Ortiz Gil, Edith Pomarol-Clotet, Raymond Salvador, Erick J Canales-Rodríguez, Salvador Sarro. THE NEURAL CORRELATES OF SEVERE COGNITIVE IMPAIRMENT IN SCHIZOPHRENIA. Schizophrenia Research April 2010 (Vol. 117, Issue 2, Page 469).

15. Edith Pomarol-Clotet, Erick J Canales-Rodríguez, Raymond Salvador, Salvador Sarró, Jesús Gomar, Fidel Vila, Jordi Ortiz-Gil, Yasser Iturria-Medina, Antoni Capdevila, Peter McKenna. Medial prefrontal cortex pathology in schizophrenia: convergent findings from multimodal imaging. Poster: 548 MT-PM, Presented at the 16th Annual Meeting of the Organization for Human Brain Mapping, June 6-10, 2010, Barcelona, Spain.

16. Erick J Canales-Rodríguez, Yasser Iturria-Medina, Yasser Alemán-Gómez, Lester Melie-García. The deconvolution of finite q-space sampling effects in diffusion spectrum imaging. Poster: 812 WTh-PM, Presented at the 16th Annual Meeting of the Organization for Human Brain Mapping, June 6-10, 2010, Barcelona, Spain.

17. Lester Melie-García, Erick J Canales-Rodríguez, Yasser Alemán-Gómez, Ching Po-Lin, Yasser Iturria-Medina, Pedro Valdés-Hernández. Bayesian framework to characterize the intravoxel anisotropy in brain tissues. Presented at the X International Workshop on Differential Equations, Number Theory, Data Analysis Methods and Geometry. University of Havana, February 19-23, 2007.

18. Erick J Canales-Rodríguez, Jorge Bouza-Domínguez, Lester Melie-García. On the Use of Orientation Tensors to Predict Fiber Orientation in Brain White Matter. Presented at the 12th Annual Meeting of the Organization for Human Brain Mapping, Florence, Italy, 11-15 June 2006.

19. Sánchez-Bornot J.M., Lage-Castellanos A., Vega-Hernández M., Bosch-Bayard J., Melie-García L., Erick J Canales-Rodríguez., Valdés-Sosa P. Brain functional connectivity changes in the processing of faces with emotional content. Presented at the IX International Conference on Cognitive Neuroscience. Sep. 5-10, 2005, Havana, Cuba.

20. Iturria-Medina Y., Erick J Canales-Rodríguez, Melie-García L., Bornot J. M. and Valdés-Hernández P. A Graphical Model for Assessing Brain Anatomical Connections using Diffusion Weighted MRI. Presented at the IX International Conference on Cognitive Neuroscience. Sep. 5-10, 2005, Havana, Cuba.

21. Erick J Canales-Rodríguez, Melie-García L., Ching-Po L., Intravoxel Anisotropy Characterization through Diffusion Weighted Imaging (DWI): Initial step in finding correlates between white matter anisotropy and cognitive variables. Presented at the IX International Conference on Cognitive Neuroscience. Sep. 5-10, 2005, Havana, Cuba.

22. Erick J Canales-Rodríguez, Melie-García L., Valdez-Hernández P., Iturria-Medina Y., Alemán-Gómez Y., Bouza-Dominguez J., 2005. A new method for extracting information from intravoxel white matter structures distribution. Presented at the 11th Annual Meeting of the Organization for Human Brain Mapping, June 12-16, 2005, Toronto, Ontario, Canada. Available on CD-Rom in NeuroImage, Vol. 26, No.1.

23. Bouza-Dominguez J., Erick J Canales-Rodríguez, 2005. Toward a new-type of Diffuse Optical Imaging. Presented at the 11th Annual Meeting of the Organization for Human Brain Mapping, June 12-16, 2005, Toronto, Ontario, Canada. Available on CD-Rom in NeuroImage, Vol. 26, No.1.

24. Alemán-Gómez Y., Melie-García L., Erick J Canales-Rodríguez., 2005. Bayesian Model Averaging for estimating nervous fiber distribution in Brain's white matter. Presented at the 11th Annual Meeting of the Organization for Human Brain Mapping, June 12-16, 2005, Toronto, Ontario, Canada. Available on CD-Rom in NeuroImage, Vol. 26, No.1

25. Iturria-Medina Y., Erick J Canales-Rodríguez, Lester Melie-García, Pedro Valdés-Hernández. 2005. Bayesian formulation for fiber tracking. Presented at the 11th Annual Meeting of the Organization for Human Brain Mapping, June 12-16, 2005, Toronto, Ontario, Canada. Available on CD-Rom in NeuroImage, Vol. 26, No.1

26. Iturria-Medina Y., Valdés-Hernández P., Erick J Canales-Rodríguez. 2005. Measures of anatomical connectivity obtained from neuro diffusion images. Presented at the 11th Annual Meeting of the Organization for Human Brain Mapping, June 12-16, 2005, Toronto, Ontario, Canada. Available on CD-Rom in NeuroImage, Vol. 26, No.1

27. Melie-García L., Erick J Canales-Rodríguez, Valdés-Hernández P.A., Anisotropy Characterization in Diffusion Weighted MRI via Reversible Jump MCMC. Presented at the 10th International Conference on Functional Mapping of the Human Brain, June 14-17, 2004, Budapest, Hungary. Available on CD-Rom in NeuroImage, Vol. 22.

APÉNDICE D: Premios y reconocimientos

- Premio de la Academia de Ciencias de Cuba por el trabajo: Determinación de Redes Funcionales en el cerebro mediante la Causalidad de Granger, Año: *2006*. Autores: Pedro A. Valdés Sosa, Jose M. Sánchez Bornot, Agustín Lage Castellanos, Mayrim Vega Hernández, Jorge Bosch Bayard, Lester Melie García y Erick Canales Rodríguez.
- Premio de la Sociedad Española de Neuroimagen al trabajo: Deconvolution in diffusion spectrum imaging, Año: *2010*. Revista: *Neuroimage,* Autores*:* Erick Jorge Canales-Rodríguez, Yasser Iturria-Medina, Yasser Alemán-Gómez y Lester Melie-García.
- Premio de la Academia de Ciencias de Cuba al resultado de la investigación científica: Métodos para el estudio de la conectividad anatómica y morfológica del cerebro. Aplicaciones en humanos y animales, Año: *2011*. Autores: Yasser Iturria-Medina, Lester Melie-García, Erick Jorge Canales-Rodríguez, Pedro Antonio Valdés-Hernández, Gretel Sanabria-Díaz y Yasser Alemán-Gómez.
- Primer lugar en el concurso internacional de reconstrucción de imágenes de resonancia magnética por difusión “High Angular Resolution Diffusion Imaging (HARDI) Reconstruction Challenge 2013”, organizado como parte del congreso “IEEE International Symposium on Biomedical Imaging (ISBI 2013)”, San Francisco (USA), *2013*, por el método: Richardson-Lucy Spherical Deconvolution under Rician noise with Total Variation Spatial Regularization". Autores: Erick Jorge Canales-Rodríguez.

NeuroImageN.es
Sociedad Española de Neuroimagen

PREMIO AL TRABAJO MÁS DESTACADO EN NEUROIMAGEN

La Sociedad Española de Neuroimagen ha seleccionado el trabajo titulado

Deconvolution in diffusion spectrum imaging

publicado en 2010 en la revista *Neuroimage* por los investigadores

Erick Jorge Canales-Rodríguez, Yasser Iturria-Medina, Yasser Alemán-Gómez, y Lester Melie-García

como el trabajo más destacado en neuroimagen del año 2010. Y para que así conste, los miembros del Comité de Selección firman el presente a 31 de julio de 2011.

Premio patrocinado por: GE Healthcare

Dr. Joaquim Radua Dr. Víctor Vicens

LA ACADEMIA DE CIENCIAS DE CUBA

Reconoce públicamente la elección como

PREMIO NACIONAL

al resultado de la investigación científica

Métodos para el estudio de la conectividad anatómica y morfológica del cerebro. Aplicaciones en humanos y animales

Autoría principal: Yasser Iturria Medina

Otros autores: Lester Melie García, Erick J. Canales Rodríguez, Pedro Antonio Valdés-Hernández, Gretel Sanabria Díaz, Yasser Alemán Gómez
Colaboradores: 7
Entidad ejecutora principal: Centro de Neurociencias de Cuba (CNEURO)

Ismael Clark Arxer
Presidente

La Habana, 25 de febrero de 2012

Hermanas Hospitalarias
PROVINCIA DE BARCELONA

FIDMAG
Hermanas Hospitalarias
Research Foundation

Reconocimiento internacional al trabajo de investigación

El pasado mes de Abril se celebró "**HARDI reconstruction challenge 2013**" en el contexto del congreso "*IEEE International Symposium on Biomedical Imaging"* (ISBI 2013) organizado en San Francisco (EE.UU). Se trata de un prestigioso concurso internacional de reconstrucción de imágenes de difusión y constituye un importante desafío para los investigadores que trabajan en el campo de la neuroimagen cerebral.

Nuestro compañero **Erick J. Canales-Rodríguez**, licenciado en Física por la Universidad de La Habana (Cuba), investigador de FIDMAG Hermanas Hospitalarias y miembro de CIBERSAM, ha sido uno de los ganadores en la categoría de muestreo "**HARDI"**, con el proyecto **"Deconvolución de Richardson-Lucy bajo ruido Riciano con regularización espacial de variación total"**. Al concurso se presentaron un total de 24 equipos de diferentes prestigiosas universidades y centros de investigación de todo el mundo.

El principal objetivo del desafío **"HARDI reconstruction challenge 2013"** fue el de proporcionar un marco común para evaluar el rendimiento de diferentes métodos y algoritmos de reconstrucción bajo condiciones controladas. En el concurso no sólo se investigó la precisión en la estimación local de la configuración de las fibras, sino que también se estudió su impacto en análisis posteriores de estimación de conectividad estructural mediante la aplicación de métodos de trazado de fibras.

La **resonancia magnética de difusión** es una potente modalidad de imagen, sensible al movimiento aleatorio de las moléculas de agua en los tejidos biológicos. Mediante el estudio de la anisotropía de este proceso de difusión en la sustancia blanca (movimiento desigual en diferentes direcciones) es posible calcular las orientaciones de los axones lo que permite inferir el cableado neuronal, de otro modo indetectable con otras modalidades de formación de imágenes. El estudio de estos patrones de conectividad es de gran importancia desde una perspectiva clínica, con especial énfasis en los trastornos neurológicos y psiquiátricos.

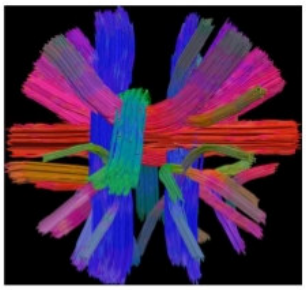

Erick J. Canales-Rodríguez es miembro del CIBERSAM dentro del grupo liderado por Peter J. McKenna. Es autor de numerosas publicaciones en revistas internacionales en el campo de la neuroimagen y los trastornos mentales. Ha recibido diferentes reconocimientos: coautor de un trabajo premiado en 2007 por la Academia de Ciencias de Cuba y autor principal de un trabajo premiado por la Sociedad Española de Neuroimagen como publicación más destacada en 2010. Forma parte de un grupo de investigadores que han sido premiados por la Academia de Ciencias de Cuba en el año 2011 por su contribución en el ámbito de la Biomedicina.

Avda. del Jordà, 8. 08035 BARCELONA
Telf.: 934 186 933. Fax: 932 124 975
www.fidmag.org


2013 HARDI reconstruction challenge winner
HARDI category
Capablanca
(SD with total variation)
E. J. Canales-Rodríguez
CSD
(Constrained SD with NLmeans Rician denoising)
E. Garyfallidis, S. St-Jean, M. Paquette, P. Coupé, M. Descoteaux

APÉNDICE E: Página web "HARDI Tools"

En la siguiente página web, alojada en de la web de la Sociedad Española de Neuroimagen, se pueden encontrar los programas computacionales desarrollados en esta tesis y ejemplos que facilitan su uso: http://neuroimagen.es/webs/hardi_tools/

REFERENCIAS

1. Valdés-Sosa PA, Kötter R, Friston KJ. Introduction: multimodal neuroimaging of brain connectivity. Philos Trans R Soc Lond B Biol Sci. 2005 May 29;360(1457):865–7.

2. Mulert C, Shenton ME, editors. MRI in Psychiatry. Medicine & Health Science Books. Springer; 2014.

3. Hashemi RH, Bradley WG, C.J. L. MRI: The Basics. Third edit. LWW; 2010.

4. Brownstein K, Tarr C. Importance of classical diffusion in NMR studies of water in biological cells. Phys Rev A. 1979 Jun;19(6):2446–53.

5. Smith S. Introduction to the NeuroImage special issue "Mapping the Connectome". Neuroimage. 2013 Oct 15;80:1.

6. LeBihan D. Diffusion and Perfusion Magnetic Resonance Imaging, Applications to Functional MRI. LeBihan D, editor. Raven Press; 1995.

7. Le Bihan D. Looking into the functional architecture of the brain with diffusion MRI. Nat Rev Neurosci. 2003/06/05 ed. 2003;4(6):469–80.

8. Mori S, Crain BJ, Chacko VP, van Zijl PC. Three-dimensional tracking of axonal projections in the brain by magnetic resonance imaging. Ann Neurol. 1999 Feb;45(2):265–9.

9. Iturria-Medina Y, Canales-Rodríguez EJ, Melie-García L, Valdés-Hernández PA, Martínez-Montes E, Alemán-Gómez Y, et al. Characterizing brain anatomical connections using diffusion weighted MRI and graph theory. Neuroimage. 2007;36(3):645–60.

10. Schmitt FC, Kaufmann J, Hoffmann MB, Tempelmann C, Kluge C, Rampp S, et al. Case report: practicability of functionally based tractography of the optic radiation during presurgical epilepsy work up. Neurosci Lett. 2014 May 7;568:56–61.

11. Fillard P, Descoteaux M, Goh A, Gouttard S, Jeurissen B, Malcolm J, et al. Quantitative Evaluation of 10 Tractography Algorithms on a Realistic Diffusion MR Phantom. Neuroimage. 2011 Jan 19;56(1):234–220.

12. Daducci A, Canales-Rodriguez EJ, Descoteaux M, Garyfallidis E, Gur Y, Lin YC, et al. Quantitative comparison of reconstruction methods for intra-voxel fiber recovery from diffusion MRI. IEEE Trans Med Imaging. 2014;33:384–99.

13. Bloch F, Hansen W, Packard M. Nuclear Induction. Phys Rev. 1946 Feb;69(3-4):127–127.

14. Bloch F, Hansen W, Packard M. The Nuclear Induction Experiment. Phys Rev. 1946 Oct;70(7-8):474–85.

15. Purcell E, Torrey H, Pound R. Resonance Absorption by Nuclear Magnetic Moments in a Solid. Phys Rev. 1946 Jan;69(1-2):37–8.

16. Hahn E. Spin Echoes. Phys Rev. 1950 Nov;80(4):580–94.

17. Carr H, Purcell E. Effects of Diffusion on Free Precession in Nuclear Magnetic Resonance Experiments. Phys Rev. 1954 May;94(3):630–8.

18. Torrey H. Bloch Equations with Diffusion Terms. Phys Rev. 1956 Nov;104(3):563–5.

19. Stejskal EO, Tanner JE. Spin Diffusion Measurements: Spin Echoes in the Presence of a Time-Dependent Field Gradient. J Chem Phys. AIP Publishing; 1965 Jul 2;42(1):288.

20. Lauterbur PC. Image Formation by Induced Local Interactions: Examples Employing Nuclear Magnetic Resonance. Nature. 1973 Mar 16;242(5394):190–1.

21. Mansfield P. Multi-planar image formation using NMR spin echoes. J Phys C Solid State Phys. 1977 Feb 14;10(3):L55–8.

22. Kumar A, Welti D, Ernst RR. NMR Fourier zeugmatography. J Magn Reson. 1975 Apr;18(1):69–83.

23. Woessner DE. N.M.R. SPIN-ECHO SELF-DIFFUSION MEASUREMENTS ON FLUIDS UNDERGOING RESTRICTED DIFFUSION. J Phys Chem. American Chemical Society; 1963 Jun;67(6):1365–7.

24. Stejskal EO. Use of Spin Echoes in a Pulsed Magnetic-Field Gradient to Study Anisotropic, Restricted Diffusion and Flow. J Chem Phys. AIP Publishing; 1965 May 19;43(10):3597.

25. Tanner JE. Restricted Self-Diffusion of Protons in Colloidal Systems by the Pulsed-Gradient, Spin-Echo Method. J Chem Phys. AIP Publishing; 1968 Sep 18;49(4):1768.

26. Wayne R, Cotts R. Nuclear-Magnetic-Resonance Study of Self-Diffusion in a Bounded Medium. Phys Rev. 1967 Jul;159(2):486–486.

27. Cooper RL, Chang DB, Young AC, Martin CJ, Ancker-Johnson D. Restricted diffusion in biophysical systems. Experiment. Biophys J. 1974/03/01 ed. 1974 Mar;14(3):161–77.

28. Basser PJ, Mattiello J, LeBihan D. Estimation of the effective self-diffusion tensor from the NMR spin echo. J Magn Reson B. 1994/03/01 ed. 1994;103(3):247–54.

29. Pierpaoli C, Jezzard P, Basser PJ, Barnett A, Di Chiro G. Diffusion tensor MR imaging of the human brain. Radiology. 1996/12/01 ed. 1996;201(3):637–48.

30. Jeurissen B, Leemans A, Tournier J-D, Jones DK, Sijbers J. Investigating the prevalence of complex fiber configurations in white matter tissue with diffusion magnetic resonance imaging. Hum Brain Mapp. 2013 May 19;

31. Frank LR. Anisotropy in high angular resolution diffusion-weighted MRI. Magn Reson Med. 2001/05/30 ed. 2001;45(6):935–9.

32. Frank LR. Characterization of anisotropy in high angular resolution diffusion-weighted MRI. Magn Reson Med. 2002/07/12 ed. 2002;47(6):1083–99.

33. Tuch DS, Reese TG, Wiegell MR, Makris N, Belliveau JW, Wedeen VJ. High angular resolution diffusion imaging reveals intravoxel white matter fiber heterogeneity. Magn Reson Med. 2002/09/28 ed. 2002;48(4):577–82.

34. Hosey T, Williams G, Ansorge R. Inference of multiple fiber orientations in high angular resolution diffusion imaging. Magn Reson Med. 2005/11/03 ed. 2005;54(6):1480–9.

35. Behrens TE, Woolrich MW, Jenkinson M, Johansen-Berg H, Nunes RG, Clare S, et al. Characterization and propagation of uncertainty in diffusion-weighted MR imaging. Magn Reson Med. 2003/10/31 ed. 2003;50(5):1077–88.

36. Behrens TE, Berg HJ, Jbabdi S, Rushworth MF, Woolrich MW. Probabilistic diffusion tractography with multiple fibre orientations: What can we gain? Neuroimage. 2006/10/31 ed. 2007;34(1):144–55.

37. Kaden E, Knösche TR, Anwander A. Parametric spherical deconvolution: Inferring anatomical connectivity using diffusion MR imaging. Neuroimage. 2007;37:474–88.

38. Tournier JD, Yeh CH, Calamante F, Cho KH, Connelly A, Lin CP. Resolving crossing fibres using constrained spherical deconvolution: Validation using diffusion-weighted imaging phantom data. Neuroimage. 2008;42:617–25.

39. Alexander DC. Maximum entropy spherical deconvolution for diffusion MRI. Inf Process Med Imaging. 2005;19:76–87.

40. Tournier J-D, Calamante F, Gadian DG, Connelly A. Direct estimation of the fiber orientation density function from diffusion-weighted MRI data using spherical deconvolution. Neuroimage. 2004 Nov;23(3):1176–85.

41. Dell'Acqua F, Scifo P, Rizzo G, Catani M, Simmons A, Scotti G, et al. A modified damped Richardson-Lucy algorithm to reduce isotropic background effects in spherical deconvolution. Neuroimage. 2010;49:1446–58.

42. Gudbjartsson H, Patz S. The Rician distribution of noisy MRI data. Magn Reson Med. 1995/12/01 ed. 1995;34(6):910–4.

43. Dietrich O, Raya JG, Reeder SB, Ingrisch M, Reiser MF, Schoenberg SO. Influence of multichannel combination, parallel imaging and other reconstruction techniques on MRI noise characteristics. Magn Reson Imaging. 2008/04/29 ed. 2008;26(6):754–62.

44. Tuch DS. Q-ball imaging. Magn Reson Med. 2004;52:1358–72.

45. Tuch DS, Reese TG, Wiegell MR, Wedeen VJ. Diffusion MRI of complex neural architecture. Neuron. 2003/12/09 ed. 2003;40(5):885–95.

46. Wedeen VJ, Hagmann P, Tseng WY, Reese TG, Weisskoff RM. Mapping complex tissue architecture with diffusion spectrum magnetic resonance imaging. Magn Reson Med. 2005/10/26 ed. 2005;54(6):1377–86.

47. Setsompop K, Kimmlingen R, Eberlein E, Witzel T, Cohen-Adad J, McNab JA, et al. Pushing the limits of in vivo diffusion MRI for the Human Connectome Project. Neuroimage. 2013 Oct 15;80:220–33.

48. Ozarslan E, Shepherd TM, Vemuri BC, Blackband SJ, Mareci TH. Resolution of complex tissue microarchitecture using the diffusion orientation transform (DOT). Neuroimage. 2006/03/21 ed. 2006;31(3):1086–103.

49. Fick A. Ueber Diffusion. Ann der Phys und Chemie. 1855;170(1):59–86.

50. Brown R. A brief account of microscopical observations made in the months of June, July and August, 1827, on the particles contained in the pollen of plants; and on the general existence of active molecules in organic and inorganic bodies. Phil Mag. 1828;4:161–73.

51. Einstein A. Über die von der molekularkinetischen Theorie der Wärme geforderte Bewegung von in ruhenden Flüssigkeiten suspendierten Teilchen. Ann Phys. 1905;322(8):549–60.

52. Perrin JB. Mouvement brownien et réalité moléculaire. Ann Chim Phys. 1909;VIII(18):5–114.

53. Einstein A. Investigations on the theory of brownian motion. DOVER PUBLICATIONS; 1956.

54. Liu C, Bammer R, Acar B, Moseley ME. Characterizing non-Gaussian diffusion by using generalized diffusion tensors. Magn Reson Med. 2004/05/04 ed. 2004;51(5):924–37.

55. Liu C, Bammer R, Moseley ME. Limitations of apparent diffusion coefficient-based models in characterizing non-gaussian diffusion. Magn Reson Med. 2005 Aug;54(2):419–28.

56. Liu C, Mang SC, Moseley ME. In vivo generalized diffusion tensor imaging (GDTI) using higher-order tensors (HOT). Magn Reson Med. 2009/12/03 ed. 2010 Jan;63(1):243–52.

57. Basser PJ, Mattiello J, LeBihan D. MR diffusion tensor spectroscopy and imaging. Biophys J. 1994/01/01 ed. 1994;66(1):259–67.

58. Basser PJ. Relationships between diffusion tensor and q-space MRI. Magn Reson Med. 2002/01/26 ed. 2002;47(2):392–7.

59. Basser PJ, Pierpaoli C. Microstructural and physiological features of tissues elucidated by quantitative-diffusion-tensor MRI. J Magn Reson B. 1996;111:209–19.

60. Basser PJ. New Histological and Physiological Stains Derived from Diffusion-Tensor MR Images. Ann N Y Acad Sci. Blackwell Publishing Ltd; 1997 May 30;820(1):123–38.

61. Hornak JP. The Basis of MRI. www.cis.rit.edu/htbooks/mri/inside.htm;

62. Liang Z, Lauterbur PC. Principles of Magnetic Resonance Imaging. A signal Processing Perspective. IEEE Press Series on Biomedical Engineering, SPIE Optical Engineering Press; 1999.

63. Johansen-Berg H, Behrens TEJ, editors. Diffusion MRI: From quantitative measurement to in-vivo neuroanatomy. Academic Press; 2009.

64. Hagmann P. From diffusion MRI to brain connectomics, PhD Thesis. EPFL; 2005.

65. Lebihan D, Breton E. Imagerie de Diffusion In Vivo par Résonance Magnétique Nucléaire. CR Académie des Sci Paris. 1985;301:1109–12.

66. Tuch DS. Diffusion MRI of Complex Tissue Structure, PhD Thesis. MIT; 2002.

67. Hagmann P, Jonasson L, Maeder P, Thiran J-P, Wedeen VJ, Meuli R. Understanding diffusion MR imaging techniques: from scalar diffusion-weighted imaging to diffusion tensor imaging and beyond. Radiographics. 2006 Oct;26 Suppl 1:S205–23.

68. Canales-Rodríguez EJ, Iturria-Medina Y, Alemán-Gómez Y, Melie-García L, Canales-Rodriguez EJ, Aleman-Gomez Y, et al. Deconvolution in diffusion spectrum imaging. Neuroimage. 2009/12/08 ed. 2010;50(1):136–49.

69. Canales-Rodriguez EJ, Melie-Garcia L, Iturria-Medina Y, Canales-Rodríguez EJ, Melie-García L. Mathematical description of q-space in spherical coordinates: Exact q-ball imaging. Magn Reson Med. 2009/03/26 ed. 2009;61(6):1350–67.

70. Canales-Rodríguez EJ, Lin CP, Iturria-Medina Y, Yeh CH, Cho KH, Melie-García L, et al. Diffusion orientation transform revisited. Neuroimage. 2009/10/10 ed. 2010;49(2):1326–39.

71. Parker GJM, Luzzi S, Alexander DC, Wheeler-Kingshott CAM, Ciccarelli O, Lambon Ralph MA. Lateralization of ventral and dorsal auditory-language pathways in the human brain. Neuroimage. 2005 Feb 1;24(3):656–66.

72. Alexander DC, Barker GJ, Arridge SR. Detection and modeling of non-Gaussian apparent diffusion coefficient profiles in human brain data. Magn Reson Med. 2002/09/05 ed. 2002;48(2):331–40.

73. Melie-Garcia L, Canales-Rodriguez EJ, Aleman-Gomez Y, Lin CP, Iturria-Medina Y, Valdes-Hernandez PA, et al. A Bayesian framework to identify principal intravoxel

diffusion profiles based on diffusion-weighted MR imaging. Neuroimage. 2008/06/24 ed. 2008;42(2):750–70.

74. Alexander DC. Maximum Entropy Spherical Deconvolution for Diffution MRI. Information Processing in Medical Imaging. 2005. p. 76–87.

75. Dell'Acqua F, Rizzo G, Scifo P, Clarke RA, Scotti G, Fazio F. A model-based deconvolution approach to solve fiber crossing in diffusion-weighted MR imaging. IEEE Trans Biomed Eng. 2007/03/16 ed. 2007;54(3):462–72.

76. Ramirez-Manzanares A, Rivera M, Vemuri BC, Carney P, Mareci T. Diffusion basis functions decomposition for estimating white matter intravoxel fiber geometry. IEEE Trans Med Imaging. 2007/08/19 ed. 2007;26(8):1091–102.

77. Daducci A, Van De Ville D, Thiran JP, Wiaux Y. Sparse regularization for fiber ODF reconstruction: From the suboptimality of ℓ2 and ℓ1 priors to ℓ0. Med Image Anal. 2014;18:820–33.

78. Descoteaux M, Deriche R, Knosche TR, Anwander A. Deterministic and probabilistic tractography based on complex fibre orientation distributions. IEEE Trans Med Imaging. 2009/02/04 ed. 2009;28(2):269–86.

79. Jian B, Vemuri BC. A unified computational framework for deconvolution to reconstruct multiple fibers from diffusion weighted MRI. IEEE Trans Med Imaging. 2007;26:1464–71.

80. Patel V, Shi Y, Thompson PM, Toga AW. Mesh-based spherical deconvolution: A flexible approach to reconstruction of non-negative fiber orientation distributions. Neuroimage. 2010;51:1071–81.

81. Tournier J-DD, Calamante F, Connelly A. Robust determination of the fibre orientation distribution in diffusion MRI: non-negativity constrained super-resolved spherical deconvolution. Neuroimage. 2007 May 1;35(4):1459–72.

82. Parker GD, Marshall D, Rosin PL, Drage N, Richmond S, Jones DK. A pitfall in the reconstruction of fibre ODFs using spherical deconvolution of diffusion MRI data. Neuroimage. 2013;65:433–48.

83. Canales-Rodríguez EJ, Daducci A, Sotiropoulos SN, Caruyer E, Aja-Fernández S, Radua J, et al. Spherical deconvolution of multichannel diffusion MRI data with non-Gaussian noise models and total variation spatial regularization. 2014 Oct 23;

84. Garyfallidis E, Brett M, Amirbekian B, Rokem A, Van Der Walt S, Descoteaux M, et al. Dipy, a library for the analysis of diffusion MRI data. Front Neuroinform. 2014;8:8.

85. Daducci A, Canales-Rodríguez EJ, Zhang H, Dyrby TB, Alexander DC, Thiran J-P. Accelerated Microstructure Imaging via Convex Optimization (AMICO) from diffusion MRI data. Neuroimage. 2015 Jan;105:32–44.

86. Assaf Y, Basser PJ. Composite hindered and restricted model of diffusion (CHARMED) MR imaging of the human brain. Neuroimage. 2005;27:48–58.

87. Jbabdi S, Sotiropoulos SN, Savio AM, Grana M, Behrens TE. Model-based analysis of multishell diffusion MR data for tractography: how to get over fitting problems. Magn Reson Med. 2012/02/16 ed. 2012;68(6):1846–55.